Geofluids

Interactions of Flowing Grout and Soil/Rock Under Different Diffusion Patterns: Permeation, Compaction, and Fracturing

Lead Guest Editor: Shanyong Wang
Guest Editors: Xinyu Ye, Qiong Wang, and Xueming Du

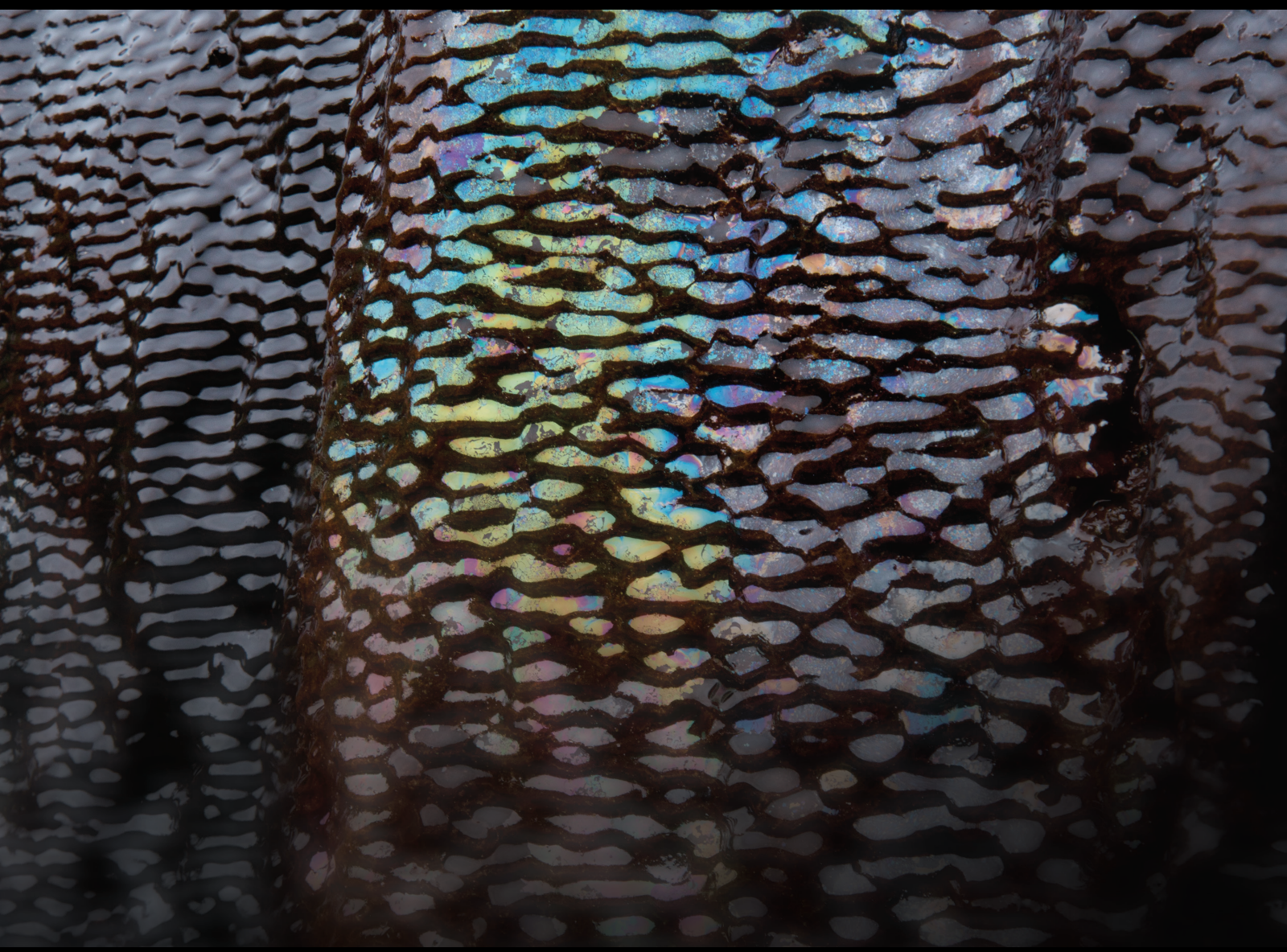

Interactions of Flowing Grout and Soil/ Rock Under Different Diffusion Patterns: Permeation, Compaction, and Fracturing

Geofluids

Interactions of Flowing Grout and Soil/Rock Under Different Diffusion Patterns: Permeation, Compaction, and Fracturing

Lead Guest Editor: Shanyong Wang
Guest Editors: Xinyu Ye, Qiong Wang, and Xueming Du

Chief Editor

Associate Editors

Academic Editors

Contents

Hindawi
Geofluids
Volume 2022, Article ID 4923385, 14 pages
https://doi.org/10.1155/2022/4923385

Research Article

Molecular Dynamics Simulations of Polymer Grouting Material: Its Mechanical Behavior under Uniaxial Tension, Cyclic Tensile Loading, and Stress Relaxation

Mingrui Du,[1,2] **Haoyue Zhang**,[1,2] **Yan Zhao**,[3] **Zongliang Huang**,[3] **Chengzhi Zheng**,[3] **Rui Wu**,[3,4] **and Xinlei Gao**[3,4]

[1]*School of Water Conservancy Engineering, Zhengzhou University, Zhengzhou 450001, China*
[2]*National Local Joint Engineering Laboratory of Major Infrastructure Testing and Rehabilitation Technology, Zhengzhou 450001, China*
[3]*Guangdong Yuehai Water Investment Co., Ltd., Shenzhen 518021, China*
[4]*Harbin Institute of Technology National Engineering Research Center of Urban Water Resources Co. Ltd., Harbin 150000, China*

Correspondence should be addressed to Mingrui Du; dumingruicumt@sina.com

Received 8 January 2022; Revised 18 February 2022; Accepted 24 August 2022; Published 21 September 2022

Academic Editor: Qiong Wang

At present, polyurethane (PU) has been extensively used as a grouting material in civil engineering. The mechanical properties of PU are the key to achieving the desirable grouting effect. This study presents the research results of the mechanical behavior of PU matrix under tensile, successive cyclic tensile, and stress relaxation at the nanoscale, using the coarse-grained molecular dynamics simulation method. The influences of the number of molecule chains and strain rate on the tensile mechanical properties are discussed, and the tensile deformation mechanism of PU matrix is revealed. The tensile strength of PU matrix is independent of loading path, and after yielding, the strain of PU matrix contains the elastic strain, plastic strain, and viscous strain. In the stress relaxation process, the evolution of the axial stress is mainly caused by the varied van der Waals interactions. The stress relaxation behavior of PU matrix can be described by the viscoelastic model consisting of one elastic element in parallel with one Maxwell element.

1. Introduction

Polyurethane (PU) [1], the product of polymerization reaction between isocyanate and polyols, is a versatile class of copolymer used in coatings [2], armors [3], and composites [4] for its properties of high durability, high toughness, high capacity to absorb and dissipate energy, and low density. At present, by virtue of the characteristics of the strong permeability resistance [5], fast-setting [6], high expansion force [7], and eco-friendliness [8], the foamed polyurethane has been increasingly adopted as grouting material in civil engineering. As shown in Figure 1, the representative applications of the polymer grouting material include filling soil cavities to lift the sedimentary underground pipelines [9, 10] or foundations [11, 12] and constructing barriers to prevent water seepage [13, 14] or the leakage of pollutants [14, 15]. In these applications, the two raw materials, isocyanate and polyols, are simultaneously injected into soil at the constant mass ratio as alternatives to cement-based grouts [16, 17], and after polymerization reaction, the PU matrices will be retained in the soil mass to play the reinforcing role [9, 10, 16]. For example, it has been reported that when the void surrounding the underground pipe was filled through PU grouting, under the same vertical load, the strain and bending moment in the pipe was declined by about 76.9% and 67.9% [10]. The mechanical properties of PU matrices are the key to achieving the

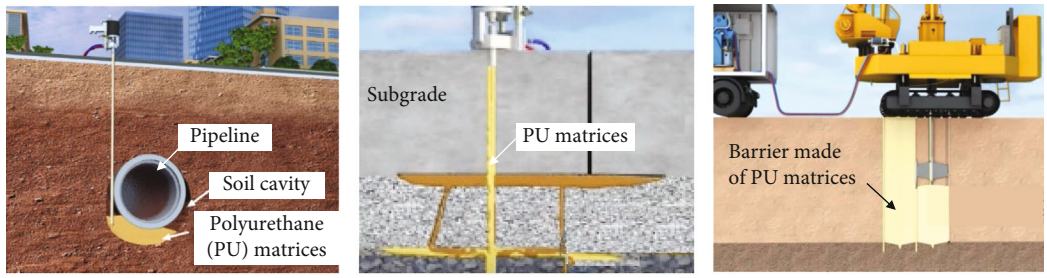

Figure 1: The representative applications of the foamed polyurethane (PU) as grouting materials in geotechnical engineering.

desirable grouting effect, and the polymer grouting materials with insufficient strength may cause the refailure of the reinforced engineering structures [9–11, 18].

To date, numerous experimental studies have been carried out to investigate the tensile, compressive, flexural, and shear strength of polymer grouting materials [19–23]. For instance, the tensile strength and compressive strength of the plain PU composites are about 44.4 MPa and 15.5 MPa, and the appropriate addition of PVA fibers can improve the mechanical properties of PU composites by about 4.5-22.3% and 9.0-12.2% [19]; in Hussain et al.'s study [21], it was found that the experimentally tested flexural strength of PU composites could be about 11.0 MPa; in the study of Zheng et al. [22], it was found that the flexural strength and compressive strength of PU grouting materials with density of 0.1-0.5 g/cm^3 were in the range of about 1.2-18.1 MPa and 1.0-7.5 MPa, respectively. It has been reported that, according to the micro morphology observations [6], PU grouting materials are porous materials containing numerous hollow closed foams, making them perform with obvious discontinuity characteristics. The foams are packed together, and their walls are made of amorphous PU [6], and under the external loading, it is the deformation of the foam walls, i.e., the PU matrix, that cause the failure of polymer grouting materials. By incorporating the beam deformation theory and the membrane stretching theory, the Gibson-Ashby equation that reflects the mechanical behavior of PU grouting materials has been proposed [24]. The Gibson-Ashby equation shows that knowing the mechanical properties of the PU matrix from the molecular scale is the foundation of the theoretical research on the mechanical properties of polymer grouting materials [24], which, however, is rarely seen at present.

In the past decades, the molecular dynamics (MD) simulation has been proven to be a reliable and promising tool to explore the nanoscale mechanical behavior of various materials. For example, studies on the mechanical behavior of amorphous polymer materials [25, 26], the microscopic deformation characteristics of inorganic minerals or metals [27, 28], the tensile strength of a single carbon nanotube [29, 30] or one layer of graphene [31, 32], and the nanoscale shear enhancing mechanism of carbon nanotubes in cement [33], all using the MD simulation method, have been reported. A large amount of significant efforts to develop the united atom [34, 35] and coarse-grained [36–38] have been carried out. When the united atom or coarse-grained MD simulation methods are used, groups of atoms are lumped into single interaction sites with the simplified interaction potentials, and thus, the total number of degrees of freedom of the simulated models can be reduced. The united atom and coarse-grained MD methods require less computation, due to which, the time and length scales of the models can be increased to simulate the bulk behavior. With the united atom or coarse-grained MD simulation methods, the nanoscale mechanical properties and deformation mechanism of amorphous polyethylene under the tensile-compressive load [25] or pure tensile load [35] have been understood. In the study of Park et al. [38], the thermomechanical behavior of the shape-memory polyurethane copolymers was also studied using the coarse-grained MD simulation method. Studies on the nanoscale modulus [39], cohesion strength [40], and self-assembly behavior [41] of PU material with coarse-grained MD simulation method have also been reported. The coarse-grained MD simulation has provided a new approach to understand the mechanical behavior of PU matrix from the molecular perspective.

In this study, using the coarse-grained MD simulation method, the mechanical behavior of the amorphous PU matrix under tensile was firstly studied, and then, both the successive cyclic tensile simulation and stress relaxation simulation were carried out. This study is aimed at addressing the mechanical properties of the amorphous PU matrices at the nanoscale under different types of loadings that are commonly seen in geotechnical engineering [9, 11, 18, 42]. The reason why the tensile simulation was firstly carried out is that under external load, the failure of the PU foams is mainly caused by the tension deformation [6, 24, 25]. This study is organized as follows: the construction of the coarse-grained model of amorphous PU and the simulation details are included in Section 2. In Section 3, both the influences of the number of the molecular chains and the strain rate on the tensile strength of PU matrix, as well as the tensile deformation mechanism of PU matrix, are discussed. The mechanical behavior of PU matrix under cyclic tensile loading and the stress relaxation characteristics of PU matrix under different tensile strains are included in Section 3. The main conclusions are summarized in Section 4.

2. Simulation Models and Methods

2.1. Coarse-Grained Method and Force Field. For the PU copolymers, different coarse-grained methods and force fields have been developed [38, 39, 43]. In Park et al.'s study

[38], the hard segment of the PU molecular was divided into two different beads, one of which includes two halves of aromatic rings, and the remaining component of the benzenes and the urethane linkage were represented with another bead. As for the coarse-grained PU model proposed by Uddin et al. [39, 43], it has the physical and mechanical properties that are a good match with the experimental results; therefore, it was adopted in this study. More details are included as follows.

As shown in Figure 2(a), a single PU molecule chain is composed of the hard and soft segments, where the formers come from diphenylmethane diisocyanate (MDI) and butanediol [44]. The hard segments were treated as separate beads to obtain interactions between them. The segments from MDI consist of two phenyl rings connected by a -CH_2 group, and the internal interactions are difficult to capture; therefore, the hard segment was divided into three types of beads [39, 43]. The –$(CH_2)_4$–O group, –(CONH)–C_6H_6–CH_2 group, and the –(C_6H_6)–NHCOO group are represented by type A bead, type B bead, and type C bead, respectively. The molecular weights of A, B, and C beads are 72.1 g/mol, 135.2 g/mol, and 135.1 g/mol, respectively. The hard segments and soft segments in the PU copolymers often have a degree of polymerization in the range of 1–10 and 15–30, respectively [44]. Based on the commonly seen polymerization degrees of the hard segments and soft segments, the coarse-grained PU model (as shown in Figure 2(b)) was built. Figure 2(b) shows one-fifth of the coarse-grained PU molecule chain, and an entire coarse-grained PU chain contains 280 beads in total, composed of 230 A beads, 25 B beads, and 25 C beads. The polymerization degrees of the hard and soft segments in the coarse-grained model are 2 and 14, respectively, and the molecular weight is 23340 g/mol. The full-atomic polyurethane model mapped from the coarse-grained model is consistent with the typical PU molecule formula presented in literature [44], and thus, it is representative. With this coarse-grained method, for a typical PU matrix with the polymerization of 100, the total number of particles is reduced to 28000 from 389000, making it possible to compute relatively large systems at a physically meaningful simulation scale.

The potential energy of the coarse-grained PU model contains three terms, the bond stretching, the bond angle bending, and the van der Waals interactions, whereas the term associated with the dihedral angle torsion is negligible [37]; therefore, the potential energy can be expressed as follows:

$$E_{\text{ptotal}} = E_{\text{bond}} + E_{\text{angle}} + E_{\text{nonbond}}. \quad (1)$$

The function forms of E_{bond}, E_{angle}, and E_{nonbond} in Equation (1) are as follows:

$$E_{\text{bond}}(r) = \frac{1}{2}K_{\text{bond}}(r - r_0)^2, \quad (2)$$

$$E_{\text{angle}}(\theta) = \frac{1}{2}K_{\text{angle}}(\theta - \theta_0)^2, \quad (3)$$

$$E_{\text{nonbond}}(r) = 4\varepsilon\left[\left(\frac{\sigma}{r}\right)^{12} - \left(\frac{\sigma}{r}\right)^{6}\right], \quad r \le r_c, \quad (4)$$

where K_{bond} and K_{angle} are the stiffness constants for the bond length and bond angle potential energy, respectively; r_0 and θ_0 are the equilibrium bond length and equilibrium bond angle, respectively; r and θ are the distance between two atoms and the angle between two bonds, respectively; ε is the energy well depth, σ is the distance between two nonbonded atoms at which the potential energy is zero; and r_c is the cutoff distance which is defined as 2.5σ [44].

In coarse-grained MD simulations [45, 46], Equation (2) and Equation (3) are the most commonly used functions to describe the variations of potential energy associated with bond length and bond angle, and the van der Waals interactions are often expressed by the Lennard-Jones 12-6 function (Equation (4)). Based on the trajectories of the full-atomic polyurethane equilibrium model developed using the polymer consistent force field, the probability distribution functions among the beads can be derived with the inverse Boltzmann (IBM) method [39, 43]. The center of mass of each group of atoms is defined as the center of mass of the corresponding bead. Then, the potentials on the bond stretching and the angle bending are fitted with Equation (2) and Equation (3), and the pair potentials are fitted with Equation (4), through which the coarse-grained force field parameters can be obtained. The coarse-grained force field parameters are listed in Tables 1–3.

2.2. Constructing the Coarse-Grained Model of Amorphous PU Matrix. Figure 3 shows the construction procedure of the coarse-grained model. First, an initially large size model was built by replicating the coarse-grained molecule chain, and then, the initial unstable model was relaxed at 600 K using a Langevin thermostat and the NVE ensemble for 10 ns. After that, the model was relaxed for another 10 ns at 600 K and then cooled to 298 K at a rate of 25 K per 50 ps, followed by a steady-state relaxation at 298 K for 10 ns, both with the NPT ensemble and the external pressure of one atmosphere (0.1 MPa). The simulation box was deformed to obtain a model with the desired density, after which, the model was equilibrated for 10 ns while keeping the density unchanged, both using the NVT ensemble at 298 K. The Berendsen thermostat was used to reset the temperature in both the NPT and NVT simulations, and the Berendsen barostat was used to reset the pressure of the system in NPT simulation.

The finally obtained coarse-grained PU models have a density of about 0.86 g/cm^3, which is comparable with the density obtained from the full-atomic simulation (about 0.90 g/cm^3) [39, 43] and the experimentally obtained density (0.97-1.24 g/cm^3) [47]. In addition, the nanoscaled mechanical properties of the coarse-grained PU model are also comparable with the experimental ones [39, 43]. The coarse-grained models are large collections of PU chains that are randomly jumbled together. The cubic simulation cells with the side lengths of 76.9, 102.3, and 162.5 Å were established, and each was composed of 10, 25, and 100 PU chains, respectively (Figure 3). With these three different models,

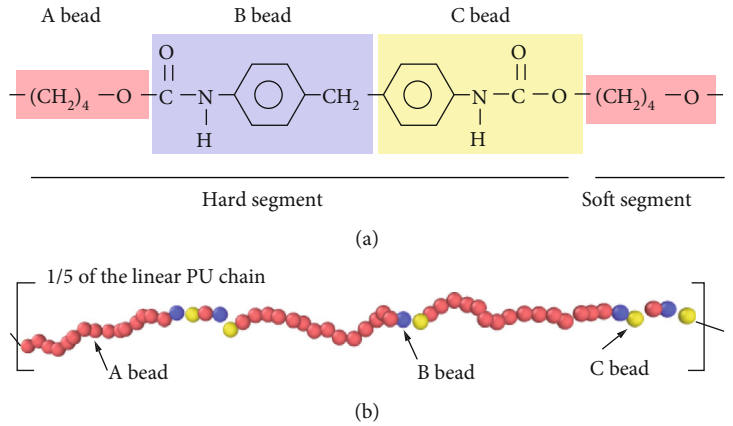

Figure 2: (a) Construction of the coarse-grained PU model with three different kinds of beads; (b) 1/5 of the coarse-grained PU molecule chain.

Table 1: Parameters of bond stretching potential energy.

Bond type	r_0 (ANG)	K_{bond} (kcal/mol/ANG^2)
A-A	5.21	1.53
A-B	6.11	1.59
B-C	7.11	5.36
C-A	6.26	1.34

Table 2: Parameters of bond angle bending potential energy.

Bond angle type	θ (degree)	K_{angle} (kcal/mol/rad^2)
A-A-A	177.8	0.83
A-A-B	148.9	1.46
A-B-C	171.6	0.87
B-C-A	167.8	0.66
C-A-B	173.0	1.58
C-A-A	159.4	2.35

Table 3: Parameters of nonbonded interactions.

Bead i	Bead j	σ (ANG)	ϵ (kcal/mol)
A	A	5.62	0.31
B	B	5.84	0.29
C	C	5.66	0.32
A	B	6.06	0.21
B	C	6.03	0.69
C	A	4.46	1.24

the influence of the number of chains on the tensile strength can be studied.

2.3. Simulation Details. For conducting the tensile simulation, a constant engineering strain rate was applied to the coarse-grained models with the NVT ensemble at the temperature of 298 K. The periodic boundary condition was adopted, and the Berendsen thermostat was used to reset the temperature of the system. According to the symmetric pressure tensor and the geometric size of the models, the tensile stress (σ) and engineering strain (ε) were computed, and the potential energy contributions associated with different terms were tracked as a function of ε. When presenting our results, true stress (σ_T) and true strain (ε_T) were used as alternatives of σ and ε, respectively, and they were calculated as follows:

$$\begin{cases} \varepsilon_T = \ln(1+\varepsilon), \\ \sigma_T = \sigma(1+\varepsilon). \end{cases} \tag{5}$$

The strain rate of 5×10^{10}/s was applied to the three models with different side lengths until ε reached 1.0, and the tensile strain was along the x-axis. For the configuration containing 100 PU molecule chains, the uniaxial tension simulation at two other strain rates (2×10^{11}/s and 1×10^{10}/s) was also conducted to study the influences of strain rate. The tensile rate adopted here is in the range suggested by previous studies [25, 35].

The successive cyclic tension loading simulation was conducted on the 100-chain coarse-grained model. Both the loading and unloading rates of the successive cyclic tensile simulation were 5×10^{10}/s, and a total of 7 cycles were simulated. For each cycle, the model was unloaded to zero stress at first and then reloaded to a larger strain than the previous cycle. ε_T at each unloading point was 0.04, 0.09, 0.18, 0.24, 0.32, 0.45, and 0.60, respectively.

Finally, the stress relaxation simulation was conducted on the 100-chain coarse-grained model. The model was stretched to different true strains (0.05, 0.1, 0.2, 0.4, 0.6, and 0.8) at the rate of 5×10^{10}/s and then relaxed for a period of time while keeping the strain constant. The evolutions of the axial stress and potential energy of the model with the relaxation time were recorded. Both the model establishment and the tensile simulations were carried out by the LAMMPS package [48], and the open visualization tool OVITO was adopted for molecular visualization [49].

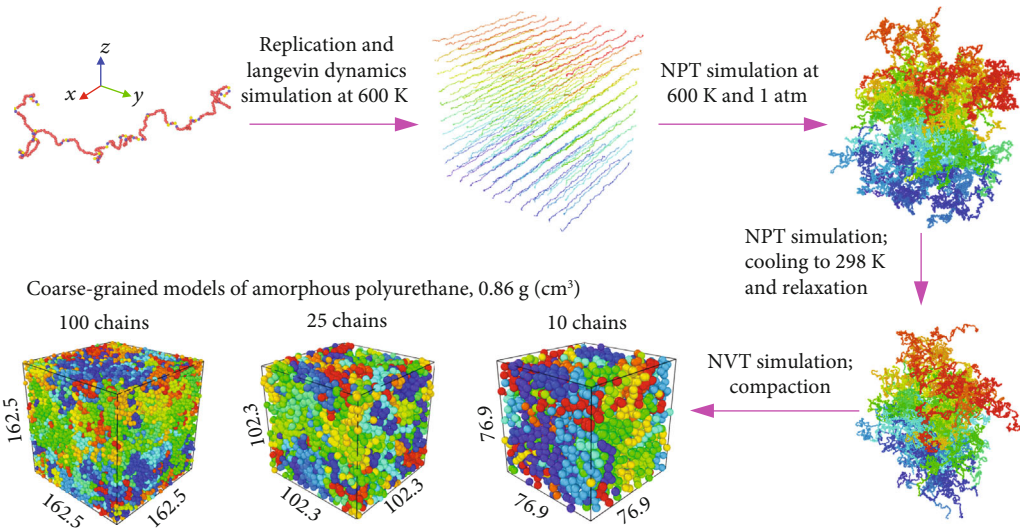

FIGURE 3: Construction of the coarse-grained model of amorphous PU matrix. The different molecular chains were painted with different colors, and the unit of side length is Å.

3. Results and Discussion

3.1. Effects of the Number of PU Chains on the Tensile Mechanical Properties. Figures 4(a)–4(c) show the variation laws of the stress of the coarse-grained PU models with different numbers of molecular chains under uniaxial tension, from which one can see that when ε_T was lower than 0.03, the stress increased almost linearly with the increasing strain, corresponding to the elastic deformation behavior. When ε_T was over 0.03, the variation rate of the tensile stress started to decline, implying that plastic deformation had occurred to the model, and at ε_T of about 0.20 (yield strain), the tensile stress achieved a plateau. It can be found that the number of molecular chains has little influence on the yield strain or yield strength (both are about 0.20 and 30 MPa). The stress-strain curve becomes smoother with a higher number of PU chains, suggesting that the simulations moved closer to the bulk behavior. Therefore, in all the subsequent simulations, the coarse-grained PU model with 100 molecular chains was used.

The snapshots of the deformation process of the configurations containing 10 PU molecule chains are presented in Figure 4(d). It can be seen that the deformation of the model mainly consists of two parts: the slippage between the PU chains and the stretching of PU chains themselves. Before the yielding, the stretching deformation of each independent PU molecule chain was less significant than the slippage between them, whereas it became more and more obvious with the increasing strain after yielding. The slippage deformation occurred mainly along the direction of tensile strain.

3.2. Effects of Strain Rate on the Tensile Mechanical Properties. Figure 5 shows the variations of the stress of the coarse-grained PU matrix containing 100 molecule chains under uniaxial tension at the strain rate of 2×10^{11}/s and 1×10^{10}/s. The curves follow the same laws as discussed in Section 3.1 except for the different yield strengths and different yield strains. According to Figures 4(c) and 5, one can see that the yield strength of the model declines with the declined strain rate. At the strain rates of 2×10^{11}/s, 5×10^{10}/s, and 1×10^{10}/s, the yield strength was about 70, 30, and 16 MPa, respectively. On the contrary, with the decreasing strain rate, the yield strain increased gradually. For example, the yield strain was about 0.20 and 0.22 at the strain rate of 5×10^{10}/s and 1×10^{10}/s, respectively, which were about double that at the strain rate of 2×10^{11}/s. Moreover, it can also be seen that when a higher strain rate was adopted, the stress-strain curves became smoother.

Figure 6 illustrates the evolution of potential energy (PE_{total}) of the coarse-grained PU matrix at different tensile strain rates, corresponding to the stress-strain behavior presented in Figures 4(c) and 5. The evolutions of individual components, i.e., the bond potential energy (PE_{bond}), bond angle potential energy (PE_{angle}), and van der Waals interactions ($PE_{nonbond}$), are also included in Figure 6. E_0 represents the potential energy at initial time.

From Figure 6(a), it can be seen that when the axial strain increased at a rate of 2×10^{11}/s, both PE_{total} and $PE_{nonbond}$ increased gradually, and the increasing trends are curves with a downward opening, and that the PE_{total} curve and $PE_{nonbond}$ curves almost coincided until ε_T reached to about 0.10 (the yield strain). PE_{total} was about 6000 kcal/mol at the yield strain, and after yielding, PE_{total} became lower than $PE_{nonbond}$; meanwhile, the PE_{angle} term started to decline in an almost linear way. PE_{angle} was about -6000 kcal/mol at ε_T of 0.70. During the tensile procedure, PE_{bond} increased with the increasing strain, but its variation was lower than those of the other two terms (with the maximum increment of lower than 1500 kcal/mol).

The changed $PE_{nonbond}$, PE_{angle}, and PE_{bond} are primarily attributed to the slippage between different molecules, bond

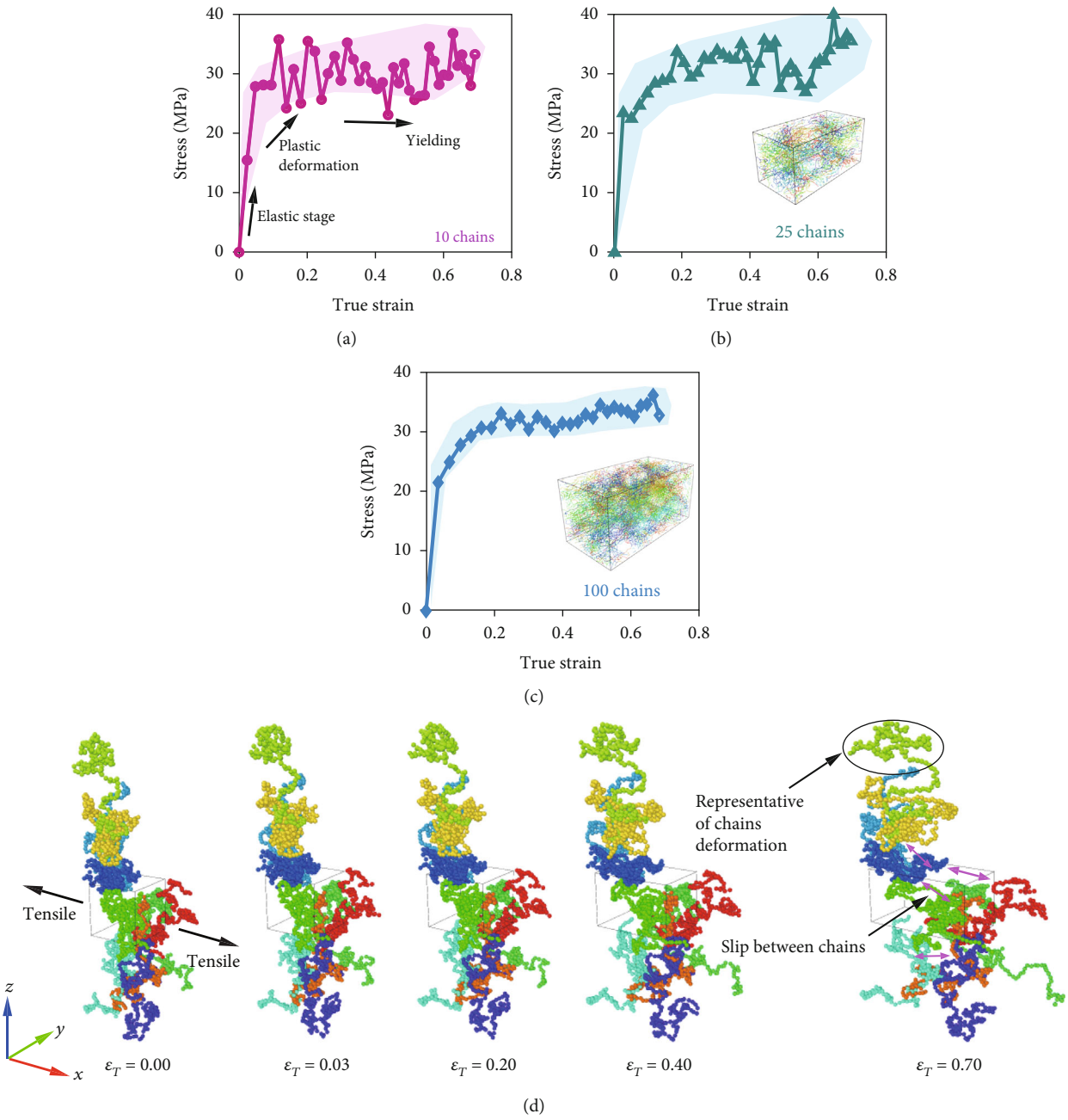

FIGURE 4: (a–c) Stress-strain curves of coarse-grained PU models with different numbers of chains under tensile at a strain rate of 5×10^{10}/s and (d) the evolution of molecular configuration containing 10 PU chains at different strains.

angle bending behavior, and bond stretching behavior, respectively. Figure 6(a) shows that, at the strain rate of 2×10^{11}/s, under uniaxial tension, only the slippage between different PU molecules occurred before yielding, but after yielding, in addition to the slippage between different PU molecules that still remained, on each PU molecule, the bond angles started to bend, and the bonds were stretched to synthetically accommodate deformation. The difference between $PE_{nonbond}$ and PE_{total} after yielding was dissipated by the bond angle bending behavior and bond stretching behavior, but primarily via the former. Figures 6(b) and 6(c) show that whether at the strain rate of 5×10^{10}/s or 1×10^{10}/s, there was little change in the overall evolution laws of PE_{total} and $PE_{nonbond}$, but PE_{angle} started to decline from the very beginning of the simulation, and that PE_{bond} was always equal to zero. This indicates that at a lower strain rate, as soon as the tensile load was applied, the bond angles displayed bending behavior, but the bond lengths were little influenced.

Figure 6 also shows that the change of total potential energy at yielding is independent of the strain rate. At the three loading rates, both PE_{total} at yielding are about 6000 kcal/mol, but after yielding, the PE_{total} of the model sustaining a lower strain rate has a lower value, which is due to that $PE_{nonbond}$ has significantly declined. With the

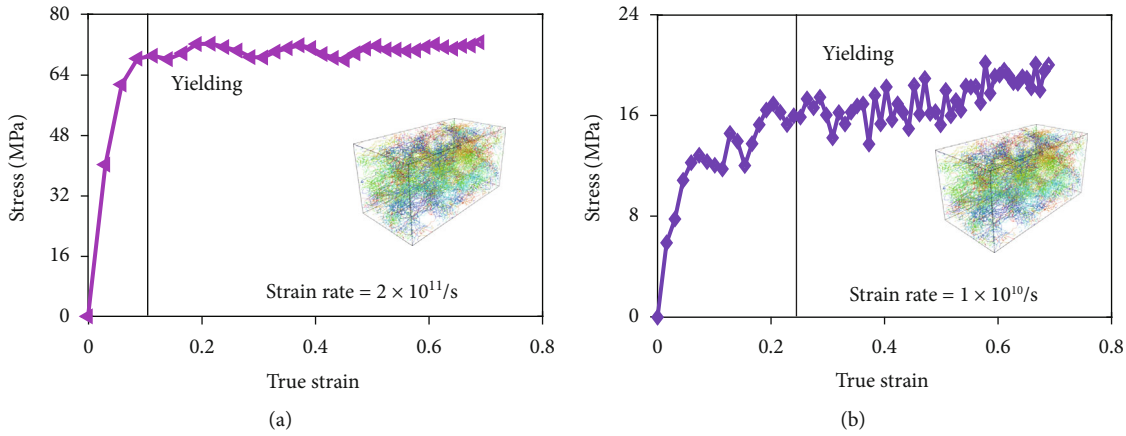

Figure 5: Stress-strain curves of the coarse-grained PU matrix containing 100 chains under tensile tension at the strain rate of (a) 2×10^{11}/s and (b) 1×10^{10}/s.

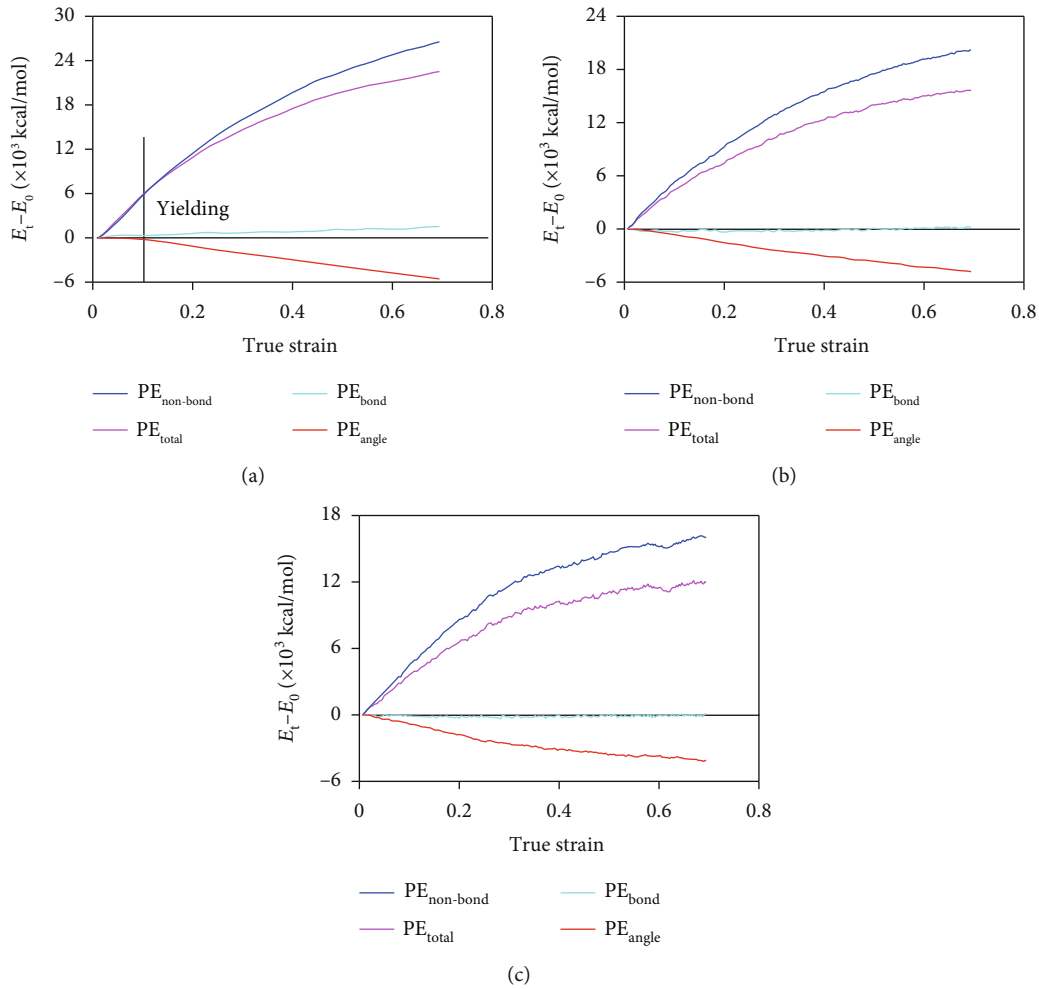

Figure 6: Variations of the potential energy of the coarse-grained PU matrix versus true strain for a strain rate of (a) 2×10^{11}/s, (b) 5×10^{10}/s, and (c) 1×10^{10}/s.

decreasing strain rate, the increased yield strain (Figures 4(c) and 5) leads to the increased volume strain of the model. Considering that the yield strength of the model is positively dependent on the potential energy but negatively influenced by the volume [50], when the strain rate declines, PE_{total} is almost unchanged, but the increased volume strain of the coarse-grained PU models at yielding is the main reason for the lower yield strength.

Figures 4(d) and 6 show that the slippage between different molecules mainly dominates the deformation of the PU matrix. The molecules in the original model are tightly compacted together, and the relative slippage between them would occur once the strain was applied (Figure 4(d)), and this would increase the average spacing between different molecules and thus change the van der Waals interactions (Figure 6). The increased molecular spacing also provides some space for the restoration of the deformed bond angles; therefore, the potential energy associated with the bond angles would decline gradually with the increasing strain. When the model is deformed to a larger size, the average distance between different molecules would be increased, which would result in the less and less pronounced van der Waals interactions (Figure 6). At a lower strain rate, the amount of slippage per unit time between different molecules is smaller, and the time for the variation of bond angles is longer. The bond angles have more time to revert to their equilibrium, and thus, the PE_{angle} begins to decline as soon as the strain appears. However, most of the bond angles are still not in their equilibrium state. This can be illustrated by Figure 7, from which one can see that even at ε_T of 0.60, for these 6 types of different bond angles, over 90% of them were smaller than the equilibrium bond angles. Therefore, the PE_{angle} term continuously and steadily declines.

To find out which types of bond angles reverted the most, the evaluations of PE_{angle} of each type of bond angle of the model at a tension rate of 2×10^{11}/s were calculated, and they are drawn in Figure 8.

From Figure 8, one can see that the potential energy of bond angles A-A-B, A-B-C, B-C-A, C-A-B, and C-A-A varied little under the tension, whereas that of bond angles A-A-A and B-C-A declined gradually with the increasing strain when the strain was over 0.10. The variations of PE_{angle} of bond angle A-A-A and bond angle B-C-A correspond well with the result shown in Figure 6(a). Moreover, even the B-C-A bond angles have the minimum K_{angle} than the others, the total change in PE_{angle} of A-A-A bond angles is more significant than that of the B-C-A bond angles. For example, at ε_T of 0.40, the total potential energy of the A-A-A bond angles decreased by about 2400 kcal/mol, which is over 6 times that of B-C-A bond angles (about 380 kcal/mol). This is because the total number of the A-A-A bond angles is the maximum (190 per PU chain); therefore, the total variation of potential energy of the A-A-A bond angles is the most significant. This implies that the change in PE_{angle} depends on both the bond angle stiffness and the total number of bond angles [35]. The A-A-A bond angles are mapped to the bond angles in the soft segment in the all-atom model (Figure 2(a)), which implies that the deformation of the polyurethane molecule mainly occurs in the soft segment.

3.3. Mechanical Behavior under Successive Cyclic Tension Loading. Figure 9 shows the stress-strain curve of the coarse-grained PU matrix under successive tensile loading-unloading cycles. It can be seen that, generally, the contour of the stress-strain curve of the coarse-grained PU sustaining the successive loading-unloading cycles follows that of the tensile stress-strain curve. The strength after each reloading was almost equal to the tensile strength at the same strain. After having passed through the unloading point, the reloading curves precisely follow the original stress-strain curve, which is known as "stress memory" behavior. The "stress memory" phenomenon has also been observed in other polymeric materials like high-density polyethylene [25]. This observation is consistent with the experimental results [51], and it indicates that the strength of polyurethane under tension is independent of the loading path.

Figure 9 also shows that, before yielding, the stress curves of unloading and subsequent reloading change linearly, and they are almost coincident, but after yielding, they display the nonlinear variation law. More specifically, the stress curves of reloading increase sharply and linearly within a small strain range, and then, they turn to increase at a much lower rate up to the value of the unloading point. Taking the fourth loop as an example, the slope of the reloading stress curve was about 1850 MPa per strain when ε_T increased from 0.22 to 0.24, but it declined to about 90 MPa prestrain in the ε_T range of 0.24 to 0.26. The unloading curves vary similarly but in a reverse direction. Due to the nonlinear variation characteristic, after yielding, hysteresis loops are seen on the stress curves of all the unloading-reloading cycles. The hysteresis loops indicate that the strain of the unloading points contains the viscous strain [25]. The viscous strain (ε_v) of polymeric materials, calculated by subtracting the elastic strain (ε_e) and plastic strain (ε_p) from the strain of the unloading point (as shown in Figure 9), originates from the chain dynamics that are determined by the friction between polymer atoms, driven by entropic effects. When the polymer is subjected to relatively small or moderate strain, the mobility of tightly bonded molecules is constrained by the van der Waals interactions that cause friction between polymer atoms. When the deformation increased, the molecules are gradually separated in the space, and the accumulated plastic deformation causes some damage which weakens the van der Waals interactions between the molecules, thus resulting in viscous strain of the polymers. From Figure 9, it can also be read that when the strain of the unloading point increases the viscous strain in PU matrix increases gradually.

3.4. Mechanical Behavior under the Stress Relaxation. Figure 10(a) shows the variations of the stress of the coarse-grained PU matrix with the running time at different strains of relaxation, from which one can see that when the stress relaxation begins, the axial stress declines sharply within a small time range, but not to zero. When the strain of relaxation is equal to 0.05 or 0.10, the axial stress declines linearly to a certain value, but when the strain of relaxation is equal to or higher than 0.20, the axial stress declines in a nonlinear way. Besides, when the strain of relaxation is lower than 0.20, after relaxation, the final values of the axial stress increase with the increasing strain of relaxation. For example, when the stress relaxation happened at ε_T of 0.20, after relaxation, the axial stress of the model was about 10 MPa, about 33% higher than that relaxed at ε_T of 0.10. However, when the strain of relaxation was equal to or higher than

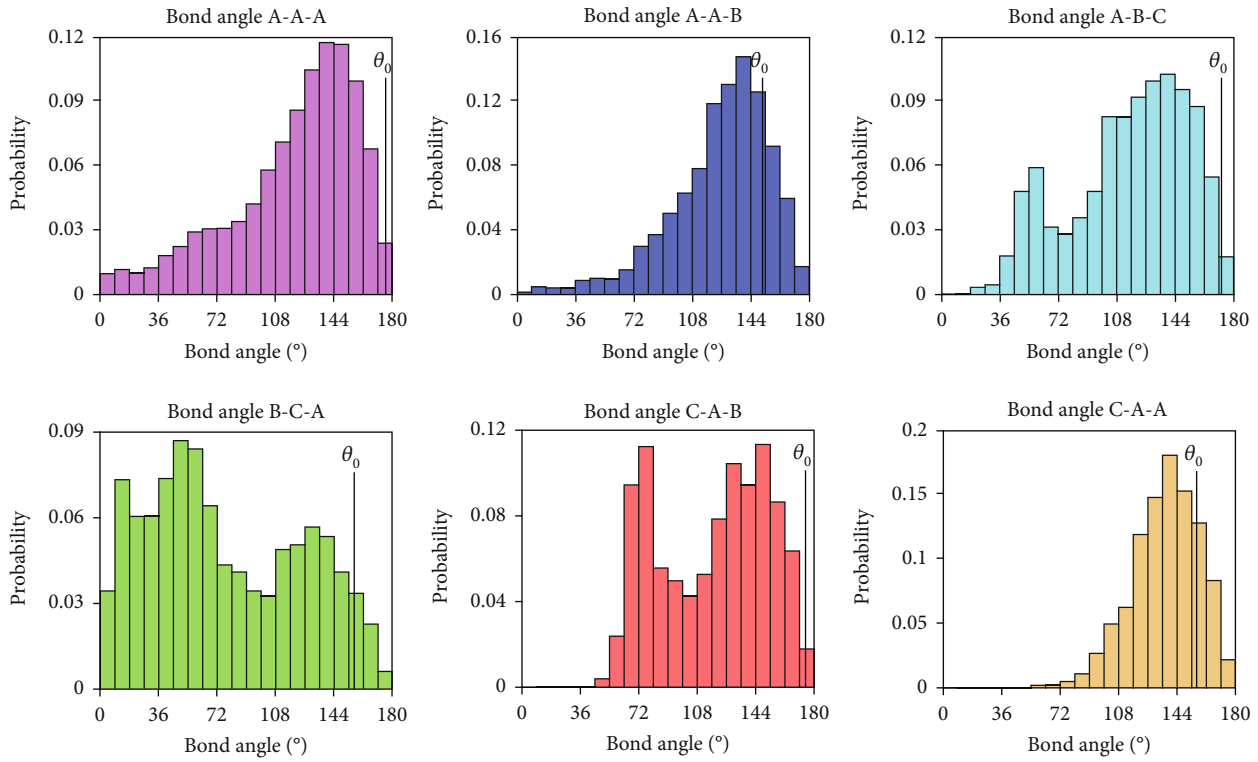

FIGURE 7: Probability fractions of values of different bond angles of the 100-chain coarse-grained PU at ε_T of 0.60. Over 90% of the bond angles were smaller than the equilibrium bond angles (θ_0).

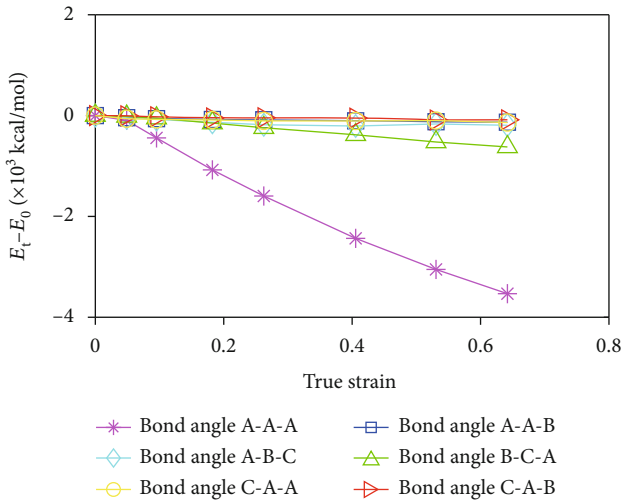

FIGURE 8: Evolution of total potential energy of different types of bond angles for a coarse-grained PU matrix containing 100 molecular chains for a strain rate of 2×10^{11}/s.

0.40, after stress relaxation, all the axial stresses were almost equal to 15 MPa. The stress variation curves of the PU model during the stress relaxation process are similar to the experimental results of the macroscopic polyurethane [52, 53], indicating the viscoelastic behavior of the material.

Figure 10(b) presents the evolutions of the potential energy of the model during tension and subsequent stress relaxation (the strain of stress relaxation was 0.40). From Figure 10(b), it can be seen that during tension, the variations of the potential energy associated with the van der Waals interactions, bond lengths, and bond angles are similar to those shown in Figure 6. In the stress relaxation process, the PE_{angle} term was maintained at about -2600 kcal/mol, but the $PE_{nonbond}$ declined gradually from about 14000 kcal/mol to 12000 kcal/mol, which lasted for around 8 ps. The $PE_{nonbond}$ was maintained at 12000 kcal/mol in the following time. Besides, in the stress relaxation process, the variation of PE_{total} was equal to that of $PE_{nonbond}$. The variation of $PE_{nonbond}$ and PE_{total} corresponds well with that of the axial stress presented in Figure 10(b), indicating that in the stress relaxation, the variation of axial stress of the PU model was mainly dominated by the varied van der Waals interactions.

According to Figure 10(a), in the stress relaxation, E_t, the relaxation modulus of the coarse-grained PU model, defined as the stress corresponding to unit strain, can be calculated. E_t is a parameter of time dependence. Considering that the general Maxwell model illustrated in Figure 11(a) can be used to describe the stress relaxation property of viscoelastic solid materials [53, 54], E_t can be expressed as the following function:

$$E_t = E_\infty + \sum_{i=1}^{N} E_i \cdot \exp\left(-\frac{t}{\lambda_i}\right), \tag{6}$$

where E_∞ represents the average of E_t when the relaxation time (t) reaches infinity, E_i and λ_i represent the real-time

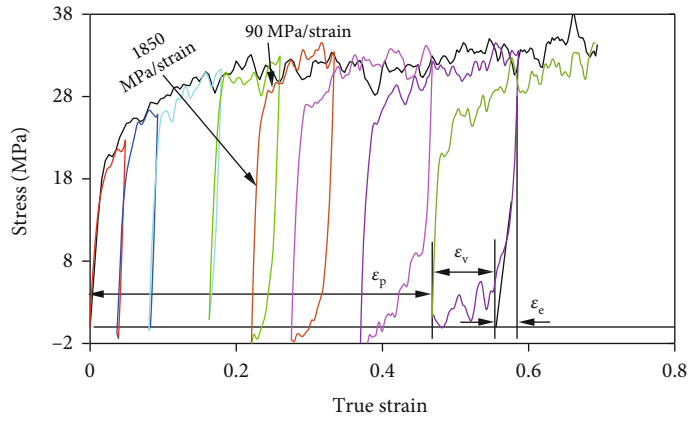

Figure 9: The stress-strain curve of the coarse-grained PU matrix under successive cyclic tensile loading (the colored one). The stress-strain curve under tensile was also drawn as the black one for comparison. The strain rate is 5×10^{10}/s.

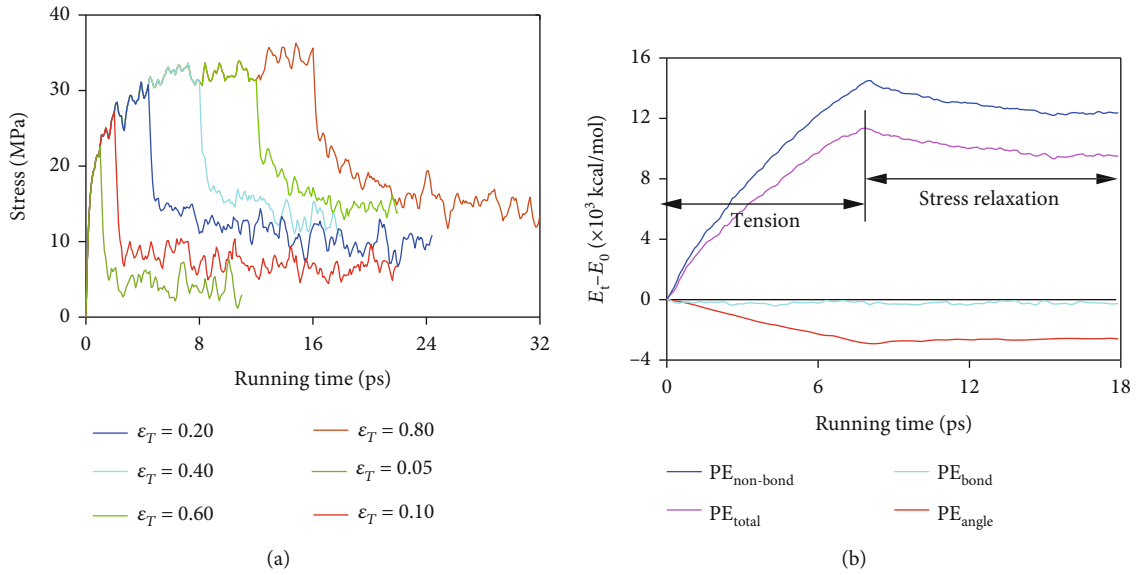

Figure 10: Evolutions of (a) stress with the relaxation time at different strains of relaxation and (b) potential energy with the relaxation time at the strain of relaxation of 0.40.

relaxation modulus and relaxation time constant of element i in the general Maxwell model, respectively, and N is the total number of the Maxwell elements.

In Equation (6), E_∞ can be calculated using the following function:

$$E_\infty = E_0 - \sum_{i=1}^{N} E_i, \tag{7}$$

where E_0 represents the relaxation modulus at the initial time.

Therefore, Equation (6) can be rewritten as the following:

$$E_t = E_0 - \sum_{i=1}^{N} E_i \cdot \left(1 - \exp\left(-\frac{t}{\lambda_i}\right)\right). \tag{8}$$

To analyze the relaxation modulus, E_t was transformed to the dimensionless form by dividing Equation (8) by E_0, and the nondimension relaxation modulus can be expressed as the following:

$$e_t = 1 - \sum_{i=1}^{N} e_i \cdot \left[1 - \exp\left(-\frac{t}{\lambda_i}\right)\right]. \tag{9}$$

The variations of e_t of the model in the stress relaxation at different ε_T are plotted in Figure 11(b) as the scatter points. The time at the beginning of stress relaxation in Figure 10(a) has been shifted to zero. The variations of e_t are fitted with Equation (9), and it was found that the best fit can be obtained for the model at different ε_T when N is equal to 1. Therefore, the viscoelastic model for PU matrix during the stress relaxation process is described by the

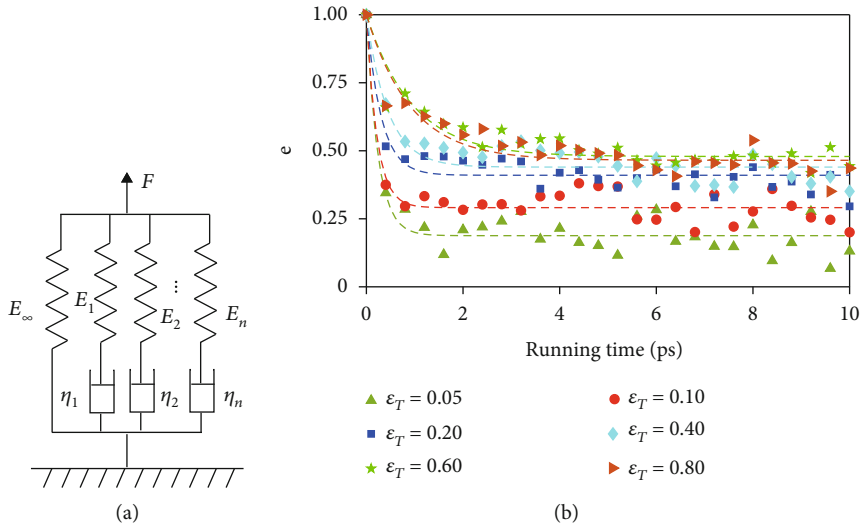

Figure 11: (a) Schematic diagram of the general Maxwell model and (b) the comparison of the nondimension relaxation modulus between simulation results (the scatter points) and theoretical values (the dashed lines) at ε_R. Here, the starting time of stress relaxation was zeroed out.

following:

$$e_t = 1 - e \cdot \left[1 - \exp\left(-\frac{t}{\lambda}\right)\right]. \quad (10)$$

The parameters of the viscoelastic model and the goodness of fit (R^2) are listed in Table 4, and the theoretical values of e_t calculated by Equation (10) have been drawn in Figure 11(b). It can be seen that even though a difference exists, the theoretical values of e_t are close to the simulation results. The theoretical e_t declines gradually with the increasing relaxation time but not to zero. With the increasing strain of relaxation, the decline of theoretical e_t becomes more nonlinear. The theoretical stress value can be obtained by multiplying the theoretical e_t with ε_T. Since ε_T is constant, it can be deduced that the theoretical stress will vary according to the same law as the theoretical e_t. Therefore, the viscoelastic model consisting of one elastic element in parallel with one Maxwell element can be used to describe the mechanical behavior of an amorphous polyurethane material under stress relaxation.

In practical engineering, polymer grouting material refers to the product of the reaction between isocyanate and polyols with a constant mass ratio [5, 9]. Therefore, in this study, only the influences of different loading types were investigated, and the influences of different raw materials or mass ratios on the mechanical properties of PU matrix will be studied in the further study.

Table 4: Parameters of the viscoelastic model for coarse-grained PU matrix at the different strains of stress relaxation.

ε_T	e	λ	R^2
0.05	0.812	0.238	0.751
0.10	0.709	0.217	0.770
0.20	0.589	0.303	0.783
0.40	0.549	0.446	0.729
0.60	0.521	0.954	0.770
0.80	0.535	0.916	0.735

4. Conclusions

The mechanical behavior of amorphous PU matrix under uniaxial tension, successive cyclic tension, and stress relaxation at nanoscale was investigated with coarse-grained MD simulation method. The conclusions are drawn as follows:

(1) The mechanical properties of PU matrix under tensile are little affected by the number of molecules but change significantly when the strain rate varies. With the increasing strain rate, the yield strength increases, and the yield strains decrease. At yield, the total change in the potential energy is independent of the strain rate, and it is about 6000 kcal/mol. When the strain rate increases, the declined volume strain of the PU matrix is the main reason for the increased yield strength

(2) Under tensile, the potential energy associated with the bond stretching varies less significantly than that associated with the bond angle bending or van der Waals interactions, indicating that the deformation of the model is mainly caused by the slippage between different molecule chains and the bending of the bond angles. The bending of bond angles mainly occurs in the soft segments of the molecule chains. After yielding, most of the bond angles are still not in equilibrium

(3) The contour of the stress-strain curve of the model under cyclic tension is consistent with that under uniaxial tension, indicating that the model performs with the stress memory behavior, and thus, its tensile

strength is independent of loading path. After yielding, the stress curves of the unloading-reloading cycles contain the hysteresis loops, which imply that the strain of the unloading points contains elastic strain, plastic strain, and viscous strain

(4) During the stress relaxation process, the evolution of the axial stress is primarily caused by the varied van der Waals interactions. The mechanical behavior of the amorphous PU matrix under stress relaxation at the nanoscale can be described by the viscoelastic model consisting of one elastic element in parallel with one Maxwell element

Data Availability

The data used to support the findings of this study are included within the article.

Conflicts of Interest

The authors declare that they have no known competing financial interests or personal relationships that could have appeared to influence the work reported in this paper.

Acknowledgments

The authors are grateful for the financial support from the National Natural Science Foundation of China (Grant No. 51908515) and formal analysis from Prof. Hongyuan Fang.

References

[1] A. Pattanayak and S. C. Jana, "Synthesis of thermoplastic polyurethane nanocomposites of reactive nanoclay by bulk polymerization methods," *Polymer*, vol. 46, no. 10, pp. 3275–3288, 2005.

[2] D. K. Chattopadhyay and K. Raju, "Structural engineering of polyurethane coatings for high performance applications," *Progress in Polymer Science*, vol. 32, no. 3, pp. 352–418, 2007.

[3] T. J. Kang, K. H. Hong, and H. Jeong, "Preparation and properties of a p-aramid fabric composite impregnated with a magnetorheological fluid for body armor applications," *Polymer Engineering and Science*, vol. 55, no. 4, pp. 729–734, 2015.

[4] J. Guan, K. L. Fujimoto, M. S. Sacks, and W. R. Wagner, "Preparation and characterization of highly porous, biodegradable polyurethane scaffolds for soft tissue applications," *Biomaterials*, vol. 26, no. 18, pp. 3961–3971, 2005.

[5] F. Wang, M. Shi, H. Li, and Y. Zhong, "Experimental study on the anti-permeability properties of polymer grouting materials," *Advanced Materials Research*, vol. 284-286, pp. 1952–1955, 2011.

[6] M. Li, M. Du, F. Wang, B. Xue, C. Zhang, and H. Fang, "Study on the mechanical properties of polyurethane (PU) grouting material of different geometric sizes under uniaxial compression," *Construction and Building Materials*, vol. 259, article 119797, 2020.

[7] D. Niedziela, I. E. Ireka, and K. Steiner, "Computational analysis of nonuniform expansion in polyurethane foams," *Polymers*, vol. 11, no. 1, p. 100, 2019.

[8] A. Chaudhari, V. Gite, S. Rajput, P. Mahulikar, and R. Kulkarni, "Development of eco-friendly polyurethane coatings based on neem oil polyetheramide," *Industrial Crops and Products*, vol. 50, pp. 550–556, 2013.

[9] H. Fang, B. Li, F. Wang, Y. Wang, and C. Cui, "The mechanical behaviour of drainage pipeline under traffic load before and after polymer grouting trenchless repairing," *Tunnelling and Underground Space Technology*, vol. 74, pp. 185–194, 2018.

[10] B. Li, F. Wang, H. Fang, K. Yang, X. Zhang, and Y. Ji, "Experimental and numerical study on polymer grouting pretreatment technology in void and corroded concrete pipes," *Tunnelling and Underground Space Technology*, vol. 113, article 103842, 2021.

[11] S. R. Iyengar, E. Masad, A. K. Rodriguez, H. S. Bazzi, and H. J. M. Hanley, "Pavement subgrade stabilization using polymers: characterization and performance," *Journal of Materials in Civil Engineering*, vol. 25, no. 4, pp. 472–483, 2013.

[12] F. Wang, W. Li, C. Guo, H. Fang, and C. Cui, "Research on bearing performance recovery of semi-rigid base pavement on the basis of permeable polymer grouting," *Journal of Beijing Jiaotong University*, vol. 43, no. 3, pp. 1–7, 2019.

[13] J. Chen, O. Ummin, T. Yu, and Y. Qi, "Applications of Rayleigh wave detection technique and polymer grouting technology in waterproof construction," *Applied Mechanics and Materials*, vol. 405-408, pp. 748–754, 2013.

[14] F. Wang, C. Guo, and Y. Gao, "Formation of a polymer thin wall using the level set method," *International Journal of Geomechanics*, vol. 14, no. 5, article 04014021, 2014.

[15] S. Li, C. Ma, R. Liu et al., "Super-absorbent swellable polymer as grouting material for treatment of karst water inrush," *International Journal of Mining Science and Technology*, vol. 31, no. 5, pp. 753–763, 2021.

[16] S. Saleh, N. Z. M. Yunus, K. Ahmad, and N. Ali, "Improving the strength of weak soil using polyurethane grouts: a review," *Construction and Building Materials*, vol. 202, pp. 738–752, 2019.

[17] F. Wang, M. Li, H. Fang, and B. Xue, "Analysis of polymer cutoff wall of Yellow River Dyke," *Yellow River*, vol. 41, no. 10, pp. 48–52, 2019.

[18] X. C. Bian, Z. Cheng, F. M. Wang, J. Q. Jiang, and Y. M. Chen, "Experimental study on dynamic performance and long-term durability of high-speed railway subgrade rehabilitated by polymer injection technology," *Chinese Journal of Geotechnical Engineering*, vol. 36, no. 3, pp. 562–568, 2013.

[19] M. Cao, C. Wang, R. Xia et al., "Preparation and performance of the modified high-strength/high-modulus polyvinyl alcohol fiber/polyurethane grouting materials," *Construction and Building Materials*, vol. 168, pp. 482–489, 2018.

[20] H. Liu, F. Wang, S. Mingsheng, and W. Tian, "Mechanical behavior of polyurethane polymer materials under triaxial cyclic loading: a particle flow code approach," *Journal of Wuhan University of Technology (Materials Science)*, vol. 33, no. 4, pp. 980–986, 2018.

[21] N. Hussain, N. N. Bonnia, R. Hirzin, E. S. Ali, and E. Zawawi, "Effect of NCO/OH ratio on physical and mechanical properties of castor-based polyurethane grouting materials," *Journal of Physics Conference Series*, vol. 1349, no. 1, article 012113, 2019.

[22] X. Zheng, S. Li, Y. Xie et al., "Study on relationship between density and mechanical behavior of high polymer grouting

materials," *Journal of Wuhan University of Technology*, vol. 36, no. 4, pp. 44–47, 2014.

[23] X. Zheng, "Expansion characteristics of polymer grouting material cured under pressure and mechanical properties of its consolidated body," *China Railway Science*, vol. 38, no. 1, pp. 9–15, 2017.

[24] S. H. Goods, C. L. Neuschwanger, C. C. Henderson, and D. M. Skala, "Mechanical properties of CRETE, a polyurethane foam," *Journal of Applied Polymer Science*, vol. 68, no. 7, pp. 1045–1055, 1998.

[25] Q. Bao, Z. Yang, and Z. Lu, "Molecular dynamics simulation of amorphous polyethylene (PE) under cyclic tensile-compressive loading below the glass transition temperature," *Polymer*, vol. 186, article 121968, 2020.

[26] S. Krishna, I. Sreedhar, and C. M. Patel, "Molecular dynamics simulation of polyamide-based materials – a review," *Computational Materials Science*, vol. 200, article 110853, 2021.

[27] Y. Zhang, M. Pirmoradian, D. Toghraie, and R. Sabetvand, "Molecular dynamics study of the mechanical properties of reinforced silicon structure with iron nanoparticles," *Computational Materials Science*, vol. 199, article 110749, 2021.

[28] F. Hasheminia, Y. Bahari, A. Rajabpour, and S. Arabha, "Elucidation of thermo-mechanical properties of silicon nanowires from a molecular dynamics perspective," *Computational Materials Science*, vol. 200, article 110821, 2021.

[29] J. Cui, J. Zhao, S. Wang, Y. Wang, and Y. Li, "Effects of carbon nanotubes functionalization on mechanical and tribological properties of nitrile rubber nanocomposites: molecular dynamics simulations," *Computational Materials Science*, vol. 196, article 110556, 2021.

[30] W. C. Liu, F. Y. Meng, and S. Q. Shi, "A theoretical investigation of the mechanical stability of single-walled carbon nanotube 3-D junctions," *Carbon*, vol. 48, no. 5, pp. 1626–1635, 2010.

[31] J. Hua, Z. Duan, S. Chen, and Q. Liu, "Molecular dynamics study on the tensile properties of graphene/Cu nanocomposite," *International Journal of Computational Materials Science and Engineering*, vol. 6, no. 3, article 1750021, 2017.

[32] L. Wang, J. Jin, P. Yang et al., "Effect of interfacial bonding on dislocation strengthening in graphene nanosheet reinforced iron composite: a molecular dynamics study," *Computational Materials Science*, vol. 191, p. 110309, 2021.

[33] M. Du, S. Chen, W. Duan, W. Chen, and H. Jing, "Role of multi-walled carbon nanotubes as shear reinforcing nanopins in quasi-brittle matrices," *ACS Applied Nano Materials*, vol. 1, no. 4, pp. 1731–1740, 2018.

[34] K. Hagita and S. Fujiwara, "Single-chain folding of a quenched isotactic polypropylene chain through united atom molecular dynamics simulations," *Polymer*, vol. 183, article 121861, 2019.

[35] D. Hossain, M. A. Tschopp, D. K. Ward, J. L. Bouvard, P. Wang, and M. F. Horstemeyer, "Molecular dynamics simulations of deformation mechanisms of amorphous polyethylene," *Polymer*, vol. 51, no. 25, pp. 6071–6083, 2010.

[36] H. Fukunaga, J. I. Takimoto, and M. Doi, "A coarse-graining procedure for flexible polymer chains with bonded and nonbonded interactions," *Journal of Chemical Physics*, vol. 116, no. 18, pp. 8183–8190, 2002.

[37] V. Agrawal, G. Arya, and J. Oswald, "Simultaneous iterative Boltzmann inversion for coarse-graining of polyurea," *Macromolecules*, vol. 47, no. 10, pp. 3378–3389, 2014.

[38] S. Park, J. Moon, B. Kim, and M. Cho, "Multi-scale coarse-grained molecular dynamics simulation to investigate the thermo-mechanical behavior of shape-memory polyurethane copolymers," *Polymer*, vol. 213, no. 20, article 123228, 2021.

[39] M. S. Uddin and J. Ju, "Enhanced coarse-graining of thermoplastic polyurethane elastomer for multiscale modeling," *Journal of Engineering Materials and Technology*, vol. 139, no. 1, pp. 011001.1–011001.11, 2017.

[40] X. L. Xu, G. X. Bo, X. He, X. K. Tian, and Y. J. Yan, "Structural effects of dimensional nano-fillers on the properties of *Sapium sebiferum* oil-based polyurethane matrix: experiments and molecular dynamics simulation," *Polymer*, vol. 202, article 122709, 2020.

[41] H. Vakili, M. Mohseni, H. Makki et al., "Self-assembly of a patterned hydrophobic-hydrophilic surface by soft segment microphase separation in a segmented polyurethane: combined experimental study and molecular dynamics simulation," *Polymer*, vol. 195, article 122424, 2020.

[42] X. Li, K. Peng, J. Peng, and D. Hou, "Effect of thermal damage on mechanical behavior of a fine-grained sandstone," *Arabian Journal of Geosciences*, vol. 14, no. 13, p. 1212, 2021.

[43] M. S. Uddin, J. Ju, and Z. Xia, "Hyperelastic multi-scale modeling of a thermoplastic polyurethane elastomer using molecular mechanics," in *Proceedings of the ASME 2015 International Mechanical Engineering Congress and Exposition. Volume 9: Mechanics of Solids, Structures and Fluids*, Houston, Texas, USA, 2015.

[44] D. Fragiadakis and J. Runt, "Molecular dynamics of segmented polyurethane copolymers: influence of soft segment composition," *Macromolecules*, vol. 46, no. 10, pp. 4184–4190, 2013.

[45] D. Ikeshima, K. Miyamoto, and A. Yonezu, "Molecular deformation mechanism of polycarbonate during nano-indentation: molecular dynamics simulation and experimentation," *Polymer*, vol. 173, pp. 80–87, 2019.

[46] M. Razi, A. Narayan, R. M. Kirby, and D. Bedrov, "Force-field coefficient optimization of coarse-grained molecular dynamics models with a small computational budget," *Computational Materials Science*, vol. 176, article 109518, 2020.

[47] F. Saint-Michel, L. Chazeau, and J. Y. Cavaille, "Mechanical properties of high density polyurethane foams: I. Effect of the density," *Effect of the Density, Composites Science & Technology*, vol. 66, no. 15, pp. 2700–2708, 2006.

[48] LAMMPS, "Molecular dynamics simulator," https://lammps.sandia.gov/.

[49] A. Stukowski, "Visualization and analysis of atomistic simulation data with OVITO–the Open Visualization Tool," *Modelling and Simulation in Materials Science and Engineering*, vol. 18, no. 1, article 015012, 2010.

[50] A. P. Thompson, S. J. Plimpton, and W. Mattson, "General formulation of pressure and stress tensor for arbitrary many-body interaction potentials under periodic boundary conditions," *Journal of Chemical Physics*, vol. 131, no. 15, article 154107, 2009.

[51] M. Staszczak, E. A. Pieczyska, M. Maj, D. Kukla, and H. Tobushi, "Infrared thermographic analysis of shape memory polymer during cyclic loading," *Measurement Science and Technology*, vol. 27, no. 12, article 124007, 2016.

[52] H. Xia, M. Song, Z. Zhang, and M. Richardson, "Microphase separation, stress relaxation, and creep behavior of polyurethane nanocomposites," *Journal of Applied Polymer Science*, vol. 103, no. 5, pp. 2992–3002, 2007.

[53] W. Dzierża, "Stress–relaxation properties of segmented polyurethane rubbers," *Journal of Applied Polymer Science*, vol. 27, no. 5, pp. 1487–1499, 1982.

[54] J. Li, J. Zhang, and S. Chen, "Study on dynamic viscoelastic properties and constitutive model of non-water reacted polyurethane grouting materials," *Measurement*, vol. 176, no. 8, article 109115, 2021.

Hindawi
Geofluids
Volume 2022, Article ID 9017792, 10 pages
https://doi.org/10.1155/2022/9017792

Research Article

Numerical Study on the Relationship between the Dominant Frequency of Blasting Vibration and the Development of Plastic Zone in Cylindrical Charge

Da Liu,[1] Xiaohua Zhao,[2] Jianglin Gao,[1] Binghan Xue,[2] Xiaobin Wu,[1] Songtao Hu,[1] and Fang Chen[1]

[1]*Jiangxi Hydraulic Safety Engineering Technology Research Center, Jiangxi Academy of Water Science and Engineering, Nanchang 330029, China*
[2]*School of Water Conservancy Engineering, Zhengzhou University, Zhengzhou 450001, China*

Correspondence should be addressed to Xiaohua Zhao; zhaoxh2014@126.com

Received 23 April 2022; Accepted 25 July 2022; Published 5 August 2022

Academic Editor: Basim Abu-Jdayil

Blasting vibration is a widely studied harmful effect of rock blasting excavations. Many factors affect its dominant frequency, which makes analyzing, evaluating, and predicting it difficult. This study explored the factors influencing the dominant frequency of blasting vibrations in the case of a spherical charge. Based on symmetry, a theoretical analysis in terms of a spherical explosion source is generally sufficient to describe a cavity excited by a spherical explosion charge. The elastic cavity radius and the dominant frequency of vibration induced by the spherical blasting source are closely related. However, there is a lack of relevant research on cylindrical charges. Therefore, a calculation model for a single-hole cylindrical charge was established. There is a relationship between the corresponding dominant frequency and the range of the plastic zone. The results indicate that the dominant frequency of the blasting vibration for both cylindrical and spherical charges is closely related to the range of the plastic zone formed by the rock blasting. As the elastic cavity radius increases, both the zero-crossing and the dominant Fourier frequencies decrease, and the amplitude spectrum shifts to lower frequencies. However, increasing the cylindrical charge diameter causes more changes in the plastic zone in the direction perpendicular to the cylindrical explosive axis. Moreover, increasing the charge length causes more changes in the plastic zone along this axis. It is therefore difficult to identify a unique dimensional parameter that characterizes the range of the plastic zone formed by the blasting. Because the plastic zone around a cylindrical charge is less regular than around a spherical charge, the charge weight Q is a more favorable parameter than the elastic cavity radius a when used as the main influencing factor and in an attenuation analysis for the dominant frequency of cylindrical charge blasting.

1. Introduction

As an efficient excavation method, borehole blasting is easy to induce harmful vibration effects, which has always been the focus of attention [1–3]. The dominant frequency induced by cylindrical charge is an important index to characterize blasting vibration [4, 5], but the theoretical research is not sufficient compared with spherical charge. Therefore, to fully understand the vibration characteristics of cylindrical charge qualitatively and quantitatively, it is often necessary to learn from the relevant spherical charge theory [6]. Previous studies have demonstrated that there are two stages of blasting vibration effect induced by spherical charge. The first stage is the initial state of explosive expansion, where the energy released by the explosive expands symmetrically in all directions, and P wave is generated, causing compression deformation in the surrounding rock mass. The second stage is the roof-like uplift caused by the expansion of soil within a certain epicenter distance due to the residual pressure of explosive gas in the spherical cavity, which is considered as the elastic vibration in the near region. For the spherical explosion source, due to the spherical symmetry of the explosion load, the problem can

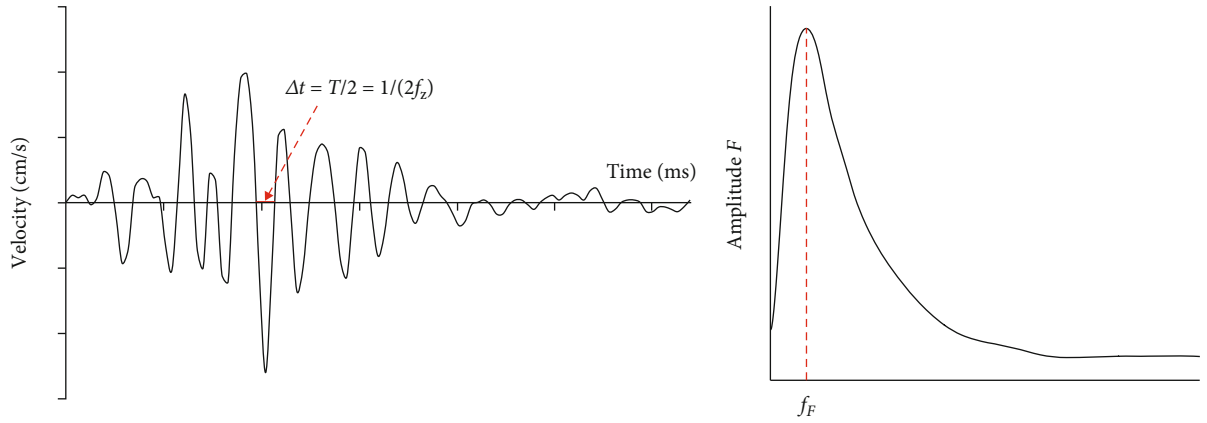

(a) Velocity–time histories of blasting

(b) Amplitude spectrum

Figure 1: Typical waveform and spectrum of blasting vibration.

be simplified to a one-dimensional problem, and the solution of the problem can be obtained through analytical calculation [7] so that the relationship between the vibration spectrum and the radius of the plastic zone can be analyzed and obtained. However, for cylindrical charge, the analytical solution of its dominant frequency is difficult to obtain due to the influence of many factors such as charge structure, explosion energy release form, and free surface [8, 9].

According to the degree of damage to the rock mass around the borehole blasting, it can be simply divided into crushed zone, cracked zone, and elastic formation zone [10]. In fact, the blasting damage of rock mass is a complex dynamic accumulation process. When discriminating the range of rock damage, most of the current methods to evaluate rock blasting damage are based on numerical modeling [11]. Grady [12] proposed an isotropic damage model for rock blasting, which uses a scalar to describe the deterioration of rock stiffness and assumes that the number of cracks obeys the two parameter Weibull distribution. Yang et al. [13] believe that the crack can propagate only when the bulk strain is greater than a certain value and proposed the concept of fracture probability, which is introduced in the definition of damage variable. Ma [14] introduced the Johnson-Holmquist (J-h) material model into LS-DYNA to simulate the rock fracture damage process caused by blasting.

To obtain the range of rock blasting damage area, most methods are trying to calculate the peak particle velocity (PPV) produced by the detonating charge compared against a PPV that is known or adopted (most of the time based on site-specific field tests) that will produce some damage in the rock or rock mass [15]. Holmberg-Perssion [16] assumes that the cylindrical charge is regarded as a small section connected in series, and the PPV distribution in the rock mass can be obtained by combining each small section of charge. Based on the cylindrical wave theory and the wavelet theory of spherical wave and long cylindrical charge, Hustrulid and Lu [17] deduced the theoretical formula for the attenuation of peak vibration velocity of blasting vibration particles by considering the detonation velocity of explosives from the viewpoint proposed by Starfield [18]. Most of the studies combine the damage range of rock with PPV, and generally, the larger the PPV induced by rock blasting, the larger the range of cracked zone caused by blasting. In fact, similar to PPV, the dominant frequency of blasting vibration is also an important parameter to characterize blasting vibration [19], which has two most commonly used definitions, including zero-crossing frequency f_z (the frequency corresponding to the peak vibration period) and Fourier frequency f_F (the frequency corresponding to the maximum amplitude in the spectrum), shown in Figure 1. And the dominant frequency is also closely related to the damage range formed by rock blasting [20]. However, there is much less research on the relationship between the dominant frequency of blasting vibration and the range of cracked zones caused by blasting. Therefore, through the research, it can provide some meaningful perspectives for exploring the propagation characteristics and attenuation characteristics of the dominant frequency of blasting vibration.

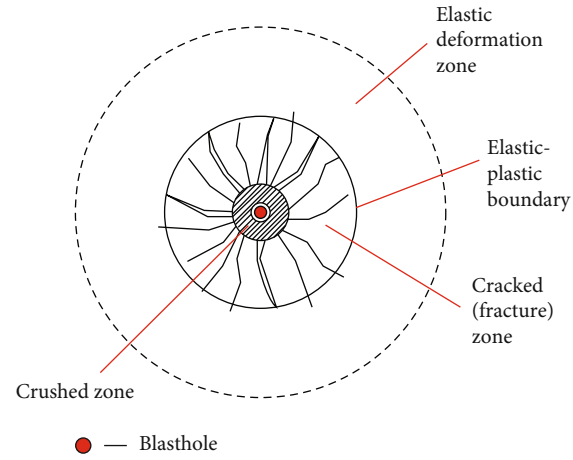

Figure 2: Damage zones surrounding a spherical detonation.

On the basis of the stress wave excited by spherical cavity explosion in an elastic rock mass, the theoretical solution of spherical wave propagation and the velocity spectrum are analyzed. By establishing the dynamic finite element model of

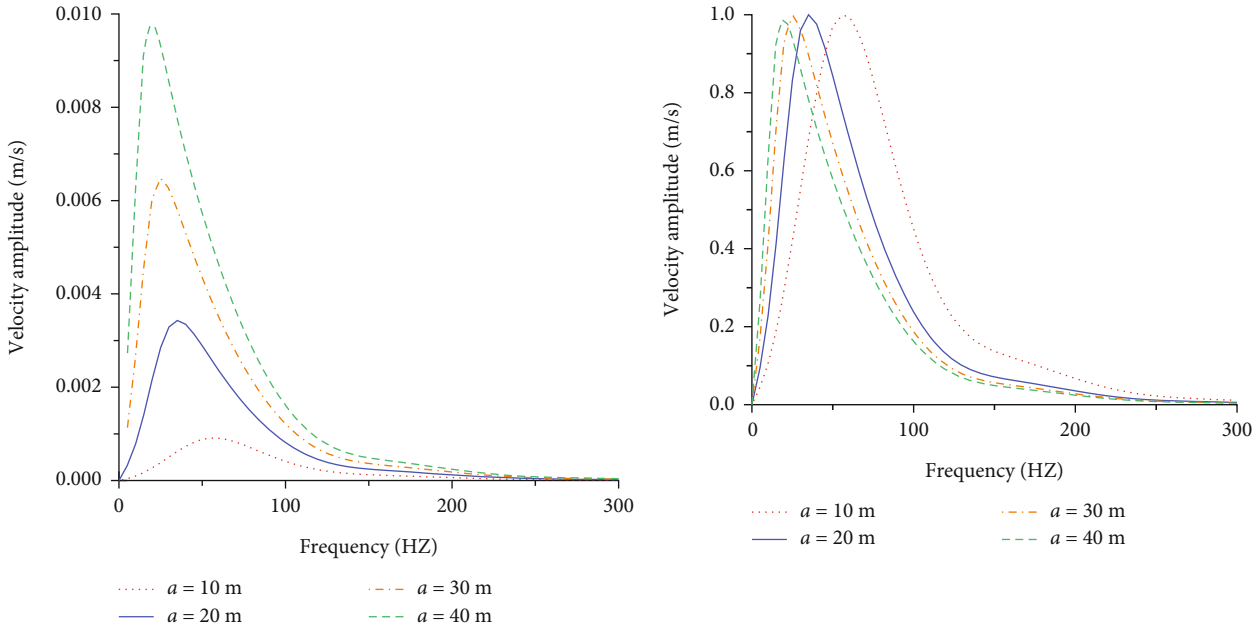

(a) Velocity amplitude spectrum

(b) Normalized to the peak value of the spectrum

Figure 3: Amplitude spectrum variation law of different elastic cavity radius.

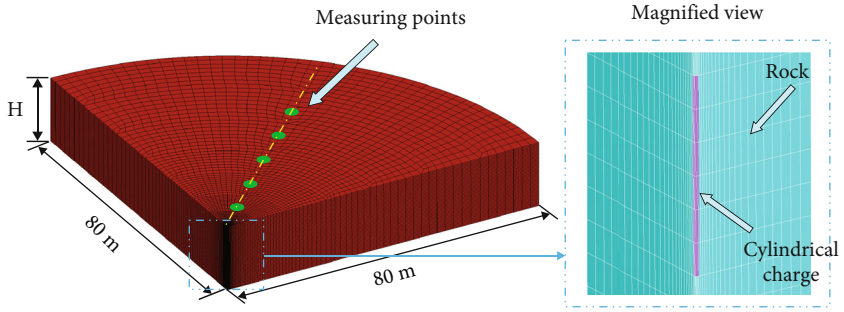

Figure 4: Quarter cylinder finite-element model.

single borehole cylindrical charge, the distribution characteristics of rock blasting cracked zone are analyzed, and the numerical relationship between the cracked zone of blasting and the dominant frequency is explored, which is helpful to understand the factors affecting the dominant frequency of blasting vibration by cylindrical charge.

2. Relationship between the Cracked Zone and the Dominant Frequency

The explosive blasting causes a large transient impact load acting on the rock, and the energy released by the explosive propagates outward in the form of stress wave. The regions encountered by a blasting stress wave propagating away from the blasting center can be approximately classified as the crushed, cracked, and elastic areas, according to the degrees of damage in the rock, and the propagation properties of shock, stress, and seismic waves vary accordingly. In the crushed zone, the rock is crushed because the pressure caused by the blasting load greatly exceeds its compressive strength. In the cracked (fracture) zone, the circumferential tensile stress of the rock mass often exceeds its tensile strength; the rock mass also undergoes an irreversible tensile deformation. In the elastic deformation zone, the load on the rock mass is only sufficient to cause elastic vibration and not plastic deformation. The blasting damage zone of the rock mass is illustrated in Figure 2.

To facilitate the analysis, the nonelastic zones (crushed zone and cracked (fracture) zone) near the blasthole are generally regarded as the equivalent blasting source, in which the elastic-plastic boundaries are applied on the blasting load [21–23]. Therefore, the theoretical solution of an elastic wave excited by a spherical cavity in an elastic medium can be adopted [7].

Introducing a potential function φ to represent the radial displacement

$$u = \frac{\partial \varphi(r,t)}{\partial r}. \tag{1}$$

Assuming the load function acting on the inner wall of the spherical cavity is $p(t)$,

Table 1: Calculation parameters of JWL equation of state for explosives.

Material	Density (g/m^3)	V (m/s)	CJ pressure (Pa)	A (GPa)	B (GPa)	R_1	R_2	ω
Explosion	1×10^3	3600	3.24×10^9	214	0.18	4.2	0.9	0.15

Table 2: Calculation parameters of rock materials.

Material	Elastic modulus (GPa)	Density (g/m^3)	Poisson's ratio	Shear modulus (GPa)	Bulk modulus (GPa)	Yield stress (MPa)
Rock	20	2400	0.24	8.06	12.8	40

Table 3: The radius of the middle section under different charge diameters.

Charge diameter d (mm)	Charge length l (m)	Charge weight Q (kg)	The radius of the middle section (m)
90	8	50.89	1.96
110	8	76.03	2.59
130	8	106.19	3.19

Table 4: Radius of plastic zone under different charge diameters.

Charge diameter d (mm)	Charge length l (m)	Charge weight Q (kg)	The radius of the middle section (m)
110	6	57.02	2.59
110	8	76.03	2.59
110	10	95.03	2.59

$$\varphi(r,t) = -\frac{a}{\rho\omega r}\int_0^s p(s-t)e^{-\eta\tau}\sin(\omega\tau)d\tau, \tag{2}$$

$$s = t - \frac{r-a}{C_P}, \tag{3}$$

$$\eta = \frac{1-2\nu}{1-\nu}\frac{C_P}{a}, \tag{4}$$

$$\omega = \frac{\sqrt{1-2\nu}}{1-\nu}\frac{C_P}{a}, \tag{5}$$

where $p(t)$ is the blasting load acting on the elastic cavity, λ and μ are the constants of lame, ν is Poisson's ratio, ρ is the density, and C_p is the longitudinal wave velocity. a is the radius of the elastic cavity (cracked zone). ω is the phase of the function φ, which is also the natural frequency of the equivalent system.

When the dynamic load of stress waves over time is adopted in the form

$$p(t) = \begin{cases} 0 & t<-\tau_1, \\ \sigma_{\max}(1+t/\tau_1) & -\tau_1 \le t \le 0, \\ \sigma_{\max}(1-t/\tau_2) & 0 \le t \le \tau_2, \\ 0 & t > \tau_2, \end{cases} \tag{6}$$

where $\sigma_{\max}$ is the peak value of blasting load, τ_1 is the rising time of blasting load, and τ_2 is the time of blasting load reduction from peak to zero.

By means of Fourier transform, the velocity spectrum of blasting vibration in elastic rock mass due to the action of $p(t)$ on the elastic boundary can be obtained as follows:

$$F(\omega) = \frac{|S_\sigma(j\omega)|a\omega C_p\sqrt{C_p^2 + r^2\omega^2}}{4\mu r^2\sqrt{(C_p/a)^4 + [1-(\lambda+2\mu)/2\mu]\omega^2(C_p/a)^2 + [(\lambda+2\mu)/4\mu]^2\omega^4}},$$
$$|S_\sigma(j\omega)| = \frac{\sigma_{\max}}{a_e b_e \tau\omega^2}\left[1 + a_e^2 + b_e^2 + 2a_e b_e\cos\omega\tau - 2(a_e\cos b_e\omega\tau + b_e\cos a_e\omega\tau)\right]^{1/2}, \tag{7}$$

where $\tau = \tau_1 + \tau_2$, $a_e = \tau_1/\tau$, and $b_e = \tau_2/\tau$.

The same rock mass parameters are selected: density $\rho = 2700\,\text{kg/m}^3$, Poisson's ratio = 0.22, peak value of blasting load $\sigma = 50\,\text{MPa}$, duration of blasting load $\tau = 10\,\text{ms}$, and rising time of blasting load $\tau_1 = 2\,\text{ms}$. The influence of elastic cavity radius on the blasting vibration spectrum is analyzed

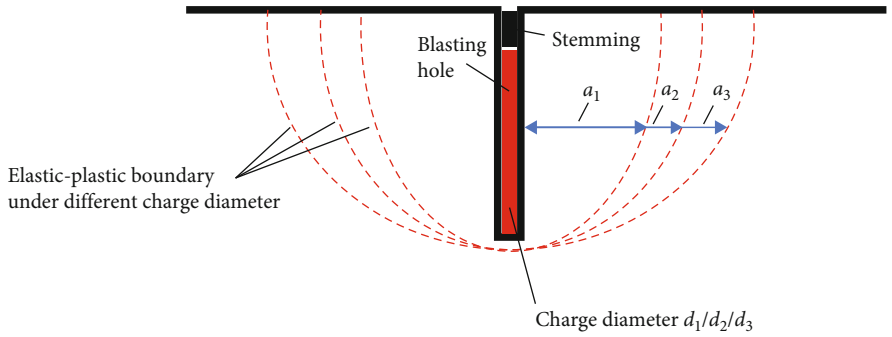

Figure 5: Elastic-plastic boundary under different charge diameter.

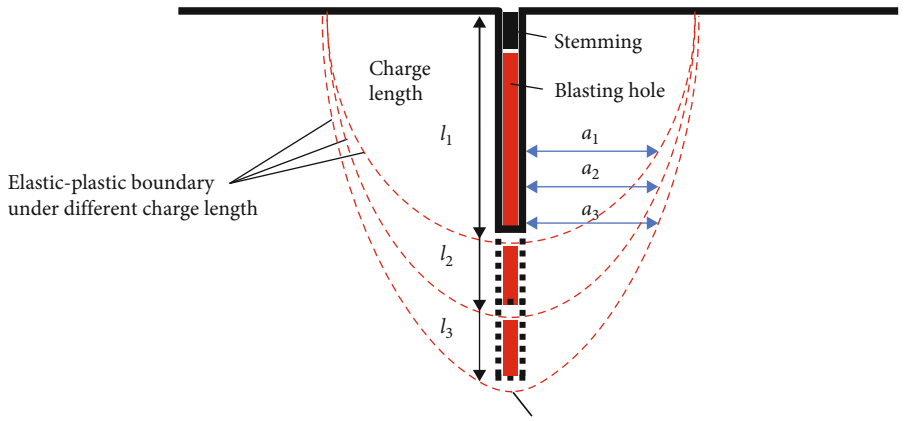

Figure 6: Elastic-plastic boundary under different charge lengths.

by substituting the rock parameters into the formula. The velocity amplitude spectra corresponding to different elastic cavity radius (elastic cavity radius $a = 10$ m, 20 m, 30 m, 40 m, 50 m) are plotted in Figure 3(a), and the normalized velocity amplitude spectra are plotted in Figure 3(b).

As shown in Figure 3, increasing the radius of the elastic cavity increases the amplitude of the vibration velocity spectrum and shifts the peak toward lower frequencies. The dominant Fourier frequency decreases with increasing radius of the elastic cavity.

3. Relationship between the Plastic Zone and the Dominant Frequency in Cylindrical Charge

3.1. Range of Plastic Zone. Under the condition of cylindrical charge, when the external load of the rock around the explosive reaches a certain value, the stress exceeds the yield strength of the rock, which brings irreversible plastic deformation. Cylindrical charge is different from the spherical charge that the plastic zone is not an approximate spherical zone, and the evolution radius of the plastic zone is not easy to define. In this study, the plastic deformation range of rock around the borehole is compared under different working conditions, and the plastic radius of the middle section of charge length with the bottom initiating cylindrical charge (hereinafter referred to as "the radius of the middle section") is taken for comparison under all different working conditions. In LS-DYNA program, when the equivalent stress is equal to the yield stress of the material, it is also used as the judgment standard for the material to enter plastic deformation. The yield criterion at coordinates i, j is as follows:

$$\frac{1}{2}s_{ij}s_{ij} - \frac{1}{3}\sigma_s^2 = 0, \tag{8}$$

where $s_{ij} = \sigma_{ij} - \sigma_m\delta_{ij}$ is the deviatoric stress tensor, $\sigma_{m=}1/3_{(\sigma_{11+}\sigma_{23+}\sigma_{33})}$ is the average stress, σ_s is the yield stress of rock, when the plastic deformation of rock occurs, and $\sigma_{11}, \sigma_{22}, \sigma_{33}$ is the first, second, and third principal stresses, respectively.

$$\bar{\sigma} = \frac{1}{\sqrt{2}}\sqrt{(\sigma_1 - \sigma_2)^2 + (\sigma_2 - \sigma_3)^2 + (\sigma_3 - \sigma_1)^2}. \tag{9}$$

Under the action of explosion load, the equivalent stress of rock $\bar{\sigma}$ is greater than the yield stress of rock σ_s.

3.2. Numerical Model and Calculation Conditions. The blasting process of a cylindrical charge in an infinite rock mass was simulated numerically using a finite-element model and numerically analyzed using the LS-DYNA software. The model represents a quarter cylinder of radius 80 m, as shown in Figure 4.

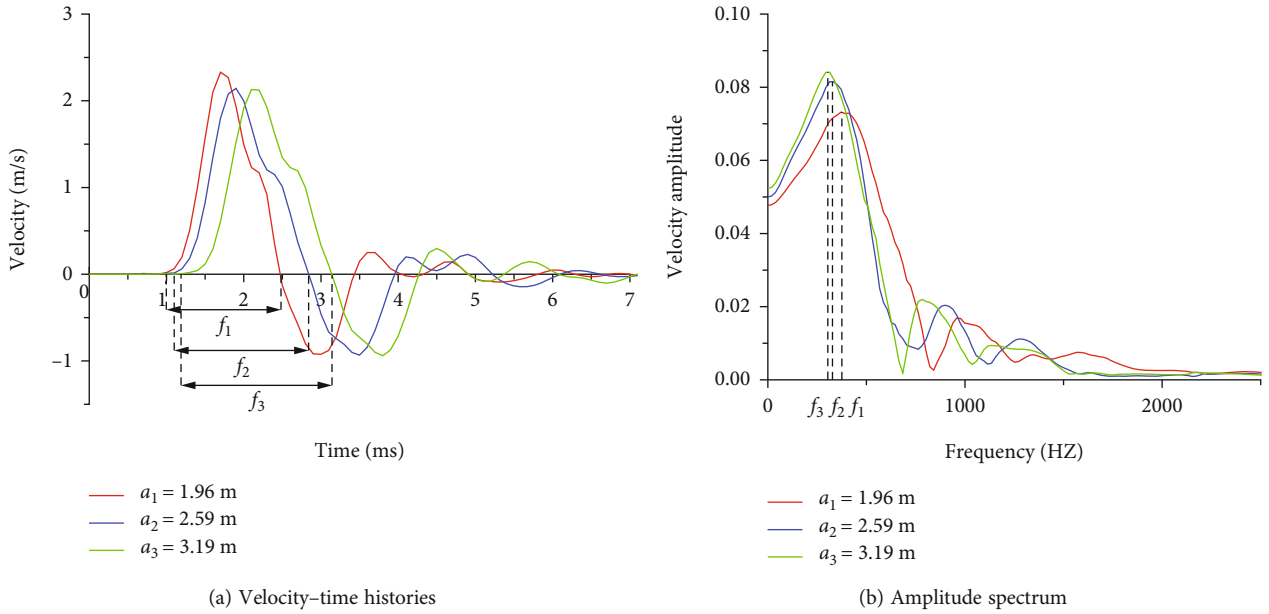

(a) Velocity–time histories

(b) Amplitude spectrum

Figure 7: Waveforms and spectra of the elastic-plastic boundary under different charge diameters.

Table 5: Radius of plastic zone under different charge diameters.

Charge diameter d (mm)	Charge weight Q (kg)	The plastic range radius of the middle section a (m)	Zero-crossing dominant frequency (Hz)	Fourier dominant frequency (Hz)
90	50.89	1.96	322.6	371.8
110	76.03	2.59	270.3	332.7
130	106.19	3.19	263.2	313.1

The dynamic impact of explosives is simulated by using the fluid-solid coupling algorithm, and the relationship between pressure and volume during the explosion is calculated by combining with JWL equation of state, in which the calculation parameters of the emulsion explosives used are shown in Table 1.

V is the velocity of detonation, A and B are the product JWL coefficient, R_1 and R_2 are the unreacted JWL coefficient, and CJ pressure is the initial pressure.

The rock mass is simplified as an isotropic ideal elastic-plastic material simulated by the bilinear elastic-plastic model in Table 2.

The development of the elastic cavity radius was analyzed by changing the radius and length of the charge, which are the dimensions commonly used in the context of foundation excavation in hydraulic engineering. The variations of the elastic cavity radius for different charge parameters are listed in Tables 3 and 4.

Under the condition of a constant charge length, we calculated the radii of the middle section formed by blasting, for charge diameters $d = 90$, 110, and 130 mm.

Under the condition of a constant charge diameter, we calculated the radii of the middle section formed by blasting, for charge length $l = 6$ m, 8 m, and 10 m.

As shown in Table 3, the plastic radius of the middle section of the charge length increases with the charge diameter between 90 and 130 mm. According to Table 4, the range of the plastic zone increases when the charge diameter remains constant at 110 mm while the charge length increases from 6 to 10 m. However, its size increases mainly along the axial direction of the cylindrical charge, and the plastic radius of the middle section for charge lengths a_1, a_2, a_3 shows no significant change.

Figures 5 and 6 suggest that an increase in the charge diameter and the charge length increases the range of the plastic zone. An increase in the charge diameter tends to increase the range of the plastic zone in the direction perpendicular to the explosive axis, and an increase in the charge length tends to increase the range of the plastic zone along the explosive axis direction. Therefore, the diameter of the plastic range of the cylindrical charge is more difficult to define owing to the shape of the charge in contrast to a spherical charge.

3.3. Analysis Results under Different Charge Diameters. Measuring points at the elastic-plastic boundary in the middle section were selected for analysis, in the case of different charge diameters $d = 90$, 110, and 130 mm. The waveform and frequency spectrum at these measuring points are compared and analyzed in Figure 7 and Table 5.

The plastic radius of the middle section shows little change for charge lengths $l = 6$, 8, and 10 m. Measuring points on the elastic-plastic boundary of the middle section

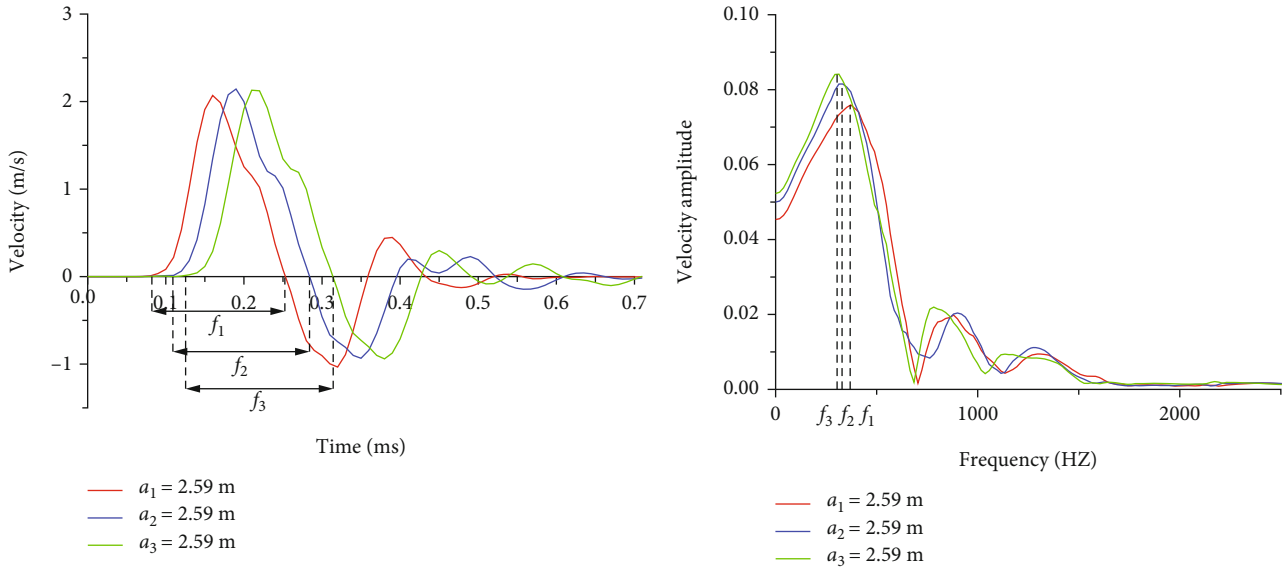

(a) Velocity–time histories

(b) Amplitude spectrum

Figure 8: Waveforms and spectra of the elastic-plastic boundary under different charge diameters.

Table 6: Radius of plastic zone under different charge length.

Charge length l (m)	Charge weight Q (kg)	The plastic range radius of the middle section a (m)	Zero-crossing dominant frequency (Hz)	Fourier dominant frequency (Hz)
6	57.02	2.59	294.1	371.8
8	76.03	2.59	270.3	332.7
10	95.03	2.59	263.2	313.1

were selected for analysis, and the corresponding waveforms and spectra are compared and analyzed in Figure 8 and Table 6 for various working conditions.

When increasing either the charge diameter or length, the plastic zone range also increases. However, changing the charge diameter and length causes the plastic zone to change in two different directions relative to the explosive geometry. This is a consequence of the more complex charge structure and load energy-release mechanism pertaining to a cylindrical charge, compared to a spherical charge. Therefore, the diameter of the plastic zone induced by the cylindrical charge is more difficult to define than in the case of a spherical charge.

Figures 7 and 8 suggest that increasing the charge diameter and length causes an increase in the range of the plastic zone and a decrease in the zero-crossing dominant frequency and in the dominant Fourier frequency. This is generally consistent with the results obtained for a spherical charge. However, the charge diameter and the charge length cause the plastic zone to change in two different directions relative to the explosive geometry. Specifically, an increase in the charge diameter causes an increase in the plastic range in the direction perpendicular to the explosive axis, and an increase in the charge length causes an increase in the plastic range along the explosive axis.

According to Equation (5), the dominant frequency of a blasting vibration often has a proportional relationship with C_p/a or C_p/Q. Most existing formulas for this frequency show C_p/a or C_p/Q as the proportionality factor [19, 24, 25]. Under the condition of spherical charge, the charge weight Q and the radius of elastic cavity a are interchangeable according to the relationship expressed as follows:

$$Q = \frac{4}{3}\pi a^3 q, \tag{10}$$

where q is the unit explosive consumption of rock.

The plastic zone radius a of a cylindrical charge is challenging to determine in an actual blasting process. (For example, as shown in Table 6, for a constant charge diameter and a charge length varying from 6 to 10 m, the plastic radius of the middle section does not change significantly.) It is therefore often replaced by the charge weight Q. A reasonable correlation is observed between the radius of the plastic zone and the dominant frequency of the cylindrical charge in Figures 9 and 10. However, owing to the complexity of the definition of plastic zone, the charge weight Q is a more favorable parameter than the elastic cavity radius a when used as the main influencing

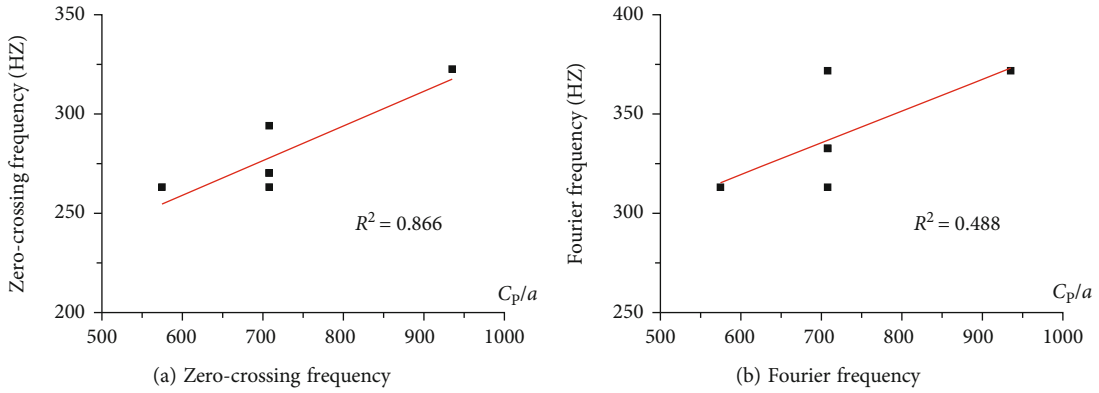

(a) Zero-crossing frequency (b) Fourier frequency

Figure 9: Linear fitting relationship between the dominant frequency and C_p/a.

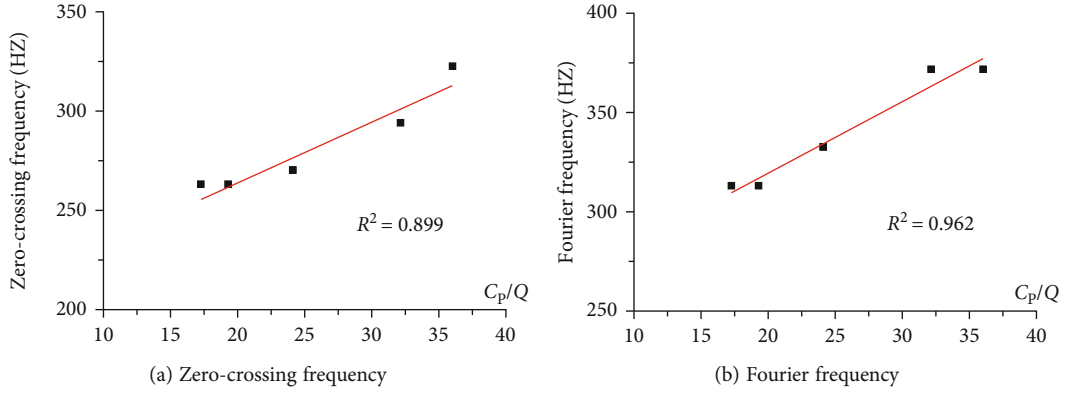

(a) Zero-crossing frequency (b) Fourier frequency

Figure 10: Linear fitting relationship between the dominant frequency and C_p/Q.

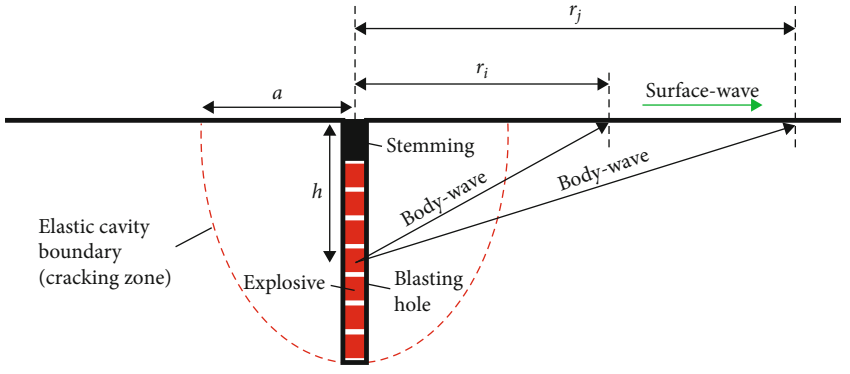

Figure 11: Schematic diagram of single-hole blasting.

factor and in the attenuation analysis of the dominant frequency of cylindrical charge blasting.

4. Discussion

Explosive blasting in rock forms a rock damage area. For cylindrical charge, there have been many studies on the definition and range of rock damage, which are different according to the rock damage criteria. For instance, Xayyraed [26] shows that when blasting a single hole in a semi-infinite rock medium with a known blasting load, the crushed zone radius r_1 and fractured (cracked) zone radius r_2 take the form

$$r_1 = \left(\frac{\rho_r C_P^2}{5\sigma_c}\right)^{1/2} \left(\frac{P}{\sigma}\right)^{1/4} a, \tag{11}$$

$$r_2 = \left[\frac{\mu P}{(1-\mu)\sigma_t}\right]^{1/\beta} a, \tag{12}$$

where μ is the Poisson ratio, C_p is the P wave velocity of the rock mass, σ_c and σ_t are the unconfined compressive strength

and tensile strength of the rock, σ is the compressive strength of the rock under multiaxial stress, P is the radial blasting load, and β is the attenuation exponent of the stress wave.

In Equations (10) and (12), the range of rock blasting damage area is comprehensively affected by rock mechanical parameters, blasting load, and charge weight (diameter). It can be seen that the range of rock plastic area is a more comprehensive index for the influencing factors of blasting vibration dominant frequency, compared with charge weight. However, it is not easy to characterize the range of rock damage zone for cylindrical charge.

In the process of excitation and propagation of blasting seismic waves, affected by the form of explosion source, the types and dominant components of blasting-induced seismic waves will be different. Different types of seismic waves will inevitably lead to the differences of blasting vibration spectrum and dominant frequency due to their differences in propagation speed and attenuation characteristics. According to the different propagation paths of the wave, it can be divided into body wave and surface wave. The propagation of body wave in rock mass can be divided into compressive wave (P wave) and shear wave (S wave), as shown in Figure 11. In terms of the existence of the surface free surface, the surface wave (S wave) will also appear on the free surface of the semi-infinite space, which further increases the complexity of analyzing the dominant frequency of cylindrical charge blasting.

5. Conclusion

In this study, the numerical relationship between the elastic cavity radius and the dominant frequency induced by cylindrical charge has been explored. It has been found that

(1) with the increase of the elastic cavity radius, the zero-crossing and the Fourier dominant frequency decreases, and the amplitude spectrum shifts to the low frequency part, which is similar to the regulation of spherical charge obtained by theoretical analysis

(2) both the increase of charge diameter and charge length will increase the plastic zone induced by cylindrical charge, but as a result of the more complex charge structure and load energy release mechanism of cylindrical charge compared with spherical charge, the charge diameter and charge length will cause the plastic zone to change in the different directions of the explosive

(3) the range of plastic zone of cylindrical charge also has an approximate logarithmic relationship with the dominant frequency. However, since the plastic zone of cylindrical charge is less regular than that of spherical charge, the charge weight Q is a more favorable parameter compared with the elastic cavity radius a when used as the main influencing factor and attenuation analysis on the dominant frequency of cylindrical charge blasting

Data Availability

The data that support the findings of this study are available from the corresponding author upon reasonable request.

Conflicts of Interest

The authors declare that they have no conflicts of interest.

Acknowledgments

This work is supported by the Natural Science Foundation of Jiangxi Province (20212BAB214044 and 20204BCJ23002), supported by the National Natural Science Foundation of China (51779190, 51779193, and 52009126), and supported by the Jiangxi Provincial Department of Water Resources Foundation (202224ZDKT08). The authors wish to express their thanks to all supporters.

References

[1] J. Henrych, *The Dynamics of Explosion and Its Use*, Elsevier Scientific Publishing Company, New York, 1979.

[2] C. H. Dowding, *Construction Vibrations*, Prentice-Hall, Upper Saddle River, NJ, 1966.

[3] P. K. Singh and M. P. Roy, "Damage to surface structures due to blast vibration," *International Journal of Rock Mechanics and Mining Sciences*, vol. 47, no. 6, pp. 946–961, 2010.

[4] J. H. Yang, W. B. Lu, Q. H. Jiang, C. Yao, S. Jiang, and L. Tian, "A study on the vibration frequency of blasting excavation in highly stressed rock masses," *Rock Mechanics and Rock Engineering*, vol. 49, no. 7, pp. 2825–2843, 2016.

[5] J. R. Zhou, W. B. Lu, P. Yan, M. Chen, and G. H. Wang, "Frequency-dependent attenuation of blasting vibration waves," *Rock Mechanics and Rock Engineering*, vol. 49, no. 10, pp. 4061–4072, 2016.

[6] C. Knock and N. Davies, "Blast waves from cylindrical charges," *Shock Waves*, vol. 23, no. 4, pp. 337–343, 2013.

[7] R. F. Favreau, "Generation of strain waves in rock by an explosion in a spherical cavity," *Journal of Geophysical Research*, vol. 74, no. 17, pp. 4267–4280, 1969.

[8] X. Jiang, S. Yan, and W. Liu, "An experimental research and analysis of the law of explosive stress wave propagation of cylindrical charge," *Applied Mechanics and Materials*, vol. 137, pp. 24–29, 2011.

[9] Y. H. Yoo, Y. Choi, J. Lee, and K. J. Yun, "Influence of the shape of explosive charge on the blast wave propagation," in *7th International Conference on Mechanical, Industrial, and Manufacturing Technologies*, Cape Town, South Africa, 2016.

[10] Z. D. Leng, W. B. Lu, M. Chen, P. Yan, and Y. G. Hu, "Improved the calculation model for the size of the crushed zone around the blasthole," *Explosion and Shock Waves*, 2015.

[11] H. Jang and E. Topal, "A review of soft computing technology applications in several mining problems," *Applied Soft Computing*, vol. 22, no. 6, pp. 38–51, 2014.

[12] D. E. Grady and M. E. Kipp, "Continuum modelling of explosive fracture in oil shale," *International Journal of Rock Mechanics and Mining Science and Geomechanics Abstracts*, vol. 17, no. 3, pp. 147–157, 1980.

[13] R. Yang, W. F. Bawden, and P. D. Katsabanis, "A new constitutive model for blast damage," *International Journal of Rock*

Mechanics and Mining ence & Geomechanics Abstracts, vol. 33, no. 3, pp. 245–254, 1996.

[14] G. W. Ma and X. M. An, "Numerical simulation of blasting-induced rock fractures," *International Journal of Rock Mechanics and Mining Sciences*, vol. 45, no. 6, pp. 966–975, 2008.

[15] A. Js, A. Tw, and B. Bl, "Practical assessment of rock damage due to blasting," *Science Direct International Journal of Mining Science and Technology*, vol. 29, no. 3, pp. 379–385, 2019.

[16] R. Holmberg and P. A. Persson, "The Swedish approach to contour blasting," *Proceedings of Conference on explosives and blasting technique*, Society of Explosives Engineers, New Orleans, 1978.

[17] W. Hustrulid and W. B. Lu, *Some General Concepts Regarding the Control of Blast-Induced Damage during Rock Slope Excavation*, 7th International symposium, rock fragmentation by blasting, Beijing: China, 2008.

[18] A. M. Starfield and J. M. Pugliese, "Compression waves generated in rock by cylindrical explosive charges: a comparison between a computer model and field measurements," *International Journal of Rock Mechanics and Mining Science and Geomechanics Abstracts*, vol. 5, no. 1, pp. 65–77, 1968.

[19] H. Li, X. Li, J. Li, X. Xia, and X. Wang, "Application of coupled analysis methods for prediction of blast-induced dominant vibration frequency," *Earthquake Engineering and Engineering Vibration*, vol. 15, no. 1, pp. 153–162, 2016.

[20] W. B. Lu, J. R. Zhou, M. Chen, P. Yan, and G. H. Wang, *Study on the Attenuation Formula of Dominant Frequency of Blasting Vibration*, Engineering Blasting, 2015.

[21] W. B. Lu, J. H. Yang, M. Chen, and C. Zhou, "An equivalent method for blasting vibration simulation," *Simulation Modelling Practice and Theory*, vol. 19, no. 9, pp. 2050–2062, 2011.

[22] Y. Hu, W. Lu, M. Chen, P. Yan, and J. Yang, "Comparison of blast-induced damage between presplit and smooth blasting of high rock slope," *Rock Mechanics and Rock Engineering*, vol. 47, no. 4, pp. 1307–1320, 2014.

[23] B. Xue, X. Du, J. Wang, and X. Yu, "A scaled boundary finite-element method with B-differentiable equations for 3D frictional contact problems," *Fractal and Fractional*, vol. 6, no. 3, p. 133, 2022.

[24] D. Liu, W. Lu, Y. Liu, M. Chen, P. Yan, and P. Sun, "Analysis of the main factors influencing the dominant frequency of blast vibration," *Shock and Vibration*, vol. 2019, 17 pages, 2019.

[25] Y. X. Peng, L. Wu, Y. Su, and C. H. Chen, "Study on the effect of elevation on the prediction of underwater drill and blasting vibration frequency," *Geosystem Engineering*, vol. 19, no. 4, pp. 170–176, 2016.

[26] A. H. Xayyraed, *Physical Process of Rock Blasting in Mining*, Mineral Press, Leningrad, 1974.

Hindawi
Geofluids
Volume 2022, Article ID 3541528, 14 pages
https://doi.org/10.1155/2022/3541528

Research Article

Research on Hanger Force and Main Arch Stability of Long-Span Concrete-Filled Steel Tube Arch Bridge

Yanli Wu,[1] **Mowei Qiu**,[1] **Shaokun Ma**,[2] **Xinlei Gao**,[3] **and Yahong Han**[3]

[1]*Huanghe Jiaotong University, Wuzhi, Henan 454950, China*
[2]*School of Civil Engineering, Guangxi University, Nanning 530004, China*
[3]*Harbin Institute of Technology National Engineering Research Center of Urban Water Resources Co., Ltd., Harbin 150006, China*

Correspondence should be addressed to Yanli Wu; 2013100221@zjtu.edu.cn

Received 28 February 2022; Revised 7 July 2022; Accepted 19 July 2022; Published 5 August 2022

Academic Editor: Dan Ma

In recent years, the construction of a CFST arch bridge has developed rapidly; however, as a kind of structural system dominated by compression, with the increase of material strength and span, the stability of the main arch of the CFST arch bridge has become more and more important. In this paper, the finite element method is used to analyze the hanger force and the main arch stability of the long-span CFST arch bridge. Combined with the Shenzhen Rainbow Bridge project, the axial force of the hanger, the internal force, and stability of the main arch of the arch bridge are studied. In the establishment of the finite element model, considering the actual operation of the arch bridge, the model simulates the interaction between steel pipe and concrete, it studies the large deformation of CFST arch bridges, and the stress distribution and overall stability of the arch bridge are analyzed. The results show that the main deformation of the CFST arch bridge is the vertical displacement of the deck, and the axial force of most members of the upper arch ribs is greater than that of the lower arch ribs. The axial force and bending moment of the lower arch rib near the arch foot are larger, and the compressive stress of the arch foot is greater than that of other positions. The axial force of the suspender of the arch bridge is the largest at both ends of the hanger and the middle hanger, and the axial force of the other hanger is close to each other, and the axial force changes little under the same case. The buckling modes of the arch are mainly the lateral buckling or flexural buckling of the arch rib outside the plane, which indicates that the vertical stiffness of the arch bridge structure is larger than that of the transverse stiffness. The research results make the load-bearing mechanism of the CFST arch bridge more clear and also provide a certain reference for the design and construction of the CFST arch bridge.

1. Introduction

The strength and performance of steel tube and concrete in the CFST arch bridge should be supplemented and improved [1]. First, the steel tube wall is reinforced by filling it with concrete [2]. Secondly, with the help of the steel tube's hoop effect on the core concrete, the core concrete is in a three-way compression state, so that the core concrete has higher compressive strength and antideformation ability, thus greatly improving the bearing capacity of the arch rib [3]. In addition, the steel tube ribbed arch can make the main arch ring itself a template for a self-erecting system and pouring concrete in the tube, which is convenient for the realization of the construction without support, thus solving the two major problems of the application and construction of the high strength material of the arch bridge [4]. And its economic benefits are more in line with the existing national conditions of our country, and it has become a new hot bridge type and is considered to be a relatively ideal structure for the construction of long-span arch bridges [5]. For the structure of the CFST arch bridge, the stability problem is particularly prominent, as the structure of the arch bridge is more complex; once the instability failure occurs, it will cause a chain reaction, resulting in huge losses. The stress of the CFST arch bridge is complicated, and it is difficult to calculate with the existing analytical methods, the finite element method is an effective method to solve complex problems, so the finite element method to analyze

the stability of the CFST arch bridge has the value of popularization and application.

The stability of long-span CFST arch bridges has been studied by many scholars at home and abroad. In order to study the structural stability and dynamic performance of the long-span CFST arch bridge, from the design form of the arch bridge hanger and different dynamic models, the influence line characteristics of the tie arch bridge and impact coefficient of bridge span under different train excitation are studied [6]. Some scholars have studied the influence of different filling schemes on the stability of CFST arch bridges from the perspective of construction [7]. For in-plane stability of a single round tubular concrete-filled steel tube arch bridge, considering the effects of equivalent slenderness ratio, span ratio, and longitudinal stiffness, the ultimate bearing capacity coefficient of the arch bridge is calculated [8]. The homogeneous generalized yield function for the compression and flexural stability analysis of CFST members was established by a comprehensive test method and regression analysis method; using a linear elastic iterative method to calculate the ultimate bearing capacity of the structure, it overcomes the limitation of the incremental nonlinear finite element method and can obtain higher calculation accuracy and efficiency [9]. Some scholars have studied the stability of the inclined concrete-filled steel tube arch bridge, the inclined arch can significantly improve the stability of the arch rib, but the bearing capacity of the arch rib should be matched with the CFST arch rib, so as not to be destroyed and lead to the overall instability of the arch rib under the ultimate load [10]. In order to study the influence of transverse braces on the concrete-filled steel tubular arch bridge, the effect of the parameters such as the spacing of transverse braces, the type of transverse braces, and the stiffness of transverse braces on the transverse elastic stability of the arch bridge is determined, and the main factors affecting the transverse stability of the arch bridge are judged [11]. In addition, the stability of the CFST arch bridge is also related to the research method, the characteristics of bridge foundation rock, and the underground water level [12–15].

2. Stability Theory Overview of CFST Arch Bridge

For CFST arch bridges, the bearing capacity of the main arch is mainly determined by its strength and stability, especially the stability, which has an important influence on the ultimate bearing capacity of CFST arch bridges. The buckling of the main arch can be divided into two types: branch point buckling and extreme point buckling.

2.1. Branch Point Buckling. Branch point buckling usually refers to the stressed structure being a perfect system; that is, the geometric shape and stress state of the arch are idealized, without defects and deviations, and the critical load of the arch can be solved by an analytical method:

$$N_{cr} = \pi^2 \frac{EI}{(kS)^2}. \quad (1)$$

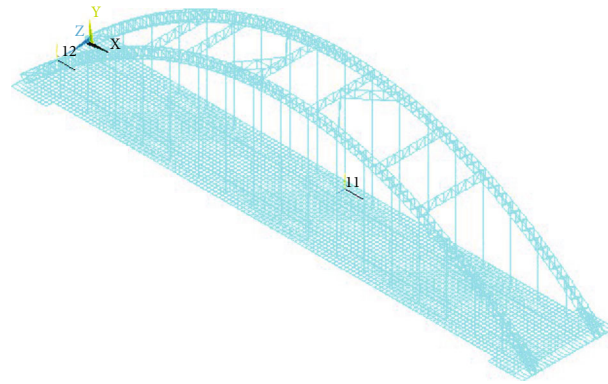

Figure 1: The finite element calculation model of CFST arch bridge.

In the equation, N_{cr} is a quarter of the cross-critical axial load of the arch, E is the elastic modulus of material, I is the moment of inertia of cross-section, S is half the length of the arch axis, and k is an effective length coefficient.

The critical load of branch point buckling can also be solved by the finite element method; usually using the virtual work principle, listing the equilibrium conditions, the element stiffness matrix of the structure is calculated and combined with the boundary conditions and load distribution of the arch. The equations of rod end displacement and rod end force are given by integrating the positioning vector and the overall stiffness matrix; the critical load and buckling mode of the arch branch point can be solved by the condition of a nonzero solution of joint displacement.

2.2. Extreme Point Buckling. Extreme point buckling generally occurs in imperfect systems; this is mainly due to the deviation of the geometry of the structure, uneven material properties, asymmetric load distribution, and other factors resulting in the buckling problem. At this time, the arch is in the state of bending and pressing, and the coupling problem between geometric nonlinearity and material nonlinearity needs to be considered simultaneously, which is very complicated to calculate. Especially for a concrete-filled steel tube arch bridge, the main arch belongs to a composite material, and the structural material property is complex, which makes the calculation of the stability of the main arch more difficult. The finite element method is generally used to calculate the buckling load of the main arch.

3. Finite Element Model

3.1. Material Parameters. In the calculation model, the constitutive relation of the CFST of the main arch is the key problem to establish the finite element model. At present, there are three methods to treat the CFST constitutive materials in China: the same node double element method, the equivalent stiffness method, and the unified theory method [16]. The equivalent stiffness method is relatively simple in modeling, and the accuracy can meet the engineering requirements when carrying out static force, but it does not consider the tightening effect of steel pipe on core

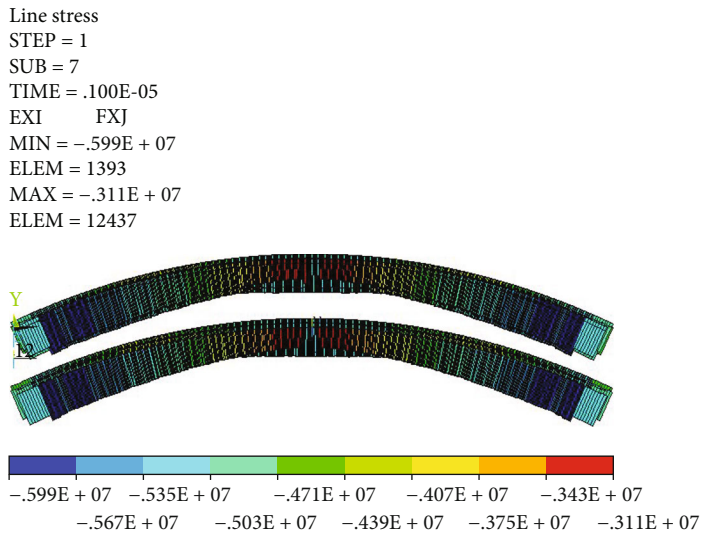

Figure 2: The axial force cloud map of main arch under case 5 (N).

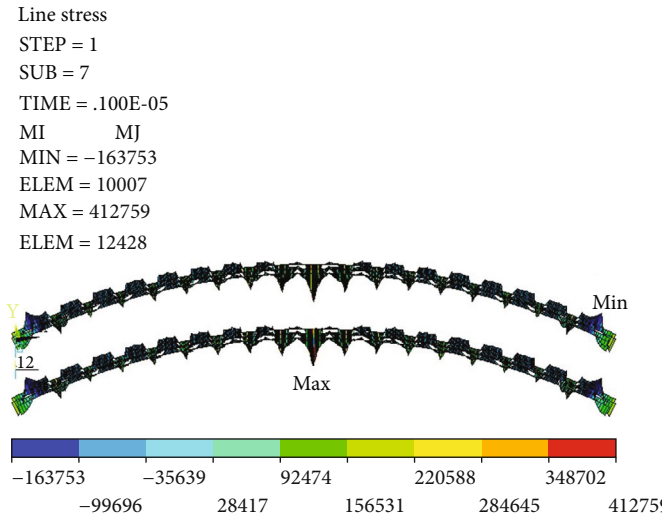

Figure 3: The bending moment cloud map of main arch under case 5 (N·m).

concrete [17]. According to the equivalent stiffness method, the comprehensive elastic modulus, area, and moment of inertia of CFST members in the limit state of normal service are calculated as follows.

The compression and tensile stiffness are

$$EA = E_a A_a + E_c A_c. \tag{2}$$

The bending stiffness is

$$EI = E_a I_a + E_c I_c. \tag{3}$$

In the expression, A_a and I_a are, respectively, the area of the cross-section of the steel tube and the moment of inertia with respect to its barycenter axis; A_c and I_c are, respectively, the area of the cross-section of concrete in the steel tube and the moment of inertia with respect to its barycenter axis; and E_a and E_c are the elastic modulus of steel and concrete, respectively.

The parameter setting of the arch bridge will affect the finite element simulation results, and the bridge stiffness will affect its deformation and vibration frequency. A bridge with high stiffness will produce small deformation and high frequency. In addition, the elastic modulus and Poisson's ratio of the material also affect the stress of the bridge.

3.2. Project Summary. Shenzhen Rainbow Bridge is 1.2 km long; it spans 29 railway channels of Shenzhen North Railway Station, making it one of the most bridges across railway channels in the world. The main bridge is a bottom-mounted CFST flexible tie arch with no thrust at the arch foot, the width of the bridge deck is 23.5 m, and the width of the bridge deck at the arch foot is 28 m. Computational span is 150 m, single span two-way four lanes, the rise-span ratio is 1/4.5, the arch axis is a catenary arch axis,

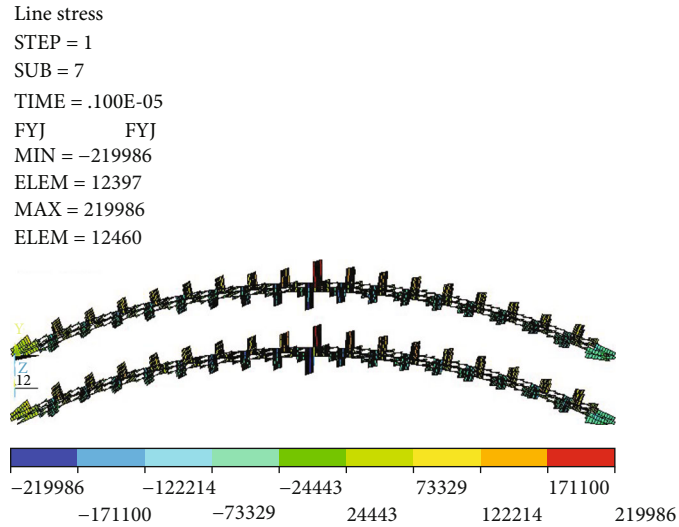

Figure 4: The shear force cloud map of main arch under case 5 (N).

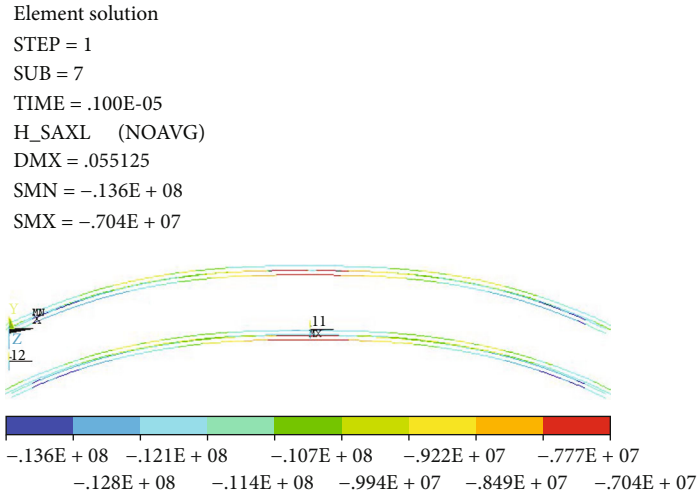

Figure 5: The axial stress cloud map of main arch under case 5 (Pa).

and the arch axis coefficient is 1.167. The bridge has double arch ribs, each arch rib is composed of $4\phi750 \times 12$ mm steel tube truss section, truss height is 3.0 m, truss width is 2.0 m, and the steel tube is filled with No.50 microexpansion concrete. A total of 17 pairs of hanger rods are set up in the arch ribs of the bridge, the hanger rods at each point are double hanger rods, and the hanger cables are extruded double-layer large pitch twisted stay cables [18]. Each hanger cable is composed of 61 galvanized high strength and low relaxation prestressed steel wires with a diameter of 7 mm; the standard strength of the steel wire is $R_y^b = 1670$ MPa. The foundation of the substructure is a single-column single-pile type, and the piers are composed of CFST columns with a diameter of 2.8-3.4 m with variable sections. The main arch and bridge pier adopt the form of arch pier consolidation, and the arch foot is the intersection point of the main arch pad, pier top, cap beam, and horizontal tie rod. The elastic modulus of steel wire $E_s = 205$ GPa, the steel bar uses HRB400, its strength design value is $f_y = f_y' = 360$ MPa, concrete strength grade is C50, and its elastic modulus is $E_c = 34.5$ GPa. The stability of the arch bridge is calculated by a linear elastic constitutive equation.

3.3. Finite Element Model. The bridge is modeled by general finite element software ANSYS; the model is divided into 56,387 elements and 510,998 nodes. The arch ribs of the bridge are modeled according to the arch axis equation, and the upper and lower strings of CFST are discretized by three-dimensional elastic beam elements; it is a uniaxial force element which can be used to bear pull, pressure, bending, and torsion and endows it with the characteristics of simulating CFST [19]. In addition, the BEAM4 beam element is also used to simulate the upper and lower horizontal joints, vertical belly bars, oblique belly bars, wind braces, and the longitudinal beams, beams, and precast hollow slabs in the bridge deck system. The suspender and the longitudinal

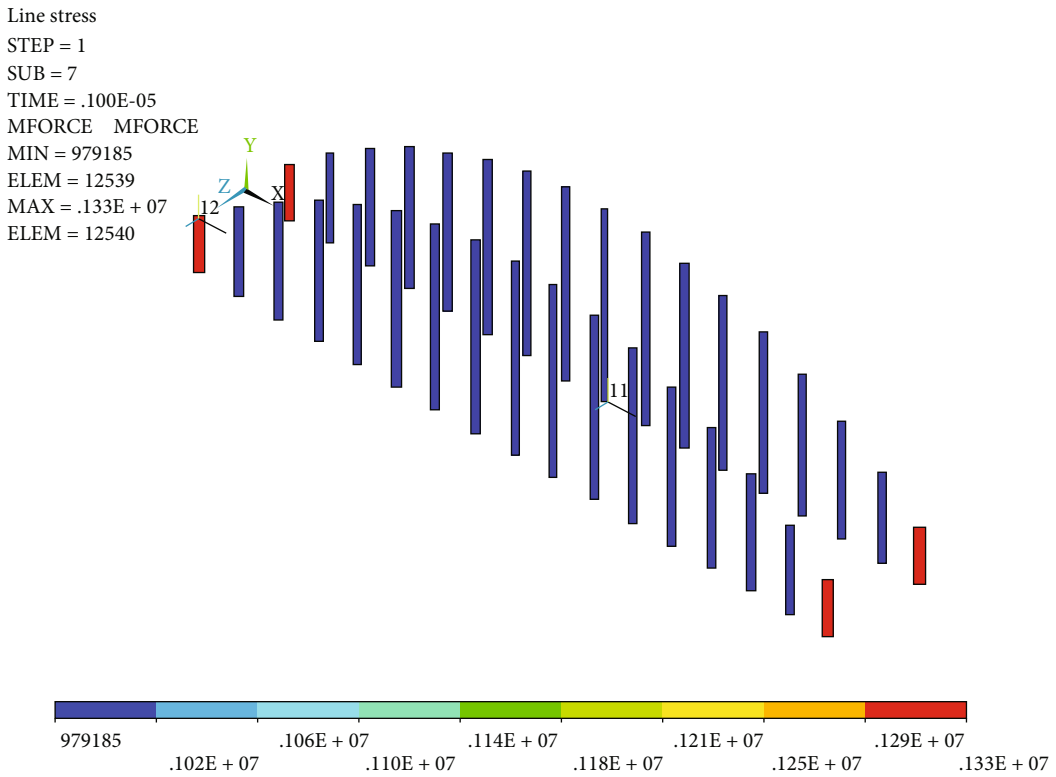

Figure 6: The axial force cloud map of hanger under case 1 (N).

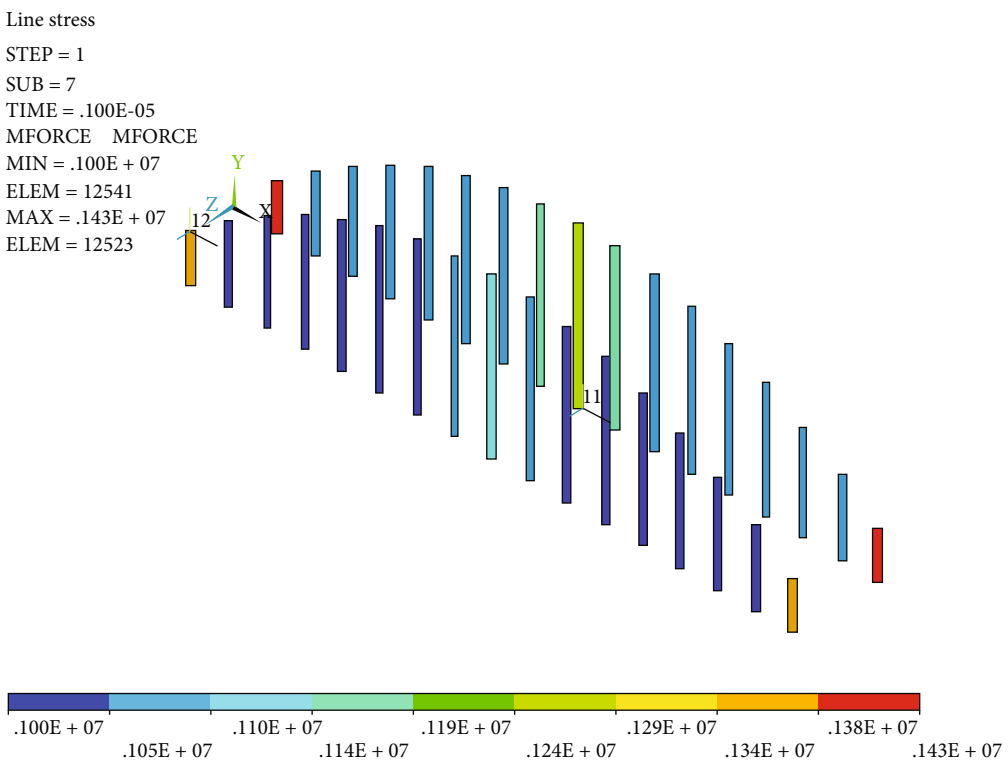

Figure 7: The axial force cloud map of hanger under case 2 (N).

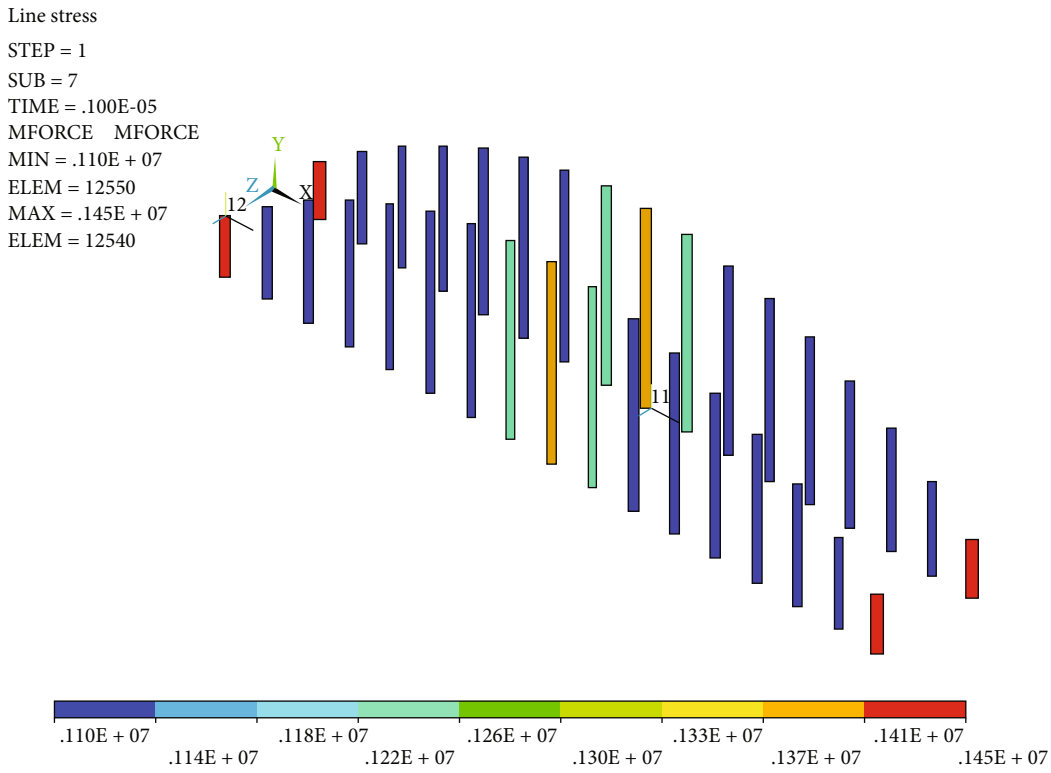

Figure 8: The axial force cloud map of hanger under case 5 (N).

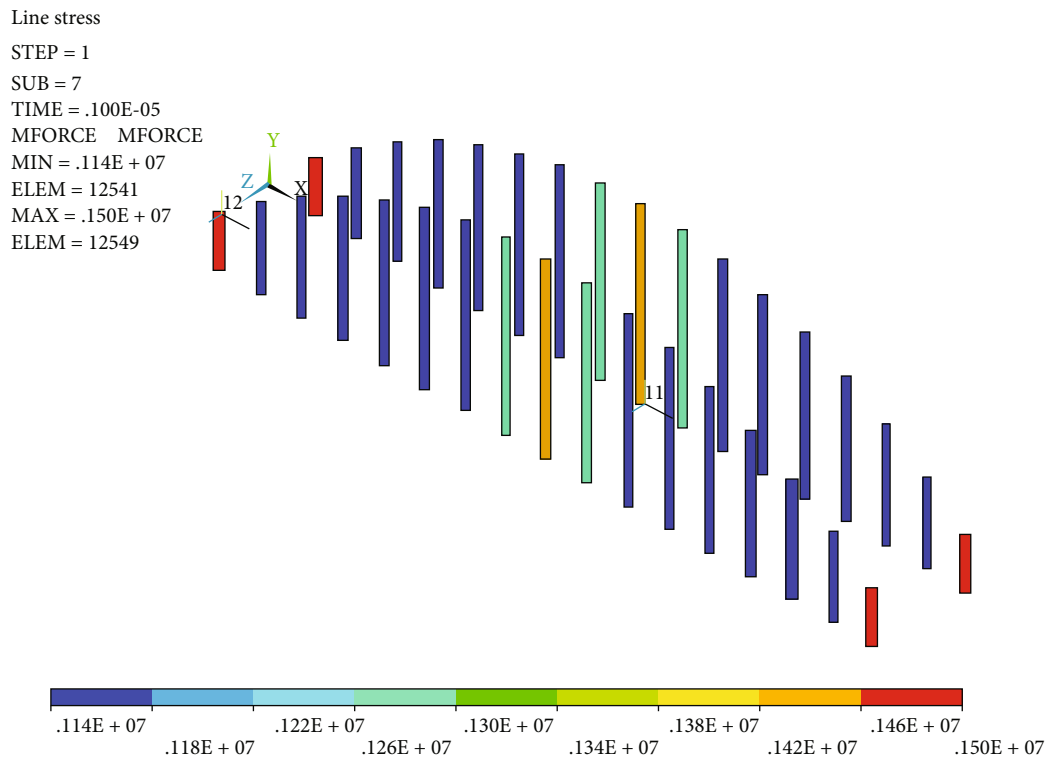

Figure 9: The axial force cloud map of hanger under case 7 (N).

horizontal tie rod are simulated by the space rod element (Link10) which only bears tension, and the element characteristics are set to only bear tension. The applied prestress is simulated by the method of equal effect variation. The principle is to generate the strain equivalent to the prestress in the structure by defining the real constant of the structure,

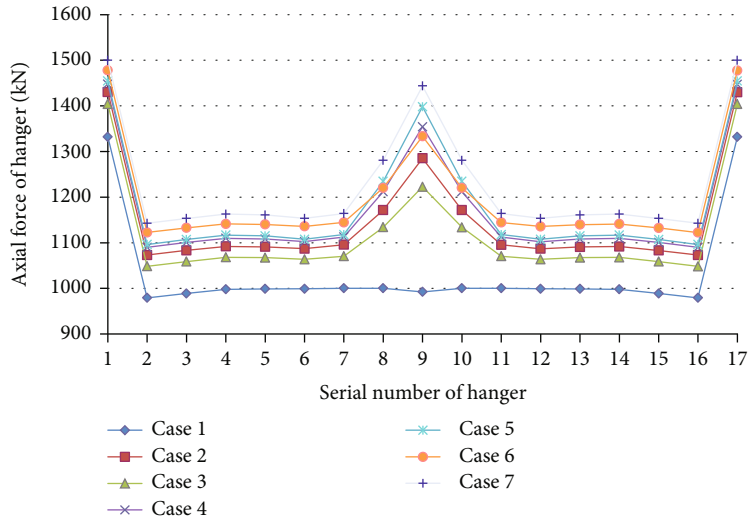

Figure 10: The variation curve of hanger axial force on the north side of arch bridge under various cases.

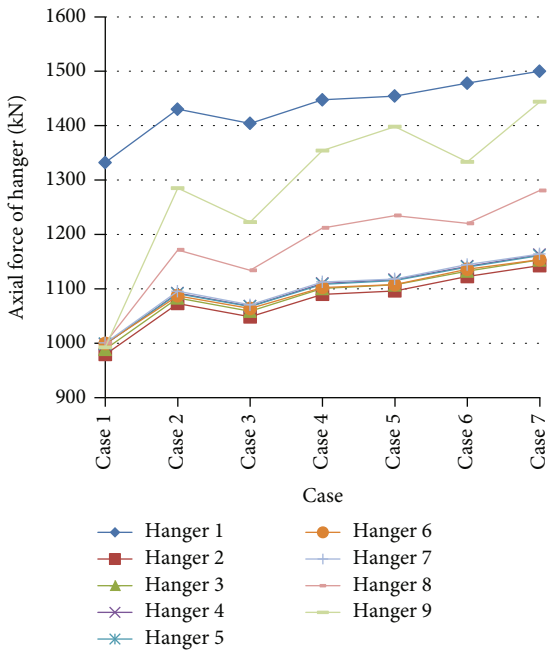

Figure 11: The variation curve of hanger axial force on north side of arch bridge with cases.

so as to achieve the purpose of indirect application of prestress [20]. The calculation model takes into account the bond between steel pipe and concrete; the connection between the main arch, suspender, and bridge slab; the structural constraints of the arch bridge; and the load during the construction and operation of the arch bridge. The finite element calculation model of the CFST arch bridge is shown in Figure 1.

3.4. Calculation Cases. In order to study the hanger force and the stability of the main arch of the CFST arch bridge, the rainbow bridge deck is arranged as four lanes in both directions, the lane load is 10.5 kN/m, and the crowd load is 2.5 kN/m^2. According to the volume and bulk density of the element, the weight of the bridge member is exerted on the element in the form of physical force; according to the principle of static equivalence, the variable loads of bridges are converted into uniform loads acting on the corresponding longitudinal beam elements. According to the stress characteristics of the arch bridge in operation and the layout of the driveway, when vehicles cross the bridge, considering the influence line of the bridge bending moment, the bridge weight, lane load, and crowd load are combined. The calculation conditions are combined as follows: case 1, weight of bridge structure; case 2, weight + 0.7 × lane 1 + 0.7 × lane 2; case 3, weight + 0.7 × lane 1 + 0.7 × lane 3; case 4, weight + 0.7 × lane 1 + 0.7 × lane 2 + 0.7 × lane 3; case 5, weight + 0.7 × lane 1 + 0.7 × lane 2 + 0.7 × lane 3 + 0.7 × lane 4; case 6, weight + 0.7 × lane 1 + 0.7 × lane 2 + crowd load 1; and case 7, weight + 0.7 × lane 1 + 0.7 × lane 2 + 0.7 × lane 3 + 0.7 × lane 4 + crowd load 1 + crowd load 2.

4. Force Analysis of Arch Bridge Structure

In order to have a clear understanding of the stress of the CFST arch bridge, a three-dimensional finite element model of the arch bridge is established based on the actual situation of the arch bridge. In the model, the bond between steel tube and concrete is simulated; the equivalent stiffness of CFST is given; the connection between the main arch, suspender, and bridge slab is simulated; and the element type used in the model of the CFST arch bridge is determined. Considering the load combination and the corresponding boundary conditions, the internal force of the suspender and the stability of the main arch of the CFST arch bridge are analyzed.

4.1. Force Analysis of Main Arch. Through the finite element analysis of the CFST arch bridge, the internal force and stress cloud maps of the main arch under various cases are obtained. The internal force and stress cloud maps of the main arch under case 5 are shown in Figures 2–5.

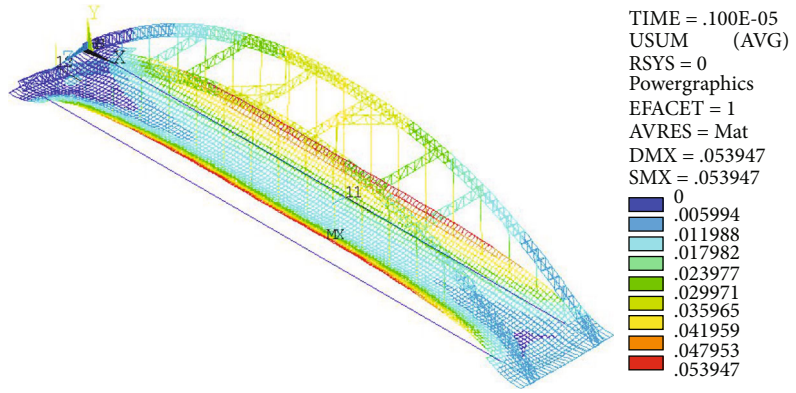

Figure 12: The overall displacement cloud map of arch bridge under case 1 (m).

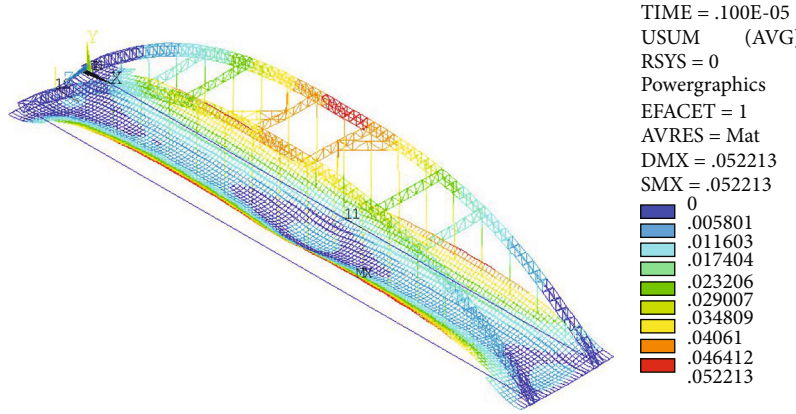

Figure 13: The overall displacement cloud map of arch bridge under case 2 (m).

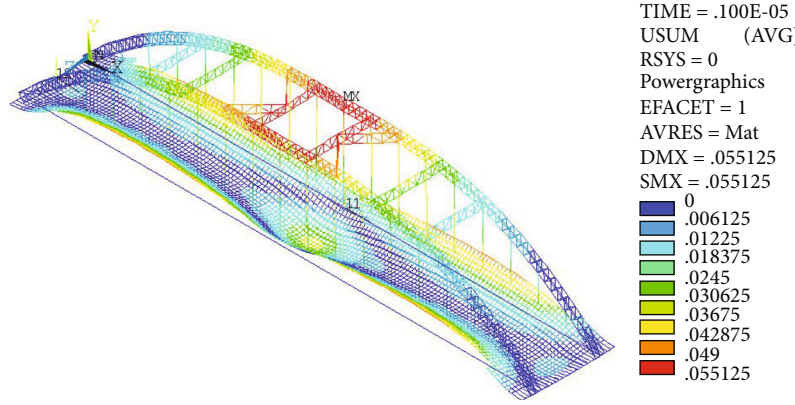

Figure 14: The overall displacement cloud map of arch bridge under case 5 (m).

As we can see from Figure 2, the whole CFST of the arch rib is in the state of compression and increases with the increase of load. The absolute value of the axial force in the middle part of the arch rib is small but increases obviously to both sides, and the maximum value of the absolute value of the axial force appears near the arch foot. In Figure 3, the maximum positive bending moment is 412.759 kN·m; the maximum negative bending moment is -163.753 kN·m. In Figure 4, the shear force in the arch rib changes at the hanger, which is due to the effect of the transmission force of the hanger, and the maximum and minimum values appear at the relatively symmetrical position in the middle of the span. In Figure 5, the axial stress of the four upper and lower string CFST in the arch rib is in a regular distribution from the top to the foot, the maximum value is 13.6 MPa, stress is less than the axial compressive strength of C50 microexpansion concrete 23.1 MPa, and the upper arch rib compressive stress is greater than the lower chord compressive stress.

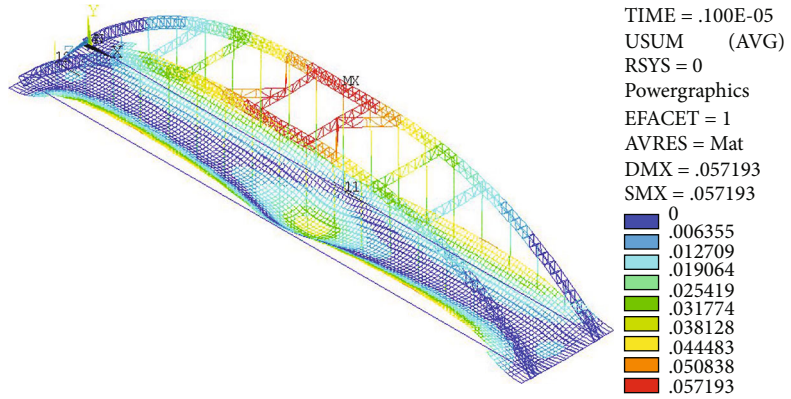

Figure 15: The overall displacement cloud map of arch bridge under case 7 (m).

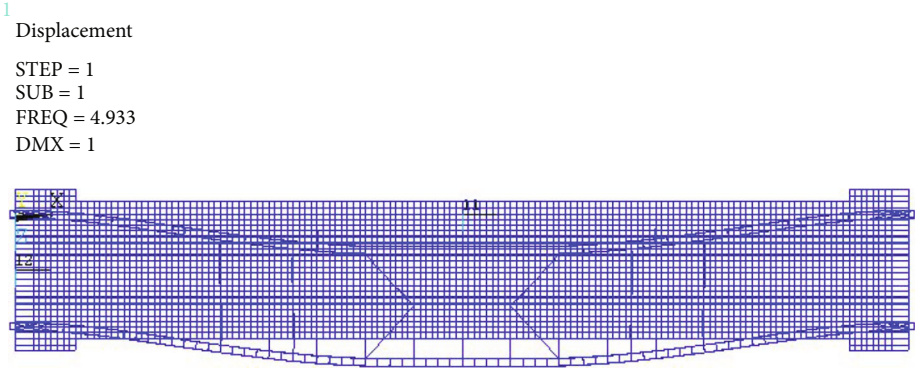

Figure 16: The first order buckling mode of arch bridge under case 1.

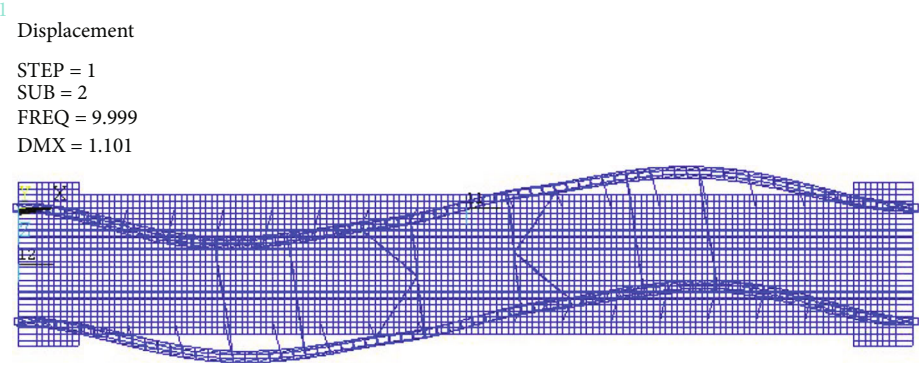

Figure 17: The second order buckling mode of arch bridge under case 1.

4.2. Force Analysis of Hanger. Through the finite element analysis of the CFST arch bridge, the axial force of the hanger under various cases is obtained. The axial force cloud map of the arch bridge hanger under cases 1, 2, 5, and 7 is shown in Figures 6–9.

We can see from Figures 6–9, under case 1, that the hanger is the main tensile component in the bridge, its main function is to transfer the weight and load of the bridge deck to the arch ribs, so its stress is large. Under case 2, compared with case 1, the axial force of each hanger varies greatly, and the force is no longer uniform, the hanger force at the middle and end of the span is larger, and the hanger force at the north side is obviously larger than that at the south side, but it still presents longitudinal symmetry. Under case 5, due to the symmetry of the lane, the force of the hanger is also symmetrical, the distribution law of the hanger force between the middle and the end of the span is larger, and the hanger force between them is smaller. Under case 7, the tension of the hanger increases obviously with the increase of the distribution load, the stress of the hanger at the end is larger, and the stress of the other hanger near the end is relatively small, with the maximum value of 1500 kN.

In order to analyze the axial force of the hanger of the arch bridge, the northern hanger of the arch bridge is numbered from one end of the arch bridge to the other end, and the numbers are 1 to 17. The variation curve of the hanger

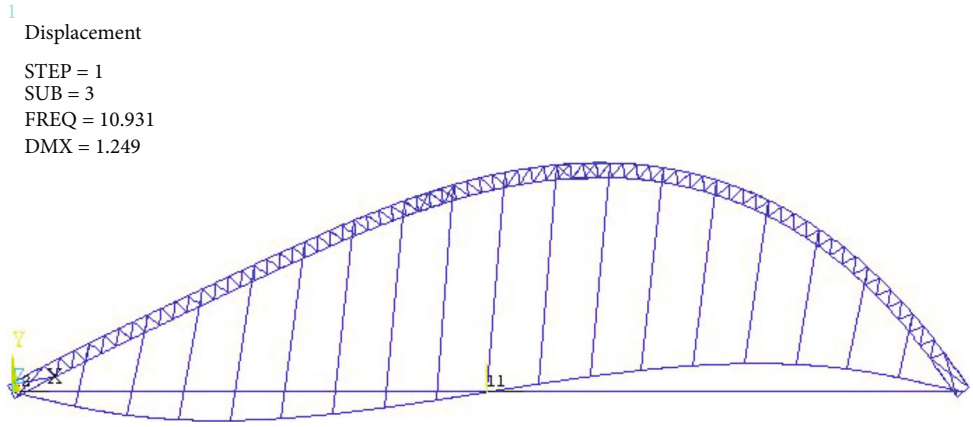

Figure 18: The third order buckling mode of arch bridge under case 1.

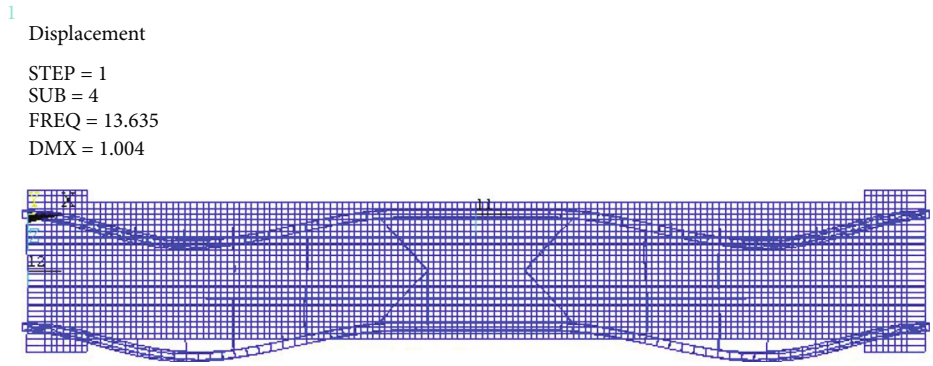

Figure 19: The fourth order buckling mode of arch bridge under case 1.

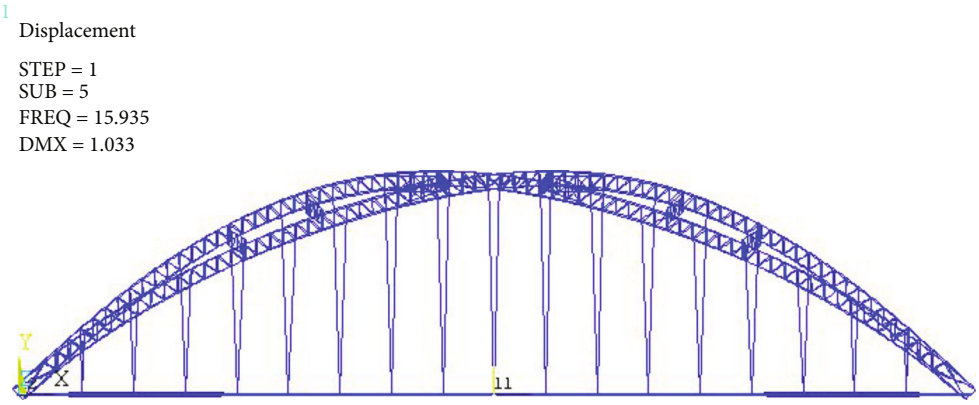

Figure 20: The fifth order buckling mode of arch bridge under case 1.

axial force on the north side of the arch bridge under various cases is shown in Figure 10; the variation curve of hanger axial force on the north side of the arch bridge with cases is shown in Figure 11.

We can see from Figure 10 that the axial force of the hanger on the north side of the arch bridge changes symmetrically; except for case 1, the axial force of the hanger on both ends and the middle suspender is the largest in all cases; the axial force of hanger 2 to hanger 5 and hanger 11 to hanger 16 has little change and tends to be stable. Under case 1, the axial force of the hanger at both ends is the largest, while the axial force of the hanger in the middle tends to be stable with little change. The maximum axial force of the hanger at both ends appears in case 7, and the maximum axial force value is 1500 kN. The maximum axial force of the middle hanger appears in case 7, and the maximum axial force value is 1443.8 kN. We can see from Figure 11 that due to the symmetry of the axial force of the hanger, only hanger 1 to hanger 9 are taken; under various cases, the axial force of hanger 1 is the largest, and it shows a trend of gradual increase with each case. The axial force of hanger 8 and hanger 9 fluctuates with the case, the

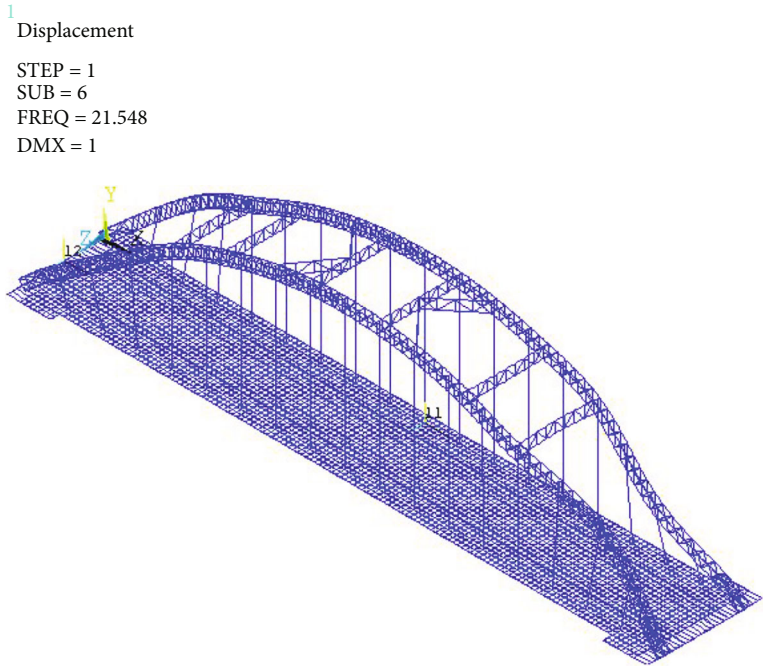

Figure 21: The sixth order buckling mode of arch bridge under case 1.

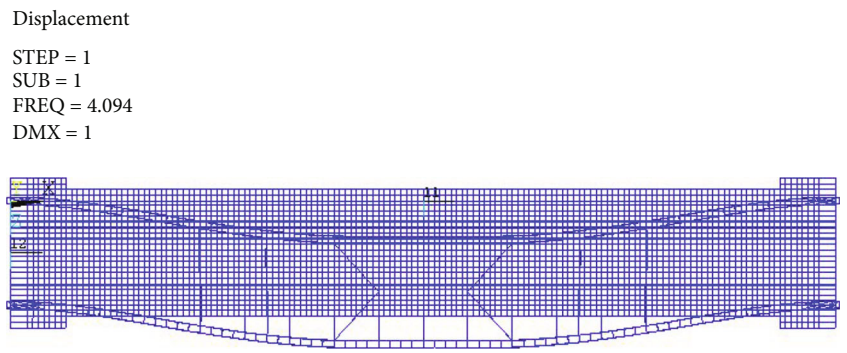

Figure 22: The first order buckling mode of arch bridge under case 7.

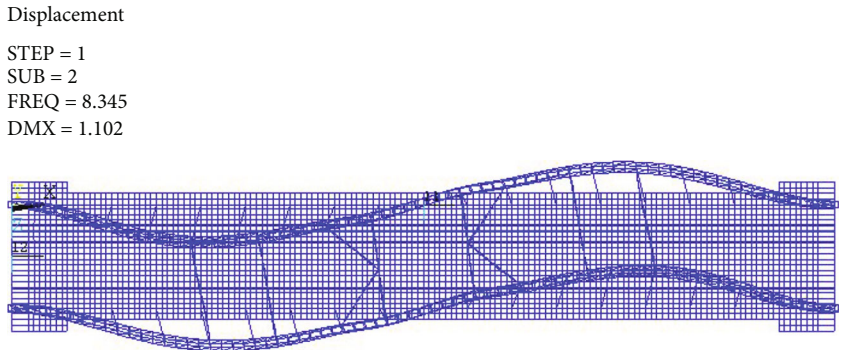

Figure 23: The second order buckling mode of arch bridge under case 7.

axial force values of other hangers are very close, and the axial force changes little under the same case. Under case 7, the axial force of each hanger is the maximum.

4.3. Displacement Analysis. Through the numerical simulation analysis of the CFST arch bridge, the overall displacement of the arch bridge under various cases is obtained.

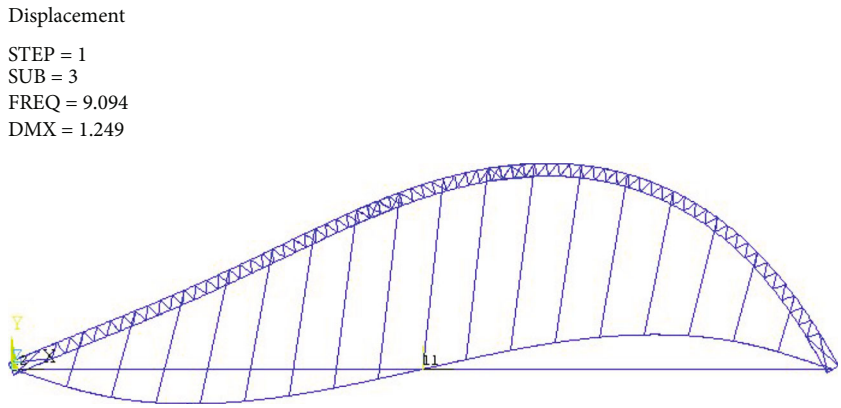

Figure 24: The third order buckling mode of arch bridge under case 7.

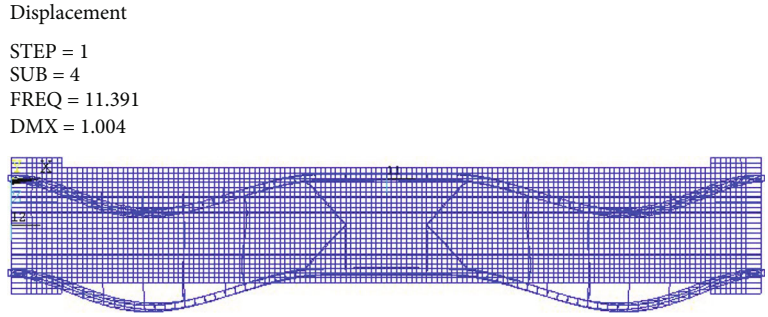

Figure 25: The fourth order buckling mode of arch bridge under case 7.

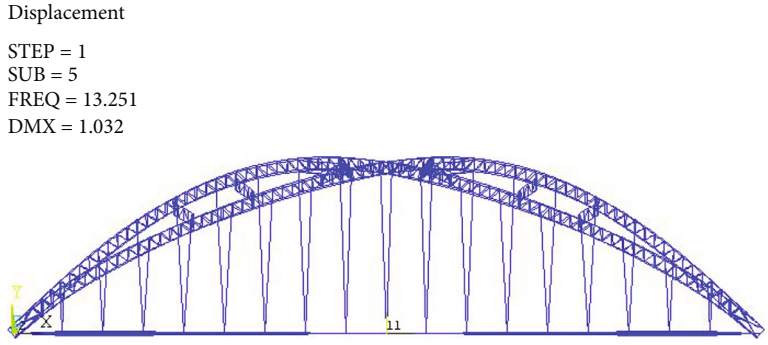

Figure 26: The fifth order buckling mode of arch bridge under case 7.

The overall displacement cloud maps of the arch bridge under cases 1, 2, 5, and 7 are shown in Figures 12–15.

We can see from Figures 12–15, under case 1, that the maximum displacement occurred near the middle span of the lower arch rib on the north side, and the maximum displacement is 5.39 cm; the deformation gradually decreased from the middle span to the bridge head and tail, showing along longitudinal and transverse symmetry. Under case 2, the maximum displacement of the arch bridge occurs near the middle of the fourth span of the south lane, and the maximum displacement is 5.22 cm, because the load applied is symmetrical along the longitudinal direction, while the transverse direction of the bridge is antisymmetric, the deformation gradually decreases from the middle span to the bridge head and tail, while the deflection increases significantly in the transverse direction where there is load. Under case 5, the maximum displacement of the arch bridge is 5.51 cm, which appears at the connection point between the horizontal beam and the hanger in the midspan; the deflection increases significantly in the place where there is load on the transverse bridge deck. Under case 7, the maximum displacement of the arch bridge is 5.72 cm, which occurs in the middle span of the arch rib on the south side, and it is less than the allowable deflection of the bridge $L/800 = 18.5$ cm.

5. Overall Stability Analysis of Arch Bridge

By analyzing the overall stability of the CFST arch bridge, the instability modes of the arch bridge under various cases are obtained. The internal force of the hanger calculated under cases 1 and 7 is equivalent to the external force and directly added to the lifting point on the upper arch rib, and the first

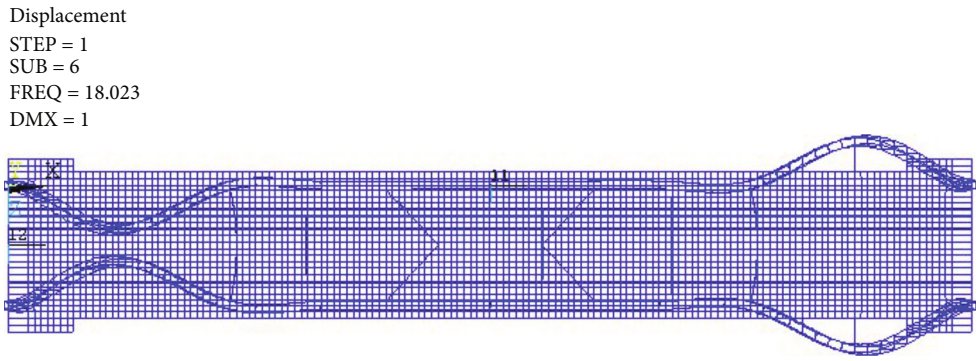

Figure 27: The sixth order buckling mode of arch bridge under case 7.

Table 1: The first six order stability coefficients of the main arch under various cases.

Buckling order	Stability coefficients						
	Case 1	Case 2	Case 3	Case 4	Case 5	Case 6	Case 7
1	4.9331	4.5693	4.5695	4.4062	4.2549	4.4732	4.0938
2	9.9988	9.2708	9.2891	8.9646	8.6754	9.0505	8.3450
3	10.931	10.158	10.141	9.7897	9.4517	9.9691	9.0945
4	13.635	12.671	12.677	12.243	11.842	12.396	11.391
5	15.935	14.758	14.778	14.249	13.773	14.417	13.251
6	21.548	19.766	20.021	19.248	18.734	19.074	18.023

six order buckling modes of the arch bridge under cases 1 and 7 are calculated, as shown in Figures 16–27.

We can see from Figures 16–21 that the first order buckling load coefficient is 4.9331, and the first, second, and fourth order buckling modes of the main arch are all out-of-plane instability; the specific modes can be divided into the first symmetrical buckling outside the arch rib plane, the second antisymmetric buckling outside the arch rib plane, and the symmetric buckling outside the arch rib plane. The sixth mode is the local antisymmetric buckling outside the rib surface near the arch foot, the third mode is antisymmetric buckling in the rib plane, and the fifth mode is torsional buckling of arch ribs. In general, for the arch bridge, considering the combined action of the arch rib, suspender, and deck system, the in-plane stiffness is larger. The out-of-plane stiffness decreases with the increase of the span, and the out-of-plane stability problem is more prominent than the in-plane stability problem. The above calculation results also fully reflect the stability characteristics of the CFST arch bridge.

We can see from Figures 22–27 that the first order buckling load coefficient is 4.0938, which is larger than the reduction in case 5. All the other modes of the arch are out-of-plane buckling except the third mode, which is in-plane buckling. The specific modes include the first symmetrical buckling outside the arch rib plane, the second antisymmetric buckling outside the arch rib plane, the fourth symmetrical buckling outside the arch rib plane, the fifth antisymmetric buckling outside the arch rib plane (torsion of the arch rib), and the local antisymmetric buckling outside the arch rib plane near the foot of the arch. These can reflect that the arch bridge outside the plane buckling problem is more prominent.

The first six order stability coefficients of the main arch under various cases are shown in Table 1. The stability coefficient refers to the application of unit load under various cases; the ratio of actual buckling load to unit load is the stability coefficient.

We can see from Table 1 that with the increase of the load, the stability coefficient of the main arch decreases gradually; that is, the stability safety reserve capacity decreases. With the increase of the buckling order, the stability coefficient gradually increases; that is to say, the possibility of high-order buckling becomes less and less. With the increase of the instability order, the stability coefficient changes more and more obviously with the load. For example, in the first instable mode, the stability coefficient of case 1 and case 2 varies by 0.3638; in the sixth instable mode, the stability coefficient of case 1 and case 2 varies by 1.782. The stability coefficients of different modes in case 2 and case 6 are very small, so the crowd load has little influence on the stability of the arch bridge.

6. Conclusion

(1) The main deformation of the arch bridge is the vertical displacement of the bridge deck; the axial force of most members of the upper arch rib is greater than that of the lower arch rib

(2) The axial force and bending moment of the lower arch rib near the arch foot are larger, which first enters the plastic state, and the stiffness should be strengthened in the structural design

(3) The maximum compressive stress appears near the arch foot, and the maximum compressive stress is less than the compressive strength of concrete; the arch bridge meets the strength requirements

(4) The maximum vertical displacement of the arch bridge is 5.72 cm, the displacement value is small, and the bridge meets the stiffness requirements

(5) The hanger axial force is symmetrically distributed, and the hanger axial force at the bridge middle span

and ends is large, while that on the other hanger has little change

(6) The vertical stiffness of the arch bridge is greater than the lateral stiffness, and the basic instability of the arch bridge is out-of-plane. The lateral support should be strengthened; it increases the lateral stiffness of the arch bridge and the ultimate bearing capacity of the main arch

Data Availability

The data used to support the findings of this study are included within the article.

Ethical Approval

The content of the thesis conforms to the moral and ethical standards. Review of essays ensures independence and fairness. The data in this paper are real and reliable, and there is no plagiarism. The paper was not duplicated. The references are in accordance with the standard.

Conflicts of Interest

There is no conflict of interest in funding, intellectual property rights, personal relationships, ideology, and academic nature. This paper was published without any conflict of interest with anyone other than the author.

Authors' Contributions

The authors of this paper are Yanli WU, Mowei QIU, Shaokun Ma, Xinlei Gao, and Yahong Han. All the authors have made scientific contributions to the results of the paper.

Acknowledgments

This paper is funded by the Cultivation Program for Young Backbone Teachers in Colleges and Universities of Henan Province (2020GGJS285) and Soft Science Research Project of Henan Province (222400410319). All thanks are due to those who contribute to this paper.

References

[1] W. Hai-jun, H. Li, W. Shao-rui, L. Jin-Quan, and L. Ping, "Geometry control method based on stress-free state theory for long-span concrete-fill steel tube arch bridge," *Bridge Construction*, vol. 50, no. 6, pp. 20–26, 2020.

[2] C. Guo and Z. Lu, "Effect of circumferential gap on dynamic performance of CFST arch bridges," *Journal of Bridge Engineering*, vol. 26, no. 2, 2021.

[3] D. Li Ji, Z. B. Xin, and L. Yan, "Sensitivity analysis of structural parameters of concrete-filled steel tube arch bridge with multiple arch ribs," *Journal of China & Foreign Highway*, vol. 40, no. 5, pp. 105–112, 2020.

[4] W. Li, Y. Lu-Song, L. Shi-Zhong, L. Zi-Qi, and L. Peng, "Seismic vulnerability analysis of irregular concrete-filled steel tube arch bridge under transverse seismic action," *Journal of Lanzhou Jiaotong University*, vol. 39, no. 5, pp. 13–19, 2020.

[5] W. Hao-Qi, Y. Jing, and W. Hai-long, "Calculation and analysis of unstressed length of suspender of concrete-filled steel tube arch bridge," *Engineering and Technological Research*, vol. 5, no. 16, pp. 241-242, 2020.

[6] Z. Siyuan and Y. Bo, "Study on structural stability and dynamic performance of concrete-filled steel tubular arch bridge with long span," *Journal of Safety Science and Technology*, vol. 18, no. 4, pp. 185–190, 2022.

[7] H. Feng and F. Yefei, "Stability analysis of arch rib grouting construction of concrete filled steel tube arch bridge," *Guangdong Architecture Civil Engineering*, vol. 27, no. 9, pp. 60–62, 2020.

[8] L. Fuzhong, L. Guangqi, and G. Baolin, "Analysis of in-plane stability parameters of single tube CFST arch bridge," *Shandong Communications Technology*, vol. 4, pp. 55–57, 2019.

[9] X. Weiwei, Y. Zhiquan, and Y. Lufeng, "Linear elastic iteration method for ultimate stability bearing capacity of concrete filled steel tubular arch bridge," *China Railway Science*, vol. 39, no. 1, pp. 39–48, 2018.

[10] W. Yuyin, L. Changyong, L. Yong, and Z. Sumei, "Nonlinear stability analysis and completed bridge test on slanting type CFST arch bridges," *Journal of Building Structures*, vol. 36, no. S1, pp. 107–113, 2015.

[11] S. Fuchun and W. Qianna, "Effects of crossbars on the lateral elastic stability of lift-basket CFST truss rib arch bridge," *Journal of Shenyang Jianzhu University(Natural Science)*, vol. 30, no. 5, pp. 850–855, 2014.

[12] B. Xue, X. Du, J. Wang, and X. Yu, "A scaled boundary finite-element method with B-differentiable equations for 3D frictional contact problems," *Fractal and Fractional*, vol. 6, no. 3, p. 133, 2022.

[13] X. Du, H. Fang, S. Wang, B. Xue, and F. Wang, "Experimental and practical investigation of the sealing efficiency of cement grouting in tortuous fractures with flowing water," *Tunneling and Underground Space Technology*, vol. 108, article 103693, 2021.

[14] D. Ma, D. Hongyu, Z. Jixiong, L. Xianwei, and L. Zhenhua, "Numerical simulation of water–silt inrush hazard of fault rock: a three-phase flow model," *Rock Mechanics and Rock Engineering*, vol. 55, no. 8, pp. 5163–5182, 2022.

[15] Q. Li, D. Ma, Y. Zhang, Y. Liu, and Y. Ma, "Insights into controlling factors of pore structure and hydraulic properties of broken rock mass in a geothermal reservoir," *Lithosphere*, vol. 2021, no. Special 5, article 3887832, 2021.

[16] X. Wei-wei, T. Rui-kai, Y. Zhi-quan, and T. Qiu-hong, "Automatic monitoring and control of initial stresses in steel tubes of concrete-filled steel tubular arch bridge," *World Bridges*, vol. 49, no. 1, pp. 83–88, 2021.

[17] Z. Qian, Z. Jian-ting, Z. Jia-cheng, and Z. Lan, "Self-regulating loading pouring method of long span CFST arch bridge," *Journal of Harbin Institute of Technology*, vol. 52, no. 3, pp. 82–89, 2020.

[18] S. Heng-li, J. Ri-chen, Z. Yu-zhu, and S. Teng-fei, "Analysis of tensioning scheme of hanger of concrete filled steel tubular tied arch bridge," *Communications Science and Technology Heilongjiang*, vol. 42, no. 6, pp. 102–105, 2019.

[19] J. Jian-Jing, L. Xin-Zheng, and Y. Lie-Ping, *Finite Element Analysis of Concrete Structures*, Tsinghua University Press, 2004.

[20] G. Shu-Guang and X. Gui-Lan, *ANSYS Operating Commands and Parameterized Programming*, Machinery Industry Press, 2004.

Hindawi
Geofluids
Volume 2022, Article ID 9610289, 16 pages
https://doi.org/10.1155/2022/9610289

Research Article

Stability Analysis of Shield Inclined Tunnel Faces under the Change Effect of Soil Heterogeneity and Pore Water with Buried Depth

Hong Sun,[1] Dao-bing Zhang,[1,2] Hua-dong Yin ,[2] and A-ping Hu[2]

[1]*School of Civil Engineering, Hunan University of Science and Technology, Xiangtan 411201, China*
[2]*School of Resource Environment and Safety Engineering, Hunan University of Science and Technology, Xiangtan 411201, China*

Correspondence should be addressed to Hua-dong Yin; 21300102001@mail.hnust.edu.cn

Received 31 March 2022; Accepted 24 May 2022; Published 7 July 2022

Academic Editor: Xinyu Ye

The purpose of this work is to look at how soil heterogeneity and pore water pressure impact shield inclined tunnel excavation face stability as burial depth varies. The calculation model of excavation face stability was established, and the supporting pressure of maintain the excavation face stability was solved via the upper bound method. The results showed that the soil heterogeneity coefficient and pore water pressure coefficient had substantial effects on the supporting pressure. The location of failure face and failure range of shield inclined tunnel under varied heterogeneity coefficient and pore water pressure coefficient were presented. In addition, the boundary depth of shallow tunnel under the influence of soil heterogeneity and pore water was obtained, which supplemented the relevant tunnel code.

1. Introduction

The shield method is widely applied in subway and tunnel construction as its benefits of safe excavation and fast driving speed. Due to the complex geological conditions, the construction requirements are relatively high, and the surface settlement is required to be controlled within the millimeter range, so it is very important to set a reasonable thrust (support pressure) to ensure the shield tunneling smoothly. Some scholars believe that most rocks and soils in nature have heterogeneity [1–3]. For shield inclined tunnels, the soil heterogeneity and pore water effect also change with the buried depth constantly changing, which seriously affects the stability of the shield tunnels. Therefore, it is statistically significant to research the stability of shield inclined tunnels under soil heterogeneity and pore water pressure effect. The key to solve this problem is to determine the reasonable support pressure under different buried depths, which has significant scientific research value and engineering significance [4–8].

For geotechnical engineering, especially tunnel engineering stability analysis, the limit analysis upper bound method has been an excellent theoretical analysis method [9–14]. Ibrahim et al. [15] established the failure mode of tunnel excavation face by "point-to-point" method for tunnels in layered soil. The representation of the support resistance of excavation face in layered soil was deduced via the virtual power principle in limit analysis method, and the upper limit solution of the support resistance was solved. Han et al. [16] analyzed the mechanical state of the multilayer soil and constructed the multiblock failure mode of the tunnel excavation face. The upper limit solution of the supporting pressure in the situation of multilayered soil was solved by the limit analysis upper bound method. It was compared to previous findings, and the accuracy of the computation procedure was confirmed. Pan and Dias [17] established the noncircular tunnel failure mechanism working face via the limit analysis method and the strength reduction method. The security factor of excavation face was estimated, and the influence of different section shapes on the safety factor was discussed. Senent et al. [18] constructed a failure mechanism including translational and rotational motions through limit analysis theory. The collapse pressure of tunnel face considering free span was calculated, and the

logic of mechanism was confirmed using numerical simulation. None of the above studies explored the pore water effect. After realizing the importance of pore water effect, some scholars also carried out research. Chen et al. [19] considered the pore water pressure effect on the critical supporting pressure of tunnel face and proposed a method to calculate it via the upper bound theorem. Finite element analysis was used to verify the validity of the suggested technique. Li et al. [20] considered the pore water effect of deep buried tunnel and used nonlinear limit analysis upper limit theorem to construct a three-dimensional collapse failure mode of deep-buried tunnels, deduced the calculation formula for the three-dimensional collapse failure range, which provides theoretical guidance for deep buried tunnel optimization design. Xu et al. [21] proposed a combined translational and rotational failure mode in the stability analysis of the tunnel excavation face. The pore water effect into calculation model was introduced. The limit analysis upper bound method is used to solve the excavation face supporting pressure and the potential failure surface under the pore water effect.

The above studies assume that the buried depth of the tunnel remains unchanged; that is, the research results are applicable to noninclined tunnels. To the shield inclined tunnels, the buried depth is constantly changing, and the shield tunnel stability is affected by the soil heterogeneity and pore water pressure effect to varying degrees. The soil heterogeneity and the effect of pore water were considered via the existing research results in this work, and the limit analysis upper bound method was adopted to calculate the supporting pressure necessary for shield inclined tunnels excavation surface stability.

2. Upper Bound Theorem of Limit Analysis considering the Pore Pressure Effect

The pore water is a vital factor leading to instability of geotechnical engineering. For the problem of tunnel stability under the pore water effect, the pore water pressure was included as an external factor in the upper limit analysis method by several scholars [22–24]. The upper limit analysis theorem of pore pressure effect was established. In this theory, the pore water pressure was regarded as external force acting on the soil particles, and the power generated by the pore water pressure was divided into two parts. One is that the pore water pressure causes volume strain in the soil, and the other is the pore water pressure effect on the velocity interruption surface. Its expression is as follows:

$$\int_V \sigma_{ij}\dot{\varepsilon}_{ij}\mathrm{d}V \geq \int_S T_i v_i dS + \int_V F_i v_i \mathrm{d}V - \int_V u\dot{\varepsilon}_{ij} dV + \int_S u n_i v_i dS, \tag{1}$$

where σ_{ij} and $\dot{\varepsilon}_{ij}$, respectively, are the stress tensor and strain rate at any point in the plastic failure zone; V and F_i are the microvolume and volume force in the plastic failure zone, respectively; T_i is the surface force acting on the boundary S in the plastic failure zone; v_i is the velocity on the discontinuous line of velocity; u is the pore water pressure; and n_i is the discontinuity face normal direction.

3. Calculation Model

A calculation model of excavation face stability of shield inclined tunnels considering soil heterogeneity and pore water pressure effect was established by the existing literature [25–28] in this work. Figure 1 depicts the inclined tunnel excavation facing AB, M is the excavation face midpoint, the tunnel diameter and buried depth are, respectively, d and h, and the tunnel inclination angle is α. When the excavation face is failure, it spins at an angular velocity ω around point O, and the body destruction is AEB. The inner and outer boundaries of the body destruction AEB are logarithmic spirals AE and BE, and their expressions are $r_1(\theta) = r_a \exp[(\theta - \theta_2)\tan\varphi]$, $r_2(\theta) = r_b \exp[(\theta_1 - \theta)\tan\varphi]$. The angle of vertex E is 2φ, and φ is the internal friction angle of soil. r_a and r_b are the lengths of OA and OB, respectively, and θ_1, θ_2, and θ_3 are the angles between the vertical direction and OB, OA, and OE, respectively. Meanwhile, u is the pore water pressure, γ is the volumetric weight of soil, and σ_T is the uniform supporting pressure on the excavation face.

The soil cohesion c varies linearly with depth, and then [29, 30]:

$$c = c_0 + \rho(h - z), \tag{2}$$

where c_0 is the initial cohesion of the soil, ρ is the coefficient of soil heterogeneity, reflecting the relationship of cohesion with depth, and z is the distance from a certain point in the soil to the ground surface.

4. Upper Bound Solution

4.1. Soil Weight Power. In Figure 1, the failure area ABE can be separated into the upper area AEB' and the bottom area ABB'. Under the action of the soil weight, the power generated in area AEB' is $W_{\gamma\text{-AEB}'}$, and in it, the area ABB' is $W_{\gamma\text{-ABB}'}$, and the expressions are as follows:

$$W_{\gamma\text{-AEB}'} = \gamma \cdot \omega \cdot r_b^3 \cdot \left[g_1 - \frac{\sin^3(\theta_1 + \alpha)}{\sin^3(\theta_2 - \theta_1)} g_2 \right], \tag{3}$$

$$W_{\gamma\text{-ABB}'} = \gamma \cdot \omega \cdot r_b^3 \cdot g_3, \tag{4}$$

where $g_1 \sim g_3$ are, respectively:

$$\begin{aligned} g_1 &= \frac{1}{3}\int_{\theta_2}^{\theta_3} e^{[3(\theta_1-\theta)\cdot\tan\varphi]} \cdot \sin\theta d\theta \\ &= \frac{\tan\varphi \cdot \left\{ \sin\theta_2 \cdot e^{[3(\theta_1-\theta_2)\cdot\tan\varphi]} - \sin\theta_3 e^{[3(\theta_1-\theta_3)\cdot\tan\varphi]} \right\}}{(1 + 9\tan^2\varphi)} \\ &\quad + \frac{\cos\theta_2 e^{[3(\theta_1-\theta_2)\cdot\tan\varphi]} - \cos\theta_3 \cdot e^{[3(\theta_1-\theta_3)\cdot\tan\varphi]}}{3(1 + 9\tan^2\varphi)}, \end{aligned} \tag{5}$$

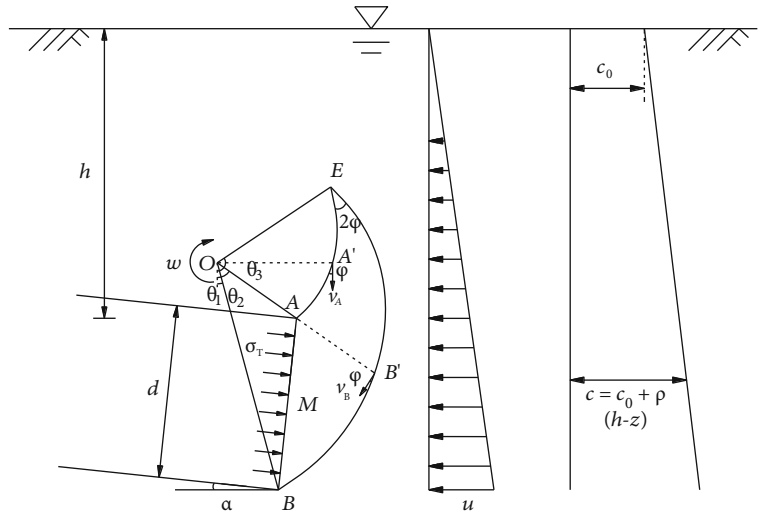

Figure 1: Calculation model for stability of excavation face of shield inclined tunnel.

$$g_2 = \frac{1}{3}\int_{\theta_2}^{\theta_3} e^{[3(\theta-\theta_2)\cdot\tan\varphi]}\cdot\sin\theta d\theta = \frac{\tan\varphi\cdot\left\{\sin\theta_3\cdot e^{[3(\theta_3-\theta_2)\cdot\tan\varphi]}-\sin\theta_2\right\}}{(1+9\tan^2\varphi)} + \frac{\cos\theta_2-\cos\theta_3\cdot e^{[3(\theta_3-\theta_2)\cdot\tan\varphi]}}{3(1+9\tan^2\varphi)}, \tag{6}$$

$$g_3 = \frac{1}{3}\left\{\int_{\theta_1}^{\theta_2} e^{[3(\theta_1-\theta)\cdot\tan\varphi]}\cdot\sin\theta d\theta - \frac{\sin(\theta_2-\theta_1)\sin^2\theta_1}{\sin(\theta_2+\alpha)}\right\} = \frac{\tan\varphi\left\{\sin\theta_1-\sin\theta_2\cdot e^{[3(\theta_1-\theta_2)\cdot\tan\varphi]}\right\}}{(1+9\tan^2\varphi)} + \frac{1}{3}\left\{\frac{\cos\theta_1-\cos\theta_2\cdot e^{[3(\theta_1-\theta_2)\cdot\tan\varphi]}}{(1+9\tan^2\varphi)} + \frac{\sin(\theta_2-\theta_1)\sin^2\theta_1}{\sin(\theta_2+\alpha)}\right\}. \tag{7}$$

Then, the total soil weight power of ABE in the failure area is:

$$W_\gamma = W_{\gamma\text{-AEB}'} + W_{\gamma\text{-ABB}'}. \tag{8}$$

4.2. Supporting Pressure Power. The power of the support force σ_T in the failure area AEB is the sum of the product of the support force σT and the tunnel face velocity:

$$W_T = \int_{\theta_1}^{\theta_2}\frac{r_b}{\sin(\theta+\alpha)}\cdot\sin(\theta_1+\alpha)\cdot\omega\cdot\cos(\theta+\alpha)\cdot\sigma_T \cdot\frac{r_b}{\sin^2(\theta+\alpha)}\cdot\sin(\theta_1+\alpha)d\theta = \frac{1}{2}\sigma_T\cdot\omega\cdot r_b^2 \cdot\left[1-\frac{\sin^2(\theta_1+\alpha)}{\sin^2(\theta_2+\alpha)}\right]. \tag{9}$$

4.3. Pore Water Pressure Power. This work assumes that the volume of the ABE in the failure area does not change; that is, the pore water pressure exerts power on the volume strain is 0, and the power only is done on the boundaries AE and BE. The powers are:

$$W_{u-\text{AE}} = \int_{\theta_2}^{\theta_3} r_1(\theta)\cos\theta\cdot r_u\cdot\gamma\cdot {r_1}^2(\theta)\cdot\omega\cdot\sin\varphi d\theta + \int_{\theta_2}^{\theta_3}(h-r_a\cos\theta_2)\cdot r_u\cdot\gamma\cdot {r_1}^2(\theta)\omega\cdot\sin\varphi d\theta = r_u\cdot\gamma\cdot\omega\cdot {r_a}^2\cdot\sin\varphi[g_4+(h-r_a\cos\theta_2)\cdot g_5], \tag{10}$$

$$W_{u-\text{BE}} = \int_{\theta_1}^{\theta_3}(h+d-r_b\cos\theta_1)\cdot r_u\cdot\gamma\cdot {r_2}^2(\theta)\cdot\omega\cdot\sin\varphi\mathrm{d}\theta + \int_{\theta_1}^{\theta_3} r_2(\theta)\cos\theta\cdot r_u\cdot\gamma\cdot {r_2}^2(\theta)\cdot\omega\cdot\sin\varphi d\theta = r_u\cdot\gamma\cdot\omega\cdot {r_b}^2\cdot\sin\varphi\cdot[(h+d-r_b\cos\theta_1)\cdot g_6+r_b\cdot g_7], \tag{11}$$

where $g_4 \sim g_7$are, respectively:

$$g_4 = \int_{\theta_2}^{\theta_3} e^{[3(\theta-\theta_2)\cdot\tan\varphi]}\cdot\cos\theta\mathrm{d}\theta = \frac{3\tan\varphi\cdot\left(\cos\theta_3\cdot e^{[3(\theta_3-\theta_2)\cdot\tan\varphi]}-\cos\theta_2\right)+\sin\theta_3\cdot e^{[3(\theta_3-\theta_2)\cdot\tan\varphi]}-\sin\theta_2}{1+9\tan^2\varphi}, \tag{12}$$

$$g_5 = \int_{\theta_2}^{\theta_3} e^{[2(\theta-\theta_2)\cdot\tan\varphi]}d\theta = \frac{e^{[2(\theta_3-\theta_2)\cdot\tan\varphi]}-1}{2\tan\varphi}, \tag{13}$$

$$g_6 = \int_{\theta_1}^{\theta_3} e^{[3(\theta_1-\theta)\cdot\tan\varphi]}\cdot\cos\theta d\theta = \frac{3\tan\varphi\cdot\left\{\cos\theta_1-\cos\theta_3\cdot e^{[3(\theta_1-\theta_3)\cdot\tan\varphi]}\right\}+\sin\theta_3\cdot e^{[3(\theta_1-\theta_3)\cdot\tan\varphi]}-\sin\theta_1}{1+9\tan^2\varphi}, \tag{14}$$

$$g_7 = \int_{\theta_1}^{\theta_3} e^{[2(\theta_1-\theta)\cdot\tan\varphi]}d\theta = \frac{1-e^{[2(\theta_1-\theta_3)\cdot\tan\varphi]}}{2\tan\varphi}. \quad (15)$$

In sum, the total power of pore water pressure is:

$$W_u = W_{u\text{–AE}} + W_{u\text{-BE}}. \quad (16)$$

4.4. Internal Energy Dissipation Rate. The internal energy dissipation occurs on the speed discontinuous lines AE and BE, denoted as $W_{V-\text{AE}}$ and $W_{V-\text{BE}}$, respectively. According to formula (2) and geometric relationship, we can get:

$$c = c_0 + \rho(h + r_1\cos\theta - r_a\cos\theta_2), \quad (17)$$

where $W_{V-\text{AE}}$ expression is:

$$\begin{aligned} W_{V\text{-AE}} &= \int_{\theta_2}^{\theta_3} c\cdot(r_1\cdot\omega\cdot\cos\varphi)\cdot\frac{r_1}{\cos\varphi}\mathrm{d}\theta \\ &= \omega\cdot r_a^2\cdot[c_0 + \rho(h - r_a\cos\theta_2)]\cdot g_8 + \omega\cdot\rho\cdot r_a^3\cdot g_9. \end{aligned} \quad (18)$$

$W_{V-\text{BE}}$ expression is:

$$\begin{aligned} W_{V\text{-BE}} &= \int_{\theta_1}^{\theta_3} c\cdot(r_2\cdot\omega\cdot\cos\varphi)\cdot\frac{r_2}{\cos\varphi}d\theta = \omega\cdot r_b^2\cdot[c_0 \\ &\quad + \rho(h - r_a\cos\theta_2)]\cdot g_{10} + \omega\cdot\rho\cdot r_b^3\cdot g_{11}. \end{aligned} \quad (19)$$

The $g_8 \sim g_{11}$ expressions are:

$$g_8 = \frac{e^{[2(\theta_3-\theta_2)\cdot\tan\varphi]} - 1}{2\tan\varphi}, \quad (20)$$

$$\begin{aligned} g_9 &= \int_{\theta_2}^{\theta_3} e^{[3(\theta-\theta_2)\cdot\tan\varphi]}\cdot\cos\theta d\theta \\ &= \frac{3\tan\varphi\cdot\left\{\cos\theta_3\cdot e^{[3(\theta_3-\theta_2)\cdot\tan\varphi]} - \cos\theta_2\right\} + \sin\theta_3\cdot e^{[3(\theta_3-\theta_2)\cdot\tan\varphi]} - \sin\theta_2}{(1+9\tan^2\varphi)}, \end{aligned} \quad (21)$$

$$g_{10} = \frac{1-e^{[2(\theta_1-\theta_3)\cdot\tan\varphi]}}{2\tan\varphi}, \quad (22)$$

$$\begin{aligned} g_{11} &= \int_{\theta_1}^{\theta_3} e^{[3(\theta_1-\theta)\cdot\tan\varphi]}\cdot\cos\theta d\theta \\ &= \frac{3\tan\varphi\cdot\left\{\cos\theta_1 - \cos\theta_3\cdot e^{[3(\theta_1-\theta_3)\cdot\tan\varphi]}\right\} + \sin\theta_3\cdot e^{[3(\theta_1-\theta_3)\cdot\tan\varphi]} - \sin\theta_1}{1+9\tan^2\varphi}. \end{aligned} \quad (23)$$

The dissipation rate of total internal energy is:

$$W_V = W_{V\text{-AE}} + W_{V\text{-BE}}. \quad (24)$$

4.5. Supporting Pressure. Combining the above formulas can derive the analytical expression of the supporting pressure σ_T:

$$\sigma_T = \sigma_a = \frac{2\left(W_\gamma + W_u - W_V\right)}{\omega\cdot r_b^2\cdot\left[1-\sin^2(\theta_1+\alpha)/\sin^2(\theta_2+\alpha)\right]}, \quad (25)$$

$$\text{s.t.}\begin{cases} 0 < \theta_1 < \theta_2 < \pi/2 \\ \theta_2 < \theta_3 < \pi \\ r_a < r_b \end{cases}. \quad (26)$$

Under the constraint condition of formula (26), the minimum value of the supporting pressure in formula (25) can be solved by Matlab software, and it is the best solution. In the final failure condition, the solved supporting pressure is equivalent to the collapse pressure on the shield inclined tunnels excavation face. That is, the failure surface $\sigma_T = \sigma_a$ is the most dangerous failure surface potentially in front of the excavation face.

Table 1: Comparison of results.

α (°)	σ_T (kPa)	Relative error (%)	ρ (kPa/m)	σ_T (kPa)	Relative error (%)	r_u	σ_T (kPa)	Relative error(%)
0	137.0	—	0	142.5	—	0	53.2	—
2	136.6	0.3	0.1	135.8	4.7	0.1	94.5	77.6
4	136.1	0.6	0.2	129.1	9.4	0.2	135.8	155.3
6	135.6	1.0	0.3	122.4	14.1	0.3	177.3	233.3
8	135.5	1.1	0.4	115.7	18.8	0.4	219.1	311.8

5. Result Analysis

5.1. Relative Error. The supporting pressure σ_T on inclined tunnel excavation face is compared with different tunnel inclination angle α, soil heterogeneity coefficient ρ, and pore water pressure coefficient r_u. The parameter results are as follows [30, 31]: the volumetric weight of soil $\gamma = 20\text{kN/m}^3$, tunnel diameter $d = 10$ m, tunnel buried depth $h = 20$ m, initial cohesion $c_0 = 10$ kPa, and internal friction angle $\varphi = 18°$. In Table 1, when the tunnel inclination angle $\alpha = 0°$ and $\alpha = 8°$ ($\rho = 0.1$ kPa/m, $r_u = 0.2$), the supporting pressure σ_T is 137.0 kPa and 135.5 kPa, respectively, and the relative error is 1.1%. When the soil heterogeneity coefficient $\rho = 0$ and $\rho = 0.4$ kPa/m ($\alpha = 5°$, $r_u = 0.2$), the supporting pressure σ_T is 142.5 kPa and 115.7 kPa, respectively, and the relative error is 18.8%. When the pore water pressure coefficient $r_u = 0$ and $r_u = 0.4$ ($\alpha = 5°$, $\rho = 0.1$ kPa/m), the supporting pressure σ_T is 53.2 kPa and 219.1 kPa, respectively, and the relative error is 311.8%. They have different degrees of influences on the supporting pressure of excavation face. The coefficient of pore water pressure r_u has a foremost effect and then is the coefficient of soil heterogeneity ρ, and the influence of the inclination angle α is relatively small.

5.2. Supporting Pressure Analysis. The influence of soil heterogeneity and pore water pressure on the supporting pressure of the excavation face is investigated, where tunnel

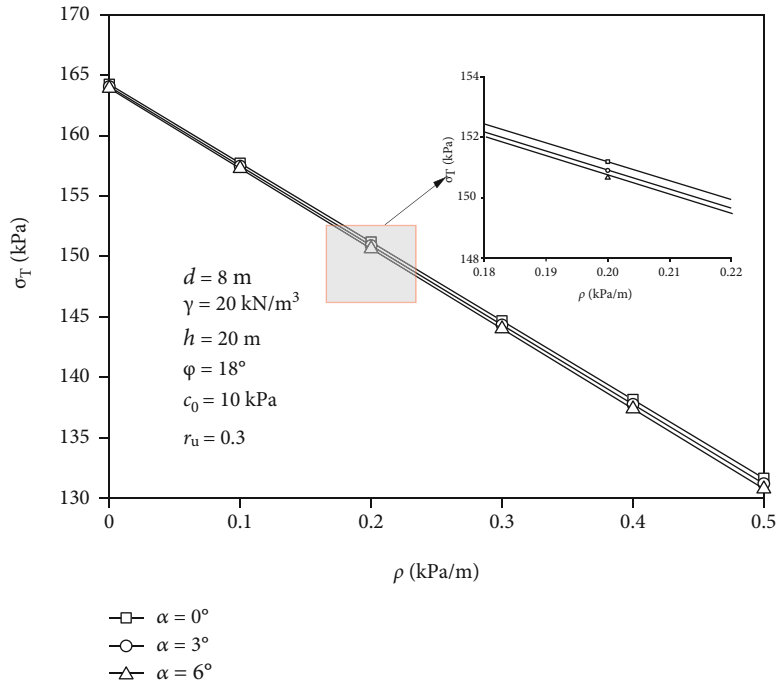

(a)

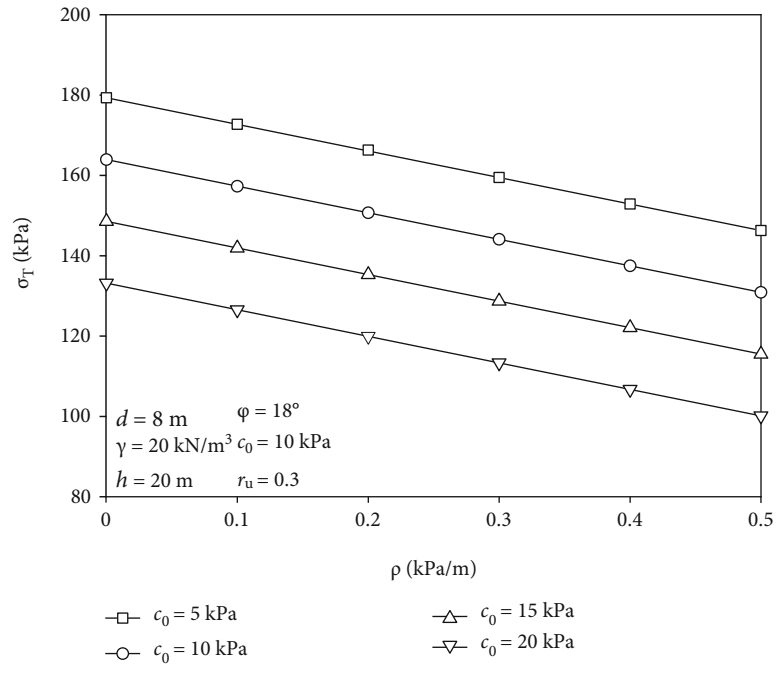

(b)

Figure 2: Continued.

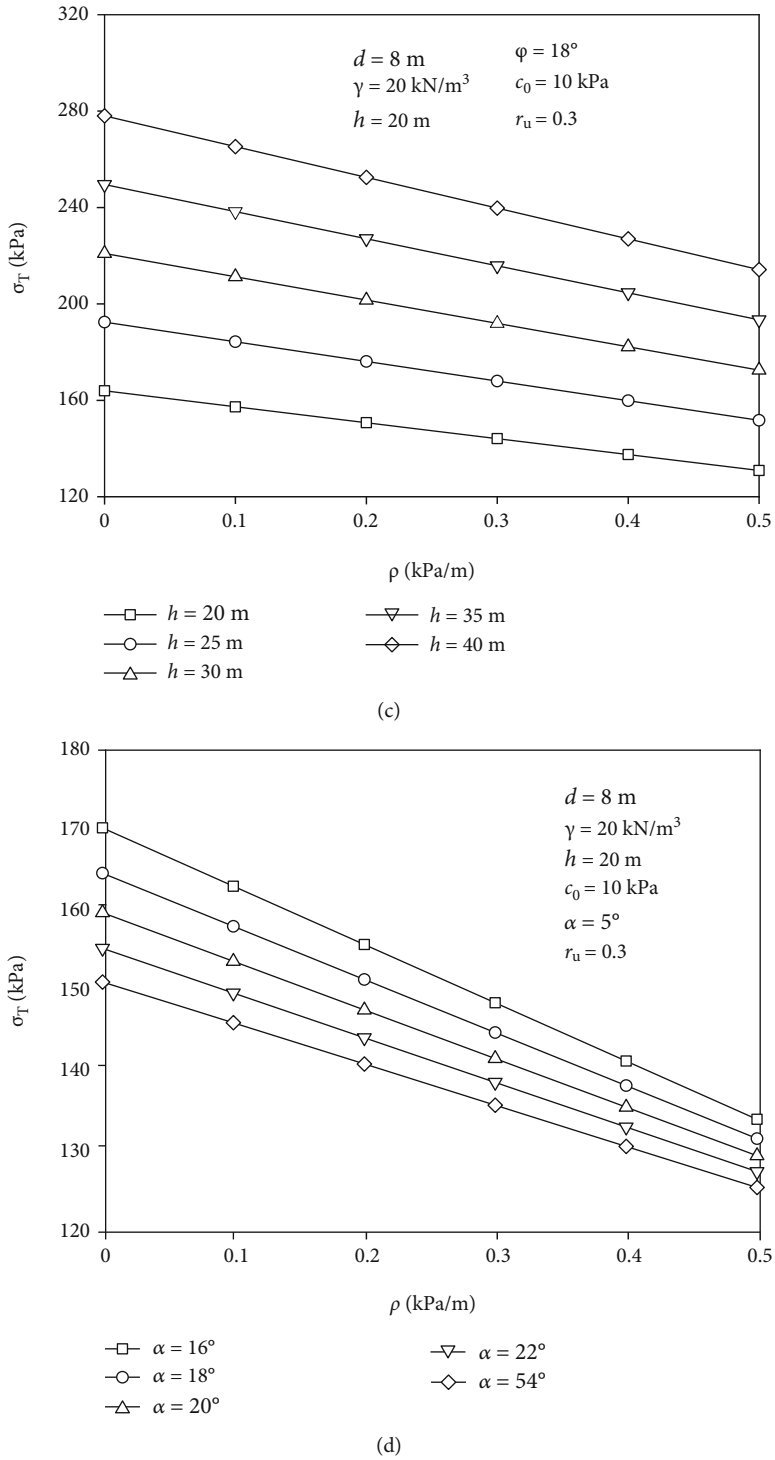

Figure 2: Influence of soil heterogeneity on the supporting pressure: (a) tunnel inclination angle α; (b) initial cohesion c_0; (c) buried depth h; and (d) internal friction angle φ.

diameter $d = 8\,m$, tunnel buried depth $h = 20\,m \sim 40\,m$, the volumetric weight of soil $\gamma = 20\text{kN/m}^3$, initial cohesion $c_0 = 5\,\text{kPa} \sim 25\,\text{kPa}$, internal friction angle $\varphi = 16^\circ \sim 24^\circ$,the tunnel inclination angle $\alpha = 0^\circ \sim 6^\circ$, the soil heterogeneity coefficient $\rho = 0\,\text{kPa/m} \sim 0.5\,\text{kPa/m}$, and the pore water pressure coefficient $r_u = 0 \sim 0.4$.

5.2.1. Influence of Soil Heterogeneity. Figure 2 reflects the effect of soil heterogeneity on the supporting pressure of excavation face. Overall, as the soil heterogeneity coefficient ρ increases, the supporting pressure σ_T gradually decreases. Because while the buried depth remains constantly, the increase of the soil heterogeneity coefficient ρ causes the

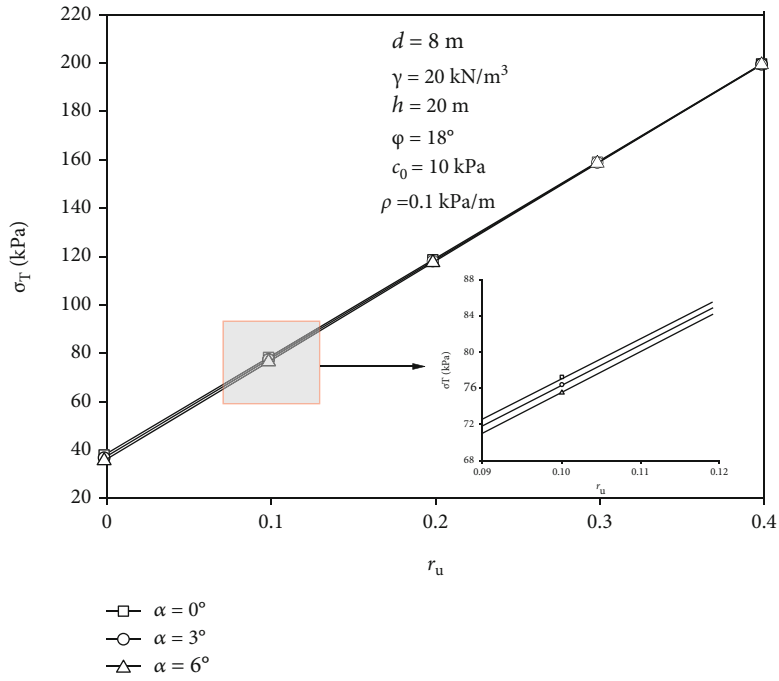

(a)

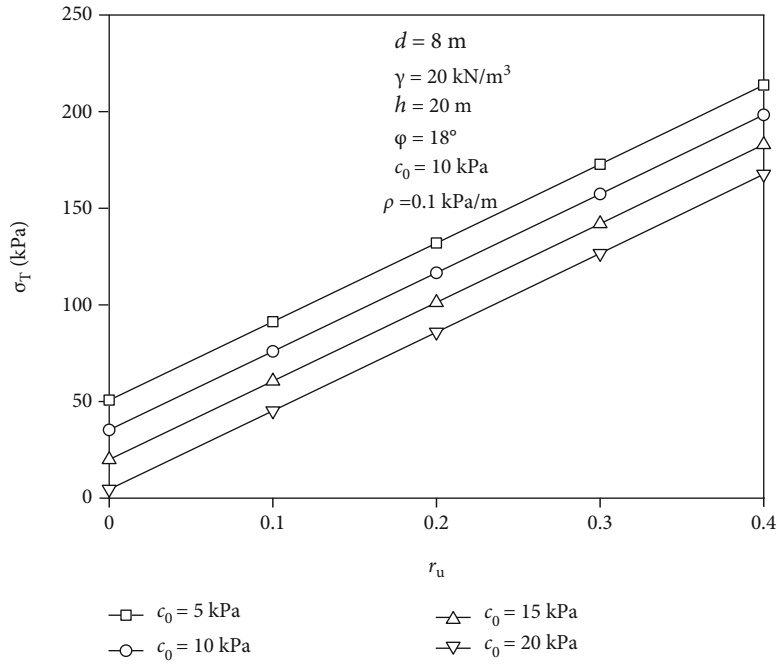

(b)

Figure 3: Continued.

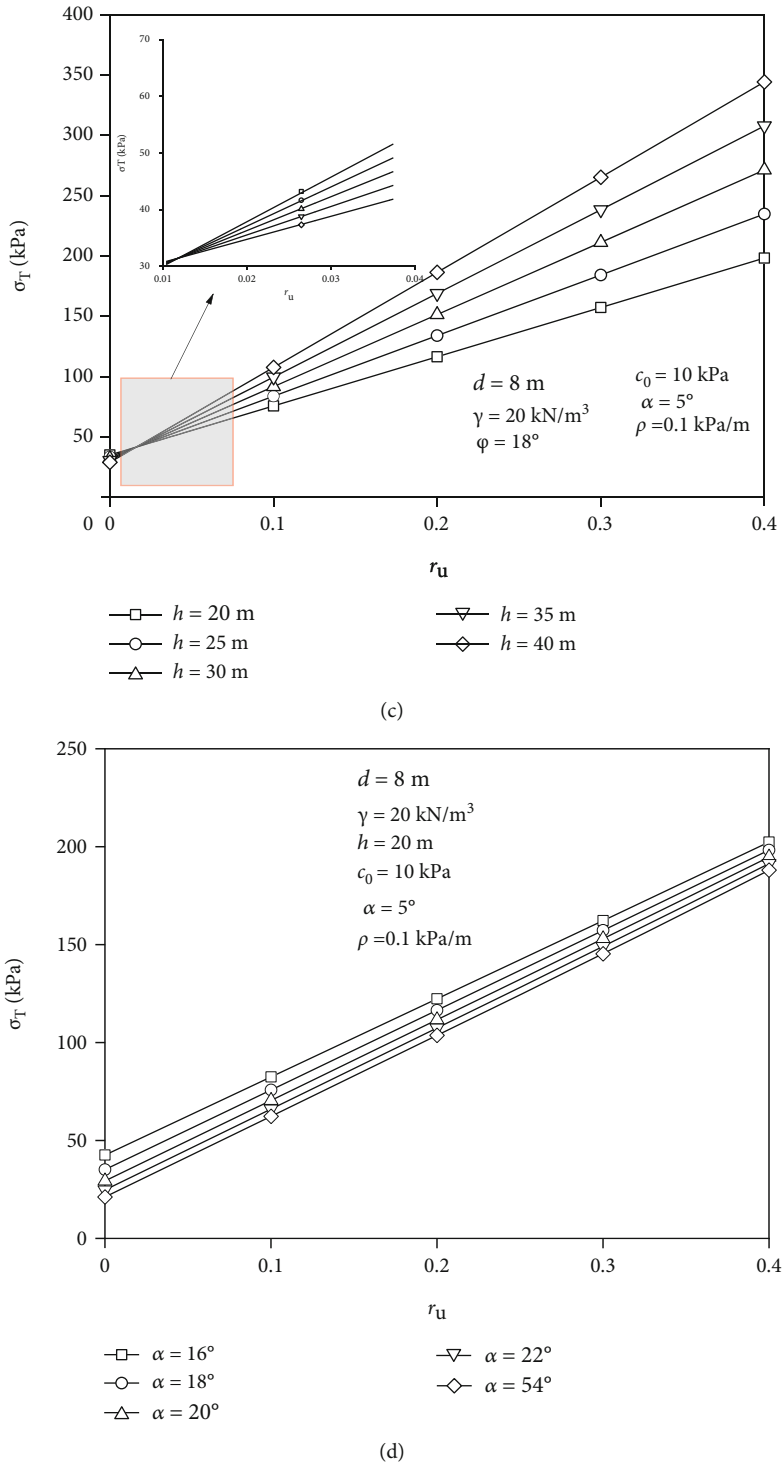

Figure 3: Influence of pore water pressure on the supporting pressure: (a) tunnel inclination angle α; (b) buried depth h; (c) initial cohesion c_0; and (d) internal friction angle φ.

increase of soil cohesion, and the stability of soil is increased accordingly.

In Figure 2(a), the three curves are very close and almost coincide. When the soil heterogeneity coefficient $\rho = 0.5$ kPa/m, the tunnel inclination angle α is 0°, 3°, and 6°, and the supporting pressures corresponding to 131.6 kPa, 131.2 kPa, 130.8 kPa, and the error is 0.4 kPa and 0.4 kPa, respectively. It indicates that a small adjustment in the tunnel inclination angle α has a relatively limited influence on the excavation face support. In Figure 2(b), the supporting pressure σ_T displays a diminishing trend as the initial cohesive c_0 increases. When the soil heterogeneity coefficient ρ

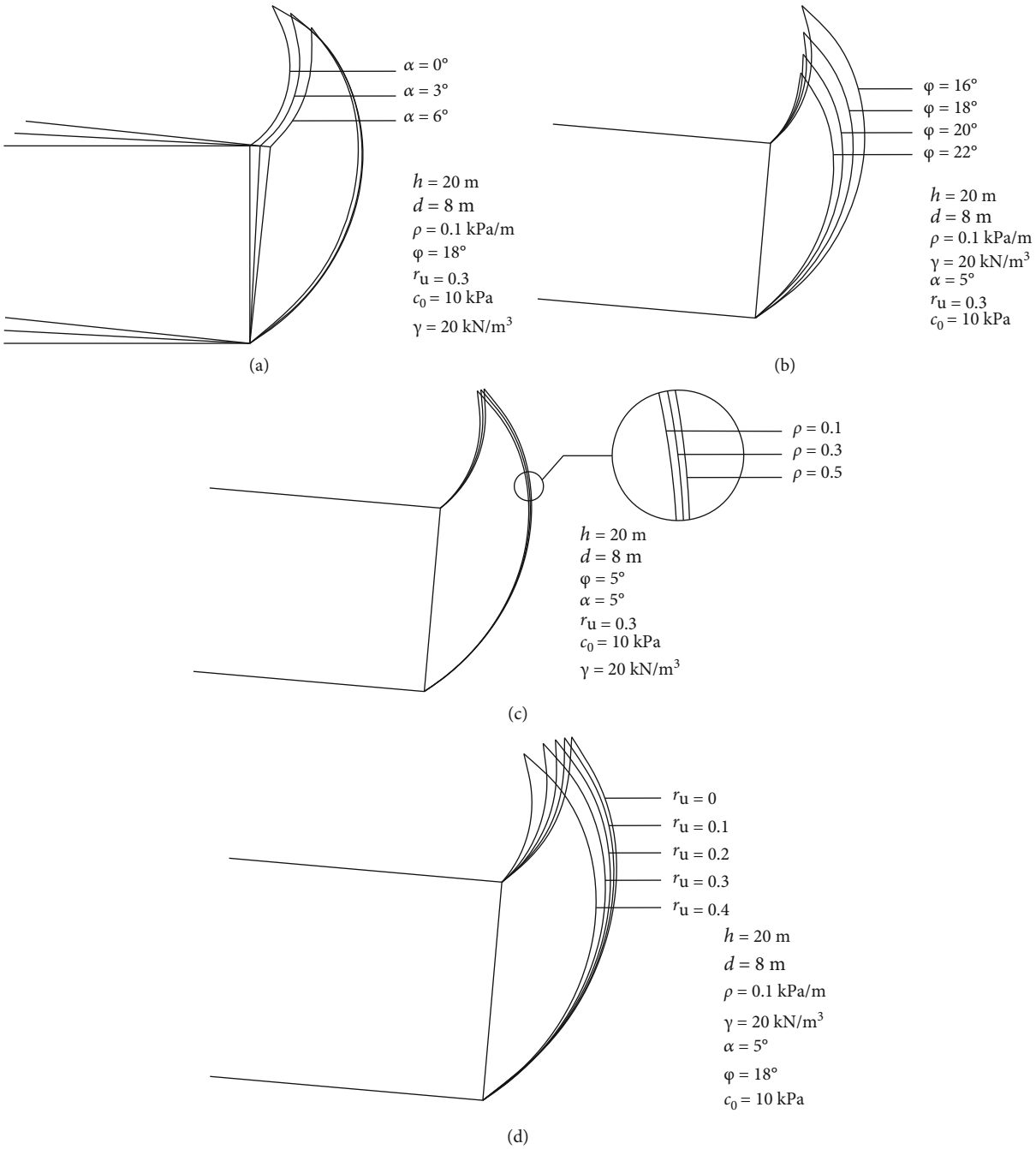

Figure 4: Influence of parameters on the position of failure surface: (a) tunnel inclination angle α; (b) internal friction angle φ; (c) coefficient of soil heterogeneity ρ; and (d) pore water pressure coefficient r_u.

= 0.5 kPa/m, the initial cohesion c_0 increases from 5 kPa to 20 kPa, and the relative error is 31.6%. It indicates that the initial cohesive has a greater effect on the supporting pressure on the inclined tunnel excavation face. The initial cohesive be greater, the supporting pressure that must be supplied to the excavation face be smaller. In Figure 2(c), as the buried depth h gradually increases, the excavation face supporting pressure σ_T increases accordingly. When the soil heterogeneity coefficient $\rho = 0.3$ kPa/m, the buried depth h increases from 20 m to 40 m, and the supporting pressure σ_T increases from 144.1 kPa to 239.8 kPa, a growth rate of 66.4%. This reflects how pore water pressure affects supporting pressure. As buried depth h increases, the cohesive and pore water pressure of the soil increases. While the cohesive increases, the supporting pressure should decrease (see Figure 2(b)), but the supporting pressure increases. It shows that pore water pressure has an obvious increase impact on support pressure. In Figure 2(d), when the soil heterogeneity coefficient is not considered ($\rho = 0$), the internal friction angle $\varphi = 16^\circ$ increases to $\varphi = 24^\circ$, the supporting pressure

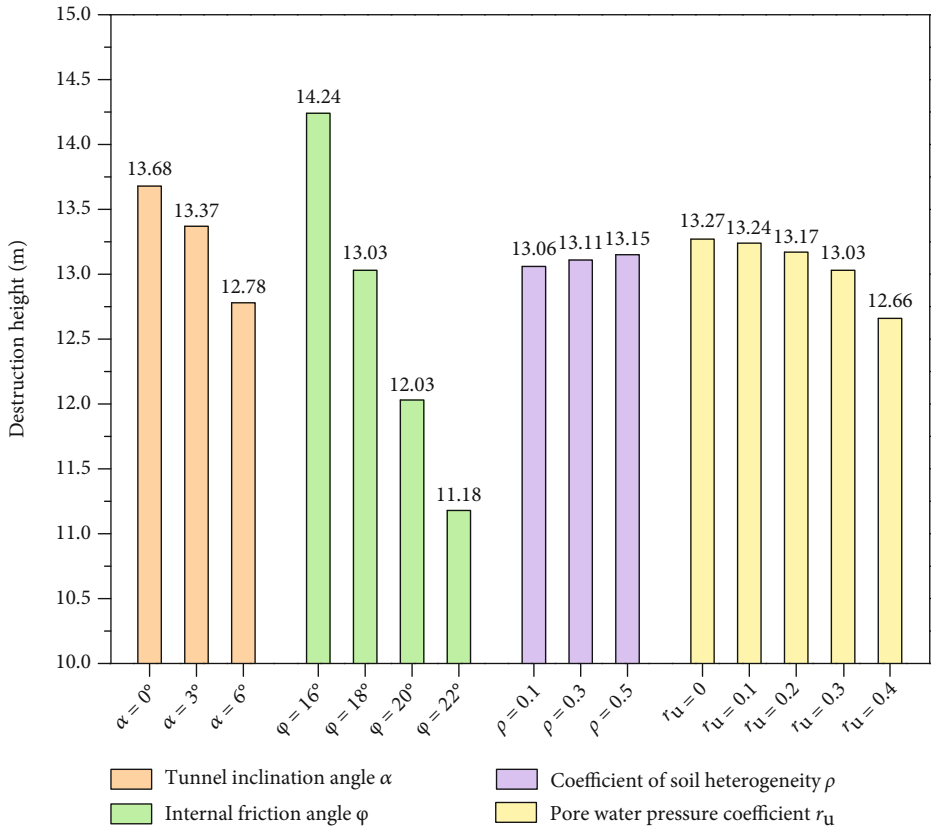

Figure 5: The influence of parameters on the height of the failure surface.

decreases from 169.6 kPa to 150.4 kPa, and the relative error is 11.3%. When considering the soil heterogeneity coefficient ($\rho = 0.5$ kPa/m), the internal friction angle $\varphi = 16^{\circ}$ increases to $\varphi = 24^{\circ}$, while the supporting pressure decreases from 133.3 kPa to 124.8 kPa, and the relative error is 6.4%. It indicates that the increase of the friction angle φ in the soil has a reduced effect on supporting pressure, which is mainly manifested when the soil heterogeneity is weak.

5.2.2. Pore Water Pressure Impact. In Figure 3 as the pore water pressure coefficient r_u gradually increases, the supporting pressure σ_T tends to increase. It indicates that pore water has a considerable impact on the supporting pressure required for the inclined tunnel excavation face. To guarantee the excavated face stability, the supporting pressure on excavation face must be strengthened.

Figure 3(a) shows that several curves almost overlap. It shows that under the action of pore water, the tunnel inclination α has a limited influence on the supporting pressure σ_T. In Figure 3(b), the supporting pressure σ_T decreases with the increase of the initial cohesive c_0. When initial cohesive c_0 increases from 5 kPa to 20 kPa ($r_u = 0.4$), the supporting pressure σ_T relative error is 21.6%, and the initial cohesion c_0 influences the supporting pressure σ_T significantly. In Figure 3(c), when the pore water pressure coefficient r_u is small, as the buried depth h increases, the supporting pressure σ_T gradually decreases. While the pore water pressure coefficient r_u increases in time, the supporting pressure σ_T increases in tandem with the buried depth h. Because as buried depth h increases, the soil heterogeneity causes the increase in the cohesive c to reduce the supporting pressure σ_T, while the pore water pressure increases caused the supporting pressure σ_T increases. Following these, when the pore water pressure coefficient r_u is between 0.01 and 0.02, the effect of the heterogeneity coefficient and the pore water pressure coefficient on the support pressure is similar. When the pore water pressure coefficient r_u is less than 0.01, the effect of soil heterogeneity on the reduction of the support pressure is dominant, while as the pore water pressure coefficient r_u increases to greater than 0.02, the pore water pressure on the support pressure increases gradually and becomes dominant. When considering pore water pressure coefficient ($r_u = 0.4$), the internal friction angle φ increases from 16° to 24°, and the corresponding supporting pressure σ_T decreases from 202.4 kPa to 188.0 kPa, with a relative error of 7.1%. It demonstrates that the smaller the pore water pressure coefficient, the more obvious the reduction effect of the soil friction angle φ on the supporting pressure.

5.2.3. Failure Surface. Figures 4 and 5 depicts the influence of related parameters on the inclined tunnel failure surface. In Figure 4(a), as the tunnel inclination α increases, the failure surface moves in the direction of excavation and the failure height decreases. In Figure 4(b), as the internal friction angle φ increases, the failure range diminishes, the location of the failure surface approaches the hole, and the failure height

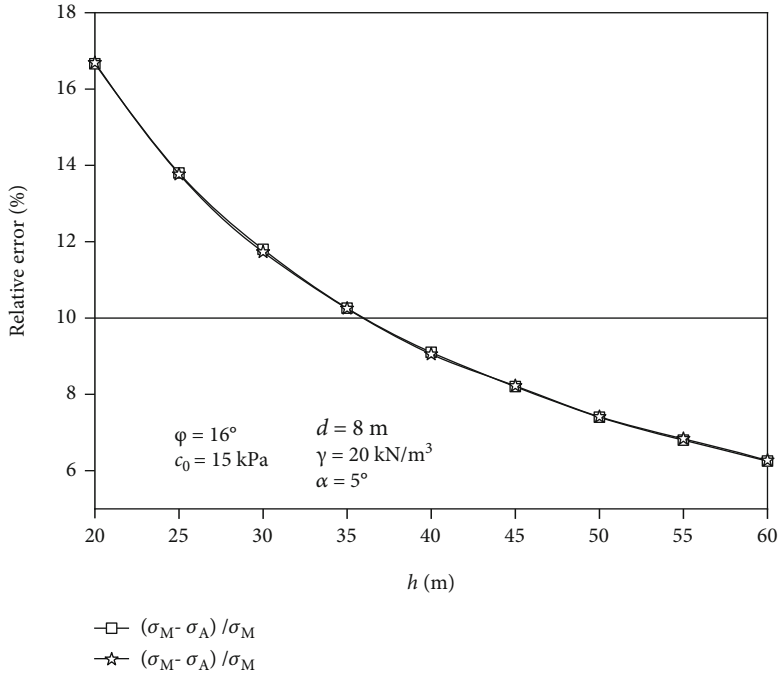

(a)

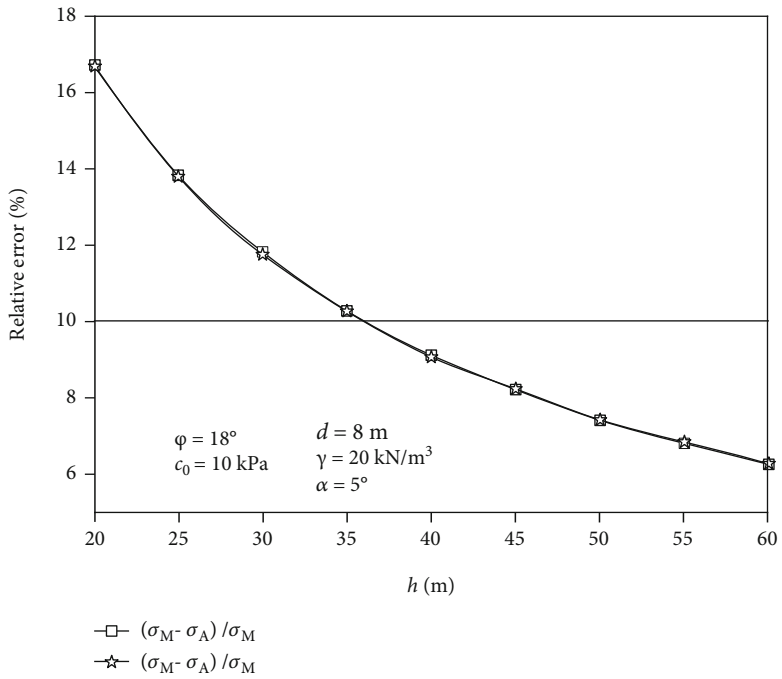

(b)

Figure 6: Continued.

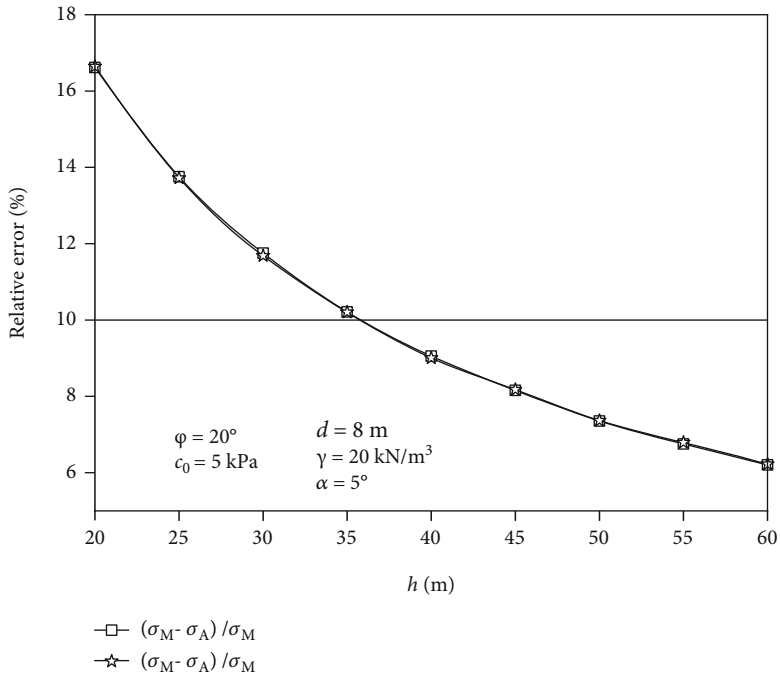

(c)

Figure 6: Variation laws of the relative error of different parts supporting pressure: (a) $\varphi = 16^\circ$, $c = 15$ kPa; (b) $\varphi = 18^\circ$, $c = 10$ kPa; and (c) $\varphi = 20^\circ$, $c = 5$ kPa.

Table 2: Boundary depth of shallow tunnels under the influence of soil heterogeneity and pore water.

	Allowable error Δ		
	10%	8%	6%
$\varphi = 16^\circ$, $c_0 = 15$ kPa	25 m ~ 30 m	35 m ~ 40 m	55 m ~ 60 m
$\varphi = 18^\circ$, $c_0 = 10$ kPa	25 m ~ 30 m	35 m ~ 40 m	50 m ~ 55 m
$\varphi = 20^\circ$, $c_0 = 5$ kPa	20 m ~25 m	35 m ~ 40 m	50 m ~ 55 m

decreases. In Figure 4(c), as the soil heterogeneity coefficient ρ increases, the failure range does not change much, the location of the failure surface develops toward the excavation direction, and the failure height decreases slightly. In Figure 4(d), as the pore water pressure coefficient r_u increases, the failure range decreases, the location of the failure surface gradually approaches the cave, and the failure height decreases. It can be shown that the internal friction angle φ, tunnel inclination angle α, and pore water pressure coefficient r_u have greater effect on the failure surface except the soil heterogeneity coefficient ρ.

5.2.4. Supporting Pressure at the Top, Middle, and Bottom of the Excavation Face in the Shallow Buried Section. The above results assume that the inclined tunnel is in the deep buried section, and the supporting pressure applied at the top, middle, and bottom of the excavation face is in a uniformly distributed form, that is, $\sigma_A = \sigma_M = \sigma_B$. However, the supporting pressure of the three parts in the shallow buried section is different, so the division of the boundary between deep buried and shallow buried is particularly important.

Assuming that the surrounding rock grade is VI, the diameter of the inclined tunnel is $d = 8$ m, and the shallow tunnel boundary $H_P = 37.4$ m ~ 46.8 m is calculated via the "Code for Design of Railway Tunnels" (TB 10003-2016) [31]. Regardless of soil heterogeneity and pore water influence ($\rho = 0$ and $r_u = 0$), using the method in the work, the relative error of three parts of the inclined tunnel excavation face can be obtained as a rule of the buried depth h. In Figure 6, the relative error between the three supporting pressures shows a decreasing trend as the buried depth h increases. If the relative error of $\Delta = 10\%$ is regarded as no difference, that is, three supporting pressures are equal, then, the shallow tunnel boundary $H_P = 35$ m ~ 40 m can be obtained. Therefore, the results of this work are in good accord with the normative results, which confirms the validity of the results of this work.

On the basis of the above research, considering the soil heterogeneity and the influence of pore water ($\rho = 0.1$ kPa/m and $r_u = 0.3$), the shallow tunnel boundary is obtained, as shown in Table 2. If the relative error of the supporting pressure is $\Delta = 10\%$ is the allowable error, then, the shallow tunnel boundary $H_P = 20$ m ~ 30 m. While it does not consider the soil heterogeneity and pore water ($\rho = 0$ and $r_u = 0$), the shallow tunnel boundary change is -15 m ~ -10 m. Depending on $\Delta = 8\%$as the allowable error, then, the boundary of the shallow tunnel $H_P = 35$ m ~ 40 m , contrast $\Delta = 10\%$, and the limit of the shallow tunnel changes 10 m ~ 15 m. Depending on $\Delta = 6\%$ is the allowable error, then the boundary of shallow tunnel $H_P = 50$ m ~ 60 m, and contrast $\Delta = 8\%$, the boundary change of the shallow

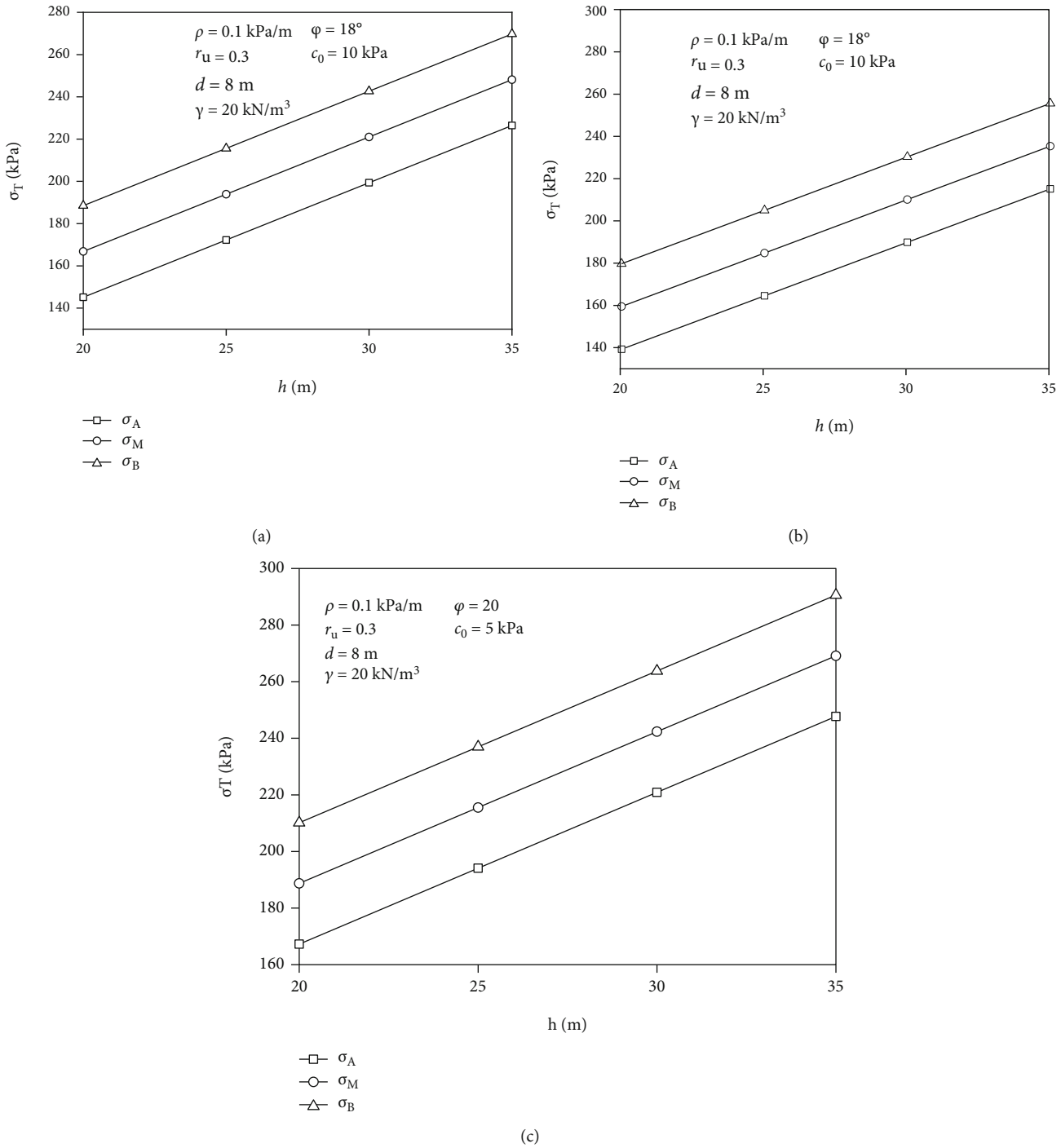

Figure 7: Change rules of different parts supporting pressure with the buried depth h considering the effect of soil heterogeneity and pore water: (a) $\varphi = 16^{\circ}$, $c_0 = 15$ kPa; (b) $\varphi = 18^{\circ}$, $c_0 = 10$ kPa; and (c) $\varphi = 20^{\circ}$, $c_0 = 5$ kPa.

Table 3: Stratum parameters.

Soil layer	Unit weight/(kN/m^3)	Cohesion/kPa	Internal friction angle/(°)	Layer thickness/m
①Artificial fill	17.3	12	28	1.4
②Silty soil	18.5	6.0	18	7.6
③Alluvial strata	19.5	0.8	18	6.0
④Strongly weathered mudstone	21.6	200	24	23.0

Table 4: Comparison of results.

Monitoring value [32]		This work	
Minimum value/kPa	Maximum value/kPa	Minimum value/kPa	Maximum value/kPa
38	174	37.6	161.9

tunnel is 15 m ~ 20 m. It can be seen that soil heterogeneity and pore water pressure have a substantial effect on the boundary of shallow tunnels, and the results of this work supplement the specification.

In addition, the supporting pressure that needs to be applied to the top, middle, and bottom of the shallow tunnel excavation face is given. In Figure 7, as the buried depth h increases, the supporting pressure σ_T of the three parts also increases accordingly, and the required supporting pressure at the bottom is the largest, followed by the middle, and the smallest at the top, that is, $\sigma_B > \sigma_M > \sigma_A$. It indicates that in the shallow buried section, the supporting pressure required from the top to the bottom of the inclined tunnel excavation face gradually increases. It is suggested that the required supporting pressure on three different parts should be reasonably applied in the actual process to prevent the tunneling direction from deviating from the design axis.

6. Application of Results

A collapse accident occurred on line 3 of a subway. The diameter of the shield tunnel is $d = 6.0$ m, the buried depth is $h = 12$ m, and the tunnel inclination angle is $\alpha = 0$. The strata that the tunnel passes through are mainly alluvial layers and strongly weathered mudstone. The physical and mechanical properties of the soil layers in this area are shown in Table 3 after site survey. After conversion, the unit weight of rock and soil masses is $\gamma = 19.3\text{kN/m}^3$, internal friction angle is $\varphi = 19.8^\circ$, initial cohesion of soil is $c_0 = 12$ kPa, heterogeneity coefficient is $\rho = -0.65$ kPa/m, and pore water pressure coefficient is $r_u = 0.51$. The surrounding rock pressure was solved via this method, and it was compared with the existing result and on-site measured result as shown in Table 4. In Table 4, the minimum value from this work is 37.6 kPa, without considering the effect of pore water pressure. The minimum field monitoring value (as no pore water situation) is 38 kPa, with a relative error of 1%. Similarly, when considering the groundwater, the maximum value is 161.9 kPa and 174 kPa, respectively, and the relative error is 7.0%. The above shows that the result from this work is in good agreement with the actual monitoring value, which verifies the applicability of this method.

7. Conclusions

(1) There are two effects in the tunneling process of shield inclined tunnels. One is as the buried depth increases, the soil heterogeneity enhances the cohesive which reduces the supporting pressure. Another is that the increase of the buried depth also causes the pore water pressure to intensify, leading to an augmenting effect on the supporting pressure. Following these when the buried depth is small, the effect of soil heterogeneity on the reduction of the supporting pressure dominates. However, when the buried depth gradually increases, the augmenting effect of pore water pressure on the supporting pressure gradually dominates

(2) Soil heterogeneity, initial cohesion, and soil heterogeneity coefficient have substantial influence on the required supporting pressure on the excavation face. But it has little effect on the position of the potential failure surface in front of the excavation. Compared the initial cohesion $c_0 = 5$ kPa and 20 kPa ($\rho = 0.5$ kPa/m), the relative error of the supporting pressure can reach 31.6%. The pore water pressure and the soil friction angle have a significant effect on the required supporting pressure on the excavation face. And as the pore water pressure and the soil friction angle increase, the potential failure surfaces are all approach to the cave, and the failure range gradually decreases. Compared the pore water pressure coefficient $r_u = 0$ and 0.4 ($\varphi = 18^\circ$), the relative error of the supporting pressure can reach 464.1%. Comparing the internal friction angle $\varphi = 16^\circ$ and 24° ($r_u = 0$), the relative error of the supporting pressure can reach 50.4%. In addition, the small increase of the tunnel inclination has little effect on the required supporting pressure on the excavation face. But, the location of its potential failure surface expands in the direction of excavation

(3) Without considering the influence of soil heterogeneity and pore water ($\rho = 0$ and $r_u = 0$), the shallow tunnel boundary $H_P = 37.4$ m ~ 46.8 m is calculated according to the specification. The shallow tunnel boundary $H_P = 35$ m ~ 40 m under the condition of allowable error $\Delta = 10\%$ is obtained by the method in this work. The results of this work are similarity to the normative results, which verifies the validity of the results of this work. In addition, considering the soil heterogeneity and the influence of pore water ($\rho = 0.1$ kPa/m and $r_u = 0.3$), according to the allowable error $\Delta = 10\%$, 8%, and 6%, the boundary of the shallow tunnel is $H_P = 20$ m ~ 30 m, 35 m ~ 40 m, and 50 m ~ 60 m, respectively. It can be seen that the soil heterogeneity and the pore water effect significantly affect the boundary of the shallow tunnel

Data Availability

The data used to support the findings of this study are available from the corresponding author upon request.

Conflicts of Interest

All authors declare that they have no conflict of interest or financial conflicts to disclose.

Acknowledgments

The work is supported by the National Natural Science Foundation of China (52074116 and 51804113).

References

[1] Q. H. Wu, L. Weng, Y. L. Zhao, and F. Feng, "Influence of infilling stiffness on mechanical and fracturing responses of hollow cylindrical sandstone under uniaxial compression tests[J]," *Journal of Central South University*, vol. 28, no. 8, pp. 2485–2498, 2021.

[2] L. Weng, Q. H. Wu, Y. L. Zhao, and S. M. Wang, "Dynamic response and failure of rock in initial gradient stress field under stress wave loading[J]," *Journal of Central South University*, vol. 27, no. 3, pp. 963–972, 2020.

[3] D. B. Zhang and B. Zhang, "Stability analysis of the pressurized 3D tunnel face in anisotropic and nonhomogeneous soils[J]," *International Journal of Geomechanics*, vol. 20, no. 4, pp. 1–18, 2020.

[4] X. Y. Hu, Z. X. Zhang, and S. Kieffer, "A real-life stability model for a large shield-driven tunnel in heterogeneous soft soils[J]," *Frontiers of Structural and Civil Engineering*, vol. 6, no. 2, pp. 176–187, 2012.

[5] A. Bobet, "Effect of pore water pressure on tunnel support during static and seismic loading," *Tunnelling and Underground Space Technology*, vol. 18, no. 4, pp. 377–393, 2003.

[6] B. Zhang, Z. Y. Ma, X. Wang, J. S. Zhang, and W. Q. Peng, "Reliability analysis of anti-seismic stability of 3D pressurized tunnel faces by response surfaces method," *Geomechanics and Engineering*, vol. 20, no. 1, pp. 43–54, 2020.

[7] D. B. Zhang, W. C. Sun, C. Y. Wang, and B. Yu, "Reliability analysis of seismic stability of shield tunnel face under multiple correlated failure modes[J]," *KSCE Journal of Civil Engineering*, vol. 25, no. 8, pp. 3172–3185, 2021.

[8] Q. J. Pan and D. Dias, "Face stability analysis for a shield-driven tunnel in anisotropic and nonhomogeneous soils by the kinematical approach[J]," *International Journal of Geomechanics*, vol. 16, no. 3, p. 04015076, 2016.

[9] G. Mollon, D. Daniei, and A. H. Soubra, "Rotational failure mechanisms for the face stability analysis of tunnels driven by a pressurized shield," *International Journal for Numerical and Analytical Methods in Geomechanics*, vol. 35, no. 12, pp. 1363–1388, 2011.

[10] B. Zhang, Y. Jiang, H. Cheng, and Z. Liu, "Upper bound analysis of the stability of 3D slopes in the saturated soft clay subjected to seismic effect[J]," *Frontiers in Earth Science*, vol. 9, p. 795854, 2021.

[11] B. Zhang, J. Jiang, D. B. Zhang, and Z. Liu, "Upper bound solution of collapse pressure and permanent displacement of 3D tunnel faces using the pseudo-dynamic method and the kinematic approach," *Geomechanics and Engineering*, vol. 25, no. 6, pp. 521–533, 2021.

[12] M. S. Huang, S. Li, J. Yu, and J. Q. W. Tan, "Continuous field based upper bound analysis for three-dimensional tunnel face stability in undrained clay," *Computers and Geotechnics*, vol. 94, pp. 207–213, 2018.

[13] J. H. Zhang, W. J. Wang, D. B. Zhang, B. Zhang, and F. Meng, "Safe range of retaining pressure for three-dimensional face of pressurized tunnels based on limit analysis and reliability method[J]," *KSCE Journal of Civil Engineering*, vol. 22, no. 11, pp. 4645–4656, 2018.

[14] H. Z. Cheng, J. Chen, R. P. Chen, and G. L. Chen, "Reliability study on shield tunnel face using a random limit analysis method in multilayered soils," *Tunnelling and Underground Space Technology*, vol. 84, pp. 353–363, 2019.

[15] E. Ibrahim, A. H. Soubra, G. Mollon, W. Raphael, D. Dias, and A. Reda, "Three-dimensional face stability analysis of pressurized tunnels driven in a multilayered purely frictional medium," *Tunnelling and Underground Space Technology*, vol. 49, no. 1, pp. 18–34, 2015.

[16] K. H. Han, C. P. Zhang, and D. L. Zhang, "Upper-bound solutions for the face stability of a shield tunnel in multilayered cohesive-frictional soils," *Computers and Geotechnics*, vol. 79, pp. 1–9, 2016.

[17] Q. J. Pan and D. Dias, "Upper-bound analysis on the face stability of a non-circular tunnel," *Tunnelling and Underground Space Technology*, vol. 62, pp. 96–102, 2017.

[18] S. Senent, C. Yi, and R. Jimenez, "An upper bound solution for tunnel face stability analysis considering the free span," *Tunnelling and Underground Space Technology*, vol. 103, p. 103515, 2020.

[19] G. H. Chen, J. F. Zou, and J. Q. Chen, "Shallow tunnel face stability considering pore water pressure in non- homogeneous and anisotropic soils," *Computers and Geotechnics*, vol. 116, p. 103205, 2019.

[20] Y. Li, C. Lyu, M. N. Wang, and T. Y. Xu, "Three-dimensional upper bound limit analysis of a deep soil-tunnel subjected to pore pressure based on the nonlinear Mohr-Coulomb criterion," *Computers and Geotechnics*, vol. 112, pp. 293–301, 2019.

[21] J. S. Xu, D. C. Du, and Z. H. Yang, "Upper bound analysis for deep tunnel face with joined failure mechanism of translation and rotation[J]," *Journal of Central South University*, vol. 22, no. 11, pp. 4310–4317, 2015.

[22] J. H. Zhang, W. J. Wang, B. Zhang, and D. B. Zhang, "Upper bound analysis for collapse failure of shield tunnel face excavated in unsaturated soils considering steady vertical flow," *Mathematical Problems in Engineering*, vol. 2019, 10 pages, 2019.

[23] F. Huang and X. L. Yang, "Upper bound limit analysis of collapse shape for circular tunnel subjected to pore pressure based on the Hoek-Brown failure criterion," *Tunnelling and Underground Space Technology incorporating Trenchless Technology Research*, vol. 26, no. 5, pp. 614–618, 2011.

[24] Q. J. Pan and D. Dias, "The effect of pore water pressure on tunnel face stability," *International Journal for Numerical and Analytical Methods in Geomechanics*, vol. 40, no. 15, pp. 2123–2136, 2016.

[25] D. B. Zhang, Z. Y. Ma, B. Yu, and H. D. Yin, "Upper bound solution of surrounding rock pressure of shallow tunnel under nonlinear failure criterion[J]," *Journal of Central South University*, vol. 26, no. 7, pp. 1696–1705, 2019.

[26] Z. W. Li, X. L. Yang, and T. Z. Li, "Face stability analysis of tunnels under steady unsaturated seepage conditions," *Tunnelling and Underground Space Technology*, vol. 93, p. 103095, 2019.

[27] J. H. Zhang and B. Zhang, "Reliability analysis for seismic stability of tunnel faces in soft rock masses based on a 3D stochastic collapse model [J]," *Journal of Central South University*, vol. 26, no. 7, pp. 1706–1718, 2019.

[28] J. H. Zhang, L. Y. Zhang, W. J. Whang, D. B. Zhang, and B. Zhang, "Probabilistic analysis of three-dimensional tunnel face stability in soft rock masses using Hoek–Brown failure

criterion," *International Journal for Numerical and Analytical Methods in Geomechanics*, vol. 44, no. 11, pp. 1601–1616, 2020.

[29] W. F. Chen, *Limit analysis and soil plasticity*, J. Ross Publishing, Inc, Florida, 2007.

[30] Q. Liang, X. L. Yang, J. H. Zhang, and W. Q. Zhou, "Upper bound analysis for supporting pressure of shield tunnel in heterogeneous soil," *Rock and Soil Mechanics*, vol. 37, no. 9, pp. 2585–2592, 2016.

[31] National Railway Administration of the People's Republic China, "TB 10003-2016, Code for Design of Rai1way Tunnel," in China Railway Publishing House Co., Ltd, 2016.

[32] J. L. Qiao, *Analysis of shield tunnel face stability*, Tianjin University, Tianjin, 2008.

Hindawi
Geofluids
Volume 2022, Article ID 2680516, 13 pages
https://doi.org/10.1155/2022/2680516

Research Article

Experimental Study on the Modification Mechanisms of Dispersive Soil Treated with Hydroxyl Aluminum

Jie Liu, Pan Chen, Zheng Lu, and Hailin Yao

State Key Laboratory of Geomechanics and Geotechnical Engineering, Institute of Rock and Soil Mechanics, Chinese Academy of Sciences, Wuhan, Hubei 430071, China

Correspondence should be addressed to Zheng Lu; zlu@whrsm.ac.cn

Received 23 February 2022; Accepted 13 May 2022; Published 23 June 2022

Academic Editor: Xueming Du

Dispersive soil is a special clay that is easy to disintegrate and disperse into particles and suspend in water, which can easily cause erosion and piping damage of dams, grooves, and road slopes. In this study, a new dispersive clay modifier hydroxyl aluminum (a positively charged aluminum hydroxide electrolyte) was proposed. Previous studies have shown that it can well coat montmorillonite in clay and combine with it to stabilize the properties of clay. The modification effect and interaction mechanism of hydroxyl aluminum on dispersive soil were studied through indoor dispersion discrimination, physical and mechanical, and micro mechanism tests (SEM and XRD). The experimental results indicate the following: With the increase of hydroxyl aluminum content, the dispersion of dispersed soil decreases and becomes nondispersive soil. Hydroxyl aluminum has an excellent inhibiting dispersion effect on dispersive soil, and it has the "agglomeration" and "cementation" effect on the dispersive soil particles. The addition of hydroxyl aluminum makes the dispersive soil agglomerated crystals arranged closely, and the number of pores between the particles reduces clearly, making the dispersed particles agglomerated. It can also reduce the alkalinity of the clay and make the clay structure more stable to restrain the dispersion of clay.

1. Introduction

Certain fine-grained soils are structurally unstable, with ease of dispersion, and therefore highly erodible. Soils in which the clay particles will detach spontaneously and go into suspension in quiet water are termed dispersive soils. Dispersive soil has existed in various climates in America, Mexico, Brazil, Australia, New Zealand, Spain, Greece, China, Iran, Malaysia, South Africa, etc. In China, dispersive soil is found in 16 provinces. Dispersion and easy erosion characteristics of dispersive soil cause serious erosion and piping failure for many engineering structures like dams, canal slopes, and road slopes [1, 2]: piping incidents of Grenada dam in Mississippi in 1949, the piping event of LAN Sulai dam in Thailand, dam failure event of Ling Luo reservoir in Hainan Province, and dam failure event of Heilongjiang diversion project in China.

It is complicated by the erosion effect on dispersive soil. It directly relates to the dispersion mechanism of dispersive soil and the electrochemical properties on the soil particle surface [3] [4], It has a high content of exchangeable sodium ions in dispersive soil, and montmorillonite is involved in the clay, which are essential affecting factors of its dispersion [5]. The surface of Na-montmorillonite in dispersive soil is liable to form a double electrical layer, which weakens the connection between mineral layers and the relationship between lamellar particles. It promotes large water entry freely. Then, the repulsion force between soil particles changes to be more significant than the attraction force, gradually resulting in the disintegration and shedding of the soil surface [6]. Some researchers developed that the relationships between the increment of the negative charge on the particle surface and pH value, pH value, and dispersion degree of the dispersive soil are all positive correlations [7].

Solving the dispersion problem of dispersive soil can reduce or eliminate related engineering accidents. To this end, aiming at the dispersion characteristics of dispersive soil in actual engineering, chemical stabilizers such as lime, cement, alum, and fly ash are added to dispersive soil.

Table 1: Physical and chemical properties of dispersive soil.

Project		Numerical value
Proportion		2.69
Natural moisture content/(%)		30.0
Particle composition/(%)	Sand >0.075 mm	6.7
	Silt 0.075~0.005 mm	49.8
	Clay particle <0.005 mm	43.5
Liquid limit (ω_L/%)		52.8
Plastic limit (ω_P/%)		20.5
Plasticity index (I_p)		32.3
Compaction parameters	Maximum dry density ρ_{dmax}/(g·cm^{-3})	1.62
	Optimum moisture content (ω_{op}/%)	21.8
Salt content/(g·kg^{-1})	Soluble salts	2.84
	Medium soluble salt	0.38
	Insoluble salt	50.60
	Organic matter	3.79
pH		9.25

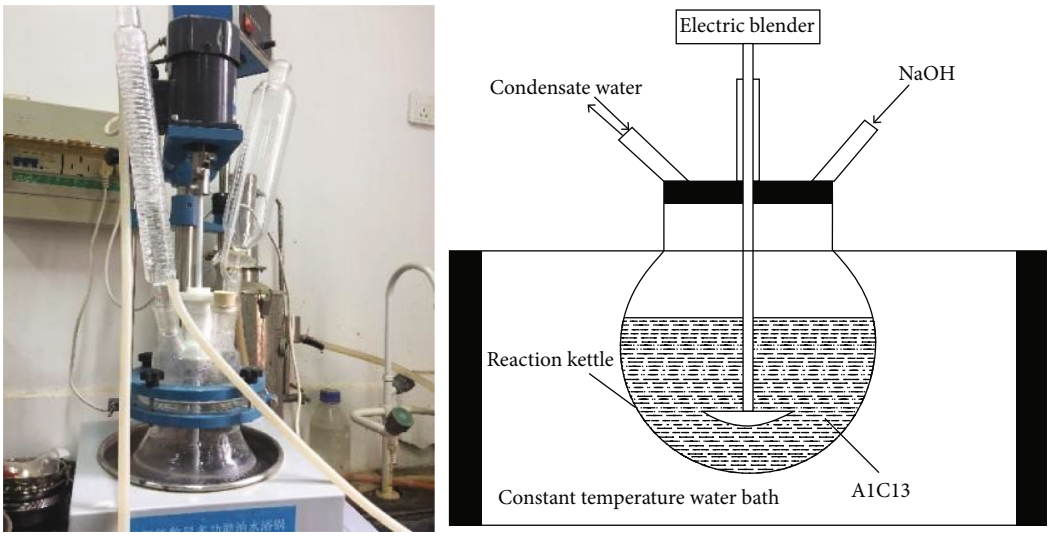

Figure 1: Device diagram and schematic diagram of the preparation of hydroxyl aluminum solution.

Figure 2: FDJ-20 direct shear apparatus.

Employing these manners, the dispersion of the dispersive soil reduces effectively, and the dispersive soil changes into nondispersive soil. In recent years, some experts have attempted to investigate new modifiers to treat dispersive soil in the laboratory, such as magnesium chloride [8, 9], slag [2], and ZELIAC (consists of zeolite, activated carbon, limestone, rice husk ash, and Portland cement) [10]. Some other experts also put forward new analysis methods for soil stability [11, 12].

Hydroxyl aluminum is a general term for the hydrolyzate produced after aluminum ions in the Al (III) solution hydrolysis equilibrium. Due to the abundance of the aluminum element, the large size, and the multichange of polyhydroxy aluminum ions, the hydroxyl aluminum system attracts researchers to explore its applications in specific

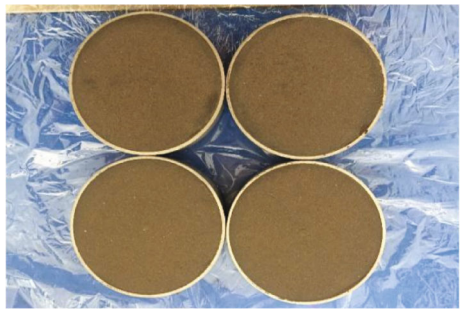

Figure 3: Soil samples of the test.

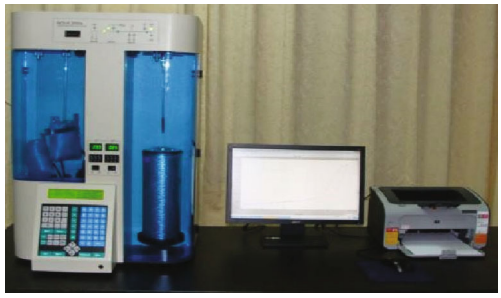

Figure 4: NOVA-1000 high-speed specific surface area and aperture analyzer.

fields. Several experts have studied the interaction between hydroxyl aluminum and montmorillonite. Hydroxyl aluminum can significantly reduce the exchange capacity for the cation of montmorillonite [13]. The cross-linking of hydroxyl aluminum with montmorillonite can form a more stable soil [14]. Clay minerals pillared by hydroxyl aluminum can change the cation exchange capacity in clay minerals, significantly increase interlayer attraction, and make it more significant than interlayer repulsion [15]. In addition, hydroxyl aluminum has a positive effect on clay consolidation that can reduce the surface acidity of montmorillonite [16]. Sludge was significantly acidified after the addition of hydroxyl aluminum. After the sludge flocs were conditioned with hydroxyl aluminum, the floc structure of the sludge was denser and more compact [17].

As experts ([5–7] said, the dispersion of dispersive soil is related to the presence of sodium montmorillonite and the acidity and alkalinity of the medium in the dispersive soil. Current studies have shown the advantages of hydroxyl aluminum in stabilizing soil properties and improving soil acidity, providing us with a research direction for effectively inhibiting the dispersion of dispersive soil. Traditional modification methods have achieved practical application effects in current engineering applications. However, there are some problems with the economy and timeliness of these traditional modifiers: choose the traditional modifier. It needs to excavate the subgrade filler and transport it to a specialized site. The modifiers are mixed into the subgrade filler to make it well-mixed and then transported to the engineering site for filling, which takes a lot of time, transportation, and labor costs. Once the hydroxyl aluminum is used as the modifier to realize engineering application, it can be prepared on a large scale. The hydroxyl aluminum can be sprayed directly on the subgrade surface filled in layers. The effect of modifying the subgrade filler can be achieved through an electrochemical reaction, which can save a lot of time and labor costs and make it more economical and environmental. Thus, in this paper, laboratory tests will be done to verify the inhibiting effect of hydroxyl aluminum on the dispersion of dispersive soil. The dispersive soil will be modified by hydroxyl aluminum. The laboratory tests of the modified soil samples will be done, including pH value, dispersion, limiting water content, permeability coefficient, cohesion, internal friction angle, shear strength, SEM, and XRD. The dispersibility, strength, and microstructure of dispersive soil with different content of hydroxyl aluminum are studied, which will provide theoretical and technical support for the engineering application of the new modifier hydroxyl aluminum.

2. Materials and Methods

2.1. Soil Samples. The soil samples are typical dispersive soil from a homogeneous dam in Northeast China and have been confirmed as dispersive soil in advance. Table 1 presents some engineering and chemical properties of dispersive soil measured in this study. According to the test results, the soil samples are divided into high plastic clay (CH). The pH value of the soil sample is 9.25, showing an alkaline state, which is a typical feature of dispersive soil.

2.2. Dispersive Soil Modifier. Hydroxyl aluminum ($Al(OH)_2^+$) is a general term for the hydrolysates of aluminum ions in Al (III) solution after reaching the hydrolysis equilibrium. It is rich in aluminum elements, large-scale polymerized hydroxyl aluminum ions, and multi charges. Hydroxyl aluminum enters the interlayer of montmorillonite through ion exchange, occupies the position of the exchangeable ions (Na^+), and improves the interlayer water rationality of montmorillonite. Hydroxyl aluminum has a significant positive charge, which can enhance clay's physical and chemical properties by neutralization reaction with clay particles (negative control) [18]. In addition, hydroxyl aluminum has also been proved to change soil's hydrophilicity and strength properties through physical and chemical reactions such as ion exchange, coating, and bonding with montmorillonite [19], significantly improving the physical properties and strength index of montmorillonite.

Different content of hydroxyl aluminum was selected to modify the dispersive soil, and the results were compared to verify the modification effect of hydroxyl aluminum. The main preparation methods of hydroxyl aluminum are as follows: adjust the ambient laboratory temperature to room temperature (20°C), add 40 ml with the concentration of 0.5 mol/l $AlCl_3$ solution into the glass reactor with an electric mixer, and reflux the condenser (Figures 1 and 2). The glass reactor is heated to the required temperature (80°C) using cauldron thermostat water bath.

50 ml NaOH solution with a concentration of 1.0 mol/l was added to the reactor through a buret at a specific dropping rate and mixed around intensely with a speed of 250 r/min. After the NaOH solution titration is finished, add

Table 2: Physical and chemical properties of the soil before and after modification with aluminum compounds.

Hydroxyl aluminum content/(mmol·g^{-1})	The specific gravity of soil particle	Particle composition/(%)			pH
		Sand 0.075 mm	Silt 0.075~0.005 mm	Clay particle <0.005 mm	
0	2.69	6.7	49.8	43.5	9.25
0.08	2.44	4.5	63.1	32.4	8.50
0.10	2.48	4.1	62.6	33.3	8.36
0.20	2.43	3.8	65.8	30.4	8.28
0.40	2.37	10.2	63.8	26.0	8.04

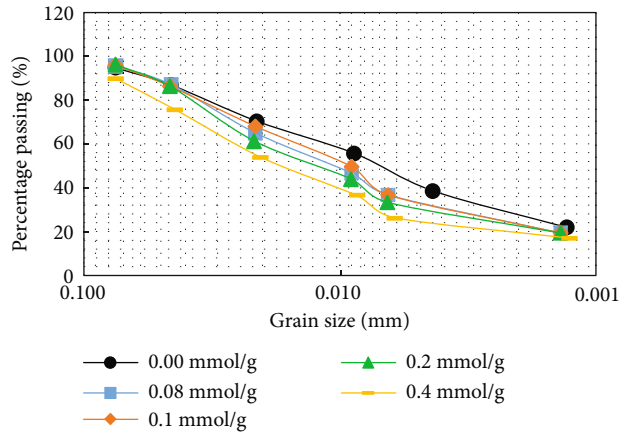

Figure 5: The curve of particle analysis under different hydroxyl aluminum contents.

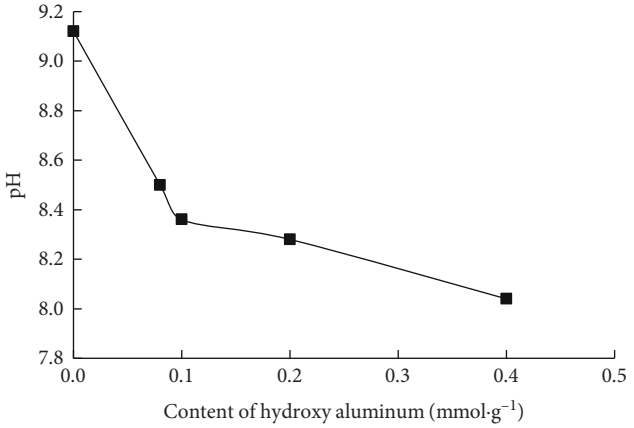

Figure 6: The curve of soil sample pH change with hydroxyl aluminum content.

110 ml distilled water through the buret, continue stirring the mixed solution for 20 min, and take samples after the hydroxyl aluminum solution turns to clear from turbidity, and leave the hydroxyl aluminum sample for one week.

The primary chemical reaction formula for the preparation of hydroxyl aluminum is shown in Formula (1). The device diagram and schematic diagram of the preparation of hydroxyl aluminum solution are shown in Figure 1.

$$Al^{3+} + 2OH^{-} \longrightarrow Al(OH)_2^{+} \quad (1)$$

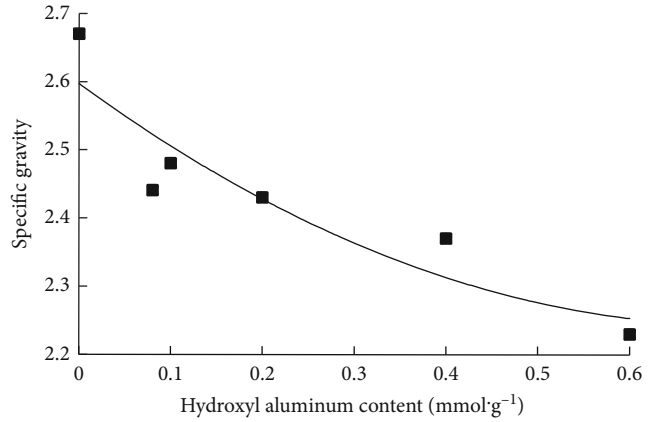

Figure 7: Variation of soil specific gravity with hydroxyl aluminum content.

2.3. Soil Sample Preparation. In air-dry soil sample before the experiments, add different dispersant inhibitors: the hydroxyl aluminum solution with varying ratios of bauxite (0.08 mmol/g, 0.1 mmol/g, 0.2 mmol/g, and 0.4 mmol/g) mixed in the sample. The mixing samples are cured at room temperature for one week.

2.4. Main Test Items of Hydroxyl Aluminum Modified Dispersive Soil. Dispersion Discrimination Test: following the attainment of equilibrium and hydroxyl aluminum to these samples, based on the pinhole and crumb test methods given in ASTM d4647-93 and ASTM d421-99, the dispersibility of soil samples before and after modification was tested. And the modification effect with different modifiers was discussed. Other laboratory tests of the modified soil samples were done, including pH value, permeability coefficient, cohesion, internal friction angle, shear strength, SEM, and XRD. The dispersibility, strength, and microstructure of dispersive soil with different modifier content of hydroxyl aluminum were studied.

Shear Strength Test: the instrument used in the shear strength test is the FDJ-20 direct shear apparatus, as shown in Figure 2. The test soil sample is made of φ 61.8 mm × 20 mm (Figure 3). Each soil sample was sheared under different vertical pressures (100 kPa, 200 kPa, 300 kPa, and 400 kPa, respectively). The controlled shear rate is 0.08 mm/min, and the shear time is 10 min. The horizontal shear stress is applied to make the soil sample shear fail.

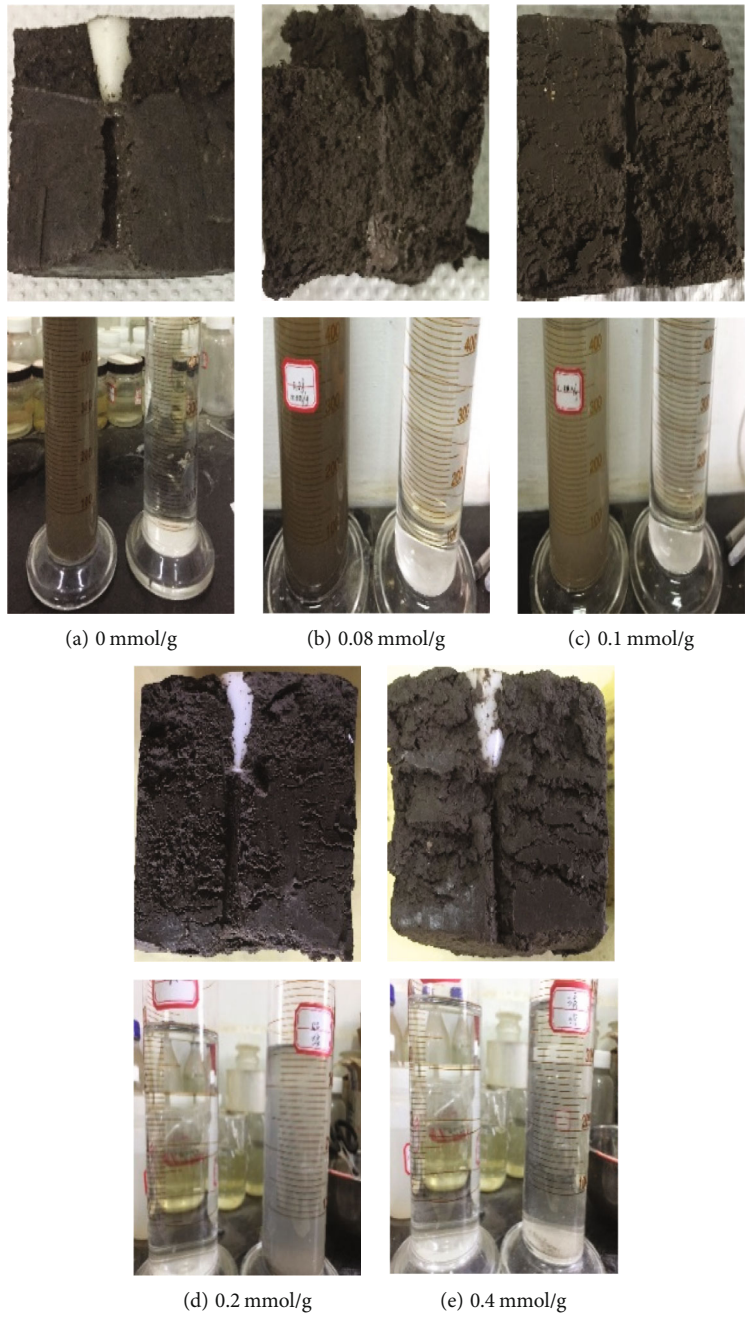

(a) 0 mmol/g (b) 0.08 mmol/g (c) 0.1 mmol/g

(d) 0.2 mmol/g (e) 0.4 mmol/g

Figure 8: Pinhole test before and after modification with different dosages of hydroxyl aluminum.

During the test, the unsaturated characteristics of the soil are not considered, and no air pressure is applied.

X-Ray Diffraction Test: the D8 advanced X-ray diffractometer of Bruker Company in Germany was used for X-ray diffraction analysis. X-ray diffraction tests were carried out on the samples before and after modification to study the changes in the phase composition of dispersive soil and crystal plane spacing of clay minerals before and after the modification of hydroxyl aluminum.

Specific Surface Area Test: according to BTE theory, all samples were analyzed using the N2 adsorption method on NOVA-1000 high-speed specific surface area and pore size analyzer of Quantan Chrome Company in the United States (in Figure 4). Working conditions are as follows: sample weight 100~500 mg, adsorbate N2 (>99.99%), carrier gas N2 (>99.99%), vacuum for 1.5 h, N2 adsorption temperature 77 K, and desorption temperature 393.15 k. Under these conditions, take the relative pressure as the abscissa and the adsorption capacity per unit sample mass as the ordinate, and draw the nitrogen adsorption isotherm and desorption isotherm. The specific surface area is calculated by the BET method, and the pore diameter is analyzed by the BJH method [20]. The T-method method obtained the micropore-specific surface area, mesopore (mesopore) specific surface area, and micropore volume. The specific surface area, particle size, pore size, and pore volume of the

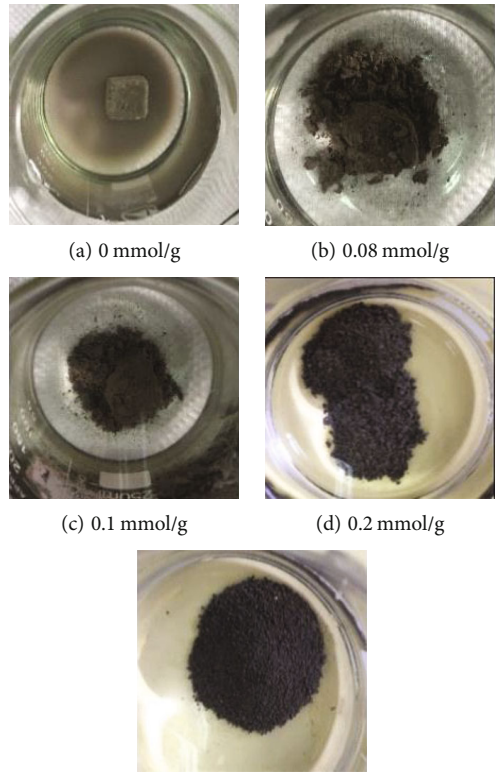

(a) 0 mmol/g (b) 0.08 mmol/g

(c) 0.1 mmol/g (d) 0.2 mmol/g

(e) 0.4 mmol/g

Figure 9: crumb test before and after modification with different dosages of hydroxyl aluminum.

Table 3: Dispersion identification results of the soil before and after hydroxy aluminum modification.

Al/soil ratio/(mmol·g^{-1})	Pinhole test			Crumb test		Comprehensive judgment
	Water head/(mm)	Time/(min)	Final aperture/(mm)	Water	Soil sample	
0	50	5	≥6	Muddy	Disintegration	Dispersive soil
0.08	50	5	≥3	Muddy	Disintegration	Dispersive soil
0.10	50	5	≥2	Little muddy	Partial disintegration	Dispersive soil
0.20	50	5	≥1.5	Little muddy	Disintegration	Transition soil
0.40	50	5	1	Clear	Disintegration	Nondispersive soil

Criteria for dispersion: Double hydrometer test: nondispersive soil: dispersion <30%; transition soil: 50%~50%; and dispersive soil: the dispersity is greater than 50%. Pinhole test: nondispersive soil: under the water head - 1020 mm, the water is transparent and the final hole diameter is less than 1.5 mm; transition soil: under 50 mm water head, the outlet water is slightly turbid and the final aperture is less than 1.5 mm or under 380 mm water head, the outlet water is more transparent and the final aperture is greater than 1.5 mm; and dispersive soil: under the water head of 50 mm, the outlet water is turbid and the final pore diameter is greater than 1.5 mm. Fragment test: nondispersive soil: there is no reaction of dispersing colloidal particles. After hydrolysis, the soil blocks are stacked horizontally in the form of fine particles at the bottom of the measuring cup. The watercolor is clear or becomes clear soon after being slightly turbid; transition soil: there is a small amount of muddy water around the soil block after hydrolysis, but the diffusion range is small; and dispersive soil: after hydrolysis, the upper block is turbid and the soil quickly diffuses to the bottom of the whole measuring cup. The water is foggy and unclear for a long time.

modified dispersive soil were obtained by studying the specific surface area of the dispersive soil modified with different amounts of hydroxyl aluminum.

3. Test Results and Analysis

3.1. Physical and Chemical Properties of the Dispersive Soil. Dispersive soil always contains predominantly expansive lattice-type minerals such as montmorillonite. The treatment of aluminum hydroxide to dispersive soil is mainly with montmorillonite. In sensitive clay, the treatment effect of aluminum hydroxide in laboratory and outdoor in situ is better than that of hydrated lime [21]. Hydroxyl aluminum has a significant positive charge, improving clay's physical and chemical properties by neutralizing the reaction with clay particles with a negative charge and coating

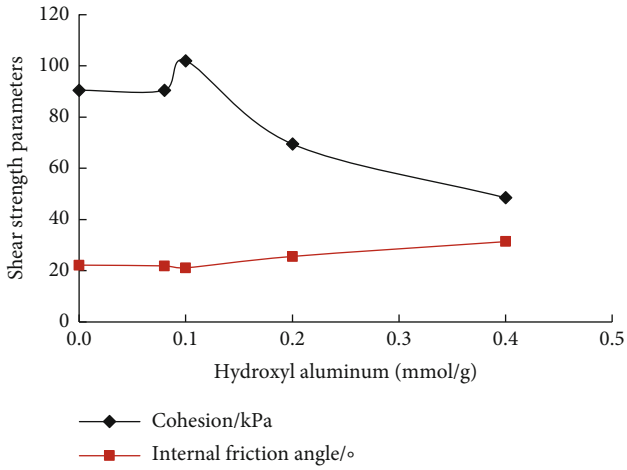

Figure 10: The adhesive force and internal friction angle change with aluminum compound content of modification clay sample.

adsorption [18]. Hydroxyl aluminum has also been proved to change soil's hydrophilicity and strength characteristics through ion exchange, coating, bonding, and other physical and chemical reactions with montmorillonite, significantly improving the physical properties and strength index of montmorillonite.

Based on the research team's previous micro experimental research results on hydroxyl aluminum-modified soil [22], different hydroxyl aluminum agent contents (0.08 mmol/g, 0.1 mmol/g, 0.2 mmol/g, and 0.4 mmol/g) are selected to be added into the dispersive soil. After modification by hydroxyl aluminum, specific gravity, particle analysis, pH test, and some other tests are carried out for the dispersive soil samples. The changes in the physical and mechanical properties of the soil samples are verified. The test results are shown in Table 2, which ululates that the physical and mechanical properties of the dispersive soil have some changes after modification.

The test results show that with the increase of hydroxyl aluminum content, the proportion and the clay content of the modified soil decrease, the silt content increases, and the alkaline weakens. After modification, the particle size increases (Figure 5), the specific surface area decreases, and the particles gather to form a more compact structure. Hydroxyl aluminum has the "agglomeration" and "cementation" effect on the dispersive soil particles, improving the dispersive soil's dispersion characteristics.

Dispersive soil is a high sodium soil formed by the secondary accumulation of weathering products due to evaporation. The pH value of the medium where the dispersive soil located is positively correlated with the degree of dispersion. The increment of negative charge on the particle surface is also positively correlated with the pH value [7]. The changing trend of pH value with the increase of hydroxyl aluminum content of the soil sample is shown in Figure 6. The result indicates that the pH of hydroxyl aluminum-modified soil decreases with hydroxyl aluminum content. The soil sample changes from strong alkali to weak alkali and even neutral with increasing hydroxyl aluminum content. It can be seen that the addition of hydroxyl aluminum changes the medium environment of the soil sample and increases the acidity of the soil sample.

Figure 7 shows the variation of soil-specific gravity with hydroxyl aluminum content. The range of soil-specific gravity is limited, generally between 2.6 and 2.8. After modifying hydroxyl aluminum, the ratio of aluminum to soil increases gradually, and the specific weight of soil particles decreases with the increase of the ratio of hydroxyl aluminum. The particular gravity value reduction range was 7.1%-16.5%, strengthening the connection between soil particles, the proportion of clay particles decreases, and the ratio of silt and sand increases. With the increase of large particle size, the particle weight per unit volume of the soil will be reduced accordingly, and the specific gravity of the soil becomes smaller.

3.2. Dispersion Change of Soil Sample Modification. Techniques are commonly used, such as the pinhole test, crumb test, and double hydrometer test. These tests may yield different results for the same soil samples; hence, multiple tests should be used to determine the dispersion of the soil [23, 24].

The results of the dispersion discrimination test of the soil samples with the modification of hydroxyl aluminum are shown in Figures 8 and 9. The results of the dispersion discrimination are shown in Table 3.

Pinhole Test: as the content of hydroxyl aluminum is 0.08 mmol/g, the pinhole diameter decreases, and the water flowing out from the pinhole is turbid; with the content of hydroxyl aluminum increasing, the pinhole diameter has a significant decreasing trend, and the turbidity degree of water flow out of the pinhole also decreases. When the content of hydroxyl aluminum is 0.4 mmol/g, the pinhole diameter hardly changes, and the water flow is bright.

Crumb Test: with the increase of hydroxyl aluminum content, all soil samples disintegrated to different degrees, but there was no turbidity in the beaker.

Double Hydrometer Test: with the increase of hydroxyl aluminum content, the dispersity of the soil sample decreases gradually. As the hydroxyl aluminum content is 0.08 mmol/g, the soil becomes transitional. As the hydroxyl aluminum content is 0.4 mmol/g, the soil turns into nondispersive soil. Hydroxyl aluminum also has a significant improvement effect on dispersive soil.

The dispersion discrimination test of hydroxyl aluminum-modified soil showed that the dispersion of soil samples had been restrained by different content of hydroxyl aluminum. With the increasing amount of modifiers, the diffusion of soil sample weakens clearly. The comprehensive test results showed that as the content of aluminum reaches 0.2-0.4 mmol/g, it has been dramatically suppressed because of the dispersion of the soil samples. Hydroxyl aluminum can bring about a good effect of restraining dispersion.

3.3. Shear Strength Changes of the Soil Samples. The adhesive force, internal friction angle, and the shear strength of the soil samples in different modifiers' content conditions are shown in Figure 10. It can be seen that the cohesion of the soil sample with different modifier content is all having an

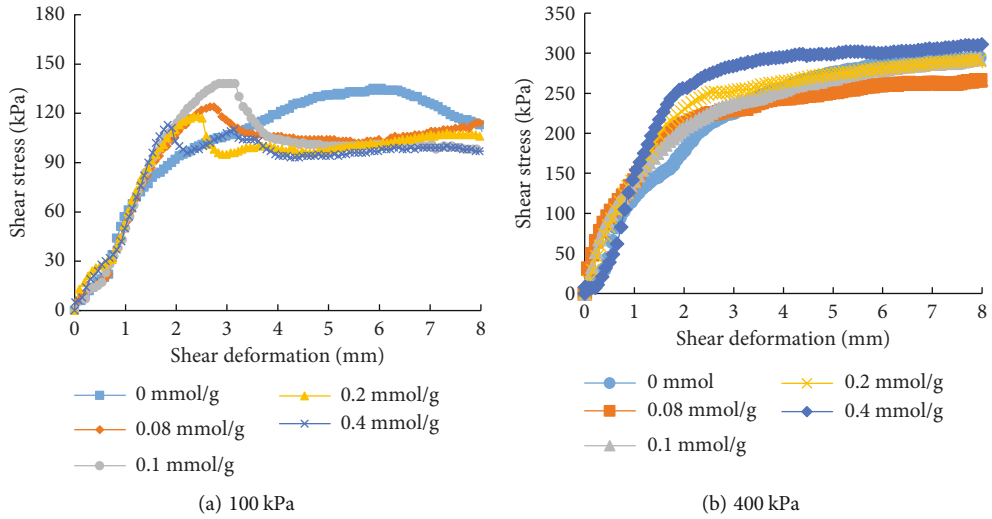

Figure 11: Stress-strain curve of hydroxyl aluminum-modified soil.

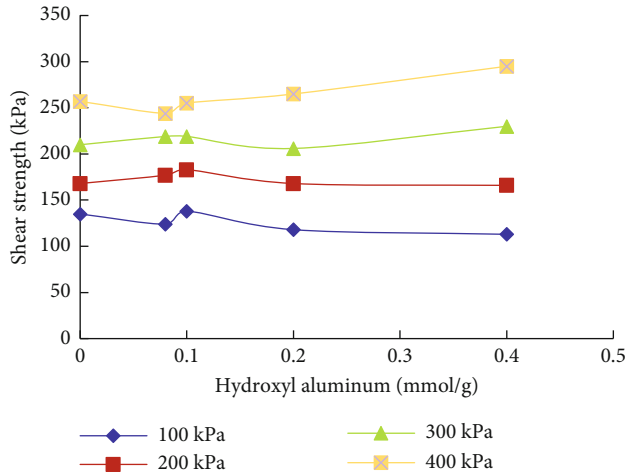

Figure 12: Shear strength changes of the modification clay sample.

Table 4: Variations of the crystal face space of montmorillonite (D001).

Hydroxyl aluminum content/(mmol·g^{-1})	0	0.08	0.1	0.2	0.4
Distance between crystal faces of montmorillonite d_{001}/(Å)	14.21	14.79	14.504	14.327	15.41

apparent downward trend, and the internal friction angle of the modification soil samples has a slight increase with the increase of the modifier content. Still, the increasing extent is smaller than that of cohesion. The increase of internal friction angle indicates that the particles can be occluded and inlaid, form some new large particle, and then increases the internal friction angle. However, the decrease of cohesion shows that aluminum's physical and chemical reactions include hydroxyl aluminum solution entering into the particles with negative electricity, such as agglomeration and coating, which change the particle size distribution of the soil sample. As the clay particles in the soil sample achieve mutual adhesion, the content of clay particles in the soil sample is reduced, and the cohesion of the modified soil is reduced.

Figures 11 and 12 show the stress-strain curves of hydroxyl aluminum-modified soil under different vertical pressures. The stress-strain curves of soil are stress hardening with the load increasing. Under the same load condition, the shear strength of soil has no noticeable linear change with the increase of hydroxyl aluminum content. When the vertical load is 100 kPa, the stress-strain curve of the soil

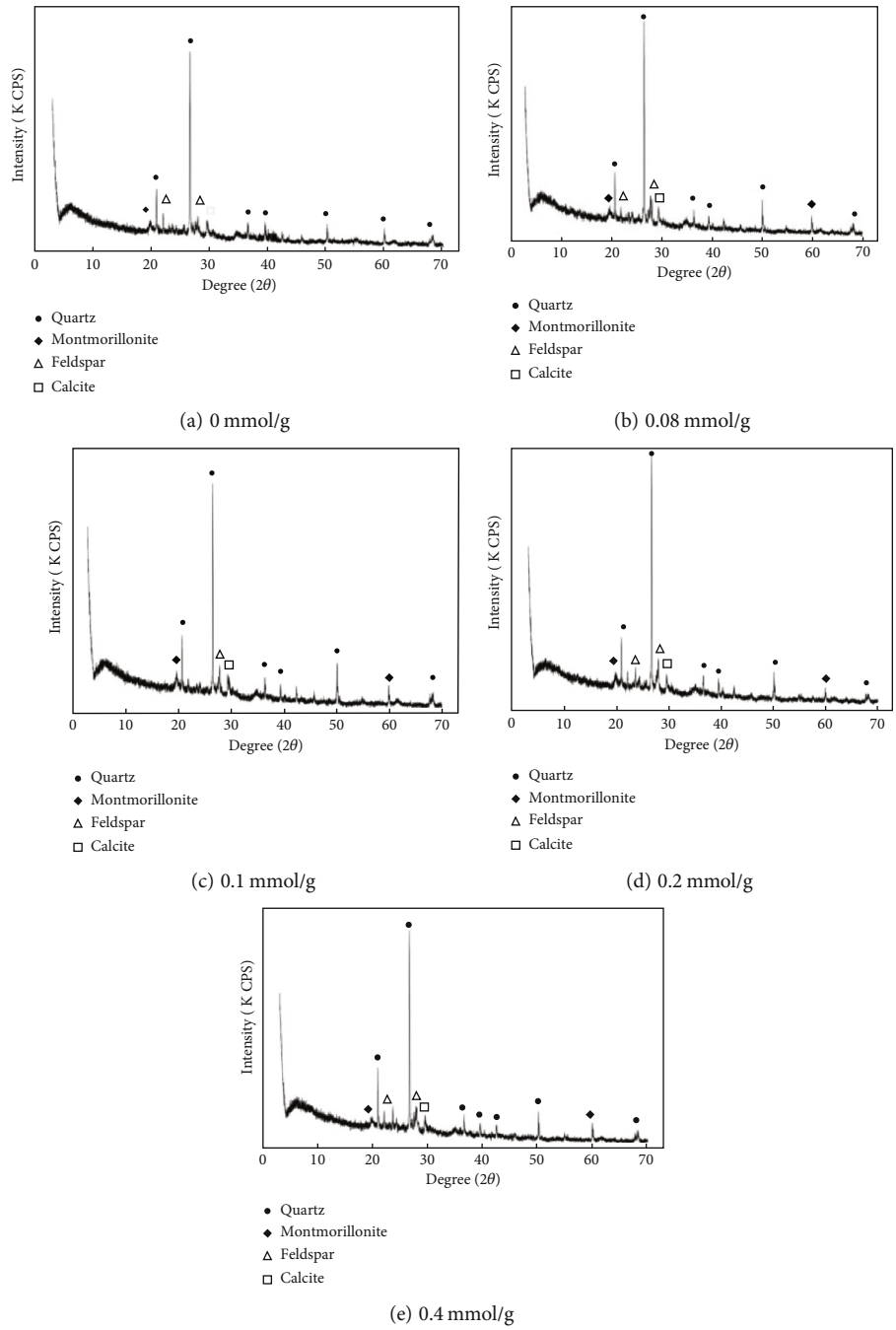

Figure 13: X-Ray diffraction pattern of soil samples with different contents of hydroxyl aluminum.

Table 5: Changes of specific surface area and pore size of hydroxyl aluminum-modified soil.

Hydroxyl aluminum content/ ($mmol \cdot g^{-1}$)	Specific surface area/ ($m^2 \cdot g^{-1}$)	Cumulative pore volume/ ($cm^3 \cdot g^{-1}$)	Average aperture/ (nm)
0	53.002	0.07089	2.6750
0.08	48.876	0.06808	2.7858
0.1	46.241	0.06083	2.7309
0.2	46.441	0.06376	2.7460
0.4	46.084	0.05892	2.8573

before modification is strain hardening type, and there is no obvious peak value of the stress-strain curve. After adding hydroxyl aluminum solution, the stress-strain curve of the modified soil increases rapidly with the increase of strain. When the stress peak value is reached, the stress decreases with the increase of shear displacement, and there is a prominent peak value characterized by strain softening. As the shear strength is significant (300 kPa and 400 kPa), the shear strength of the modified soil with 0.4 mmol/g hydroxyl aluminum content is significantly higher than that of the modified soil with other contents.

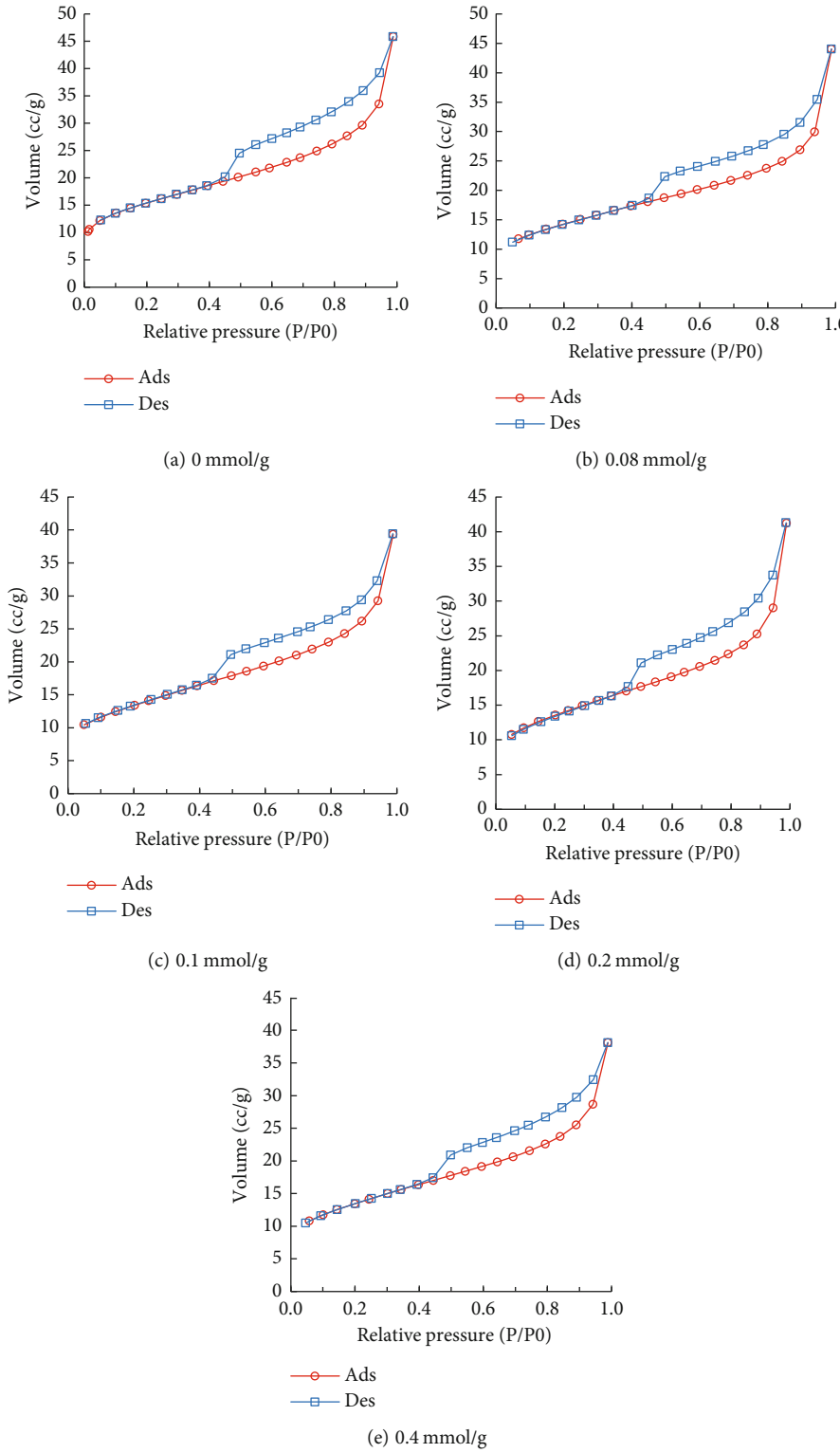

Figure 14: N2 adsorption-desorption isotherms with different amounts of hydroxyl aluminum.

4. Microscopic Changes of Hydroxyl Aluminum-Modified Soil

4.1. X-Ray Diffraction Test. Variations of the crystal face space of montmorillonite are listed in Table 4. As shown in Figure 13, montmorillonite is the main clay mineral composition, while the nonclay mineral composition is quartz, calcite, and feldspar. In the main clay mineral in the soil, the crystal surface spacing of montmorillonite increases with the content of hydroxyl aluminum increasing, which indicates that after the interaction of hydroxyl aluminum and soil samples, aluminum ions enter the interlayer of the soil

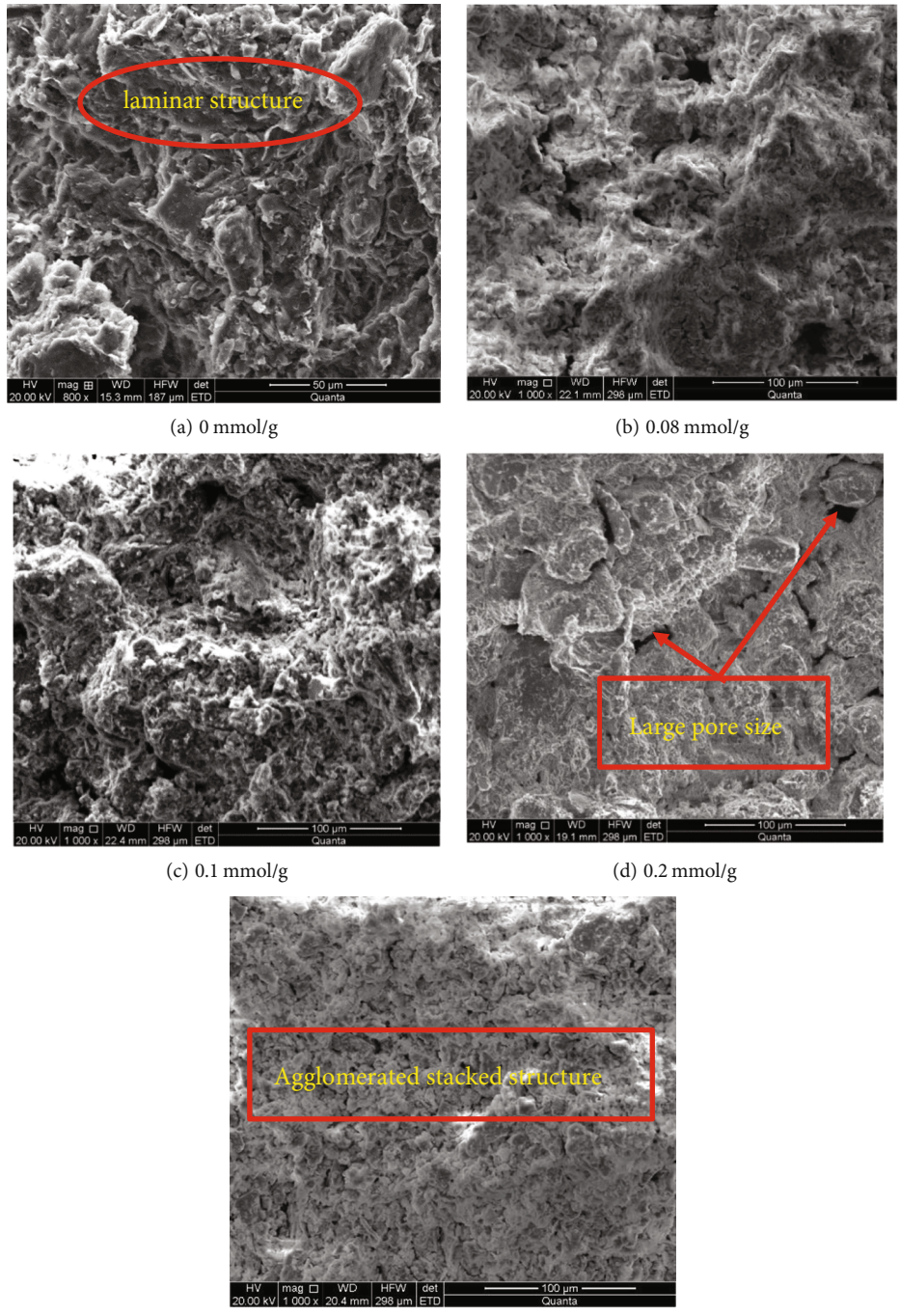

(a) 0 mmol/g (b) 0.08 mmol/g

(c) 0.1 mmol/g (d) 0.2 mmol/g

(e) 0.4 mmol/g

Figure 15: SEM test results of soil samples with different contents of hydroxyl aluminum.

and replace the interlayer water, reducing the amount of water absorbed by the soil, to reduce its hydrophobicity.

The diffraction pattern is the same before and after the interaction of hydroxyl aluminum with the soil sample. No new peak appears and disappears, which indicates no new phase appears. It can be explained that the physicochemical reaction between hydroxyl aluminum and dispersive soil is mainly the ion exchange adsorption on the surface of soil particles and the formation process of hydrogen bonds between the groups carried by polymer organic compounds and the crystal surface of minerals. Hydroxyl aluminum does not react with the soil to form new crystal compounds.

4.2. Specific Surface Area Test. The specific surface areas of soil samples with different hydroxyl aluminum contents are shown in Table 5.

Figure 14 shows the N2 adsorption-desorption isotherms with different amounts of hydroxyl aluminum; with the increase of hydroxyl aluminum content, the specific surface area and pore volume of dispersive soil gradually

decrease, while the average pore size gradually increases. This result is because that hydroxyl aluminum promotes the connection between particles in the soil after entering the dispersive soil; the agglomerated particles increase. The pore volume also decreases gradually due to the stronger polymerization between soil particles and the increase of agglomerated particles. It also indirectly makes the grading of soil poor and increasing of the pore size. The adsorption isotherm of the modified soil given in Figure 13 belongs to a type II isotherm. It can be seen that the modified soil with different content shows the typical situation of multilayer adsorption of porous media. The hysteresis loop belongs to the H3 type, indicating that the pore shape is similar to the slit formed by parallel plates. The slope of the adsorption isotherm before modification is slightly more significant in the relative pressure range of 0.98~1.0. After modification, the slope decreases, indicating that the number of pores in the modified soil sample decreases. It also indirectly shows that the modification increases the large agglomerated particles in the soil, reducing the number of pores between the particles.

4.3. SEM Test Analysis. The micro view of dispersive soil modified with hydroxyl aluminum was tested by scanning electron microscope.

Figure 15 shows the SEM image of the soil sample at 1000 times magnification under different contents of hydroxyl aluminum. It can be seen that the connection between the particles of the soil sample with low content of hydroxyl aluminum is relatively loose, and the pores are strongly developed. The soil sample shows a laminar structure with large and thin clay flakes and clay minerals' typical soil morphology, agreeing with Ouhadi and Goodarzi [25]. With the addition of hydroxyl aluminum solution, the structural unit of the soil sample is mainly composed of the agglomerated stacked structure. The agglomerated crystals are arranged closely, and the number of large pores between the particles reduces clearly. The particles are stacked together to form a tight structure. The agglomeration, cementation, and other effects of hydroxyl aluminum on the dispersive soil make the content of significant and coarse powder increase and the content of clay decrease—the connection between the soil samples becomes closer. The structure becomes more stable to restrain the dispersion of soil samples. The scanning electron microscope shows that with the increase of hydroxyl aluminum content, the pore size of particles in the soil increases, and the significant aggregate particles increase. The results also directly verify the calculation results of specific surface area and pore diameter given in Table 5.

5. Conclusion

In this study, a new type of dispersive soil modifier, hydroxyl aluminum, is introduced. The effects of treating dispersive soil samples with different hydroxyl aluminum additive contents are investigated. The following conclusions of this study can be summarized from the test results:

(1) The test soil sample is highly dispersed. The dispersibility of the soil sample modified by hydroxyl aluminum decreases significantly and changes into nondispersive soil with the content increase of the modifier. In addition, with the increase of modifier content, the internal friction angle of the soil sample increases slightly, which shows that the modified soil particles are occluded and embedded to form new large particles to increase the internal friction angle. The clay particles in the soil sample adhere to each other, and the content of clay particles in the soil sample decreases, resulting in the cohesion decrease of the soil sample

(2) Under the same load condition, the shear strength of soil has no noticeable linear change with the increase of hydroxyl aluminum content. However, as the shear strength is large (300 kPa and 400 kPa), the shear strength of the modified soil with 0.4 mmol/g hydroxyl aluminum content is significantly higher than that of the modified soil with other contents

(3) The SEM and X-ray analyses depict a laminar structure with large and thin clay flakes of the sample without the additive. And the structural unit of the soil sample is mainly composed of the agglomerated stacked structure of the model with the additive. The addition of hydroxyl aluminum caused the sample agglomerated crystals to be arranged closely, and the number of large pores between the particles was reduced. This result is explained by the flocculation of the clay and the subsequent increase in particle size with the addition of the additive. This change in the microstructure corresponded to changes in the geotechnical properties of the soil

(4) The successful modification of dispersive soil by hydroxyl aluminum is expected to provide a scientific basis for the later engineering application of hydroxyl aluminum. The method of electrochemical injection of hydroxyl aluminum can be considered to treat the dispersed soil in situ. Hydroxyl aluminum solution diffuses to the extreme under electric pressure and cementates with dispersed clay to the greatest extent to realize the in situ treatment of dispersed clay subgrade. The application of hydroxyl aluminum will significantly improve the on-site project's economic, human and material costs and realize rapid treatment

Data Availability

Some or all data, models, or codes that support the findings of this study are available from the corresponding author upon reasonable request.

Conflicts of Interest

The authors declare that there are no conflicts of interest regarding the publication of this article.

Acknowledgments

This research is supported by the National Natural Science Foundation of China (Nos. 41672311, 42077261, and 41672312, these financial supports are gratefully acknowledged.

References

[1] A. R. Goodarzi and H. R. Akbari, "Assessing the anion type effect on the hydro-mechanical properties of smectite from macro and micro-structure aspects," *Geomechanics and Engineering*, vol. 7, no. 2, pp. 183–200, 2014.

[2] A. Goodarzi and M. Salimi, "Stabilization treatment of a dispersive clayey soil using granulated blast furnace slag and basic oxygen furnace slag," *Applied Clay Science*, vol. 108, pp. 61–69, 2015.

[3] J. L. Sherard, R. S. Decker, and R. L. Ryken, "Piping in earth of dispersive clay," in *Proceedings of the ASCE Speciality Conference on the Performance of Earth-supported Structure*, pp. 589–626, Purdue University, 1972.

[4] R. N. Yong and B. P. Warkentin, *Introduction to Soil Behavior*, MacMillan, New York, NY, USA, 1966.

[5] G. D. A. Ingles, "Soil-water disequilibrium as the cause of subsidence in natural soils and earth dams," *Proceedings of the Tokyo Symposium on Land Subsidence*, 1969, pp. 342–353, Tokyo, 1969.

[6] J. L. Sherard et al., "Identification and nature of dispersive soil," *Proceedings of ASCE*, vol. 102, no. GT4, pp. 287–301, 1976.

[7] G. G. S. Holmgren and C. P. Flanagan, "Factors affecting spontaneous dispersion of soil materials as evidenced by the crumb test," in *Dispersive Soils, Related Piping, and Erosion in Geotechnical Projects, ASTM STP 623*, J. L. Sherard and R. S. Decker, Eds., pp. 218–239, American Society for Testing and Material, Chicago, IL, USA, 1977.

[8] M. Turkoza, H. Savasa, A. Acaza, and H. Tosun, "The effect of magnesium chloride solution on the engineering properties of clay soil with expansive and dispersive characteristics," *Applied Clay Science*, vol. 101, pp. 1–9, 2014.

[9] M. Sajadi, E. Nikooee, and G. Habibagahi, "Biological treatment of swelling soils using microbial calcite precipitation," in *Unsaturated Soils: Research and Applications*, pp. 917–922, Unsaturated Soils, 2014.

[10] A. H. Vakili, M. R. b. Selamat, H. B. A. Aziz, A. Mojiri, Z. Ahmad, and M. Safarzadeh, "Treatment of dispersive clay soil by ZELIAC," *Geoderma*, vol. 285, pp. 270–279, 2017.

[11] X. Du, H. Fang, S. Wang, B. Xue, and F. Wang, "Experimental and practical investigation of the sealing efficiency of cement grouting in tortuous fractures with flowing water," *Tunnelling and Underground Space Technology*, vol. 108, article 103693, 2021.

[12] B. Xue, X. Du, J. Wang, and X. Yu, "A scaled boundary finite-element method with B-differentiable equations for 3D frictional contact problems," *Fractal and Fractional*, vol. 6, no. 3, p. 133, 2022.

[13] H. Jobstmann and B. Singh, "Sorption by hydroxy-aluminium interlayered montmorillonite," *Water, Air, and Soil Pollution*, vol. 131, no. 1/4, pp. 203–215, 2001.

[14] G. W. Brindley and R. E. Sempels, "Preparation and properties of some hydroxy-aluminium beidellites," *Clay Minerals*, vol. 12, no. 3, pp. 229–237, 1977.

[15] G. S. Kidder, "Characteristics of hydroxy-aluminum interlayered clays," *Clays and Clay Minerals*, vol. 20, no. 1, pp. 13–19, 1972.

[16] L. Wang, S. Xiang, J. Zhang, and T. Hua, "Study on the surface acidity of hydroxyl-aluminum montmorillonite," *Acta Scientiarum Naturalium Univeraitstia Pekinenais*, vol. 27, no. 4, 1991.

[17] B. Cao, W. Zhang, Q. Wang, Y. Huang, C. Meng, and D. Wang, "Wastewater sludge dewaterability enhancement using hydroxyl aluminum conditioning: role of aluminum speciation," *Water Research*, vol. 105, pp. 615–624, 2016.

[18] W. P. Cheng, F. H. Chi, C. C. Li, and R. F. Yu, "A study on the removal of organic substances from low-turbidity and low-alkalinity water with metal-polysilicate coagulants," *Colloids and Surfaces, A: Physicochemical and Engineering Aspects*, vol. 312, no. 2-3, pp. 238–244, 2008.

[19] H. H. Fan, M. X. Gao, P. Li, and P. T. Wu, "Study on the dispersive clay of the core wall of a dam," *Chinese Journal of Geotechnical Engineering*, vol. 25, no. 5, pp. 615–618, 2003.

[20] M. L. Ojeda, J. M. Esparza, A. Campero, S. Cordero, I. Kornhauser, and F. Rojas, "On comparing BJH and NLDFT Pore-size distributions determined from N2 sorption on SBA-15 substrata," *Physical Chemistry Chemical Physics*, vol. 5, no. 9, pp. 1859–1866, 2003.

[21] T. Bryhn and G. Aas, "Stabilization of sensitive clays with hydroxy-aluminium compared with unslaked lime," *Proceedings of the European Conference On Soil Mechanics and Foundation Engineering*, 1984, pp. 261–270, Stockholm, 1984.

[22] H. Yao, L. Liu, S. Sun, and R. Fang, "Swelling behavior of montmorillonites noncolloidally crosslinked with ε-Al13," *Soil Science Society of America Journal*, vol. 80, no. 5, pp. 1190–1196, 2016.

[23] ASTM, *D4647-93 Standard test method for Identification and classification of clayey soil by the pinhole test*ASTM International, West Conshohocken, PA, USA.

[24] ASTM, *D6572-00 Standard test method for determining dispersive characteristics of clay soil by the crumb test*ASTM International, West Conshohocken, PA, USA.

[25] V. R. Ouhadi and A. R. Goodarzi, "Assessment of the stability of a dispersive soil treated by alum," *Engineering Geology*, vol. 85, no. 1-2, pp. 91–101, 2006.

Hindawi
Geofluids
Volume 2022, Article ID 2041924, 10 pages
https://doi.org/10.1155/2022/2041924

Research Article

Study on the Floating of Large Diameter Underwater Shield Tunnel Caused by Synchronous Grouting

Yu Liang,[1] **Xumin Huang**,[2] **Shijun Gao**,[3] **and Yihao Yin**[3]

[1]*School of Civil Engineering, Sun Yat-Sen University, Zhuhai 519000, China*
[2]*School of Aeronautics and Astronautics, Sun Yat-Sen University, Shenzhen 518000, China*
[3]*China Railway 14th Bureau Group Mega Shield Construction Engineering Co., Ltd., Nanjing 210000, China*

Correspondence should be addressed to Yu Liang; liangyu25@mail.sysu.edu.cn

Received 20 January 2022; Revised 31 March 2022; Accepted 23 May 2022; Published 23 June 2022

Academic Editor: Xinyu Ye

Synchronous grouting is the key factor causing segment floating during the construction of shield tunnel, especially the grout ratio and the control of the grouting pressure. In this paper, the ratio of grout material was optimized through multiple groups of physical and mechanical tests. The results showed that 0.3% content of water reducing agent in grout could improve the ability of water resistance significantly. 2.9% content of bentonite could reduce bleeding rate of grout and grout setting time and improve the fluidity in the meantime. Then, the distribution law of grout along the segment ring in the filling stage was studied based on a typical underwater tunnel in China. The results showed that the theoretical calculation of grouting pressure was between 0.15 MPa and 0.18 MPa, which were in good agreement with the measured data. The grouting pressure distribution is affected by four parts including the lateral earth pressure, foundation reaction, grout shear stress, and gravity.

1. Introduction

Shield tunnel has been widely used in traffic engineering crossing river and sea due to its advantages, and it tends to be larger in diameter and deeper in depth [1–3]. With the increase of the diameter of the shield tunnel, the buoyancy of the tunnel would be multiplied. During the process of shield tunnelling, a gap between the segment and the soil will occur after the segments come out from the shield tail [4, 5]. The segment tends to float upward due to the geological conditions and synchronous grouting [6, 7]. In particular, when the overlaying soil is shallow, segment floating is more prominent. For example, during the construction of underwater shield tunnels such as Dalian Road Tunnel (Shanghai), Yangtze River Tunnel (Shanghai), Qingchun Road Tunnel (Hangzhou), and Shiziyang Tunnel (Guangzhou) of China, the tunnel segments have appeared to varying degrees of buoyancy [4, 8, 9].

Another example is shown in Figure 1, which presented the floating situation of an underwater tunnel in China. The diameter of the tunnel is 13.8 m, and it passes through the stratum of silty clay, silty fine sand, and medium sand. Due to the large hydraulic conductivity of the sand layer and the abundant groundwater, serious floating of the segment occurs during construction.

The segment floating is often accompanied by segment damage and dislocation, and even the connection bolts could be cut off or lead to water leakage, which directly affects the safety of the tunnel construction, as shown in Figure 2. Therefore, it is necessary to study the mechanical action mechanism of shield tunnel and the reasons of tunnel uplift to ensure the safety of tunnel structure [10, 11].

2. Analysis of Floating Mechanism of Tunnel Segments

As known in Figure 1, serious segments floating occurred during shield tunnelling, segment installation, and synchronous grouting. The cumulative float of segments in some sections had exceeded the warning value, which will cause

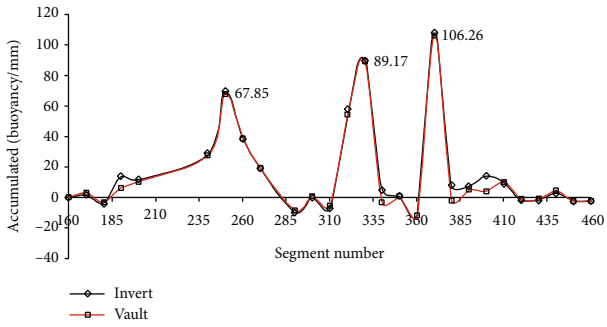

Figure 1: The floating situation of the underwater tunnel.

uneven stress on the segment, resulting in stress concentration and segment damage.

Many factors could affect tunnel floating, and these factors are often interrelated mutually such as geological conditions [6], synchronous grouting [12–14], and shield attitude control [15]. Based on the field monitoring data from the underwater tunnel mentioned above, two factors were discussed in this paper. The first factor is the change of surrounding rock properties. The underwater tunnel passed through many stratums including silty clay, silty fine sand, and medium sand. And the change of surrounding rock may lead to the change of rock strength and structural integrity. After shield excavation, the surrounding rock will not immediately fill the gap at the shield tail so that there is enough space for the segment to float. It is necessary to prepare grout with better fluidity, shorter setting time, and higher compressive strength when conducting synchronous grouting in this zone. The second factor is the control of the synchronous grouting. According to the construction record, the grout amount in the grout circulation system increased significantly when there is shield tunnelling through this area. Once the stratum conditions changed especially in the soft soil layer, the grouting pressure would be over large if the corresponding construction parameters were not adjusted in time. And then, the tunnel axis could deviate, resulting in segment floating.

Whether the construction control measures are appropriate has a great impact on the segment floating. In particular, when the stratum conditions are the same, the properties of the grout, grout buoyancy, and grouting pressure will have the greatest impact on it.

In this paper, the ratio of grout materials was optimized to improve the ability of water resistance and shorten the setting time. Then, the mechanism of grouting pressure in the filling stage was studied, and the flow law of grout along the circumferential direction in this stage was analyzed. Finally, taking the typical section of an underwater tunnel in China as an example, the distribution law of grout along the outer wall of segment and the floating situation of segment in the filling stage were verified, which would provide a theoretical reference for the floating control of segment in large diameter shield tunnel excavation in water-rich strata.

3. Study on the Properties of Synchronous Grouting Material

3.1. Performance Requirements of Underwater Synchronous Grouting. When synchronous grouting is carried out in the water-rich layer, the grout is easy to be lost from the layer with groundwater after spraying out, due to the poor water resistance. It is difficult to fill the gap of shield tail, resulting in the floating and leakage of the segment. For the water-rich layer with large hydraulic conductivity, synchronous grouting material requires the properties including fast filling, small bleeding rate, short setting time, good water resistance, and sufficient strength after the grout consolidation process is done. According to engineering experience, synchronous grouting material should meet the following requirements when shield tunnelling in water-rich layer area:

(1) Degree of fluidity: 230~250 mm

(2) Bleeding rate: 5%~10%;

(3) Setting time: 6~7 hours

(4) Shear strength: the 24-hour shear strength of grout should be greater than or equal to that of equivalent strata

(5) Compressive strength: the 7-day strength of grout should be greater than 0.50 MPa, and the 28-day strength of grout should be greater than 1.65 MPa

(6) Water resistance: a test method for the stability of grout in water was developed in this paper as shown in Figure 3. Firstly, put the test mold of grout into the water tank to make the water surface 10 cm above the mold. Connect it with the pipe and funnel, and inject the fresh grout into the mold until the grout overflows from the mold. Then, the mold and grout are placed in the water tank together to maintain until the specified time, and then, the grout is taken out for uniaxial compressive strength test. The water-land strength ratio is the strength ratio of grout with two different curing conditions (water and land) and with the same proportion at the same age after molding, so as to determine the water resistance of grout. The closer the water-land strength ratio is to 1, the better the water resistance of grout

3.2. The Optimization of Grout Ratio. According to the statistics of grout ratios in many similar projects, the commonly used water-binder (fly ash+cement) ratio ranges from 0.6 to 1, the binder-sand ratio ranges from 0.5 to 0.7, the bentonite-water ratio ranges from 0 to 0.2, and the fly ash-cement ratio ranges from 1.6 to 3.2. In order to reduce the test times, a series of physical mechanics and construction performance tests were carried out by using U15 (15^5) uniform design method [16]. Finally, a group of grout ratio was optimized as follows: cement 187 g, fly ash 313 g, bentonite 37.5 g, sand 770 g, and water 375 g. The test results of the grout ratio are shown in Table 1. Grout ratio 1 in the table is the one used in the tunnel at first, and ratio 2

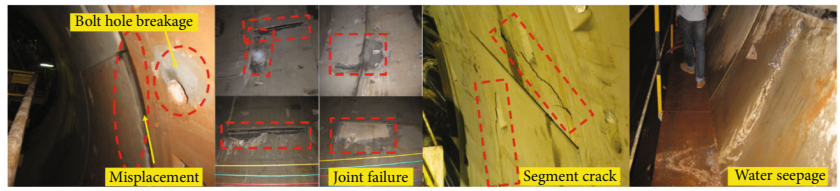

Figure 2: Segment damage during construction.

(a) Specimen preparation process (b) Mortar specimen

Figure 3: The test of water resistance of grout.

was the optimized grout ratio mentioned above. The test results showed that ratio 2 effectively reduced the grout bleeding rate and improved the compressive strength, but the fluidity was too small and the solidification time was too long, so it was still not fully suitable for grouting in water-rich layers. In this paper, ratio 2 would be further optimized to meet the requirements of grout properties.

High-efficiency water reducing agent is a polymer surfactant with strong activity, which can be adsorbed on the surface of cement particles, forming a strong electric field to disperse cement paste and improving grout workability and strength. Besides, water reducing agent has no air entraining effect on cement and can improve the fluidity of cement under the same water amount effectively. Based on grout ratio 2, polyhydroxy acid water reducing agent (PHWR-S) was added to further improve its material performance. The grout specimen is shown in Figure 4. The left specimen was added with water reducing agent, and the right one was not. The specimen without water reducing agent was dark and grey, with fine particles on it. The grout specimen was greyish with water reducing agent and was smoother and uniform.

Too little addition of water reducing agent cannot shorten the initial setting time and improve strength of grout effectively, while excessive addition would cause waste and larger bleeding rate. The reasonable content of water reducing agent is about 0.3%, according to multigroup comparison test (ratio 3 in Table 1). Onshore and underwater compressive strength tests of ratio 3 were carried out and compared the test results with ratio 2. It can be seen from Table 1 that the initial strength of ratio 3 in land was slightly smaller than that of ratio 2, but the later strength increased rapidly. The strength of ratio 3 in water was greater than that of ratio 2, but the water resistance was not effectively improved.

The above tests showed that the active role of water reducing agent would improve the fluidity and reduce the setting time of grout. However, due to the increase of free water in the grout, the bleeding rate of the grout was higher than that without the water reducing agent, which may affect the overall performance of the grout.

To reduce the setting time and the bleeding rate of grout, the content of bentonite is increased without changing ratio 3 in Table 1. Based on the comparison of the field test, the reasonable content value was about 2.9%. Setting the number of the grout ratio with 2.9% bentonite as fourth. Compared with ratio 2, after adding water reducing agent and bentonite, the bleeding rate of grout was reduced to a certain extent, the fluidity of grout was improved, and the setting time of grout was further shortened, due to the unique sliding effect and water absorption of bentonite. The compressive strength of land and underwater changed little in the early stage of ratio 4, compared with ratio 3. But the 28-day compressive strength increased significantly later, and the water resistance was also improved. This showed that the addition of bentonite makes the grout structure more reasonable.

Based on ratio 4, the measured grout void ratio e_0 was 0.98 through specific gravity tests. The compression test of grout with ratio 4 was carried out to detect the compressibility of grout. After different curing time, the compression test results in the pressure range of 100 kPa-200 kPa are shown in Figure 5.

Figure 5 shows that the compressive modulus of grout increased slowly in the early stage and increased rapidly in the later stage. After 42.4 hours of curing, the compressive modulus of the improved grout was 24.4 MPa, which was similar to that of the layer (24.1 MPa) around the tunnel in the west bank of the river. However, the grout compression

Table 1: The test results of the optimized grout ratio.

Ratio number	Bleeding rate	Degree of fluidity (cm)	Initial setting time (h)	Compressive strength (7 d)	Compressive strength (28 d)	Water-land strength ratio (7 d)	Water-land strength ratio (28 d)
1	10%	28.1	8.5	0.71	/	Small*	/
2	5%	23.5	9.5	0.79	1.38	0.49	0.37
3	10.1%	26.0	8	0.65	3.66	0.86	0.36
4	6.6%	24.5	7	0.67	4.56	0.76	0.40

Notes: * means it is less than the instrument range.

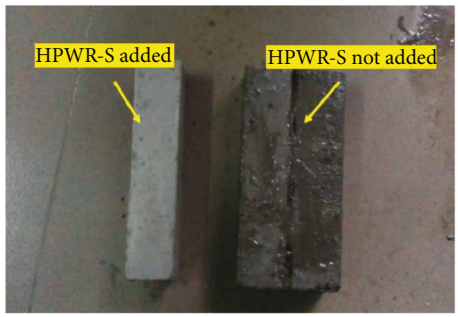

Figure 4: The specimen with or without water reducing agent.

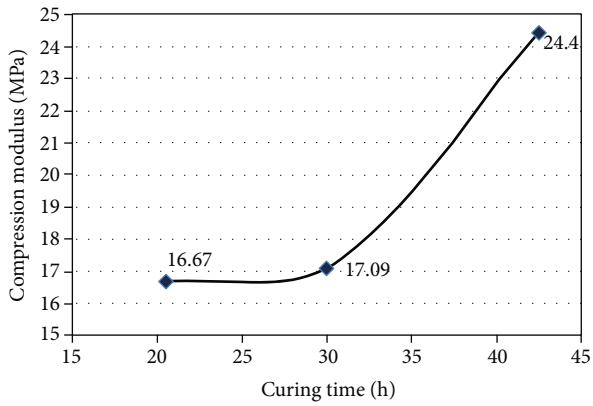

Figure 5: The change of the compressive modulus with the curing time.

modulus growth rate was slow. Therefore, when the shield crossed the stratum in the west bank, the tunnelling speed should be controlled as far as possible to ensure that no large settlement and deformation would occur.

4. Analysis of Grouting Pressure in Filling Stage

During shield tunnel construction, synchronous grouting can be divided into four stages including filling grouting, seepage grouting, compaction grouting, and fracture grouting. The filling grouting is at the stage of filling the gap of shield tail, which has the greatest impact on the segment floating. In the filling stage, grout filling along the circumferential direction and expansion along the longitudinal direction are considered to be two relatively independent processes. During synchronous grouting, it takes only a few dozen seconds for the grout to fill along the circumferential direction to the farthest distance after ejecting from the grouting hole [17]. Relative to the speed of shield tunnelling, grout has enough time to form a three-dimensional annular "grout cake" along the circumferential shield tail gap, as shown in Figure 6. The longitudinal thickness δ of annular cake is much smaller than its width b, and its thickness is equal to the advancing distance of shield in the filling time. In the process of filling grouting, it is assumed that the grout only flows circumferentially along the shield tail gap without considering its longitudinal diffusion along the longitudinal direction.

Taking the horizontal direction of the segment ring as the x-axis, the vertical direction as the y-axis, and the tunnel axis as the z-axis, the spatial rectangular coordinate system was established as shown in Figure 7. In the diagram, α represents the angle between the grout filling position and the y-axis, and R represents the outer radius of the segment. The grout flow in the range of grouting hole 1 was taken as the research object. When the grout was sprayed from the grouting hole and filled downward, a microelement of the grout was studied [18].

Equation (1) can be obtained according to the force equilibrium. Thus,

$$\begin{aligned} Pbdz - (P + dP)bdz + \rho g \sin\alpha \cdot b \cdot \left(\frac{R+b}{2}\right) d\alpha \cdot dz \\ + \tau b \left(\frac{R+b}{2}\right) d\alpha - (\tau + d\tau) b \left(\frac{R+b}{2}\right) d\alpha = 0, \end{aligned} \tag{1}$$

where P is the filling pressure of the grout, τ is the shear stress, and ρ is the density of the grout. Since $b << R$, it can be obtained that $R \approx (R+b)/2$. So, equation (1) can be simplified as follows:

$$d\tau = \frac{1}{R}\left(\rho g R \sin\alpha - \frac{dP}{d\alpha}\right) dz. \tag{2}$$

According to the boundary conditions, we can know that $\tau = 0$ when $z = 0$. The distribution formula of shear stress along the z-axis was obtained by integrating along the z -axis as follows:

$$\tau = \frac{z}{R}\left(\rho g R \sin\alpha - \frac{dP}{d\alpha}\right). \tag{3}$$

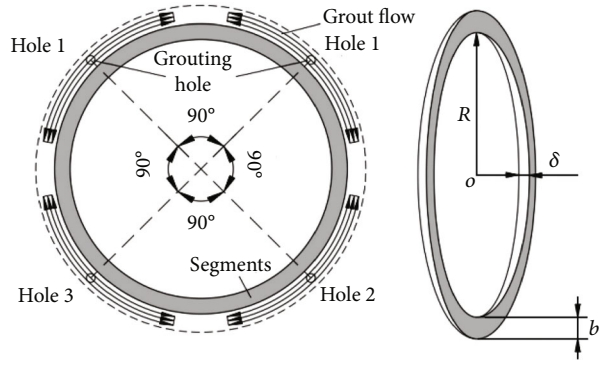

Figure 6: The grout filling the gap of shield tail along circumferential direction.

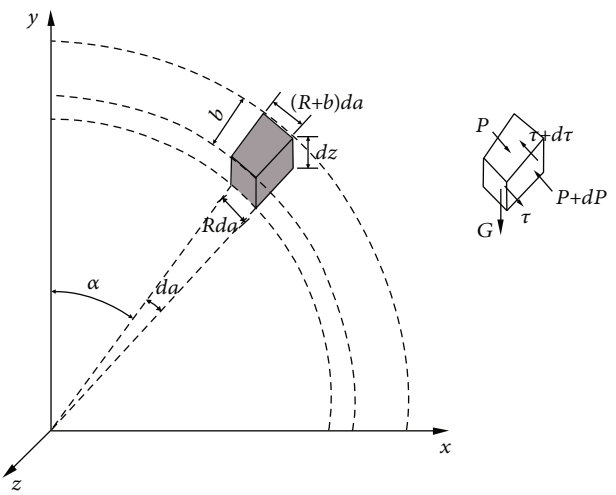

Figure 7: Model of grout filling and force analysis.

Let

$$\rho g R \sin\alpha - \frac{dP}{d\alpha} = B. \tag{4}$$

Then, equation (4) can be simplified to equation (5) as follows:

$$\tau = \frac{Bz}{R}. \tag{5}$$

Based on the test results by Ruan [19], it was assumed that cement grout is Bingham fluid in filling stage. The shear stress of the grout can be expressed:

$$\tau = \tau_0 + \mu\gamma = \tau_0 - \mu\frac{dv}{dz}, \tag{6}$$

where τ_0 is the shear stress of grout in static stage, μ is the grout viscosity coefficient, v is the flow speed of the grout, and γ is the shear rate. Substituting equation (5) into equation (6), equation (7) can be obtained:

$$dv = \frac{1}{\mu}\left(\tau_0 - \frac{Bz}{R}\right)dz. \tag{7}$$

Let $\tau_0 = Bz/R$, in equation (5), the flow core radius of the grout can be expressed as

$$r_p = \frac{\tau_0 R}{B}. \tag{8}$$

The speed distribution of classical Bingham fluid is shown in Figure 8. When $|z| \le r_p$, fluid moves forward smoothly without shear force. And when $r_p \le |z| \le \delta/2$, the whole fluid is in motion relative to the adjacent layer fluid due to shear force. According to the boundary conditions, we can know that when $z = \delta/2$, $v = 0$. By integrating equation (7) along the z-axis, the speed distribution of the grout in the range of $r_p \le |z| \le \delta/2$ was obtained as follows:

$$v = \frac{1}{\mu}\left[\frac{B}{2R}\left(\frac{\delta^2}{4} - z^2\right) - \tau_0\left(\frac{\delta}{2} - z\right)\right]. \tag{9}$$

By substituting z for r_p in equation (9), the flow speed of the grout in the range of $|z| \le r_p$ can be obtained:

$$v_p = \frac{1}{\mu}\left[\frac{B}{2R}\left(\frac{\delta^2}{4} - r_p^2\right) - \tau_0\left(\frac{\delta}{2} - r_p\right)\right]. \tag{10}$$

In summary, the speed distribution of the grout along the z-axis can be obtained:

$$v = \begin{cases} \dfrac{1}{\mu}\left[\dfrac{B}{2R}\left(\dfrac{\delta^2}{4} - r_p^2\right) - \tau_0\left(\dfrac{\delta}{2} - r_p\right)\right] & -r_p \le z \le r_p, \\ \dfrac{1}{\mu}\left[\dfrac{B}{2R}\left(\dfrac{\delta^2}{4} - z^2\right) - \tau_0\left(\dfrac{\delta}{2} - z\right)\right] & r_p < |z| \le \dfrac{\delta}{2}. \end{cases} \tag{11}$$

By integrating, the flow on the section was obtained:

$$q = b\int_{-\delta/2}^{\delta/2} v dz = \frac{b}{\mu}\left[\frac{2B}{3R}\left(\frac{\delta^3}{8} - r_p^3\right) - \tau_0\left(\frac{\delta^2}{4} - r_p^2\right)\right]. \tag{12}$$

By substituting equation (8) into equation (12), one-dimensional cubic equation about B can be obtained:

$$B^3 - \left(\frac{3R\tau_0}{\delta} + \frac{12R\mu q}{b\delta^3}\right)B^2 - \frac{4R^3\tau_0^3}{\delta^3} = 0. \tag{13}$$

B can be solved by equation (13). And combining equation (4), differential P can be expressed:

$$dP = (\rho g R \sin\alpha - B)d\alpha. \tag{14}$$

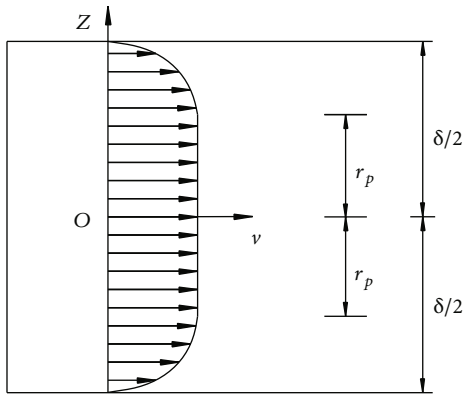

Figure 8: The speed distribution of Bingham fluid.

When $\alpha = \alpha 1$, $P = P_1$ (P_1 is the actual grouting pressure for grouting hole 1). By integrating equation (14), the pressure distribution of the grout filling downward from grouting hole 1 can be obtained:

$$P = P_1 + \rho g R(\cos\alpha_1 - \cos\alpha) + B(\alpha_1 - \alpha). \quad (15)$$

Similarly, the pressure distribution of the grout filling upward from grouting hole 1 can be obtained:

$$P = P_1 + \rho g R(\cos\alpha_1 - \cos\alpha) - B(\alpha_1 - \alpha). \quad (16)$$

Let $\rho g R = A$. According to the above derivation, the grout pressure distribution of the ith grouting hole during filling stage can be obtained:

$$P = P_i + A(\cos\alpha_i - \cos\alpha) \pm B(\alpha_1 - \alpha), \quad (17)$$

where " + " represents the grout fills downward and "–" represents the grout fills upward.

5. Engineering Verification and Analysis

5.1. Grouting Pressure Monitoring and Verification. According to the above analysis, the grouting pressure in the synchronous grouting filling stage has a great influence on the floating of the segment. Taking the typical stratigraphic section of an underwater tunnel in China as an example, the grout buoyancy of the segment was calculated. Due to the short duration of filling stage, the influence of time varying of grout viscosity was not considered. The synchronous grouting hole at the tail of shield was arranged at the positions of 45°, 135°, 225°, and 315° respectively. And the grouting pressure at the outlet of grouting pipe was controlled at about 0.2 MPa.

The typical section of underwater tunnel is located at the bottom of the river. The surrounding strata of the tunnel are silty clay and silty fine sand. The relevant calculation parameters of stratum are shown in Table 2.

In order to understand the force variation of segments and the influence of synchronous grouting pressure on segment floating, pressure cells were set up in the typical stratigraphic section to monitor the fluctuation of grouting pressure and other external loads during shield tunnelling.

The typical pressure variation of the segments with time measured by the pressure cells is shown in Figure 9. The axial pressure immediately increased after the segment was removed from the shield tail. And then, due to the suspension of the shield tunnelling (replacement of the partial cutting tools on the cutter), the grouting behind the segment stopped, and the measured axial pressure decreased to about 0 rapidly. After normal tunnelling restarted, the measured axial pressure returned to the previous level. It was also proved from the measured curve that, after the segment was removed from the shield tail, the surrounding rock will not immediately act on the segment due to the good self-stability. A relatively complete gap in the shield tail will be formed around the segment, and the grouting pressure is the most important external load acting on the segment.

5.2. Calculation of the Grout Pressure Distribution. The main calculation parameters are listed in Table 3.

5.2.1. Thickness of the Ring Cake of Grout (δ). It is assumed that the grout is in a circumferential flow state within the range of thickness δ. According to the grout filling time and the shield tunnelling speed, the thickness of the flow ring cake can be express as

$$\delta = v_s t_0, \quad (18)$$

where v_s is the tunnelling speed of the shield and t_0 is the time required for the grout to fill the shield tail gap completely. Grout filling can be completed in about tens of seconds. If the parameter t_0 is 50 seconds, then $\delta =$ 0.0175 m.

5.2.2. Sectional Flow (q). Four-hole synchronous grouting was adopted with the 0.2 MPa grouting pressure in each hole, and the injection rate is 150%. Assuming that the upward and downward filling flow from grouting hole is equal, the sectional flow q can be expressed as

$$\begin{aligned} q &= \frac{\pi\left[(R+b)^2 - R^2\right] v_s \lambda}{2n} \\ &= \frac{\pi\left[(5.65+0.165)^2 - 5.65^2\right] \times 0.00035 \times 150\%}{2 \times 4} \\ &= 3.9 \times 10^{-4}\ \mathrm{m^3/s}. \end{aligned} \quad (19)$$

5.2.3. The Pressure Distribution of the Grout (P). Substituting the relevant parameters into equation (17), the grouting pressure distribution along the outer wall of the segment in the filling stage can be obtained. Comparison between calculated and measured grouting pressure is shown in Figure 10. The theoretical calculation results were between 150 kPa and 180 kPa, which were in good agreement with the measured pressure on the vault, but the measured values on both sides of the arch waist and arch bottom were 50% larger than the calculated values. The pressure measured by the pressure cells was affected by the lateral earth pressure at the arch waist in addition to the grouting pressure. At the bottom

Table 2: Calculation parameters of surrounding strata.

(a) Silty clay

Unit weight γ_{mc}(kN/m^3)	Cohesion c (kPa)	Internal friction angle φ (°)	Hydraulic conductivity q_{mc} (m/d)	Poisson's ratio μ	Static lateral pressure coefficient K_{mc}	Foundation coefficient (MPa/m)	Elastic modulus (MPa)
18	31.7	9.6	0.05	0.3	0.43	20.2	5.17

(b) Silty fine sand

Unit weight γ_{mc}(kN/m^3)	Cohesion c (kPa)	Internal friction angle φ (°)	Hydraulic conductivity q_{mc} (m/d)	Poisson's ratio μ	Static lateral pressure coefficient K_{mc}	Foundation coefficient (MPa/m)	Elastic modulus (MPa)
19	/	24	8	0.31	0.45	13	8

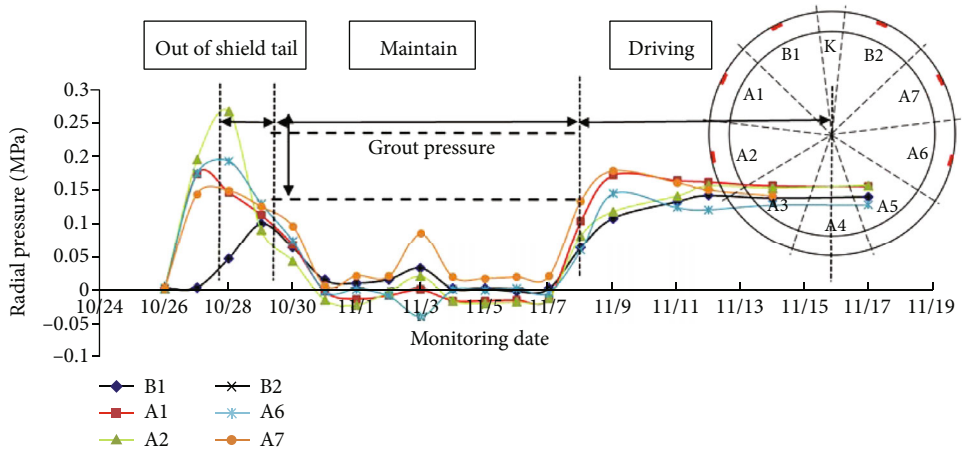

Figure 9: Measured axial pressure of the segment in typical section.

Table 3: The main calculation parameters of underwater tunnel.

Tunnelling speed (m/s)	Outer radius of segment (R/m)	Thickness of shield tail gap (m)	Grout density (kg/m^3)	Plastic viscosity (Pa · s)	Dynamic shear force (Pa)
0.00035	6.9	0.25	1900	2	15

of the arch, it was mainly affected by the foundation reaction and the grout buoyancy caused by the concentration of liquid grout at the bottom.

5.3. Analysis of the Influence Factors. According to the calculation equation, the distribution and size of grout pressure along the segment are mainly affected by the grout weight (parameter A) and grout shear stress (parameter B). The gravity and shear stress of grout slow down the filling speed of grout when the grout is sprayed from bottom to top. When the grout is sprayed from top to bottom, the shear stress still slows down the filling speed, while the grout weight accelerates the filling process.

Substituting equation (19) into equation (13), it can be obtained:

$$B^3 - \left(\frac{3R\tau_0}{\delta} + \frac{12\pi R^2 \mu v_s \lambda}{\delta^3 n}\right) B^2 - \frac{4R^3\tau_0^3}{\delta^3} = 0. \quad (20)$$

The shear pressure (parameter B) is positively correlated with grout viscosityμ, grout injection rate λ, section area of segment ring πR^2, and shield tunnelling speed v_s, while negatively correlated with the thickness of grout cake δ (cubic). Parameter δ has the greatest influence on the shear pressure of the grout. When the other parameters are constant, δ is taken between 1 cm and 3.5 cm at 0.25 cm intervals. The

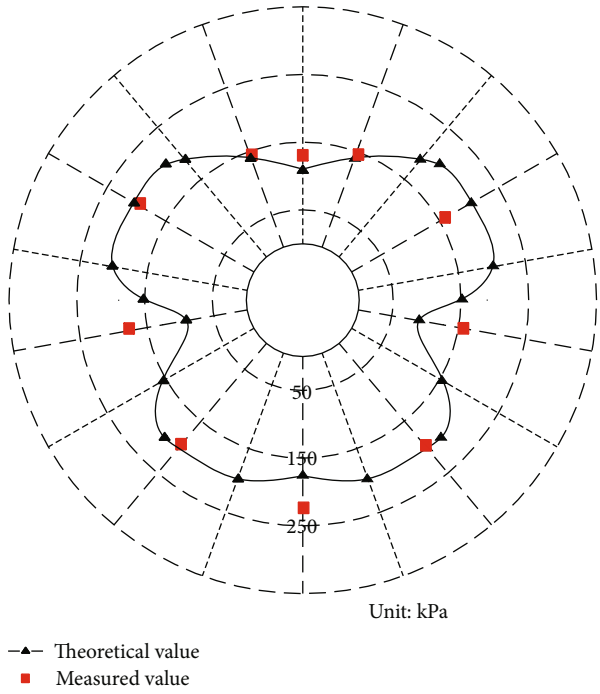

Figure 10: Comparison between calculated and measured values of filling grouting pressure.

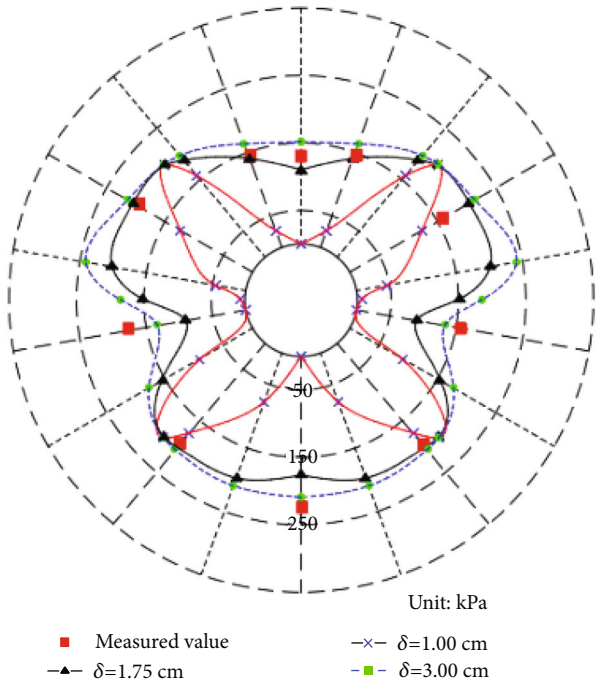

Figure 12: Grouting filling pressure curve of Bingham fluid in different δ.

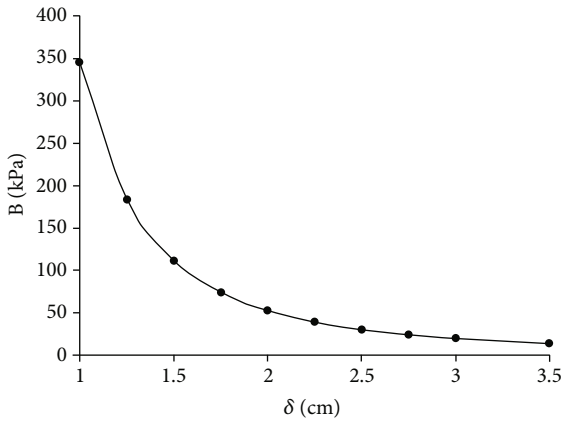

Figure 11: The relationship curve of parameter B with the change of δ.

relationship curve of parameter B with the change of δ is shown in Figure 11.

Parameters B increased sharply when δ was less than 2 cm, and when δ was larger than 3.5 cm, parameter B approached to 0. With the increase of the thickness of the grout annular cake, the grouting filling pressure c would decrease sharply. When δ was 1 cm, 1.75 cm, and 3 cm, respectively, the comparison between the calculated values and the measured values of grout filling pressure is shown in Figure 12.

Figure 12 shows that B was relatively large when δ was 1 cm. The shear resistance of grout was large, and the grouting pressure decays rapidly in the process of circumferential filling. When the grout was filled to the vault and waist of the tunnel, the grouting pressure gradually decreased to 0. The calculated values were quite different from the measured values, which was obviously not in line with the actual situation. When δ was 1.75 cm and 3 cm, the corresponding B was relatively small with little difference according to Figure 11. The shear resistance of the grout was small, and the grouting pressure was evenly distributed along the whole ring. The measured values were basically in the two grouting pressure envelopes. Combined with Figure 12, it can be considered that the value of parameter δ under this condition was 1.75~3 cm.

Learned from the previous construction experience, corresponding adjustments had been adopted when excavating to the underwater section. Firstly, the tunnelling parameters had been adjusted in time according to the conditions of surrounding rock, so as to minimize overexcavation. Then, in the area with large floating amount, the tunnelling speed had been reduced relatively, and the binary grout with shorter setting time had been used for second grouting to fill the gap at the shield tail. The optimized ratio of grout had been used to reduce the fluidity and setting time of grout and ensure the quality of synchronous grouting. The cumulative floating and subsidence of the segments were controlled within 21 mm as shown in Figure 13, which ensured the safety and stability for the later tunnelling process. The maximum buoyancy was 20.47 mm, due to the change of the ground conditions. Compared with Figure 1, both buoyancy and settlement shown in Figure 13 were effectively controlled, especially the amount of uplift is significantly reduced.

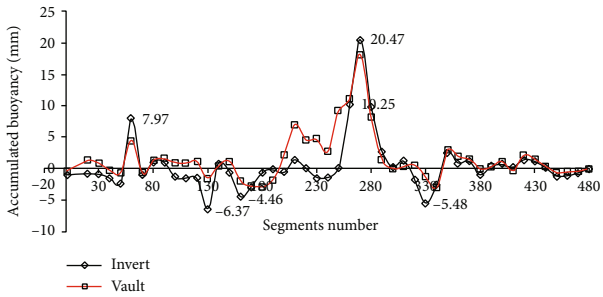

Figure 13: The deformation situation of underwater tunnel.

Compared with the floating situation of different segments in underwater tunnel, it is known that the synchronous grouting pressure is an important factor causing the floating of the segment, and it is also a key to control the floating of the segment. There are two conditions for segment floating: one is the space available for segment floating deformation, and the other is the force causing segment floating [20]. When the geological conditions change, the synchronous grouting parameters should be adjusted in time, the grout ratio should be optimized, and the synchronous grouting process should be optimized and controlled combining with secondary grouting and supplementary grouting.

6. Conclusion

In this paper, a test experiment was carried out to optimize the ratio of grout material. And then, the distribution law of grout along the outer wall of the segment in the filling stage was studied. The following conclusions can be drawn:

(1) In the test experiment of grout material ratio, 0.3% content of water reducing agent in grout could improve the ability of water resistance significantly. 2.9% content of bentonite could reduce bleeding rate of grout and grout setting time and improve the fluidity in the meantime

(2) The pressure distribution of grout along the outer wall was affected by gravity and grout shear stress. The gravity and shear stress of grout would slow down the filling speed of grout when the grout was sprayed from bottom to top. When the grout was sprayed from top to bottom, the shear stress still slowed down the falling speed of the grout, while the grout weight accelerated the filling process

(3) The typical stratigraphic section of underwater tunnel in China was taken as an example to verify the theoretical distribution law of the grouting pressure in the filling stage. The theoretical value was in good agreement with the measured one on the whole, but the errors of arch waist and arch bottom on both sides are relatively large. The errors were affected by the lateral earth pressure and foundation reaction

Data Availability

The data that support the finding of this study are available on request from the corresponding author. The data are not publicly available due to privacy or ethical restrictions.

Conflicts of Interest

The authors declare that they have no conflicts of interest.

Acknowledgments

This work was sponsored by Guangdong Basic and Applied Basic Research Foundation (No. 2020A1515011271) and Sustainable Development Project of Shenzhen Natural Science Foundation (No. KCXFZ20201221173207020). The authors are grateful to these institutions for their support.

References

[1] M. Q. Xiao, W. H. Sun, and X. Y. Han, "Research on upward moving of segments of shield segment," *Rock and Soil Mechanics*, vol. 30, no. 4, pp. 1041–1056, 2009.

[2] F. Zhang, Y. F. Gao, and Y. X. Wu, "Face stability analysis of large-diameter slurry shield-driven tunnels with linearly increasing undrained strength," *Tunnelling and Underground Space Technology*, vol. 78, pp. 178–187, 2018.

[3] Q. H. Qian and J. Chen, "Analysis of tunnelling risks of large-diameter shield and thoughts on its challenges," *Tunnel Constructions*, vol. 41, no. 2, pp. 157–164, 2021.

[4] A. M. Talmon and A. Bezuijen, "Calculation of longitudinal bending moment and shear force for shanghai Yangtze River Tunnel: application of lessons from Dutch research," *Tunnelling and Underground Space Technology*, vol. 35, no. 3, pp. 161–171, 2013.

[5] M. Theews and C. Budach, "Grouting of the annular gap in shield tunneling-an importance factor for minimization of settlements and production performance," in *Proceeding of World Tunnel Congress 2009*, Budapest, 2009.

[6] W.-C. Cheng, Z.-P. Song, W. Tian, and Z.-F. Wang, "Shield tunnel uplift and deformation characterisation: a case study from Zhengzhou metro," *Tunnelling and Underground Space Technology*, vol. 79, pp. 83–95, 2018.

[7] S. L. Shen, Y. J. Du, and C. Y. Luo, "Evaluation of the effect of rolling correction of double-o-tunnel shields via one-side loading," *Canadian Geotechnical Journal*, vol. 47, no. 10, pp. 1060–1070, 2010.

[8] X. Y. Zeng, Y. Liang, and K. Li, "Study on segment floating and its control measures during construction of large diameter cross river shield tunnel with shallow covering," *Railway Engineering*, vol. 57, no. 5, pp. 71–75, 2018.

[9] Y. Liang, J. Zhang, Z. S. Lai, Q. Y. Huang, and L. C. Huang, "Temporal and spatial distribution of the grout pressure and its effects on lining segments during synchronous grouting in shield tunnelling," *European Journal of Environmental and Civil Engineering*, vol. 24, no. 1, pp. 79–96, 2020.

[10] Z. Li, S. Zhou, H. Di, and P. Wang, "Evaluation and experimental study on the sealant behaviour of double gaskets for shield tunnel lining," *Tunnelling and Underground Space Technology*, vol. 75, pp. 81–89, 2018.

[11] S. Zhou, J. Xiao, H. Di, and Y. Zhu, "Differential settlement remediation for new shield metro tunnel in soft soils using corrective grouting method: case study," *Canadian Geotechnical Journal*, vol. 55, no. 12, pp. 1877–1887, 2018.

[12] A. M. Talmon and A. Bezuijen, "Simulating the consolidation of TBM grout at Noordplaspolder," *Space Technology*, vol. 24, no. 5, pp. 493–499, 2009.

[13] A. Bezuijen, A. M. Talmon, F. J. Kaalberg, and R. Plugge, "Field measurements of grout pressures during tunnelling of the Sophia Rail Tunnel," *Soils and Foundations*, vol. 44, no. 1, pp. 39–48, 2004.

[14] J. Liu, P. N. Li, L. Shi, J. Fan, X. Y. Kou, and D. Z. Huang, "Spatial distribution model of the filling and diffusion pressure of synchronous grouting in a quasi-rectangular shield and its experimental verification," *Underground Space*, vol. 6, no. 6, pp. 650–664, 2021.

[15] X. Xie, Q. Wang, I. Shahrour, J. Li, and B. Zhou, "A real-time interaction platform for settlement control during shield tunnelling construction," *Automation in Construction*, vol. 94, pp. 154–167, 2018.

[16] Z. Zhao, Y. G. Zhao, and P. P. Li, "Efficient approach for dynamic reliability analysis based on uniform design method and Box-Cox transformation," *Mechanical Systems and Signal Processing*, vol. 172, article 108967, 2022.

[17] Z. P. Fan, Y. W. Han, and Z. Q. Fang, "Calculation model of back filling grouting distribution for shield tunnel," *Journal of Highway and Transportation Research and Development*, vol. 28, no. 3, pp. 95–100, 2011.

[18] C. F. Gou, F. Ye, J. L. Zhang, and Y. P. Liu, "Ring distribution model of filling pressure for shield tunnels under synchronous grouting," *Chinese Journal of Geotechnical Engineering*, vol. 35, no. 3, pp. 590–598, 2013.

[19] W. J. Ruan, "Spread model of grouting in rock mass fissures based on time-varying behavior of viscosity of cement-based grouts," *Chinese Journal of Rock Mechanics and Engineering*, vol. 24, no. 15, pp. 2709–2714, 2005.

[20] W. R. Huang and W. B. Zhu, "To control the displacement of a shield tunnel during construction," *Modern Tunnelling Technology*, vol. 42, no. 1, pp. 71–76, 2005.

Hindawi
Geofluids
Volume 2022, Article ID 1410560, 10 pages
https://doi.org/10.1155/2022/1410560

Research Article

Impermeability Characteristics of Treated Marine Soft Soil with Ferronickel Slag Powder

Feng Chen[1,2] **and Shenghao Tong**[3]

[1]*College of Engineering, Fujian Jiangxia University, Fuzhou 350108, China*
[2]*Research and Development Center of Transport Industry of New Materials, Technologies Application for Highway Construction and Maintenance of Offshore Areas, Fuzhou 353404, China*
[3]*College of Civil Engineering, Fuzhou University, Fuzhou 350108, China*

Correspondence should be addressed to Feng Chen; cfxh@fzu.edu.cn

Received 12 December 2021; Revised 25 April 2022; Accepted 4 May 2022; Published 25 May 2022

Academic Editor: Xinyu Ye

In order to study the law of evolution of erosion time on the impermeability of soil-cement in the marine environment, permeability tests, X-ray diffraction (XRD) tests, and scanning electron microscopy (SEM) tests were conducted on ferronickel slag powder (FSP) soil-cement. The changes in the permeability properties of the soil-cement under different soaking age conditions were investigated. The results show that the marine environment has little influence on the impermeability of soil-cement at an early age, and that their permeability coefficient is essentially identical to that of clear water. The impermeability of soil-cement in the marine environment decreases significantly after 28 days, and it continues to decrease with age. However, the deterioration in impermeability of soil-cement caused by the marine environment can be alleviated after FSP is added to the soil-cement, and a better mixing value of 40% is obtained. At the same time, the regression curve equation of the permeability coefficient of soil-cement with the change of age is established. FSP exerts a microaggregate effect and chemical activity in the soil-cement. It not only improves the compactness of the soil-cement matrix but also prevents the penetration of corrosive ions into the soil-cement, thereby improving the impermeability of the soil-cement.

1. Introduction

Construction projects are being implemented worldwide for urban development, and coastal areas have been used for engineering construction [1, 2]. Marine clay, which usually exists in offshore areas, has a high level of uncertainty in its properties and is considered a problematic soil [3–5]. Pakir et al. [6] showed that marine clay exhibited weak physical and mechanical properties, making it unsuitable to even bear its self-weight. Thus, the mechanical properties of marine clay should be improved for the land demands. The soft soil can be stabilized by compaction [7], chemical [8, 9], electro-kinetically applications [10], bacteria [11], and hydrological processes. Research studies indicated that the soil-cement is the effective technique to strengthen marine clay given soil characteristics and site conditions [12, 13].

Soil-cement is a composite material composed primarily of soil, cement, and water. Cement-soil is widely applied to treating soft soil foundations for roads, airports, and ports [14, 15]. It plays an irreplaceable role in soil improvement in coastal areas. However, the soluble salt content of soft sea soil in coastal areas is high. It will corrode cement soil for a long time and even reduce the durability of cement soil [16]. For example, Shihata and Baghdadi [17] and Nan et al. [18] investigated the deterioration of cement strength in the marine environment. Xing et al. [19–21] studied the effect of the content of soluble salt ions on the strength of cement soil. The results show that the Cl^-, SO_4^{2-}, and Mg^{2+} soluble salt ions have distinct adverse effects on the strength of cement soil samples. The impermeability of soil-cement is an important indicator for evaluating the durability and useful service life. Therefore, research into the impermeability of soil-cement has attracted more and more attention.

Table 1: The main salt content of seawater.

Salt of seawater	NaCl	$MgCl_2$	$MgSO_4$	$CaSO_4$	K_2SO_4	$CaCO_3$	$MgBr_2$	Total
Content (‰)	27.21	3.81	1.66	1.26	0.86	0.12	0.08	35

Table 2: Chemical composition of common Portland cement (P.O 42.5).

Composition	CaO	SiO_2	Al_2O_3	Fe_2O_3	SO_3	MgO	f-CaO	Others	LOI
Portland cement (%)	62.55	21.69	4.38	3.34	2.89	2.05	0.57	0.84	1.59

Table 3: Chemical composition of compound admixture.

Composition	SiO_2	Al_2O_3	CaO	MgO	TiO_2	MnO	Fe_2O_3	SO_3	LOI
Ferronickel slag powder (%)	35.82	21.46	29.22	9.46	0.78	0.57	1.33	0.16	2.43
Granulated blast furnace slag powder (%)	32.00	16.81	36.12	10.59	0.93	0.9	2.29	0.14	0.16

Table 4: Permeability test of soil-cement.

No.	Cement mixing ratio (%)	Water binder ratio	Mixing ratio (%)	Environment
A-0	15	0.5	0	
A-1	15	0.5	10	
A-2	15	0.5	20	Fresh water
A-3	15	0.5	30	
A-4	15	0.5	40	
B-0	15	0.5	0	
B-1	15	0.5	10	
B-2	15	0.5	20	Seawater
B-3	15	0.5	30	
B-4	15	0.5	40	

Mixing ratio: the ratio of composite FSP to replace cement mass.

Goreham and Lake [22] examined the influence of water on the diffusion and porosity parameters of soil-cement materials. Wang et al. [23] studied the impermeability of soil-cement by adding fly ash, and the results showed that the optimal mass ratio of CMK to cement is between 1 : 6.5 and 1 : 4. Quang and Chai [24] researched the permeability (k) of lime- and cement-treated clayey soils. The results indicate that the k value decreases when the amount of cement or lime added is large enough that the cementation products formed during the pozzolanic reactions begin to fill the interaggregate pores. However, there are relatively few studies on the permeability of soil-cement eroded by seawater.

Soil-cement has good adaptability to complex environmental conditions of construction and sites [25]. The adverse effects of erosion on the soil-cement can be reduced or prevented by selecting appropriate cement types, mixing ratios, and admixtures. The addition of mineral admixtures is the most economical, effective, and environmentally friendly measure to improve the performance of soil-cement [26–28]. Lin et al. [29], Ali and Yousuf [30], and Karpisz and Jaworski [31] researched the influence of fly ash on the strength and stability of soil-cement. The use of fly ash as an admixture in stabilizing a soft marine clay resulted in stabilized samples with improved strength, more than 75 times that of the untreated clay. Rocha et al. [32] evaluated the compressive strength characteristics of soil-cement when rice husk ash (RHA) was used as a substitute for Portland cement, and the results indicated that RHA was feasible as a substitute for cement. Li et al. [33] added a certain amount of ultrafine silica powder to cement-stabilized soil to inhibit the expansion of cement-stabilized soil in seawater. Wang et al. [34] reported that China had discharged about 40 million tons of ferronickel waste residue every year. It accounts for about 20% of the total discharge of metallurgical waste slag. Meanwhile, the chemical activity of ferronickel slag was demonstrated by Chen and Tong [35] and Yang et al. [36]. It can be used as the raw material for slag cement.

Recycled materials are a matter of global concern in recent research on soil stabilization [37]. Ferronickel slag is a metal waste product produced by smelting steel or nickel. Generally, it is dumped as sand containing fine powder, which is nonbiodegradable. In this paper, FSP refers to the regenerated ferronickel slag powder obtained by grinding

Figure 1: Screening marine soft soil.

ferronickel slag into powder. Dredged marine soft soil is problematic soil because of its weak engineering performance. FSP is mixed into cement soil as a mineral admixture to strengthen the marine soft soil. Treating soft soil with this ferronickel waste would be an environmentally friendly, cost-effective, and green technology. Hence, FSP is used to improve the durability of cement reinforced marine soft soil. Permeability test and X-ray diffraction (XRD) test were conducted to evaluate the applicability of FSP for treating marine soft soil. The influence of erosion time on soil-cement permeability in the marine environment was investigated.

2. Materials and Methods

2.1. Test Materials. The marine soft soil used in the test is the sludge in a subway foundation pit in the coastal area of Fujian Province, with a pH of 6.82, moisture content of 58.5%, a void ratio of 1.53, and a plasticity index of 19.8. The cement used in the test is ordinary Portland cement (P.O. 42.5). Ferronickel slag powder (FSP) is produced by Fujian Yuanxin Group Co., Ltd. (Fujian Province, China). There is no harm in corrosive, leaching toxicity, and radioactivity. Because of the weak chemical activity of FSP [35], some granulated blast furnace slag powder with strong chemical activity is mixed into the FSP to form a mineral admixture. The mass ratio of FSP to ore powder is 2 : 1. The water used in the test is pure water extracted from running water after purification by water purification equipment. The seawater maintenance environment is simulated by manual configuration in the laboratory. The seawater environment is manually prepared following the *Salt Manufacturing Industry Manual* [35]. The salinity of seawater is 35‰, and the main saline content is shown in Table 1. The main performance indicators of cement, FSP, and slag used are listed in Tables 2 and 3 [38].

2.2. Test Plan. The mixing ratio of cementitious material in soil-cement was 15%, and the water binder ratio was 0.5. Three influencing factors were set up in the test: the mixing ratio of FSP, the immersion environment, and the curing age. The mixing ratios of the composite FSP in the soil-cement were 0%, 10%, 20%, 30%, and 40%, respectively.

Figure 2: Mixing the components.

Figure 3: The standard penetration mold.

Figure 4: Mixing the components.

The mix proportion is shown in Table 4. The methods and procedures used to prepare the samples for testing followed the *Chinese Standard JGJT 233-2011 Specification for mix proportion design of soil-cement: Part B5*. The untreated marine soft soil was first over dried and passed through a

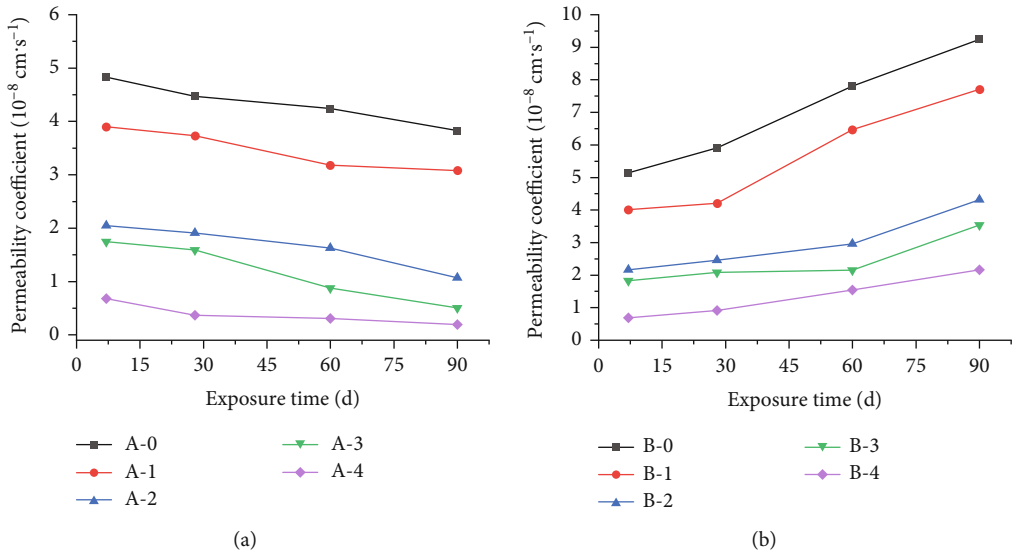

Figure 5: Permeability coefficient of soil-cement: (a) permeability coefficient of soil-cement in clear water; (b) permeability coefficient of soil-cement in marine environment.

2 mm mesh sieve (Figure 1). When preparing soil-cement laboratory samples, the sieved soil, FSP, and cement were first mixed for 3 min, and then, the mixture was poured into the water and thoroughly mixed for 5 min to achieve a homogeneous mixture (Figure 2). The standard penetration mold (Figure 3) was 30 mm high, and the upper mouth has an inner diameter of 70 mm and an inner diameter of 80 mm. The soil-cement slurry was placed in three equal layers inside the standard penetration mold. The vibration time of each layer of cement soil should not be less than 1 minute. The soil-cement slurry was trimmed and troweled to eliminate the extra soil-cement when the compaction process was completed. After 24 h, the prepared cement soil test block (Figure 4) was demoted and immersed in clear water and seawater. The samples were cured for 7 days, 28 days, 60 days, and 90 days.

The TJSS-25 infiltration device for soil-cement was adopted in the permeability test. In the first place, paraffin was used to seal the side wall of the cement soil. The methods and operation steps of the permeability test followed the Chinese Standard JGJT 233-2011 *Specification for mix proportion design of soil-cement*. A QUANTA 250 scanning electron microscope (SEM) and a Miniflex 300 X-ray diffractometer (XRD) were used to perform microscopic experiments on the soil-cement.

The permeability coefficient is calculated using Equation (1) and Equation (2), and the correction formula is as Equation (3).

$$k_T = \frac{V}{iAt}, \tag{1}$$

$$i = \frac{P}{100\gamma_w h}, \tag{2}$$

Where k_T is the permeability coefficient of soil-cement at T°C of water temperature (cm/s), accurate down to 0.01×10^{-n} cm/s; i is the hydraulic gradient, accurate down to 0.01; t is the interval time (s); V is the water seepage in time period t (ml); A is the cross-sectional area in the middle of the sample (cm^2); p is the osmotic pressure (MPa); and γ_w is the gravity of water, which is regarded as 0.0098 N/cm^3.

$$k_{20} = k_T \times \frac{\eta_T}{\eta_{20}}, \tag{3}$$

where k_{20} is the permeability coefficient of soil-cement at 20°C of standard water temperature (cm/s), accurate down to 0.01×10^{-n} cm/s; η_T is the dynamic viscosity coefficient of water at T°C of water temperature (kPa·s); and η_{20} is the dynamic viscosity coefficient of water at 20°C of water temperature (kPa·s).

3. Results

3.1. Analysis of Permeability Test Results. The permeability tests of different soil-cement samples were conducted at immersion time of 7 days, 28 days, 60 days, and 90 days. The relationship between permeability coefficient and immersion time is shown in Figure 5.

It can be seen from Figure 5 that the relationship curve between the permeability system and age of the soil-cement with five admixture amounts of FSP (0%, 10%, 20%, 30%, and 40%) in clear water showed a slow downward trend with a small range of change and an overall stable coefficient of permeability of the soil-cement of each mixture proportion. In contrast, the relationship curve between the permeability coefficient and the age of the soil-cement in the marine environment showed an increasing trend. The permeability coefficients of soil-cement in the two environments were substantially the same by the age of 7 days, and the growth rate of permeability coefficient in the marine environment before the age of 28 days is slow, while the

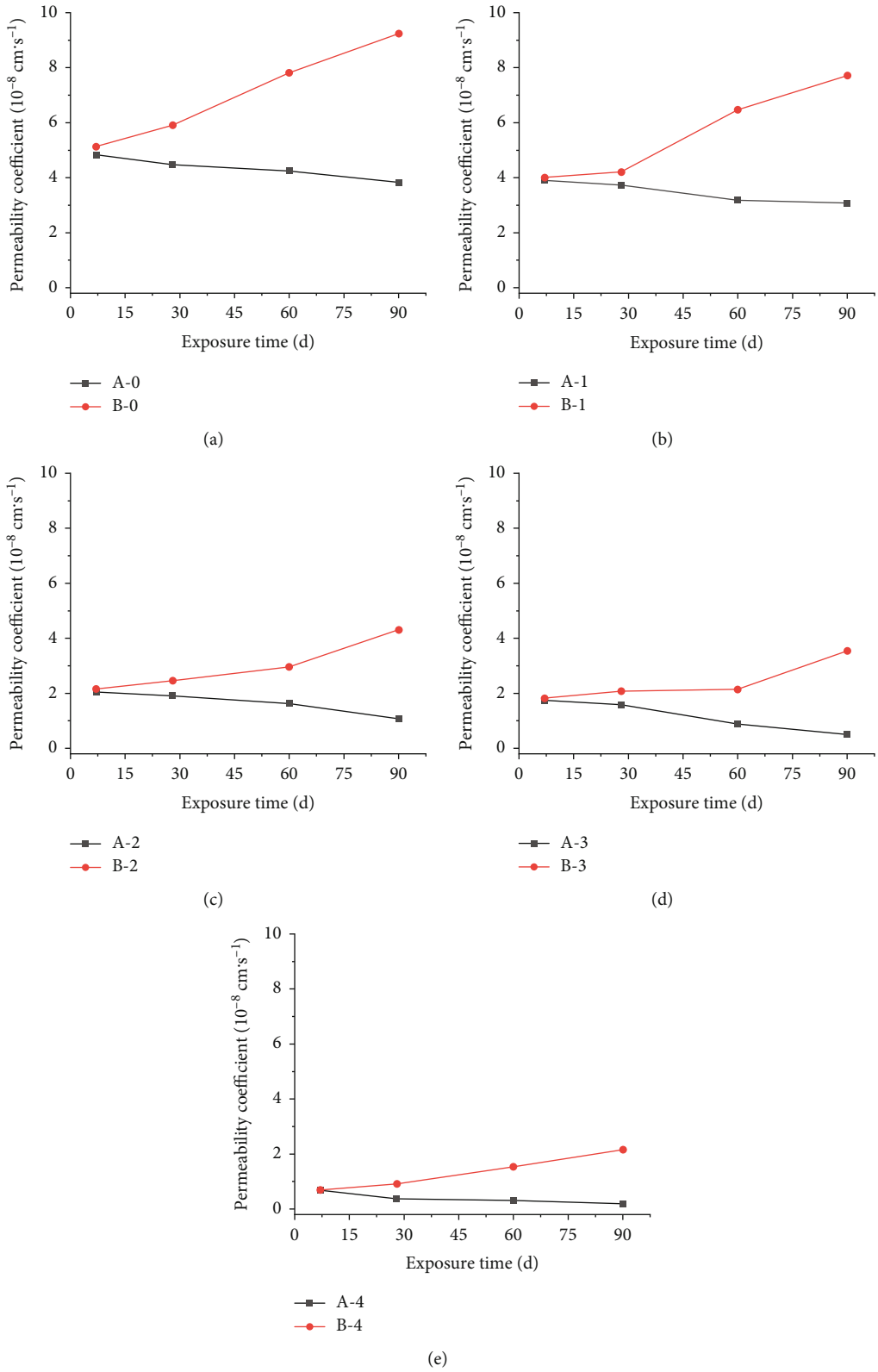

Figure 6: Comparison curve of soil-cement permeability coefficient and age: (a) admixture amount of ferronickel slag is 0%; (b) admixture amount of ferronickel slag is 10%; (c) admixture amount of ferronickel slag is 20%; (d) admixture amount of ferronickel slag is 30%; (e) admixture amount of ferronickel slag is 40%.

Table 5: Temperature and wildlife count in the three areas covered by the study.

Sample no.	Compound admixture addition	Regression curve equation	Determination coefficient
A-0	0%	$K = 0.000008725t^2 - 0.012t + 4.88$	$(R^2 = 0.979)$
A-1	10%	$K = 0.00007t^2 - 0.0176t + 4.066$	$(R^2 = 0.959)$
A-2	20%	$K = -0.000113t^2 - 0.00055t + 4.066$	$(R^2 = 0.996)$
A-3	30%	$K = -0.0000107t^2 - 0.0149t + 1.905$	$(R^2 = 0.977)$
A-4	40%	$K = 0.000074t^2 - 0.0124t + 0.730$	$(R^2 = 0.926)$
B-0	0%	$K = 0.00005t^2 + 0.046t + 4.74$	$(R^2 = 0.995)$
B-1	10%	$K = 0.0002t^2 + 0.033t + 3.58$	$(R^2 = 0.965)$
B-2	20%	$K = 0.0003t^2 - 0.004t + 2.23$	$(R^2 = 0.990)$
B-3	30%	$K = 0.0004t^2 - 0.017t + 2.03$	$(R^2 = 0.998)$
B-4	40%	$K = 0.00008t^2 - 0.011t + 0.59$	$(R^2 = 0.997)$

permeability coefficient of soil-cement increased greatly with the passage of time after 28 days of age. The results showed that if the age is less than 28 days, the marine environment has little influence on the permeability system of ferronickel slag containing soil-cement, while the negative effects of the marine environment on soil-cement increased greatly over time.

The comparison curves of permeability coefficient of soil-cement in clear water and seawater erosion environment are shown in Figure 6. According to the comparison chart in Figure 6, the curve of clear water shows an upward trend, while the one of marine environment shows a downward trend. As the immersion age progresses, the difference in permeability coefficient of the FSP containing soil-cement in the two environments becomes increasingly larger. Therefore, each group of comparison curve shows an opening shape that expands to the right, and the opening shape gradually decreases with the increase in the admixture amount. In other words, the opening shape is largest when the admixture amount of FSP is 0%, whereas the opening shape is smallest when the admixture amount of FSP is 40%. Under the designed immersion time, the permeability coefficients of the soil-cement with 40% admixture amount of FSP in seawater environment were 0.69×10^{-8} cm/s, 0.92×10^{-8} cm/s, 1.54×10^{-8} cm/s, and 2.16×10^{-8} cm/s, respectively. Compared with that in clear water, they increase by 0.01 times, 1.49 times, 3.97 times, and 10.37 times, respectively. The results show that the marine environment will deteriorate the impermeability of soil-cement, and the negative effect of this deterioration on the impermeability increases with the increase of the erosion time of seawater, while FSP can slow down the erosion of soil-cement by seawater.

In short, after analyzing the reasons, the chemical activity of FSP is weaker than that of cement [39]. The soil-cement mixed with FSP can play the role of filling voids better in the early stages and improve the workability of the soil-cement, as a result of which the soil-cement formed becomes denser [35]. Therefore, after FSP was added to the soil-cement, the permeability coefficient of the soil-cement would be decreased while the impermeability of the soil-cement would be improved. At the age of 7 days, the solidification effect of the soil-cement was strong, and the effect of improving performance was greater than the negative influence of the marine environment on the soil-cement. Therefore, by 7 days of age, the permeability coefficient of soil-cement was essentially the same in both environments. However, after 28 days of age, the hydration of the cement in the soil-cement slowed, while the erosion of soil-cement by the marine environment continued. At this time, the deterioration of the soil-cement by the marine environment was greater than the consolidation of the soil-cement itself. Therefore, after 28 days, the permeability coefficient of soil-cement in the marine environment increased, and even the increased amplitude became larger. Although the performance enhancing effect of soil-cement after 28 days of age was weaker than the deterioration of the soil-cement by the marine environment, the activity of FSP began to play a strong role, slowing the influence of the marine environment on the soil-cement. Therefore, the opening of the curve with the large admixture amount of FSP is significantly smaller than that with the small admixture amount of FSP.

3.2. Regression Model Analysis of Permeability Coefficient and Age. The permeability coefficient of cement soil is related to the content of cementitious materials and the age of maintenance. It showed a quadratic polynomial pattern variation with age [40]. Quadratic polynomial fitting analysis was used to figure out the permeability coefficient of the FSP in the soil-cement at different ages. In both clear water and marine situations, the permeability coefficient of an FSP-cement soil varies quadratically polynomially. The regression equation is shown in Table 5, where K is the permeability coefficient of the FSP containing soil-cement, t is the immersion age, and R^2 is the coefficient of determination. The regression curve is established according to the law of change of permeability coefficient and the age of the FSP containing soil-cement, as shown in Figure 7, respectively.

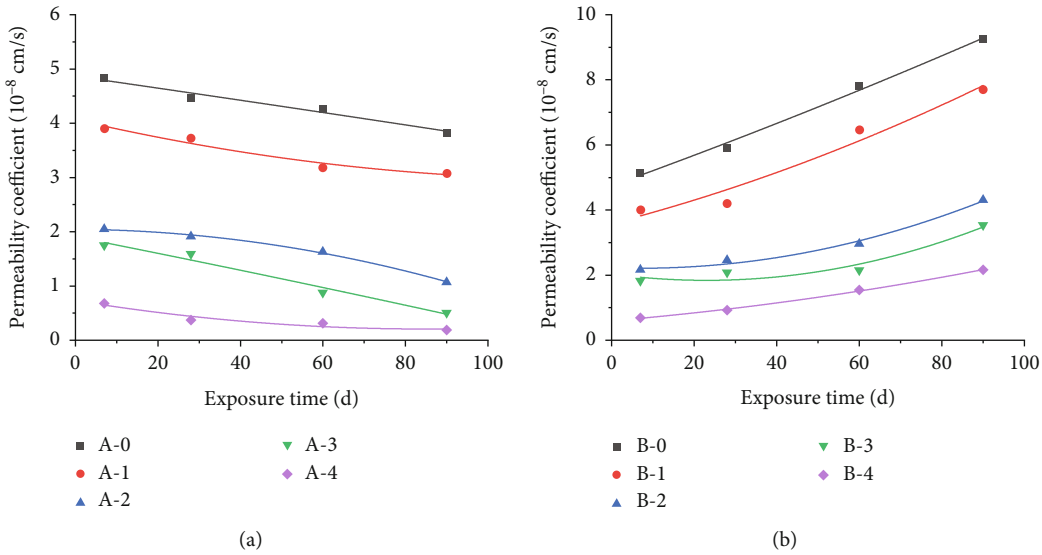

Figure 7: Regression curve of permeability coefficient with immersion age: (a) soil-cement soaked in clean water; (b) soil-cement soaked in seawater.

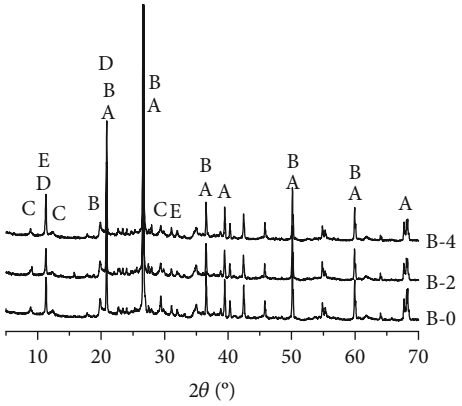

A: SiO_2
B: $CaAl_2Si_2O8{\cdot}4H_2O$
C: $Ca_6Al_2\ (SO_4)_3\ (OH)_{12}{\cdot}26H_2O$
D: $Ca\ (SO)_4{\cdot}2H_2O$
E: $3CaO{\cdot}Al_2O_3{\cdot}CaCl_2{\cdot}10H_2O$

Figure 8: XRD energy spectrum of soil-cement at 60 d.

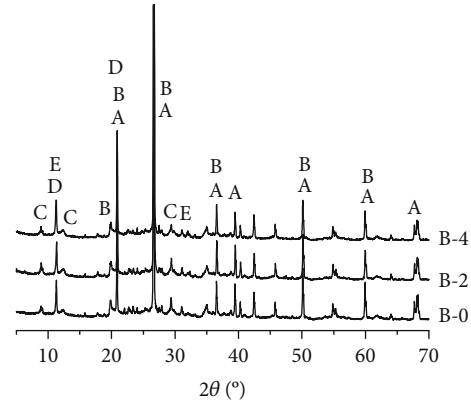

A: SiO_2
B: $CaAl_2Si_2O8{\cdot}4H_2O$
C: $Ca_6Al_2\ (SO_4)_3\ (OH)_{12}{\cdot}26H_2O$
D: $Ca\ (SO)_4{\cdot}2H_2O$
E: $3CaO{\cdot}Al_2O_3{\cdot}CaCl_2{\cdot}10H_2O$

Figure 9: XRD energy spectrum of soil-cement at 90 d.

From Figure 7 and the corresponding fitting formulas, it can be seen that the coefficient of determination R^2 of the fitting curve of the permeability coefficient of soil-cement changing with immersion age is not less than 0.95, indicating that the fitting curve is very similar to the law of change of the permeability coefficient of soil-cement in the paper. The curing effect of soil-cement is usually completed at the age of 90 days, so the development of impermeability of soil-cement usually needs 90 days to be stable. However, in the actual engineering construction, due to reasons such as the construction period and cost, the impermeability of soil-cement can not be tested until the soil-cement reaches the age of 90 days. If the functional relationship between the early permeability coefficient of the soil-cement and the permeability coefficient of 90 days can be established, and the early calculation of the permeability coefficient of 90 days can be achieved, it can provide references for the prediction of the impermeability of soil-cement.

3.3. Microstructure Characteristics of Soil-Cement. The FSP soil-cement is a complex multiphase system. In this paper, the main crystalline substances of the soil-cement were analyzed. The XRD pattern of the soil-cement is shown in Figures 8 and 9. The main crystalline substances of soil-cement with different admixture amounts of FSP are quartz (SiO_2), gismondine ($CaAl_2Si_2O_8{\cdot}4H_2O$), ettringite (AFt: $Ca_6Al_2\ (SO_4)_3\ (OH)_{12}{\cdot}26H_2O$), gypsum ($CaSO_4{\cdot}2H_2O$), and Friedel's salt ($3CaO{\cdot}Al_2O_3{\cdot}CaCl{\cdot}10H_2O$). The intensity

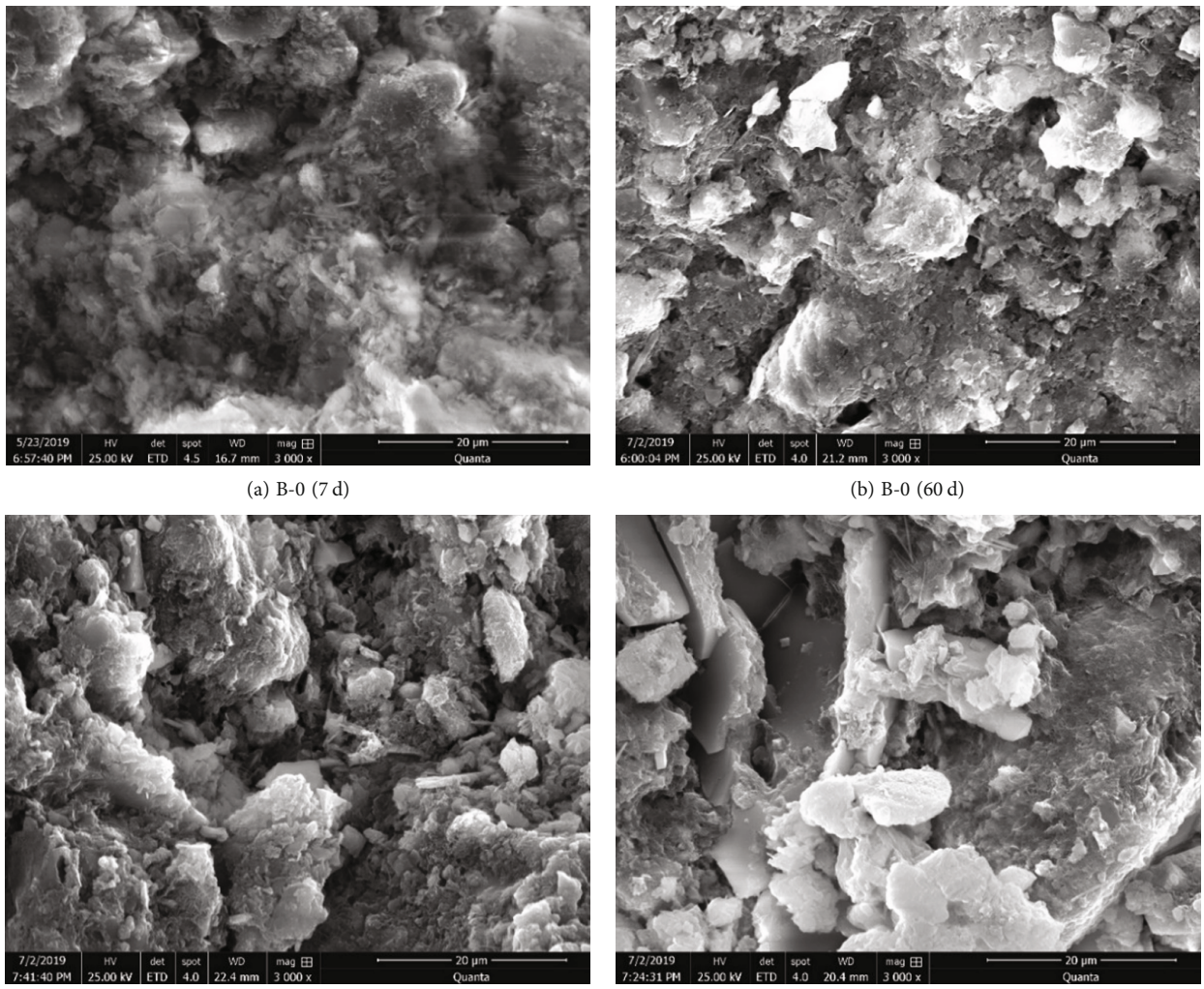

(a) B-0 (7 d)

(b) B-0 (60 d)

(c) B-4 (7 d)

(d) B-4 (60 d)

Figure 10: Microscopic morphology of soil-cement: (a) SEM image of B-0 at 7 days (×3000); (b) SEM image of B-0 at 60 days (×3000); (c) SEM image of B-4 at 7 days (×3000); (d) SEM image of B-4 at 60 days (×3000).

of the main diffraction peak of SiO_2 in soil-cement is very strong, so it is difficult to distinguish the difference in the diffraction peak intensity of each group. Orthorhombic scolecite and ettringite are mainly the hydration products of soil-cement, and their diffraction peak intensity increases with the passage of age.

The microstructures of the FSP soil-cement are depicted in Figure 10. The SEM images were analyzed by comparison with known crystal microstructures to discern the compositions. The soil-cement exhibits a loose microstructure, and the soft soil particles are bound by flocculating material. This flocculent is a calcium silicate hydrate (C-S-H) gel formed by the mixed hydrolysis and hydration reactions of cement and soft soil [21]. At 60 days, the cement soil's flocculation and clustered structures become more evident, while the pore structure becomes less pronounced. The flocculation and clustering phenomena are enhanced by the hydration reaction [41]. The flocculent colloid (C-S-H) is more abundant, but a trace of needle-like AFt, hexagonal prismatic CH crystals, and F salts is also visible. They result in a reduction in the number of soil-cement pores and an increase in density.

Portland cement in soil-cement contains a large number of mineral components, such as C_3S, C_2S, C_3A, and C_4AF. So, a hydration reaction will occur after cement contacts with water. At the same time, FSP contains a large number of potentially active vitreous substances, including SiO_2, Al_2O_3, and Fe_2O_3 [38]. With the passage of time, vitreous substances can give better play to the chemical activity effect and produce hydration products such as C-S-H, C-A-H, $CaO{\cdot}Fe_2O_3{\cdot}mH_2O$, Aft, and AFm, which is conducive to the improvement of impermeability of soil-cement. The erosion effect of the marine environment on soil-cement is mainly a series of physical and chemical reactions between Cl^-, SO_4^{2-}, and Mg^{2+} and mineral composition or hydrated products in soil-cement [35], which can produce expansive substances such as Friedel's salt, gypsum, Aft, and M-S-H gel. When there is an excessive amount of expansive substances, spalling and softening will occur in the soil-cement. When FSP is added to soil-cement, the binding

capacity of soil-cement to Cl^- can be improved. At the same time, the low activity of FSP can make the soil-cement structure denser, which can alleviate the erosion effect of corrosive ions.

4. Conclusions

In this paper, the permeability comparison test of the FSP containing soil-cement in clear water and the marine environment was conducted with the pressurized soil-cement infiltration device. The permeability characteristics of the soil-cement with different admixtures of FSP under the erosion of seawater were studied. The following conclusions can be drawn from this research:

(1) Prior to the age of 28 days, the difference in the permeability coefficients of cement soils in clear water and marine environments is minimal, and the values are nearly identical. After 28 days, the permeability coefficient of cement soils in a clear water environment decreased with age and remained relatively stable. In comparison, the permeability coefficient of cement soil in the marine environment tends to increase with age, and the permeability coefficient increases with age. The marine environment would then deteriorate the cement soil's permeability performance in the long run

(2) In both clear water and marine environments, the permeability coefficients of cement soils follow a quadratic polynomial pattern with age. By increasing the amount of nickel-iron slag powder admixture in the cement soil, the permeability coefficient gradually decreases, thereby improving its permeability resistance. By increasing the amount of nickel-iron slag powder in the cement soil, the seepage resistance of the soil-cement can be slowed down by the marine environment. The soil-cement containing 40% FSP has excellent impermeability

(3) From XRD and SEM test results, FSP has a microaggregate filling effect and can fill the pore structure of cement soil. With the hydration reaction of cement, FSP exerts a chemical activity effect and improves the quality of hydration products. FSP improves the compactness of the cement soil matrix and hinders the invasion of erosion ions, improving the impermeability and erosion resistance of cement soil

Data Availability

The data used to support the findings of this study are available from the corresponding author upon request.

Conflicts of Interest

The authors declare that they have no conflicts of interest regarding the publication of this paper.

Acknowledgments

This study was supported by the Research and Development Center of Transport Industry of New Materials, Technologies Application for Highway Construction and Maintenance of Offshore Areas (Fujian Communications Planning and Design Institute Co., Ltd.). This research was funded by the Natural Science Foundation of Fujian Province (grant number 2019J01883) and the National Natural Science Foundation of China Strait Joint Fund Project (grant number U1605242).

References

[1] L. Zhang, Z. Pan, B. Wang et al., "Experimental investigation on electro-osmotic treatment combined with vacuum preloading for marine clay," *Geotextiles and Geomembranes*, vol. 49, no. 6, pp. 1495–1505, 2021.

[2] A. V. S. A. Srujana, M. A. Hemanadh, K. A. Ravi Kumar, S. A. Preethi, and S. A. C. Manchikanti, "A study on the performance of marine clay stabilized with waste," in *Ground Improvement and Reinforced Soil Structures. Lecture Notes in Civil Engineering*, C. N. V. Satyanarayana Reddy, S. Saride, and A. M. Krishna, Eds., vol. 152, pp. 459–470, Springer, Singapore, 2022.

[3] M. A. M. Al-Bared and A. Marto, "A review on the geotechnical and engineering characteristics of marine clay and the modern methods of improvements," *Malaysian Journal of Fundamental and Applied Sciences*, vol. 13, no. 4, pp. 825–831, 2017.

[4] N. Zainuddin, N. Z. Mohd Yunus, M. A. M. Al-Bared, A. Marto, I. S. H. Harahap, and A. S. A. Rashid, "Measuring the engineering properties of marine clay treated with disposed granite waste," *Measurement*, vol. 131, pp. 50–60, 2019.

[5] M. Al-Bared, I. Harahap, A. Marto, H. Mohamad, and Z. Mustaffa, "Cyclic behavior of RT-cement treated marine clay subjected to low and high loading frequencies," *Geomechanics and Engineering*, vol. 21, no. 5, pp. 433–445, 2020.

[6] F. Pakir, A. Marto, N. Z. Mohd Yunus, S. A. Ahmad Tajudin, and C. S. Tan, "Effect of sodium silicate as liquid based stabilizer on shear strength of marine clay," *Jurnal Teknologi*, vol. 76, no. 2, pp. 45–50, 2015.

[7] P. Narloch, P. Woyciechowski, J. Kotowski, I. Gawriuczenkow, and E. Wójcik, "The effect of soil mineral composition on the compressive strength of cement stabilized rammed earth," *Materials*, vol. 13, no. 2, p. 324, 2020.

[8] A. L. Yong, K. Ahmad, S. Saleh, N. Z. Mohd Yunus, and K. N. Mat Said, "Improving the bearing capacity of marine clay using polyurethane columns," *IOP Conference Series: Earth and Environmental Science*, vol. 682, no. 1, article 12023, 2021.

[9] H. Kou, H. Jia, J. Chu, P. Zheng, and A. Liu, "Effect of polymer on strength and permeability of marine clay," *Marine Georesources & Geotechnology*, vol. 39, no. 2, pp. 234–240, 2021.

[10] Z. Tian, X. Tang, J. Li, Z. Xiu, and Z. Xue, "Improving settlement and reinforcement uniformity of marine clay in electro-osmotic consolidation using microbially induced carbonate precipitation," *Bulletin of Engineering Geology and the Environment*, vol. 80, no. 8, pp. 6457–6471, 2021.

[11] D. Kimand and K. Park, "An environmentally friendly soil improvement technology with microorganism," *International Journal of Railway*, vol. 6, no. 3, pp. 90–94, 2013.

[12] Q. Cheng, H. Xiao, Y. Liu, W. Wang, and L. Jia, "Primary yielding locus of cement-stabilized marine clay and its applications," *Marine Georesources & Geotechnology*, vol. 37, no. 4, pp. 488–505, 2019.

[13] D. G. A. Grubb, D. R. V. B. Berggren, J. C. C. Cullen, K. D. Barfoot, and M. E. Janes, "Waterfront Toronto: soil–cement mix designs in sands and peats for proposed brownfields redevelopment project," *Journal of Hazardous, Toxic, and Radioactive Waste*, vol. 25, no. 1, pp. 2153–5493, 2021.

[14] H. Liuand and W. Wu, "E3S Web of ConferencesAnalysis of the influence of different soil properties on the strength characteristics of cement soil," vol. 283, Article ID 01010, 2021.

[15] G. Zhang, C. Chen, K. Li et al., "Multi-objective optimisation design for GFRP tendon reinforced cemented soil," *Construction and Building Materials*, vol. 320, article 126297, 2022.

[16] H. Bayesteh, M. Sharifi, and A. Haghshenas, "Effect of stone powder on the rheological and mechanical performance of cement-stabilized marine clay/sand," *Construction and Building Materials*, vol. 262, article 120792, 2020.

[17] S. A. Shihata and Z. A. Baghdadi, "Long-term strength and durability of soil cement," *Journal of Materials in Civil Engineering*, vol. 13, no. 3, pp. 161–165, 2001.

[18] Y. Nan, Y. Junjie, L. Qiang, and D. Mengrong, "Laboratory test on strength deterioration process of soil cement in seawater environment," *Tumu Gongcheng Xuebao/China Civil Engineering Journal*, vol. 50, no. 11, pp. 115–124, 2017.

[19] X. Haofeng, X. Feng, Z. Feng, D. Wang, and J. Wiltshire, "Improvement for the strength of salt-rich soft soil reinforced by cement," *Marine Georesources & Geotechnology*, vol. 36, no. 1, pp. 38–42, 2018.

[20] F. Xiong, H. Xing, and H. Li, "Experimental study on the effects of multiple corrosive ion coexistence on soil-cement characteristics," *Soils and Foundations*, vol. 59, no. 2, pp. 398–406, 2019.

[21] H. Zhang, H. Xing, and H. Li, "Mechanical characteristic and microstructure of salt-rich cement soil," *Bulletin of Engineering Geology and the Environment*, vol. 81, no. 3, 2022.

[22] V. C. Goreham and C. B. Lake, "Influence of water on diffusion and porosity parameters of soil–cement materials," *Canadian Geotechnical Journal*, vol. 50, no. 4, pp. 351–358, 2013.

[23] L. Wang, X. Li, Y. Cheng, Y. Zhang, and X. Bai, "Effects of coal-bearing metakaolin on the compressive strength and permeability of cemented silty soil and mechanisms," *Construction and Building Materials*, vol. 186, pp. 174–181, 2018.

[24] N. D. Quang and J. C. Chai, "Permeability of lime- and cement-treated clayey soils," *Canadian Geotechnical Journal*, vol. 52, no. 9, pp. 1221–1227, 2015.

[25] S. Caro, J. P. Agudelo, B. Caicedo, L. F. Orozco, F. Patiño, and N. Rodado, "Advanced characterisation of cement-stabilised lateritic soils to be used as road materials," *The International Journal of Pavement Engineering*, vol. 20, no. 12, pp. 1425–1434, 2019.

[26] P. Sudla, J. Donrak, M. Hoy et al., "Laboratory investigation of cement-stabilized marginal lateritic soil by crushed slag–fly ash replacement for pavement applications," *Journal of Materials in Civil Engineering*, vol. 32, no. 2, article 4019353, 2019.

[27] T. Chu, J. Zheng, D. Chen, T. Nguyen, E. Elbashiry, and V. Tang, "Utilization of industrial waste in cement in a marine environment with a tropical climate," *Journal of Marine Science and Engineering*, vol. 7, no. 8, p. 245, 2019.

[28] P. Rai, W. Qiu, H. Pei et al., "Effect of fly ash and cement on the engineering characteristic of stabilized subgrade soil: an experimental study," *Geofluids*, vol. 2021, 11 pages, 2021.

[29] D. Lin, K. Lin, and H. Luo, "A comparison between sludge ash and fly ash on the improvement in soft soil," *Journal of the Air & Waste Management Association*, vol. 57, no. 1, pp. 59–64, 2007.

[30] D. H. A. Ali and M. S. Y. M. Yousuf, "Improvement of shear strength of sandy soil by cement grout with fly ash," *Journal of Engineering*, vol. 16, no. 22, pp. 16–34, 2016.

[31] I. Karpisz and K. Jaworski, "Study of compressive strength evolution in soil cement samples with fly-ash admixtures," *IOP Conference Series: Materials Science and Engineering*, vol. 365, no. 3, article 032049, 2018.

[32] J. H. A. Rocha, M. H. Rosas, N. G. C. Chileno, and G. S. C. Tapia, "Physical-mechanical assessment for soil-cement blocks including rice husk ash," *Case Studies in Construction Materials*, vol. 14, article e548, Article ID e00548, 2021.

[33] Q. Li, J. Chen, Q. Shi, and S. Zhao, "Macroscopic and microscopic mechanisms of cement-stabilized soft clay mixed with seawater by adding ultrafine silica fume," *Advances in Materials Science and Engineering*, vol. 2014, Article ID 810652, 12 pages, 2014.

[34] Q. A. Wang, M. A. Shi, Y. B. Zhou, and C. C. Yu, "Influence of ferro-nickel slag powder on the sulfate attack resistance of concrete," *Qinghua Daxue Xuebao/Journal of Tsinghua University*, vol. 57, no. 3, pp. 306–311, 2017.

[35] F. Chen and S. Tong, "Effect of ferronickel slag powder on strength of soil in marine environment," *Advances in Civil Engineering*, vol. 2020, Article ID 8856055, 10 pages, 2020.

[36] H. J. Yang, C. Lee, S. Shim, J. H. J. Kim, H. J. Lee, and J. W. Park, "Performance evaluation of cement paste incorporating ferro-nickel slag powder under elevated temperatures," *Case Studies in Construction Materials*, vol. 15, article e00727, 2021.

[37] M. A. M. Al-Bared and A. Marto, "Evaluating the compaction behaviour of soft marine clay stabilized with two sizes of recycled crushed tiles," in *GCEC 2017*, B. Pradhan, Ed., vol. 9 of Lecture Notes in Civil Engineering, pp. 1273–1284, Springer, Singapore, 2018.

[38] F. Chen and S. Tong, "Effect of ferronickel slag powder on strength of soil in marine environment," *Journal of Hydroelectric Engineering*, vol. 2020, no. 10, pp. 1–10, 2020.

[39] F. Chen, "Experimental research on the strength of cement soil with nickel iron slag powder," *Bulletin of the Chinese Ceramic Society*, vol. 37, no. 10, pp. 3113–3118, 2018.

[40] Y. Yang, *Experimental Study on Effects of Polluted Water Environment on Permeability of Cemented Soil*, Shenyang University of Technology, 2014.

[41] H. Xing, X. Yang, C. Xu, and G. Ye, "Strength characteristics and mechanisms of salt-rich soil-cement," *Engineering Geology*, vol. 103, no. 1-2, pp. 33–38, 2009.

Hindawi
Geofluids
Volume 2022, Article ID 9682371, 10 pages
https://doi.org/10.1155/2022/9682371

Research Article

Hydrochemical Characteristics and Genetic Analysis of Shallow High-Fluorine Groundwater in Fuyang River Basin

Zhiwei Zhai,[1] **Chuanda Zhang**,[1] **Tiansong Tang**,[2] **Chunyan Zhang**,[3] **Xing Bao**,[1] **Kunchao Li**,[1] **and Bo Han**[1]

[1]*Shanxi Institute of Energy, Taiyuan 030006, China*
[2]*Geological Survey Team No. 1, Hebei Bureau of Geology and Mineral Resources Exploration, Handan 056000, China*
[3]*Disaster Reduction and Disaster Preparedness Center of Jiangxi, Nanchang 330036, China*

Correspondence should be addressed to Zhiwei Zhai; zhaizw@sxie.edu.cn

Received 21 January 2022; Revised 2 April 2022; Accepted 19 April 2022; Published 16 May 2022

Academic Editor: Xueming Du

In order to understand the sustainable and effective utilization of groundwater resources in Fuyang River Basin, the chemical characteristics and genetic evolution process of characteristic shallow fluoride groundwater in the region were carried out. The results show that the chemical characteristics of groundwater are zonal in horizontal direction. From the piedmont plain to the central plain, the hydrochemical types of the first and second aquifers are mainly HCO_3-Ca-Mg-type water, HCO_3-Cl-Ca-Mg-type water, Cl-SO_4-Na-Ca-type water, and Cl-SO_4-Na-Mg-type water. The main mineral sources of hydrochemical ions are salt rock, carbonate rock, sulfate rock, and silicate rock. F^- has a significant positive correlation with HCO_3^- while it is negatively correlated with K^+. In the strong evaporation and alkaline environment created by climatic conditions in the study area, F^- mainly comes from the dissolution of minerals. Gypsum and fluorite are in a relatively stable dissolved state continuously providing F^- and Ca^{2+} for groundwater; the adsorption of cation was gradually strengthened from the piedmont plain to the central plain. The high HCO_3^- content is also conducive to F^- desorption in alkaline environments. The samples with F^- concentration greater than 1 mg·L^{-1} accounted for 35.7% and mainly distributed in the south of the study area. In summary, the chemical characteristics of shallow groundwater in Fuyang River Basin are affected by the combined effects including leaching effect, evaporation concentration, ion exchange-desorption, and human factors.

1. Introduction

As one of the essential trace elements in human bodies, fluoride can affect bone metabolism. Fluorine exists mostly in mineral form in nature, such as fluorite (CaF_2), cryolite ($Na_3[AlF_6]$), and fluorapatite ($Ca_{10}(PO_4)_6F_2$). If excessive fluoride is ingested through the digestive tract or respiratory tract for an extended period, it will be toxic to human bodies and endanger bone health, which is reflected in dental fluorosis and skeletal fluorosis. Endemic fluorosis is widely distributed and harmful. It has been found in all parts of China, involving a population of 100 million, seriously endangering the life and safety of people [1]. Due to the complex and changeable natural environment, meteorological climate, and hydrogeological conditions in northern China, the diversity of fluorine ion enrichment in regional groundwater is caused, and the coexistence of high-fluorine water of various causes is often formed in some areas. North China Plain is the lowest level of terrain ladder in China. It has experienced complex geological environment changes in its geological history, forming quite a complex stratigraphic structure and water flow field [2]. The main water resource problems in Fuyang River Basin include the increasingly serious water shortage and water pollution, the intensification of competition among water users, and the incompatibility of regional economic structure and water resource conditions. With the rapid decline of groundwater level and increasing of environmental problems, the basin has changed from open to closed [3, 4]. There are nearly 2,500,000 permanent residents in the study area, where endemic fluorosis has occurred [5]. However, the hydrogeological conditions in the study area are complex, the types and quantities of surface water

systems are various, and the corresponding chemical causes and influencing factors of groundwater are diverse, specific analysis of regional. In this study, the hydrochemical characteristics and genetic analysis of shallow high-fluorine risk groundwater in the study area are expounded through field geological survey and water sample analysis. The concentration of fluoride in groundwater is affected by many components like pH, precipitated ions and colloids, temperature, the anion exchange capacity of aquifer materials, solubility of fluorine-containing minerals, and the size besides sorts of the geological establishment that the water passes through, as well as the contact time for the water towards maintaining contact with the specific creation. Analyzing the characteristics of fluorine content in groundwater in this area, finding out the distribution regularity of high-fluorine groundwater, and revealing the hydrochemical factors affecting high-fluorine groundwater are helpful for controlling endemic diseases and understanding the hydrogeochemical origin and influencing factors of high-fluorine groundwater in the research area.

2. General Situation of Research Area

The Fuyang River is 413 km long and has a catchment area of 21737 km^2 (Figure 1). It originates in Hecun town and converges with the Hutuo River in Xian County. Fuyang River meanders with more than 20 tributaries joining on the left bank, which mostly are seasonal rivers. The Fuyang River Basin, located in dry subhumid areas, has a temperate monsoon climate [6].

On hydrogeological conditions, Fuyang River Basin belongs to the hydrogeological area of Hebei Plain, covering the Hutuo River alluvial-pluvial hydrogeological subarea and Fuyang River alluvial-lake hydrogeological subarea [7]. According to the formation age of strata, the Quaternary sedimentary strata are vertically divided into four water-bearing groups. The first water-bearing group of Holocene strata formed by fluvial alluvial deposits and marsh depressions. The second water-bearing group of Upper Pleistocene strata was dominated by fluvial alluvial deposits. The third water-bearing group of Middle Pleistocene strata was dominated by coarse sand in fluvial alluvial deposits. The fourth water-bearing group of Lower Pleistocene strata was dominated by fine sand in fluvial-lake facies [8].

According to the evolution of regional hydrogeological conditions and the current situation of local mining, we take 110~140 m as the boundary. The Quaternary aquifer rock group is divided into shallow aquifer rock group and deep aquifer rock group. The samples of this study were taken from the shallow aquifer rock group, equivalent to the first aquifer group and upper half of the second aquifer group.

3. Materials and Methods

The samples collected in this study are shallow groundwater samples with a total of 31 groups, which are collected in September 2019 and December 2020. The source is national, local, and factory monitoring wells. The depth of the wells ranges from 4.5 to 100 meters, and that of the filter pipe is from 1.85 to 90 meters. The samples were collected at a depth of 2.05-17.57 m. According to the requirements of the specification, the water sampling place of the centralized water supply source is selected for water sample collection, and then, the preservation agent is added and stored in cold storage at 4°C. Groundwater collection and preservation are carried out according to the requirements of "Standard Test Method for Drinking Water" (GB/T 5750-2006). Shallow geological profile of Fuyang River Basin is shown in Figure 2.

The pH value was measured according to the Hash water quality multiparameter tester HQ40, and the TDS was measured by dry weighing method. The most accurate way to estimate the mass of a solid sample quantitatively is done through weighing by difference. The specified technique entails weighing a weighing container holding an amount of solid reagent on a regular basis. The mass of the weighing bottle contents reduces as the solid is removed towards another vessel. Cl^-, SO_4^{2-}, NO_3^-, and F^- were determined by ICS-600 ion chromatograph; K^+, Na^+, Ca^{2+}, and Mg^{2+} were determined by ICP-OES; and HCO_3^- and CO_3^{2-} were determined by titration. After the test, the reliability analysis was carried out according to the "Standard Test Methods for Drinking Water Quality Analysis Quality Control (GBT 5750.3-2006)" standard issued by the Ministry of Health. The pretreatment of each batch of samples shall include travel blank, laboratory blank, quality control sample, parallel sample, and actual sample, which shall be carried out in the same batch according to the pretreatment method of samples. According to the requirements of laboratory quality control, the travel blank value shall be deducted from the analysis results, the laboratory blank value shall be lower than the detection limit of the instrument, the recovery rate of quality control samples shall meet the requirements of method recovery rate, and the difference between parallel samples shall be less than 30%.

MapGIS software was used to analyze spatial distribution characteristics. Excel 2007 and SPSS 25.0 were used for data collection and statistical analysis. SPSS statistics is the world's most widely utilized statistical programme for ad-hoc analysis and hypothesis testing, in addition to predictive analytics in business as well as research. Along with the trial, a person can download the traditional user interface after enrolling. A geographic information framework (GIS) is a computer-based framework that assists in the storage, dissemination of data, collection, production, and information as well as analysis by MapGIS software. Spatial distribution patterns might have an outwardly balanced, central place distribution mode; an outwardly unbalanced distribution mode; a multicore central place distribution mode; and otherwise, a corridor balanced else imbalanced distribution mode, depending on the natural circumstances of various regions. Mineral saturation index was calculated using PHREEQC software llnl.dat database to analyze the water-rock interaction of related minerals in groundwater and to determine the direction and intensity of dissolution-precipitation of gypsum, fluorite, and other minerals [9, 10]. Through the

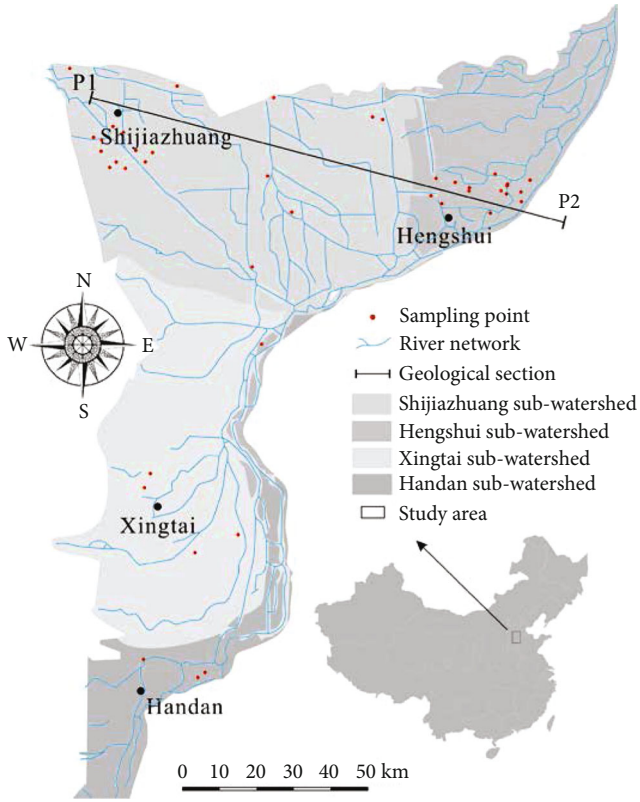

Figure 1: Distribution map of groundwater sampling points in Fuyang River Basin.

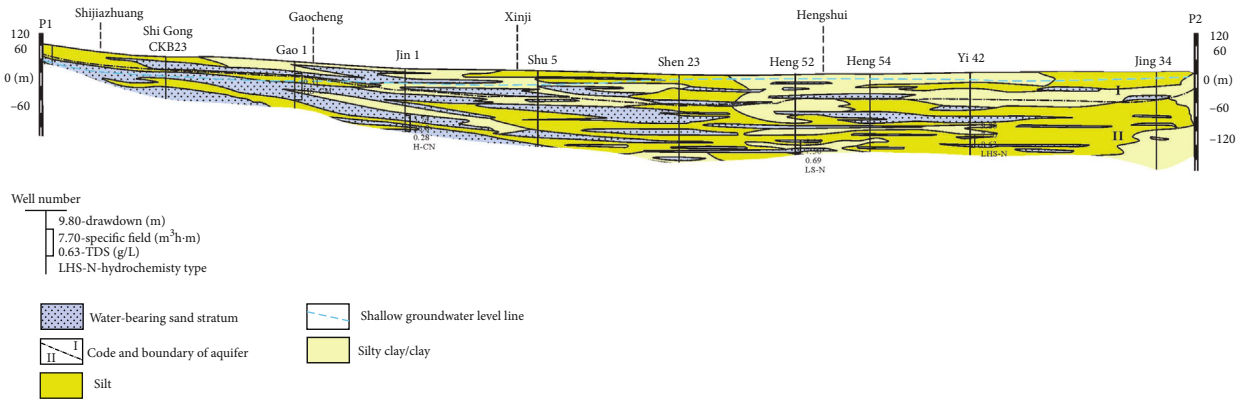

Figure 2: Shallow geological profile of Fuyang River Basin.

comparison of chemical activity (ionic activity product, IAP) of a dissolved mineral ion with its solubility product (Ksp), the saturation index (SI) is computed; then, the formula is SI = log (IAP/Ksp). The hydrochemical characteristics and related causes were analyzed and studied by Piper trilinear diagram, Gibbs diagram, and chlor-alkali index. A form of graph that is utilized to chart the chemistry of water samples is termed as Piper trilinear diagram. Origin generates a Piper diagram from spreadsheet information with the XYZXY column plot designations. The percentage value of every ion group is listed in every column. Piper plots are extremely useful in the disciplines of hydrogeology besides groundwater studies for displaying the relative concentration of common ions in water samples.

A popular tool for determining the connection betwixt water composition in addition to lithological features of aquifers is termed as Gibb's diagram. Evaporation dominance, rock-water interaction, and then precipitation dominance are 3 dissimilar disciplines. It is a useful tool for identifying the key natural geochemical processes that affect the hydrogeochemical properties of groundwater in an aquifer like the specified disciplines above. The word chlor-alkali refers to the 2 chemicals generated concurrently as an

Table 1: Main ion contents of shallow groundwater in Fuyang River Basin.

	Parameters	pH	TDS	SO_4^{2-}	Cl^-	HCO_3^-	CO_3^{2-}	NO_3^-	K^+	Na^+	Ca^{2+}	Mg^{2+}	F^-
All samples ($N = 42$)	Mean value	7.77	4908.92	1345.10	1700.79	429.13	3.32	2.00	9.84	1134.36	228.40	339.56	0.81
	Maximum value	9.59	17800.00	5532.84	6480.00	1167.78	43.31	19.67	54.14	4332.90	843.32	1570.99	3.14
	Minimum value	7.13	179.95	24.56	19.78	85.10	0.07	0.01	0.94	32.00	3.77	3.27	0.01
Samples $m(F^-) \geq 1\,mg{\cdot}L^{-1}$ ($N = 12$)	Mean value	7.54	4036.12	1033.04	1413.45	638.09	0.42	0.12	5.45	1094.69	146.34	259.55	1.93
	Maximum value	7.98	6700.00	2148.67	2720.00	1167.78	0.76	0.43	12.65	1844.26	287.38	450.99	3.14
	Minimum value	7.13	1838.64	324.91	358.90	272.69	0.07	0.01	1.10	475.00	10.43	102.00	1.10

Note: unit $mg{\cdot}L^{-1}$.

Table 2: Relationship between main ions in shallow groundwater in Fuyang River Basin.

	TDS	SO_4^{2-}	Cl^-	HCO_3^-	CO_3^{2-}	NO_3^{2-}	K^+	Na^+	Ca^{2+}	Mg^{2+}	F^-
TDS	1										
SO_4^{2-}	0.975**	1									
Cl^-	0.984**	0.937**	1								
HCO_3^-	0.096	0.061	0.026	1							
CO_3^{2-}	0.273	0.221	0.334*	0.048	1						
NO_3^-	-0.302	-0.284	-0.296	-0.281	-0.109	1					
K^+	0.096	0.094	0.108	-0.300	-0.017	-0.191	1				
Na^+	0.983**	0.954**	0.961**	0.143	0.181	-0.323*	0.045	1			
Ca^{2+}	0.929**	0.952**	0.894**	-0.019	0.166	-0.251	0.225	0.881**	1		
Mg^{2+}	0.992**	0.969**	0.975**	0.077	0.257	-0.264	0.082	0.979**	0.926**	1	
F^-	-0.274	-0.279	-0.271	0.52**	-0.16	-0.224	-0.357*	-0.199	-0.335*	-0.264	1

Note: **significant correlation in 0.01 level (double tail); *significant correlation at 0.05 level (double tail).

outcome of saltwater electrolysis (chlorine and an alkali). Chlorine besides sodium hydroxide (caustic soda) is the most frequent chlor-alkali compound, but potassium hydroxide besides muriatic acid is also possible.

4. Chemical Characteristics of Groundwater

The pH value of shallow groundwater in Fuyang River Basin was 7.17-9.59, with an average of 7.77, which was generally alkaline. The main cations in groundwater are Na^+, Mg^{2+}, and Ca^{2+}, and the main anions are Cl^-, SO_4^{2-}, and HCO_3^-. The content of soluble solids ranged from 179.95 to 17800 $mg{\cdot}L^{-1}$, with an average of 4908.92 $mg{\cdot}L^{-1}$. The F^- concentration was 0.01-3.14 $mg{\cdot}L^{-1}$, and the average was 0.81 $mg{\cdot}L^{-1}$ (Table 1). The concentration of F^- has a certain influence on the content of anions and cations in groundwater, reflecting a certain regularity. According to the toxicological requirements of groundwater quality standard (GB/T 14848-2017), fluoride content higher than 1 $mg{\cdot}L^{-1}$ is regarded as exceeding the standard and classified as Class IV and Class V water [1, 11, 12].

The chemical characteristics of groundwater in the Shijiazhuang-Hengshui section are zonal in the horizontal direction, and the distribution of high-fluorine samples from the piedmont plain to the central plain in the southeast of the basin. The content of Ca^{2+} and Mg^{2+} decreased obviously in this part of the samples, and the content of Ca^{2+} was 10.43-287.38 $mg{\cdot}L^{-1}$, the content of Mg^{2+} was 102-450.99 $mg{\cdot}L^{-1}$, the concentration of HCO_3^- increased to 272.69-1167.78 $mg{\cdot}L^{-1}$, and the values of TDS, Cl^-, and SO_4^{2-} decreased in varying degrees. The relationship between the source and content of groundwater ions in Fuyang River Basin is shown in Table 2; one must extract samples from said distract and use SPSS 25.0 to establish the correlation matrix between water chemical components. There was a significant positive correlation between TDS and Na^+, Mg^{2+}, Ca^{2+}, Cl^-, and SO_4^{2-}. The correlation coefficient showed a consistent trend, and the values were between 0.929 and 0.992, indicating that the above ions were the main sources of TDS in the study area, and the sources were highly consistent. There is a negative correlation between F- and the above main ions. In a large number of ions, the correlation coefficient with K^+ content is the largest, reaching -0.357 with a significant negative correlation. The difference shows there is a significant positive correlation between F^- and HCO_3^-; the correlation is 0.52. The

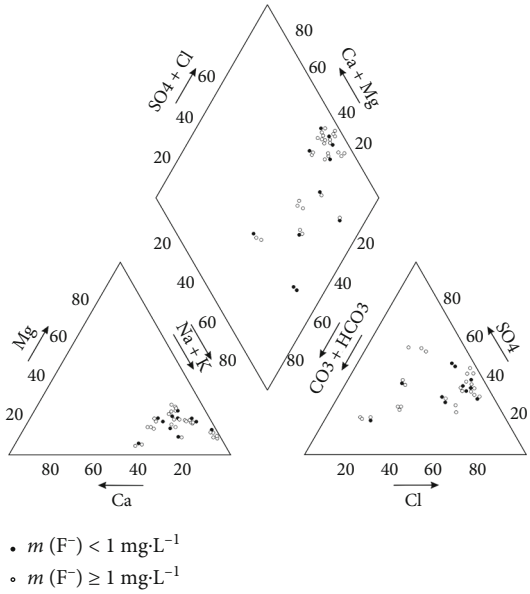

FIGURE 3: Piper diagram of shallow groundwater in Fuyang River Basin.

results showed that the high-fluorine water in Fuyang River Basin had the characteristics of high HCO_3^- and low K^+ in water chemistry.

Hydrochemical types of shallow groundwater in the study area are relatively complex. According to the Shukalev classification, the chemical characteristics of groundwater in the Shijiazhuang-Hengshui section are zonal in horizontal direction; from the piedmont plain to the central plain, the hydrochemical types of the first and second aquifers are mainly HCO_3-Cl-Ca-Mg-type water, Cl-SO_4-Na-Ca-type water, and Cl-SO_4-Na-Mg-type water (Figure 3). It can be seen from the Piper trilinear diagram that the anion distribution of the samples in the study area is relatively dispersed, and the cations are relatively concentrated. In addition, with the increase of F^- content, part of Ca^{2+} and Mg^{2+} in cations changes to Na^+, while anions gradually change from the combination of SO_4^{2-} and Cl^- to Cl^- and HCO_3^-, and the trend is obvious. The ion composition of groundwater mainly comes from carbonate rock such as salt rock, calcite and dolomite, gypsum, and silicate rock. A widely used mineral is termed as gypsum. It can be discovered in strata that developed millions of years ago beneath salt water. Calcium sulphate ($CaSO_4$) besides water (H_2O) makes up gypsum. Calcium sulphate dihydrate is its chemical name ($CaSO_4{\cdot}2H_2O$); because the capillary suction of the mentioned porous substance is responsible for slip dewatering, the gypsum mold is essential in slip casting. This phenomenon to some extent reflects the evolution characteristics of shallow high-fluoride water in the study area.

5. Analysis of Hydrochemical Causes

5.1. Filtration Effect. The soil and groundwater in the study area are alkaline-weakly alkaline under the influence of long hydrological geochemistry and supergene. Plants accumulate nitrogen and organic matter through respiration, while microorganisms transport carbon from organic matter such as animal, plant remains at the surface to deep groundwater systems, and large quantities of HCO_3^- and soluble mineral components are supplied to groundwater. The mineral saturation index can be used to judge the precipitation-dissolution dynamic process of the target minerals [9]. When the saturation index is negative, the mineral is in an unsaturated state in the water body, which is still in the phase of dissolution but not precipitation when the mineral saturation index is positive; the amount of substance in water solution has exceeded the solubility and is in the state of supersaturation. Fluorite is the main source mineral of F^-, which is usually formed in the vadose zone of pore water environment as secondary mineral [13]. This research uses the PHREEQC software llnl.dat database to calculate the saturation indices of calcite, dolomite, gypsum, and fluorite. A programme that simulates a wide range of reactions as well as processes in natural waters besides laboratory studies is termed as PHREEQC. It is a hydrogeochemistry simulation programme that can act out a wide range of geochemical situations. The results show that the saturation index of dolomite is positive, that of calcite is near 0 or slightly higher than 0, and that of fluorite and gypsum is negative, but the stone and the fluorite are still in dissolved state. The average saturation indices of dolomite and fluorite are 2.09 and -2.49, respectively, which indicates that the equilibrium of dissolution and precipitation is the main controlling factor of high-fluorine water chemical composition.

The saturation index of fluorite is negative in all groundwater samples, which indicates that the fluorite is in dissolved state. The dissolving process of fluorite is the reaction of Ca^{2+} with OH^-, and HCO_3^- in the environment forms $Ca(OH)_2$ precipitation with $CaCO_3$. It is also the main reason of enrichment of F^- in groundwater in the study area. From the correlation diagram of F^- content and mineral saturation index, it can be seen that with the increase of F^- content, the saturation indices of $CaCO_3$(calcite), $CaMg(CO_3)_2$(dolomite), and $CaSO_4$(gypsum) all decrease slightly, because SI_{CaCO3} and $SI_{CaMg(CO3)2}$ are larger than 0; the effect of Ca^{2+} provided by the dissolution of fluorite on the saturation index is not obvious. In contrast, the dissolution of $CaSO_4$ provides a large amount of Ca^{2+}, which weakens the dissolution and rate of fluorite to a certain extent, thus inhibiting the enrichment of F^- in groundwater. It can be seen from the correlation diagram between Ca^{2+} content and saturation index of minerals that the saturation index of the four minerals as a whole tends to increase with the increase of Ca^{2+} content, which indicates that excess Ca^{2+} promotes the precipitation of dolomite and calcite; it also inhibited the dissolution of fluorite. In Table 3, it can be seen that the Ca^{2+} concentration is significantly or very significantly correlated with SI_{CaSO4}, respectively, indicating that the Ca^{2+} in water mainly comes from the dissolution of gypsum and the formation of SO_4^{2-} changes the composition of anions in water chemistry. The dissolution of $CaSO_4$ inhibited the enrichment of F^-, so the concentration of SO_4^{2-} was lower in the groundwater with higher F^- concentration. In addition, HCO_3^- is positively correlated with F^-, and with the increase of F^-, the saturation index of

Table 3: Correlation between F^- and Ca^{2+} concentrations and SI.

	Calcite	Dolomite	Gypsum	Fluorite	Ca^{2+}	F^-
Calcite	1					
Dolomite	0.819**	1				
Gypsum	0.600**	0.35	1			
Fluorite	-0.12	-0.266	0.152	1		
Ca^{2+}	0.234	0.07	0.428*	0.166	1	
F^-	-0.232	-0.137	-0.039	0.687**	-0.067	1

Note: **significant correlation in 0.01 level (double tail); *significant correlation at 0.05 level (double tail).

dolomite and calcite decreases (Figures 4 and 5), especially calcite which becomes less and less saturated, indicating that calcite in higher F^- groundwater is still dissolving and producing HCO_3^-.

5.2. Evaporation Concentration. The study area belongs to the continental semiarid monsoon, with an average annual rainfall of 498.5 mm and evaporation of 1545.4 mm in the past 10 years [10]. The evaporation concentration is very strong. Considering the depth of the water table in the study area, the evaporation makes the shallow groundwater move up through the capillary pores of the soil layer, and all kinds of ions carried in the groundwater are trapped in the soil, and the soil alkalinity in the unsaturated zone increases accordingly. Since it shields other buffers from fast pH fluctuations, alkalinity is vital for fish as well as aquatic life. Acid rain besides other acid pollutants will be buffered through higher alkalinity levels in surface waters, preventing pH fluctuations that are detrimental towards aquatic life.

When it rained, the precipitation through the soil vadose zone vertical infiltration recharges to groundwater, water, and soil between the dissolution, hydration, hydrolysis, ion adsorption, and a series of physical and chemical reactions; the fluoride salts that had previously been deposited by evaporation in the soil, as well as the fluorine salts contained in the soil itself, are transferred to the groundwater through dissolution and leaching, resulting in an increase in the fluorine content of the groundwater; under the continuous action of "strong evaporation concentration-leaching-infiltration-strong evaporation concentration," the fluorine groundwater is finally enriched. Gibbs diagrams can be divided into three types: evaporative concentration type, rock-soil weathering type, and precipitation control type by the proportion of specific ions [4]. A phrase that refers to any circumstance in which salt-containing water evaporates off the surface, leaving the salts behind, causing the salts to build up towards a greater level than the concrete over time is said to be an evaporative conservation. The disintegration of rocks as well as minerals into soils is known as weathering. Sedimentary, igneous, and metamorphic rocks are the 3 primary types of rocks. The rock cycle depicts the formation of many types of rocks. Precipitation is any result of the buildup of air water fume that falls under gravitational draw from clouds in meteorology which is termed as precipitation control. Rain, ice particles, drizzle, sleet, slush, graupel, and hail are the primary types of precipitation. It happens at the time when the climate becomes soaked with water fume (arriving at 100% relative stickiness), so the water gathers then accelerates else falls. In this way, haze and fog are not precipitation but rather colloids, on the grounds that the water fume does not consolidate adequately to encourage.

In Figure 6, the samples are mainly distributed in the upper right corner, indicating that the evaporation and concentration of groundwater in the study area are strong, and a few substances (such as HCO_3^-) come from rock and soil weathering. From Figure 6(a), it can be seen that the distribution of the high F^- sample is near the right, which means that the Mg^{2+} equivalent concentration of Ca^{2+} in the high F^- sample is relatively low in the cations.

The distribution of the samples in Figure 6(b) is relatively dispersed. Some of the samples, together with the two high F^- points on the far right, are moved to the left of the image. This shows that the matter in the groundwater of the study area is affected by evaporation concentration; there is also a fair percentage of F^- that comes from the weathering of rock and soil.

5.3. Ion Alternating Adsorption. Ion exchange and adsorption are surface chemistry else surface complexing processes that result in the conversation of chemical substances betwixt the aqueous solution and the surface of minerals that appeared in geologically porous formations. Influenced by the change of environment and medium, the underground water exchanges with the top and bottom soil and rock mass all the time [14]. In this process, the main cations K^+, Na^+, Ca^{2+}, and Mg^{2+} and anion F^-, HCO_3^-, and OH^- exchange at the same time in the selective adsorption; this role is the ion exchange adsorption. It has been found that F^- can be replaced by OH^- when alkalinity is low, because the ionic radius of F^- and OH^- is very close [15]. The high-fluorine water in the study area has a low pH value between 7.17 and 8.25, which provides the conditions for the adsorption-desorption of anions. The cation exchange is mainly between Na^+/Ca^{2+} ions. The chlorine-alkali index (I_{CAI-1}, I_{CAI-2}) can directly reflect the direction and intensity of cation exchange in groundwater:

$$\begin{aligned} I_{CAI-1} &= (\gamma(Cl^-) - (\gamma(Na^+) - \gamma(K^+))) \cdot \gamma(Cl^-)^{-1}, \\ I_{CAI-2} &= (\gamma(Cl^-) - (\gamma(Na^+) - \gamma(K^+))) \cdot (\gamma(HCO_3^-) \\ &\quad + \gamma(SO_4^{2-}) + \gamma(CO_3^{2-}) + \gamma(NO_3^-))^{-1}. \end{aligned} \quad (1)$$

When the chlorine-alkali index (I_{CAI-1}, I_{CAI-2}) is negative, Ca^{2+} and Mg^{2+} exchange from groundwater to soil in the direction of K^+ and Na^+; when it is positive, Ca^{2+} and Mg^{2+} migrate from soil to groundwater, replacing K^+ and Na^+ ions in groundwater; the absolute value represents the strength of the ion exchange reaction [3].

As can be seen from Figure 7, when the content of F^- is low, the distribution of chlor-alkali index is relatively uniform near 0, and the direction of ion migration in groundwater and soil is not clear, but with the increase of the content of F^-, the chlor-alkali index decreases and the

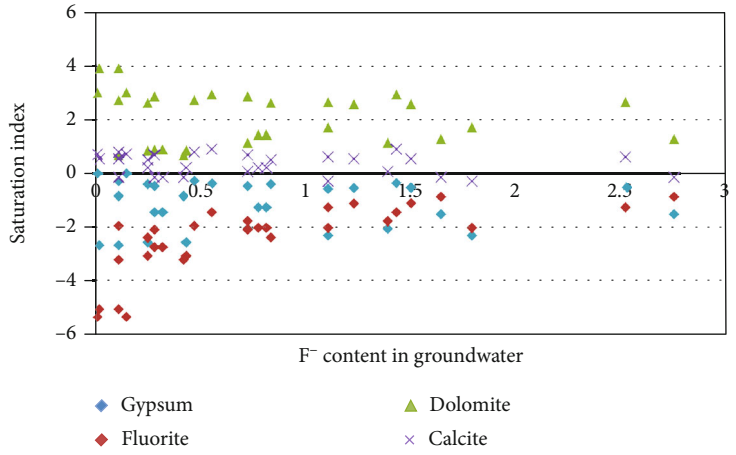

Figure 4: Relationship between SI and F^- content.

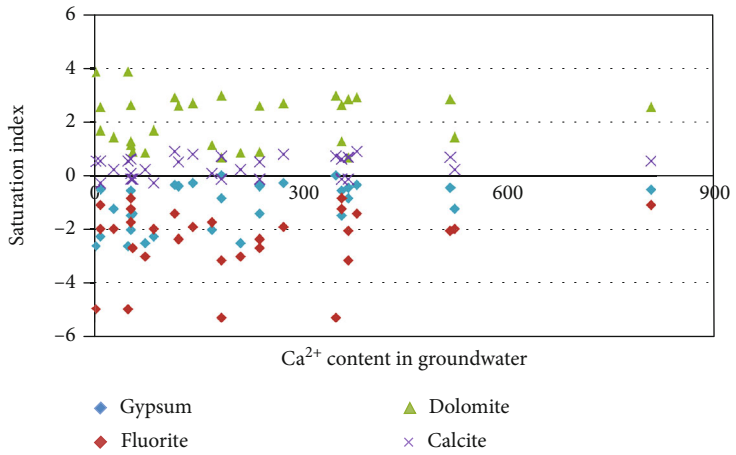

Figure 5: Relationship between SI and Ca^{2+} content.

absolute value increases; with the increase of ion exchange intensity, K^+ and Na^+ were gradually replaced from the soil into the solution, and Ca^{2+} and Mg^{2+} gradually left the water body in the form of precipitation [16].

In high-fluoride water, the average molar fraction of Na^+ in cations (76.48%) was significantly higher than that in other samples (70.54%). The correlation diagram of $\gamma(Na^+) - \gamma(Cl^-)$ and $\gamma(Ca^{2+}) + \gamma(Mg^{2+}) - (\gamma(HCO_3^-) + \gamma(SO_4^{2-}))$ can also be used to show cation exchange [17]. It is generally believed that the fitting line with a slope of -1 represents the most ideal negative correlation of $Na^+/(Ca^{2+} + Mg^{2+})$. As can be seen from Figure 8, the shallow groundwater samples in the study area are distributed near the fitting line with a slope of -0.446, and the $\gamma(Na^+) - \gamma(Cl^-)$ values of most samples are between -15 and 10, indicating that the cation alternation is not very strong on the whole; however, the distribution of high-fluorine water samples is relatively to the right of the image, and the slope of the fitting line is closer to -1, indicating that the enrichment of F^- is still dependent on the cation alternation. The results show that clay minerals are important sites and media for ion adsorption in groundwater due to their large negative charges and large specific surface area [18]. This characteristic is very suitable for the ionic adsorption of fluorine.

Because the ionic radius of F^- (0.133 nm) is very close to that of OH^- (0.137 nm) and the electric charge of OH^- (0.137 nm) is the same, the competition between F^- and OH^- is easily formed; as alkalinity increases, more F^- ions are released into groundwater [19, 20]. The adsorption capacity of HCO_3^- is the weakest among the three, and it cannot form direct alternating adsorption with F^-. However, after HCO_3^- enters the water body, it can be hydrolyzed to increase the alkalinity of the water body and finally create the alkalinity environment which is beneficial to the enrichment of F^-.

5.4. Human Factors. Through the hydrogeological investigation in the region, the surface Yellow River water is used for farmland irrigation in many places [21, 22]. In this process, because the water from the Yellow River has a high content of fluorine, the fluorine enters into the shallow groundwater through irrigation, which leads to the increase of the fluorine

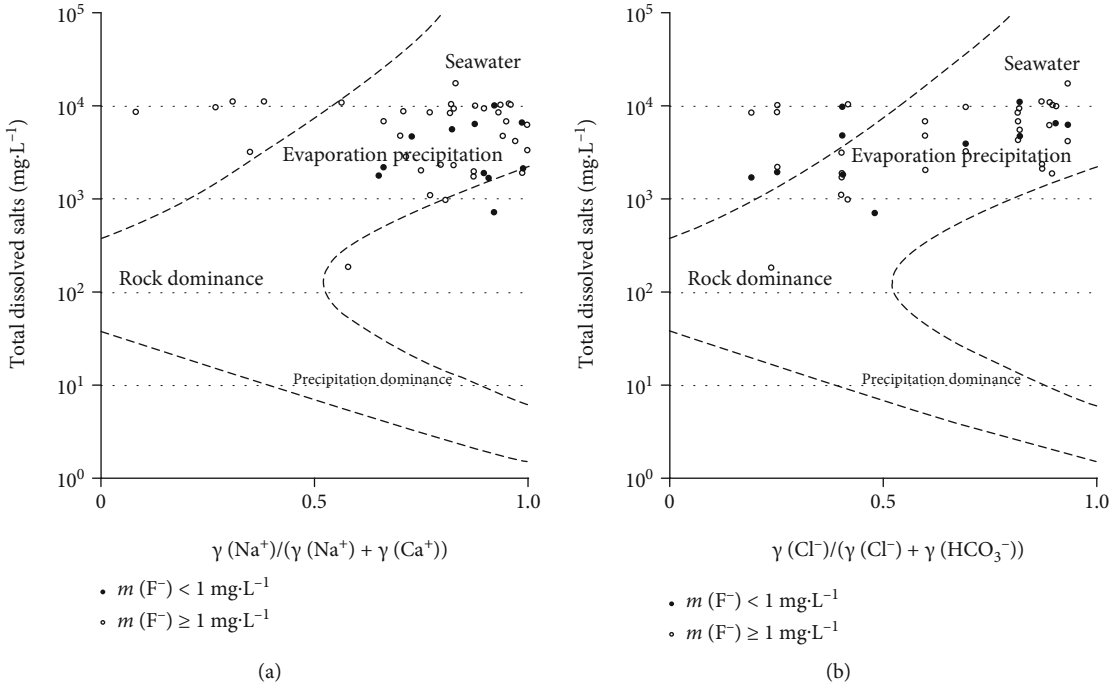

Figure 6: Gibbs diagram of shallow groundwater in Fuyang River Basin.

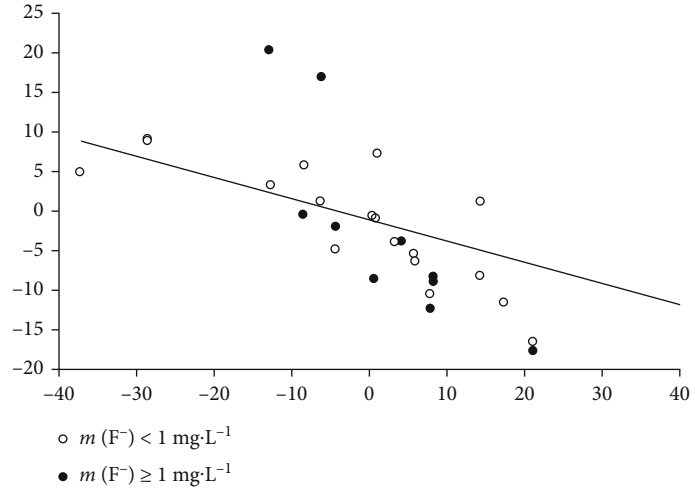

Figure 7: Relationship between chlor alkali index and F^- content.

ion content in the shallow groundwater [23]. At the same time, irrigation led to the accumulation of some fluoride ions in shallow soil; under the action of rainfall leaching, fluoride ions from the soil enter into shallow groundwater again, resulting in an increase in the content of fluorine in shallow groundwater; it can be said that the more frequent the exploitation of surface water for irrigation, the higher the content of fluorine in shallow groundwater will be. In addition, the study area belongs to the river alluvial plain [24]. Some studies show that the frequent human activities in this area result in a single plant community structure and often cannot form a perfect root group layer [25, 26]. At the same time, the reduction of vegetation coverage can weaken the interception and purification function of nutrients and mud and sand lost by surface slope flow in most areas, resulting in the infiltration of fluorine in the aeration zone into the phreatic layer with the leaching of soil water, resulting in the enrichment of fluorine.

6. Conclusion

The geological background is the material basis for the formation of all kinds of high-fluorine water. The strong adsorption of fluorine by soil containing most clay is the main source of F^-, and the alkalinity of circulating water is also the reason for the existence of F^-. The fluorine content

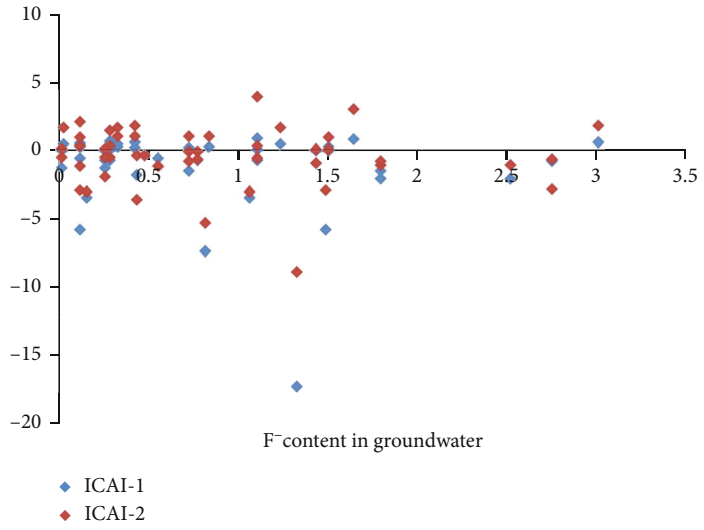

Figure 8: Relationship between $\gamma(Na^+) - \gamma(Cl^-)$ and $\gamma(Ca^{2+}) + \gamma(Mg^{2+}) - (\gamma(HCO_3^-) + \gamma(SO_4^{2-}))$.

in the distribution area of sodium water is high, but it is opposite in the distribution area of calcium water. The arid climate determines the wide distribution of high-fluorine water. The closed or semiclosed terrain, poor groundwater runoff conditions, high evapotranspiration rate, and low head conductivity of weathered area lead to the long retention time of water in the aquifer, which is also one of the reasons for the dissolution of fluorine-containing minerals and the increase of F^- content in groundwater. The main conclusions of this paper are as follows:

(1) The F^- concentration of shallow groundwater in Fuyang River Basin is 0.11-2.75 mg·L^{-1}, and the average is 0.80 mg·L^{-1}. The main ions in groundwater are Cl^-, SO_4^{2-}, HCO_3^-, Na^+, Ca^{2+}, and Mg^{2+}. The hydrochemical types are mainly Cl-SO_4-Na and HCO_3-Cl-Na; the reason lies in the change process of anions and cations from Ca^{2+}, Mg^{2+} to Na^+ and Cl^-, SO_4^{2-} to HCO_3^- in water

(2) The samples with F^- concentration greater than 1 mg·L^{-1} accounted for 35.7% and mainly distributed in the south of the study area. The distribution regularity of high-fluorine water in the shallow underground is poor, which is caused by the control of hydrochemical environment, climate, and human influence. In the groundwater with different concentrations of F^-, the composition ratio and change law of anion and cation are also different

(3) The soil and groundwater in the study area are alkaline; the regional climate and hydrochemical environment promote the dissolution of F^- from minerals or soil and enhance the concentration of F^- in water to a certain extent. An important condition for the formation of high-fluoride water is the coexistence of alkaline and high HCO_3^- with evaporation and condensation; the dissolution-precipitation equilibrium of fluorite, gypsum, calcite, and dolomite and the alternating adsorption of anions and cations are the main controlling factors for the formation and distribution of high-fluoride water

Data Availability

The data used and/or analyzed during the current study are available from the corresponding author on reasonable request.

Conflicts of Interest

The authors declare that they have no conflicts of interest.

Acknowledgments

The authors acknowledge the Major Science and Technology Projects of Shanxi Province (Grant: 20191102002); the Key R&D Plan of Jinzhong City, Shanxi Province (industry) (Grant: Y201026); and subproject of environmental geological survey and evaluation project of Hebei Bureau of Geology and Mineral Exploration and Development (Grant: 2200113).

References

[1] Y. Liu and W. H. Zhu, "Environmental characteristics of regional groundwater in relation to fluoride poisoning in North China," *Environmental Geology and Water Sciences*, vol. 18, no. 1, pp. 3–10, 1991.

[2] S. Di, C. Jia, S. Zhang, P. Ding, M. Shao, and A. Y. Zhang, "Regional characteristics and evolutionary trend prediction of land subsidence caused by groundwater over exploitation in North Shandong of the North China Plain," *Acta Geologica Sinica*, vol. 94, no. 5, pp. 1638–1654, 2020.

[3] L. N. Xing, H. M. Guo, L. Wei et al., "Evolution feature and gensis of fluoride groundwater in shallow aquifer from North

China," *Journal of Earth Science and Environment*, vol. 34, no. 4, pp. 57–67, 2012.

[4] J. Chen, "Holistic assessment of groundwater resources and regional environmental problems in the North China Plain," *Environmental Earth Sciences*, vol. 61, no. 5, pp. 1037–1047, 2010.

[5] H. Guo, W. Li, L. Wang et al., "Present situation and research prospects of the land subsidence driven by groundwater levels in the North China Plain," *Hydrogeology & Engineering Geology*, vol. 48, no. 3, pp. 162–171, 2021.

[6] Z. Xi, W. Guiling, M. Feng, Z. Wei, Z. Qinglian, and Z. Hanxiong, "Hydrogeochemistry of geothermal waters from Taihang Mountain-Xiong'an new area and its indicating significance," *Earth Science*, vol. 46, no. 7, pp. 2594–2608, 2020.

[7] D. G. Wen, F. C. Zhang, E. Y. Zhang, C. Wang, S. Han, and Y. Zheng, "Arsenic, fluoride and iodine in groundwater of China," *Journal of Geochemical Exploration*, vol. 135, pp. 1–21, 2013.

[8] Z. He, M. Zhang, Z. Ning et al., "The environmental evolution research of regional groundwater using molecular biotechnologies: a case from the shallow groundwater in front of the Taihang Mountains," *China Environmental Science*, vol. 39, no. 8, pp. 3484–3492, 2019.

[9] H. S. Zhang, W. T. Cai, C. Bian, and J. W. Liu, "Hydrochemical characteristics and genetic analysis of shallow high-flourine groundwater in Taocheng District, Hengshui City," *Science Technology and Engineering*, vol. 21, no. 24, pp. 93–100, 2021.

[10] J. P. Chen, H. T. Mao, and M. Y. Wang, "Distribution characteristics and development mechanism of fluorine in deep groundwater in Cangzhou area. China," *Earth and Environment*, vol. 43, no. 6, pp. 607–618, 2015.

[11] L. Li, J. L. Zhou, W. Q. Qi, F. Chen, Y. Y. Zeng, and Y. F. Chen, "Distribution and formation process of fluorine in groundwater in oasis area of Hotan River basin," *Journal of Arid Land Resources and Environment*, vol. 33, no. 1, pp. 112–118, 2019.

[12] H. Y. Liu, H. M. Guo, L. J. Yang et al., "Occurrence and formation of high fluoride groundwater in the Hengshui area of the North China Plain," *Environmental Earth Sciences*, vol. 74, no. 3, pp. 2329–2340, 2015.

[13] T. Berger, F. A. Mathurin, H. Drake, and M. E. Åström, "Fluoride abundance and controls in fresh groundwater in Quaternary deposits and bedrock fractures in an area with fluorine-rich granitoid rocks," *Science of the Total Environment*, vol. 569-570, pp. 948–960, 2016.

[14] J. X. Li, H. L. Zhou, K. Qian et al., "Fluoride and iodine enrichment in groundwater of North China Plain: evidences from speciation analysis and geochemical modeling," *Science of the Total Environment*, vol. 598, pp. 239–248, 2017.

[15] J. Lü, H. Qiu, H. Lin, Y. Yuan, Z. Chen, and R. Zhao, "Source apportionment of fluorine pollution in regional shallow groundwater at *You'xi* County southeast China," *Chemosphere*, vol. 158, pp. 50–55, 2016.

[16] Z. P. Dai, Y. L. Luo, and X. Wang, "Distribution characteristics of high arsenic and fluorine in groundwater of Kuitun River Basin in XinJiang," *Journal of Arid Land Resources and Environment*, vol. 45, no. 4, pp. 81–86, 2019.

[17] J. T. Liu, W. T. Cai, Y. T. Cao et al., "Hydrochemical characteristics of groundwater and the origin in alluvial-proluvial fan of Qinhe River," *Huan Jing ke Xue= Huanjing Kexue*, vol. 39, no. 12, pp. 5428–5439, 2018.

[18] C. Peng, J. T. He, L. Liao, and Z. G. Zhang, "Research on the influence degree of human activities on groundwater quality by the method of geochemistry: a case study from Liujiang Basin," *Earth Science Frontiers*, vol. 24, no. 1, pp. 321–331, 2017.

[19] R. Fuge, "Fluorine in the environment, a review of its sources and geochemistry," *Applied Geochemistry*, vol. 100, pp. 393–406, 2019.

[20] Y. Zhai, "Distribution, formation and human health risk of fluorine in groundwater in Songnen Plain, NE China," *Water*, vol. 13, no. 22, p. 3236, 2021.

[21] J. Liu, X. Wang, W. Xu et al., "Hydrogeochemistry of fluorine in groundwater in humid mountainous areas: a case study at Xingguo County, southern China," *Journal of Chemistry*, vol. 2021, Article ID 5567353, 11 pages, 2021.

[22] L. N. Xing, H. M. Guo, L. Wei et al., "Evolution feature and gensis of fluoride groundwater in shallow aquifer from Qin Wangchuan Basin," *Journal of Arid Land Resources and Environment*, vol. 34, no. 4, pp. 57–67, 2012.

[23] J. Huan, "Geochemical characteristics and environmental quality assessment of fluorine in soil and water environment of Jinbei," *IOP Conference Series Earth and Environmental Science*, vol. 514, no. 2, article 022021, 2020.

[24] L. Zhou, S. Zheng, D. Chen et al., "Hydrogeochemistry of fluoride in shallow groundwater of the abandoned Yellow River delta, China," *Hydrology Research*, vol. 52, no. 2, pp. 572–584, 2021.

[25] H. Su, W. Kang, Y. Li, and Z. Li, "Fluoride and nitrate contamination of groundwater in the Loess Plateau, China: sources and related human health risks," *Environmental Pollution*, vol. 286, article 117287, 2021.

[26] A. Ben Moussa, S. Chandoul, H. Mzali et al., "Hydrogeochemistry and evaluation of groundwater suitability for irrigation purpose in the Mornag region, northeastern Tunisia," *Environment, Development and Sustainability: A Multidisciplinary Approach to the Theory and Practice of Sustainable Development*, vol. 23, no. 2, pp. 2698–2718, 2021.

Hindawi
Geofluids
Volume 2022, Article ID 2332743, 12 pages
https://doi.org/10.1155/2022/2332743

Research Article

Mechanism of Filtration Behaviors of Cement-Based Grout in Saturated Sand under Different Grouting Conditions

Shanlin Xu, Hongtao Cao, Yanzhen Zhu, Honglei Sun, Jingling Lu, and Junqiang Shi

College of Civil Engineering, Zhejiang University of Technology, Hangzhou, Zhejiang 310023, China

Correspondence should be addressed to Honglei Sun; sunhonglei@zju.edu.cn

Received 21 January 2022; Accepted 31 March 2022; Published 5 May 2022

Academic Editor: Xueming Du

Cement-based grout has been widely used in various civil engineering applications. However, the filtration behaviors of it when grouting the porous geological masses vary a lot under different grouting conditions, which significantly influences its penetration and the enhancement effect. The purpose of this work was to better understand the filtration of cement-based grout in porous sand by conducting a series of visualized laboratory tests and EDTA titration tests. The experimental results show that the cement filtration, including the penetration, retention, and formation of cement filter cake above the grouting body, is collectively influenced by different grouting factors. With the increase of the soil samples' pore size and the cement slurry's water-cement ratio, the penetrated distance and amount of cement in sand increase. However, the penetration does not increase monotonically with the grouting pressure. Too excessive grouting pressure (e.g., 300 kPa in this study) accelerates the formation of cement filter cake and thus stops the subsequent cement infiltration. The mechanisms of different filtration behaviors were explained from microscopic particle clogging in the pore throat of the porous media. Furthermore, the reduced permeability of the sand column with the retained cement due to filtration was discussed, and the dewatering phenomenon of the cement slurry after filter cake formation was first revealed.

1. Introduction

Grouting is widely used in geotechnical applications, including sealing tunnels and underground excavations, reducing or stopping water inflow, and enhancing the fractured rock and soil [1–3]. At present, there are mainly two types of materials used for grouting reinforcement, e.g., cement-based grout and chemical grout. As the cement-based grout has a low environmental impact and affordable cost, it is extensively utilized in numerous civil engineering applications [4–7]. However, with the cement suspensions (cement slurry) seeping into the grouting body, the solid cement particles are retained by the pore throat of porous media at different locations (called filtration effect [8]). The void ratio of the porous grouting body decreases significantly due to the filtration, reducing the cement's infiltration (penetration) and influencing the enhancement effect. Thus, much experimental and analytical research has been conducted to investigate the filtration effect of cement and its deciding factors.

Herzig et al. [8] proposed that the filtration of the suspensions through porous media is related to various factors, namely, the carrier fluid (including flow rate, viscosity), the suspensions of particles (e.g., concentration, particle size), and the porous medium filter (porosity, pore size). Xu and Bezuijen [1] studied the bentonite slurry penetration in front of the slurry TBM. They proposed two stages of penetration: mud spurt and filter cake formation. Additionally, they indicated that the theoretically maximum penetration distance estimated by the well-known penetration distance function proposed by Krause [9] and Broere [10] is much greater than the measured value, as the filtration is not considered accurately. Yousif et al. [11] discussed the effect of pore levels on physical plugging and proposed the value of the reduced permeability after plugging is proportional to the square of D_{15} of the porous media and d_{85} of suspensions. Ma et al. [12, 13] studied the non-Darcy hydraulic properties, deformation behaviors, and failure patterns of rock in underground mining. Zhou et al. [14] studied the effect of

different grouting methods, i.e., constant flow rate and constant pressure, on the penetration of cement slurry and proposed that the excessive grouting rate or pressure is not conducive to the penetration. Additionally, the water-cement ratio (W/C ratio), defined as the weight ratio between water and cement in the cementitious mix, is a critical grouting factor that determines both the carrier fluid's viscosity and the solid particle concentration. Axelsson et al. [15] discussed the influence of the water-cement ratio (W/C = 1 ~ 3) on the sand's penetrability and proposed that the higher water-to-cement ratios result in a larger penetration area. Additionally, the water-cement ratio and the pore size of the porous media collectively determine the cement penetration.

Previous research has shown that the filtration behaviors of cement-based grouts differ considerably under different grouting conditions, which are influenced by the pore size of porous media, the water-cement ratio, and the grouting rate or pressure simultaneously. However, the mechanisms of different filtration behaviors remain unclear, and the coupled effects of these grouting conditions are not well understood. In addition, in previous studies about saturated sand column grouting, the water-cement ratio of the grouting materials was typically greater than 1. The study of the low W/C-ratio grout in saturated sand, which is a common grouting condition for the backfill grouting for shield tunnels, is rare. Therefore, the purpose of the present work is to better understand how the abovementioned grouting factors influence the filtration behaviors under low W/C ratio grouting conditions and discuss the filtration mechanisms from a microscopic view of particle clogging.

To predict the slurry penetration process in most numerical or analytical studies (Herzig et al. [8], Bouchelaghem and Vulliet [16], Saada et al. [17], Kim and Whittle [18], and Zhou et al. [19]), the variation of the grouting body's porosity and the permeability due to filtration is critical for both constructing the theoretical equations and determining the value of filtration-relevant coefficients. The measurement of the penetrated cement content is fundamental to understand the filtration and predict the grout penetration in porous media. However, for sand samples, the loose packing structure increases the difficulties and inaccuracy of the cement content's measurement at different depths. Recently, Li et al. [5] studied the dispersion of cement grout in sand through the Ethylenediaminetetraacetic Acid (EDTA) titration test. As this method could obtain the accurate cement content from loose sand samples, it was utilized in this work to study the distribution of the penetrated cement content in the soil after grouting.

By conducting a series of visualized laboratory tests and EDTA titration tests, the development of the cement's penetrated distance and content in the sand under different grouting conditions was systematically analyzed. The main aim of the paper is to investigate the following key questions:

(1) To evaluate the effect of the pore size of the soil column, water-cement ratio, and grouting pressure on cement filtration in saturated sand. And the turning points of different conditions were analyzed

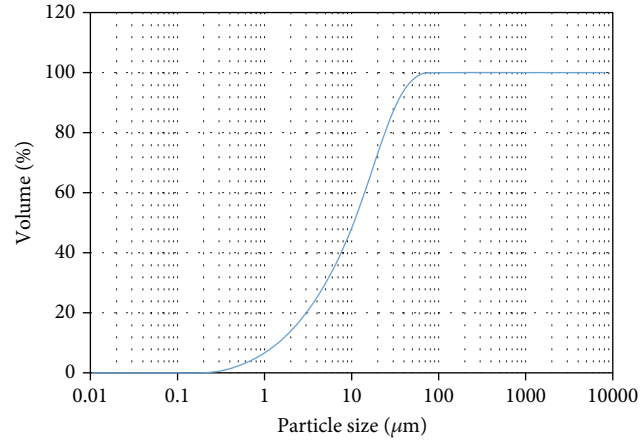

Figure 1: The particle size distribution of the P.O42.5 Portland cement.

(2) To calculate the contribution of cement content due to the filtration on the permeability coefficient of saturated sand column

(3) To explain the mechanism of the cement filtration in the grouting body and the formation of the cement filter cake above the grouting body

2. Materials and Methods

2.1. Materials. The grouting material used in this study is P.O42.5 Portland cement, and its grading curve is shown in Figure 1. The particle size distribution of the cement particles was obtained by the laser particle size analyzer; and ethanol was used as the dispersing solvent to avoid the hydration reaction of the cement slurry. The DV3T rotational rheometer was utilized to acquire the viscosity and access the rheological properties of slurries with different water-cement ratios (see Figure 2).

Three kinds of sand samples with different particle size ranges were utilized as the grouting body, named fine sand (0.1-0.5 mm), medium sand (0.25-1.2 mm), and coarse sand (0.5-5 mm), in the study. The grading curves of these three sand samples are shown in Figure 3. The parameters of these three sand samples are shown in Table 1.

2.2. Methods

2.2.1. Grouting Tests. A fully saturated sand column was grouted based on the self-developed transparent one-dimensional grouting device (see Figures 4 and 5). Before the grouting, the grouting barrel was filled with air, cement slurry, saturated sand, filter paper, and porous stone from top to bottom. In the grouting stage, the air compressor was connected to the upper vent of the grouting barrel to provide the constant grouting pressure. A pressure regulating valve was used for constant pressure control. The lower vent of the grouting barrel was connected to a bucket where the water with a free surface was stored. The water level in the bucket was always controlled at the same height as the saturated sand column to provide the conditions of pressure-

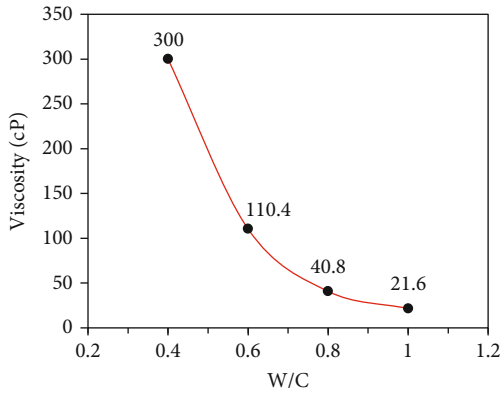

Figure 2: The viscosity of cement grout with different water-cement ratios.

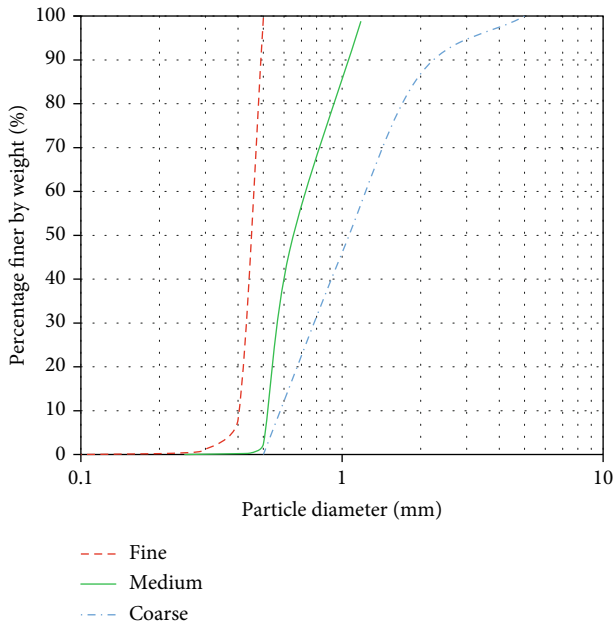

Figure 3: The grading curves of three sand samples.

limited drainage of the actual grouted soil. The grouting time under constant pressure is set as 3 min. We monitored and recorded the real-time penetration (or diffusion) of the cement slurry into the sand column during the grouting. After grouting, the cement-sand mixed specimens were sampled in layers (the thickness of all samples is 1 cm, and a total of 10 were taken). The EDTA (the Ethylenediaminetetraacetic Acid) titration method was used to determine the cement content at different depths of the infiltration into the soil column.

In this experiment, the effects of three factors, namely, the averaged pore size of sand samples, water-cement ratio of cement slurry, and the value of constant grouting pressure, on the filtration effect were studied separately. The details of the grouting tests are shown in Table 2. Tests 1, 2, and 3 used three kinds of sand samples with different particle size ranges of 0.1-0.5 mm, 0.25-1.2 mm, and 0.5-5.0 mm. Tests 4, 2, 5, and 6 utilized cement slurry with different water-cement ratios of 0.4, 0.6, 0.8, and 1.0 for grouting. The cement slurry was both prepared with a vertical mixer. The mixing time is 20 min, and the mixing speed keeps constant with the value of 1000 r/min. The grouting pressure used in tests 7, 2, 8, and 9 is 100, 200, 300, and 400 kPa. The experimental setups of different grouting tests were set based on a backfill grouting project for the shield tunnel.

Table 1: Parameters for sand samples in the study.

Sand	Nonuniformity coefficient	Coefficient of curvature	Relative compactness
Coarse	2.02	0.84	0.72
Medium	1.44	0.80	0.70
Fine	1.15	1.00	0.66

2.2.2. EDTA Titration Tests. This work used the EDTA titration method to determine the cement content in grouted soil samples. We first obtained the EDTA titration curve that indicates the relationship between the cement content of sand samples and the titration amount of disodium EDTA solution by calibration test. Six kinds of samples were prepared in advance, that is, 100 g of saturated sand samples with the cement content of 0%, 2%, 4%, 6%, 8%, and 10%, respectively. After leaving the prepared mixed samples to hydrate for 1 h, we put them into a 105°C oven for 12 h. After this, the dried samples were taken out, ground, and poured into a 500 ml beaker, and then added an appropriate amount of weak acid solvent, 10% NH_4Cl solution. After dissolving Ca^{2+} with sufficient stirring, left them for 3 h. A large amount of Ca^{2+} ions and a small amount of Fe^{3+}, Al^{3+}, etc. were left in the solution. The following is the chemical formula of this process:

$$Ca(OH)_2 + NH_4Cl = CaCl_2 + 2NH_3 \cdot H_2O \quad (1)$$

Subsequently, 10 ml of the clear upper solution was pipetted into a 200 ml conical flask, and 50 ml of 1.8% NaOH solution and 2 ml triethanolamine were added, adjusting the pH of the solution to be greater than 12.5. In the alkaline environment, triethanolamine made Fe^{3+}, Al^{3+} and a small amount of Mg^{2+}, Mn^{2+} form a precipitate, so the reaction between the disodium EDTA standard solution and Ca^{2+} was not interfered. Then, 0.2 g of calconcarboxylic acid indicator was added to the filtrate, and the filtrate was shaken well to form a red chromium complex of Ca^{2+}. Later, the filtrate was titrated with 0.1 mol/m^3 of disodium EDTA standard solution and kept shaking. The chemical formula for the reaction occurring in the mixture is as follows:

$$\begin{aligned} &Ca^2{+}{+}Xn^{2-} \_\_\_\_\_ CaX_n(\text{rose}) \\ &Ca^{2+} + Y^2 - \_\_\_\_\_ CaY(\text{colorless}) \\ &CaX_n + Y^{2-} \_\_\_\_ CaY(\text{colorless}) + Xn^{2-}(\text{solid blue}) \end{aligned} \quad (2)$$

where $X_n{}^{2-}$ stands for the anions involved in the reaction in the calconcarboxylic acid indicator, and Y^{2-} represents the anions involved in the reaction in EDTA disodium.

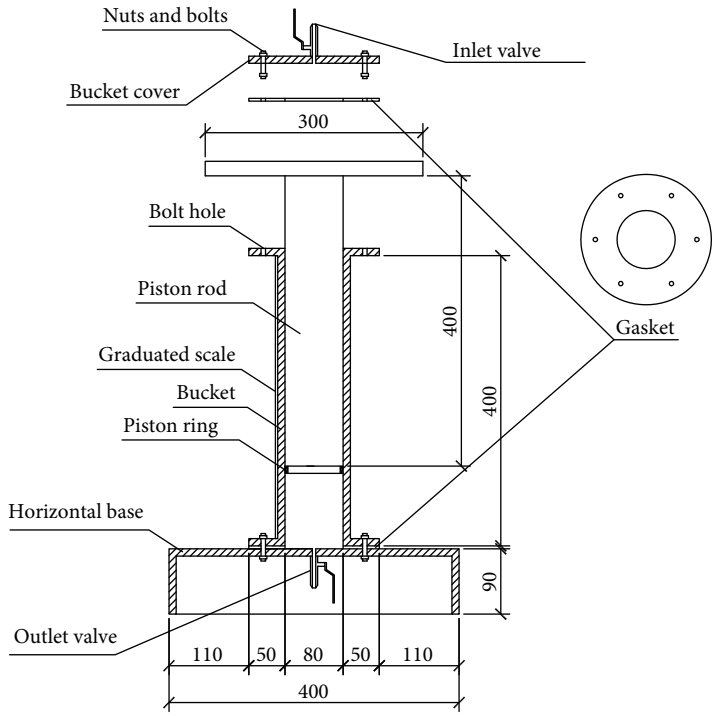

Figure 4: Grouting device.

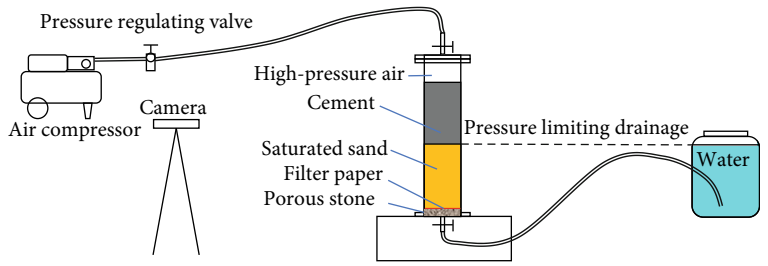

(a) Schematic diagram of the grouting process

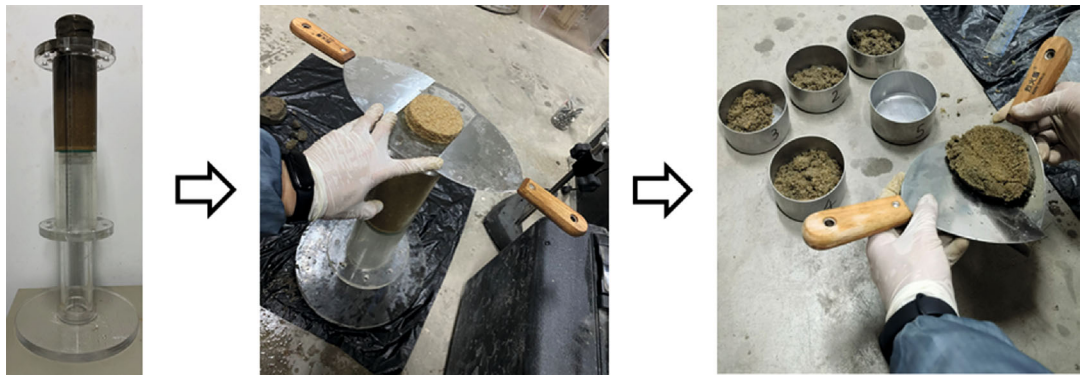

(b) Photos of sampling process

Figure 5: Grouting and sampling methods.

In the solution with pH greater than 12.5, Y^{2-} is easy to combine with Ca^{2+}, forming a colorless chromium complex CaY, which is more stable than the chromium complex Ca X_n formed by the $X_n{}^{2-}$ and Ca^{2+}. Therefore, when the C a^{2+} solution in the presence of calconcarboxylic acid dropped into the standard solution of EDTA disodium, the EDTA disodium would take away Ca^{2+} in CaX_n (rose complex) and make the calconcarboxylic acid $X_n{}^{2-}$ free out. When the rose complex is completely consumed, the mixed solution changes to its original color of calconcarboxylic acid, which is solid blue (see Figure 6). This titration amount is the consumption of EDTA disodium titration amount

Table 2: Parameters for grouting experiments.

No. of tests	Influencing factor 1 Particle size range (mm)	Influencing factor 2 W/C	Influencing factor 3 Grouting pressure (kPa)
1	0.1-0.5	0.6	200
2	0.25-1.2	0.6	200
3	0.5-5.0	0.6	200
4	0.25-1.2	0.4	200
5	0.25-1.2	0.8	200
6	0.25-1.2	1	200
7	0.25-1.2	0.6	100
8	0.25-1.2	0.6	300
9	0.25-1.2	0.6	400

corresponding to the cement content of saturated sand samples.

For each type of soil (with different particle sizes), we conducted titrations on six kinds of samples with different cement contents (each was titrated twice) to obtain titration curves. The expressions of the titration curve for soil samples were determined by linear fitting, as shown in Figure 7 and Table 3.

3. Results

3.1. Penetration Variation of the Cement Slurry in the Soil Column. The penetration of the cement slurry in the sand column can be observed through the transparent cylindrical column. Based on EDTA test results, the observed farthest penetration surface has the cement content of 2.8%. The variations of the penetration with time under different grouting conditions are shown in Figures 8–10. The solid lines in these figures indicate the location of the farthest penetration surface of the slurry, and the dashed lines represent the location of the top surface of the cement slurry (interface between the slurry and the air). The initial penetration distance of the slurry at $t = 0$ s before grouting is not zero because the slurry seeps and diffuses in porous sand due to gravity. As shown in Figure 8, the initial penetration rate is high under the constant grouting pressure and then gradually decreases. Gradually, the penetration in soil will no longer increase under grouting. It is because, with the development of the filtration (retention) of cement, the retained cement reduces the injectability and the permeability of the soil column, resulting in a decrease or stoppage of subsequent cement penetration. After the penetrated slurry stabilizes, the top surface of the cement slurry still varies slowly. It indicates that the cement filter cake forms above the soil column (discussed in Section 4.3) stops cement particles' injecting but allows the water in cement-slurry passing through. The cement is dewatered instead of penetrating the soil under pressure. This study defines the maximum stable penetration length as the maximum slurry penetration distance. By comparing the slurry penetration in different sand columns, the cement slurry penetrates faster in coarse-grained sand columns, with a larger maximum penetration distance and a longer time to reach the maximum penetration.

Figure 9 demonstrates the effect of grouting pressure on the penetration. As the grouting pressure is in the range of 100-300 kPa, the slurry penetration rate and the maximum penetration distance increase with the growth of the grouting pressure. However, when the slurry develops from 300 kPa to 400 kPa, the slurry penetration rate and maximum penetration distance decrease. The maximum penetration distance of the slurry under the constant pressure of 100-400 kPa is 27 mm, 36 mm, 44 mm, and 38 mm, respectively. This study's maximum penetration occurs at a grouting pressure of 300 kPa. Since the maximum penetration distance is not always positively correlated with the grouting pressure, the enhancement effect in practical grouting projects does not increase continuously with the growth of the grouting pressure. In some grouting conditions (where particles are blocked and a filter cake forms), too high grouting pressure will aggravate cement filtration and reduce cement penetration.

As shown in Figure 10, with the growth of the water-cement ratio, the cement slurry penetration rate and the maximum penetration distance increase, and the time to reach the maximum penetration distance is delayed. It is noteworthy that in all of our grouting tests, the cement top surface continues to decrease after penetration has stabilized. It implies that the cement filter cake forms above the soil column (discussed in Section 4.1) in all grouting tests.

3.2. The Penetrated Cement Content and Total Injected Amount in the Soil Column. From Figure 11, the penetrated cement content increases with the growth of the particle sizes of the sand column. The larger the sand particle size is, the larger the averaged pore sizes of the saturated sand column will be. The cement particles are less likely to be retained, and more cement particles can be injected and penetrate soil. However, with the increase of grouting pressure, the penetrated cement content in the soil exhibits a trend of increasing first and then decreasing (see Figure 12). When the grouting pressure increases from 100 kPa to 300 kPa, the cement contents at different depths increase with the growth of the grouting pressure. However, the cement content decreases as the grouting pressure increases from 300 kPa to 400 kPa. It is because the excessive grouting pressure results in a significant filtration effect. The cement filter cake that prevents the subsequent cement particles from penetrating soil forms more quickly at the higher grouting pressure.

Additionally, as is shown in Figure 13, the penetrated cement contents in the soil increase with the development of the cement slurry's water-cement ratio. The viscosity of cement slurry decreases as the water-cement ratio increases (see Figure 2). Thus, the slurry with the greater water-cement ratio can be injected into soil at a higher rate under the same grouting pressure. In addition, the cement particle clogging decreases as the solid volume concentration of the high-water-cement slurry is lower (as discussed in Section 4.1), thus the penetration increases. However, when the water-cement ratio is greater than 0.8 in this work, the

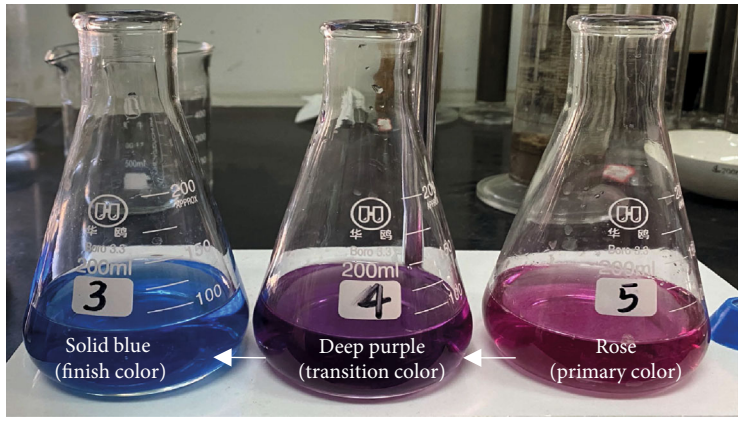

Figure 6: Colors of titrated solution.

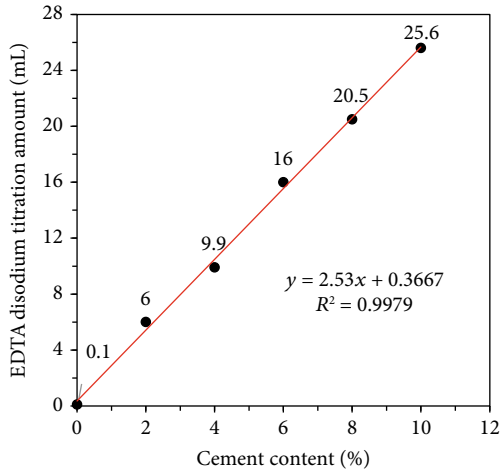

Figure 7: Correlation between cement content in medium sand and EDTA disodium titration amount.

increase of cement penetration with the growth of the water-cement ratio is not significant. It is inferred that the injected cement particle concentration decreases with the increase of the water-cement ratio, and thus, the solid cement content in the soil does not increase significantly.

The total penetrated amounts of cement in the soil column under different grouting conditions are calculated based on the distribution of cement content in the soil column. According to Axelsson et al. [15], the ratio between the cement grain size and the available opening of the pores is critical to assess the extent of cement's stoppage. In this work, the size of the available opening is calculated by hydraulic measuring method based on Kozeny-Carmans equation [19] and Axelsson et al. [15], as shown below:

$$b_{K-C} = \frac{n}{(1-n)\cdot S_0}\cdot\sqrt{12\cdot C_3}, \quad (3)$$

where n is the porosity of the soil column, measured during the experiments (see Table 4). S_0 represents the specific surface area, determined from the grain distribution curves (see Figure 1). v is the fluid's kinematic viscosity, and C_3 represents the shape factor constant that is set as 0.2 for spherical grains according to Carman [20], who conducted an extensive literature survey and concluded that this value is relatively constant for spherical grains. Additionally, the size ratio of the opening to the d_{90} of cement particle b_{K-C}/d_{90} can be obtained, as shown in Table 4.

Table 3: Calibration curve of EDTA titration method in the study.

Size	Rating curve	R^2
Coarse sand	$y = 2.4129x + 1.919$	0.9722
Medium sand	$y = 2.53x + 0.3667$	0.9979
Fine sand	$y = 2.6314x + 0.2095$	0.9948

The relationship between the b_{K-C}/d_{90} and the total amount of injected cement is shown in Figure 14. With the increase of the value of b_{K-C}/d_{90}, the penetrability of the soil is greater, and thus, more cement particles are penetrated the soil column. The relationship between the water-cement ratio and the total amount of injected cement is also presented. From Figure 15, the total cement amount positively correlates to the water-cement ratio. Nevertheless, when the water-cement ratio is greater than 0.8, the solid grouting amount no longer increases with the improvement of the water-cement ratio. As for the grouting pressure, with the increase of the grouting pressure, the total amount of cement injection is positively correlated with the grouting pressure when pressure is lower than 300 kPa (see Figure 16). With the further increase of the pressure, the total amount of cement penetration decreases due to the cement filter cake forming more quickly. The cement particles could not be injected into the soil after the formation of cement filter cake, which will be discussed in Section 4.1.

4. Discussion

4.1. Mechanism of Filtration Effects from the View of Particle Clogging in the Pore Throat. From a microscopic view, when cement particles pass through porous media, they can clog or get stuck in the pore throats (openings) of the porous media (filtration). The particle clogging in the pore throats could be classified as two types (see Figure 17): (a) interception, as the cement particle is larger than the pore throat; (b)

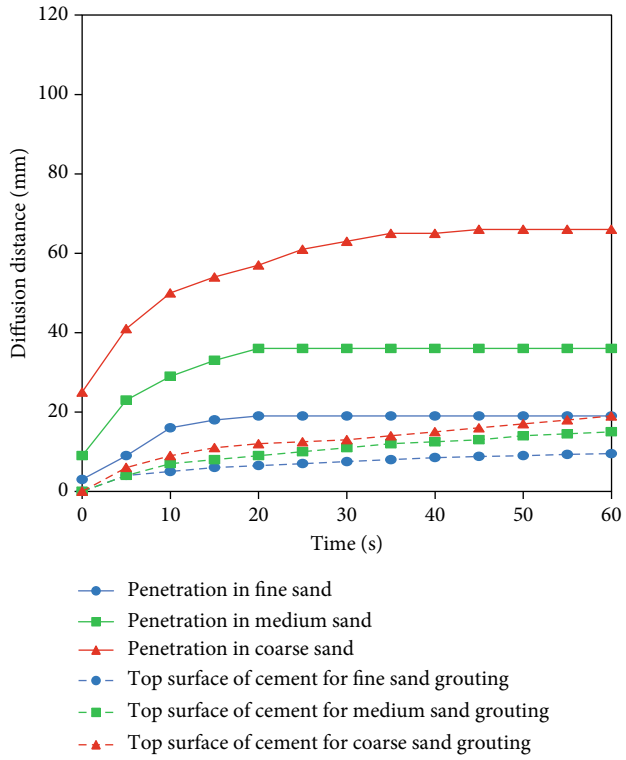

Figure 8: The development of cement farthest penetration surface and the top surface of cement slurry with time (tests 1, 2, and 3).

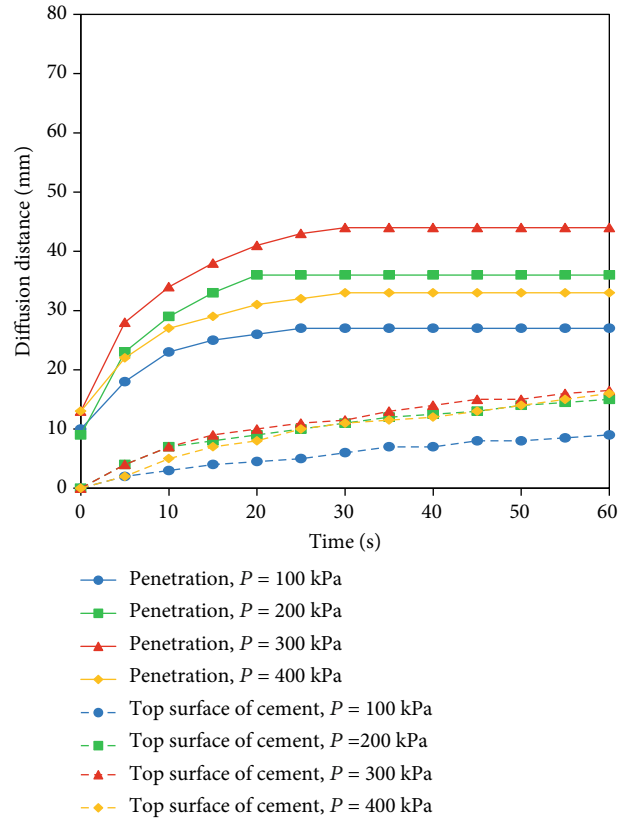

Figure 9: The development of cement farthest penetration surface and the top surface of cement slurry with time (tests 2, 7, 8, and 9).

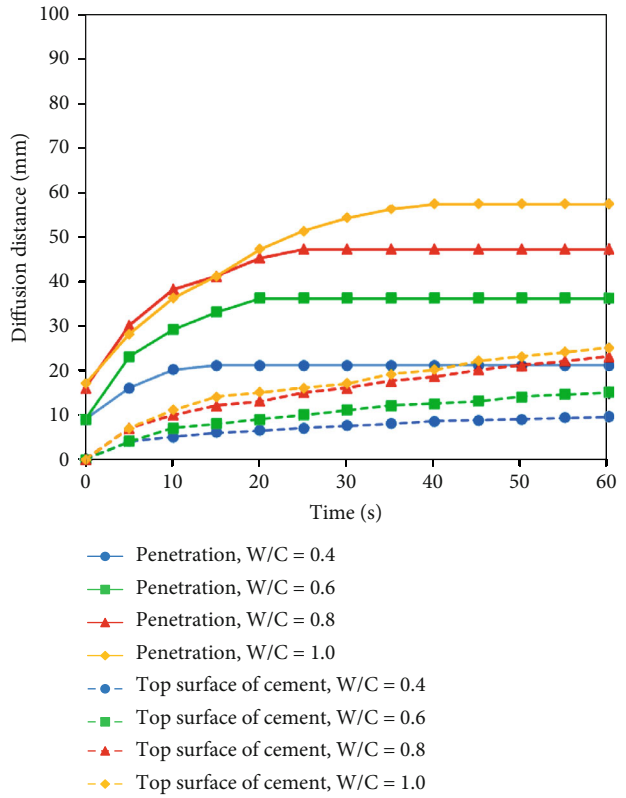

Figure 10: The development of cement farthest penetration surface and the top surface of cement slurry with time (tests 2, 4, 5, and 6).

formation of clogging arch (or named jamming arch), as an arc containing particles can build up in the pore throat which stops the particle flow (the cement particle is smaller than the pore throat). For the latter type of particle clogging, the occurrence of particle clogging at an opening (pore throat) has stochastic property [21–26]. Based on previous studies, the clogging probability is determined by three factors: (a) the solid concentration of the particle flow; (b) the size ratio of the particle to the opening; and (c) the fluid velocity through the opening. These three factors have a coupled effect on the particle clogging probability and the occurrence time of the clogging.

The probability of particle clogging decreases as the solid concentration of the suspension decreases. For cement-based grouting, a higher water-cement ratio means a lower solid concentration of particles. Therefore, particle clogging is less likely to happen as the water-cement ratio increases. Fewer particles are clogged and retained by the pores, and thus, more cement particles can penetrate the soil. Additionally, the clogging probability decreases with increasing the size ratio of opening to the passing particles. Therefore, the cement particles are less likely to become clogged in the pores of the coarse sand column, and the penetration of subsequent particles increases. As for the effect of grouting pressure on filtration, it can be explained from the effect of the passing velocity of particles on the particle clogging.

Mondal et al. [22] and Dai and Grace [23] found that with increasing the flow velocity of the suspension, the clogging probability increases, and the clogging occurs more

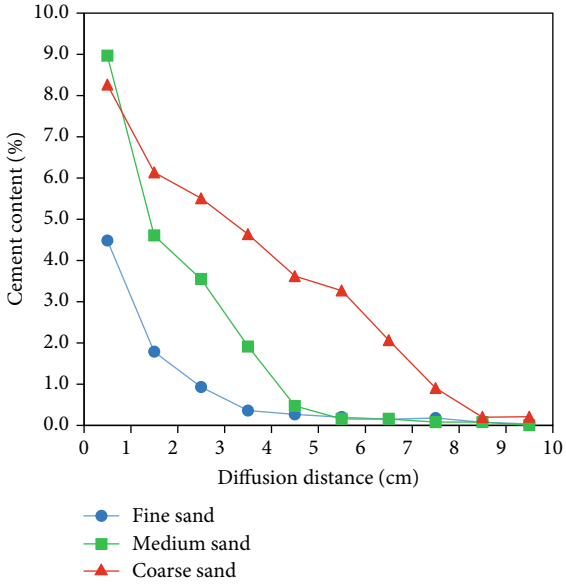

Figure 11: The distribution of penetrated cement content in sand columns (tests 1, 2, and 3).

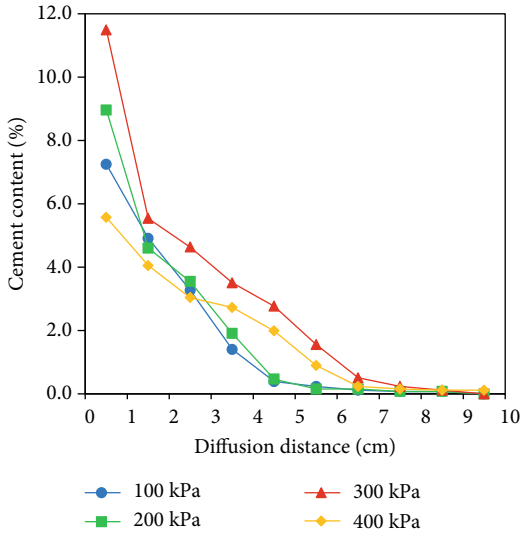

Figure 12: The distribution of penetrated cement content in sand columns (test 2, 7, 8, and 9).

quickly. A higher fluid velocity causes more particles to pass through the opening simultaneously, which is prone to forming the clogging arch. In this work, with the increase of the grouting pressure, the flow velocity of cement slurry increases. More particles pass through the pore throat simultaneously, and thus, more particles are clogged and retained in the pores. Although more cement particles are injected at higher pressure, excessive pressure will accelerate the clogging occurrence and stop the subsequent penetration of cement particles. Thus, the cement penetration distance and amount do not increase monotonously with the growth of the pressure. It is noted that in the laboratory test of Ma et al. [4], the penetration increases monotonously with pressure. It is because the other two factors also influence particle clogging. There is a threshold opening-particle size ratio for the clogging occurrence, which means that regardless of hydraulic grouting conditions, clogging will not occur [23] (particle clogging probability is 0). In this situation, the higher pressure lets more cement particles penetrate the soil without increasing particle clogging. Thus, the cement penetration shows a positive correlation to the grouting pressure.

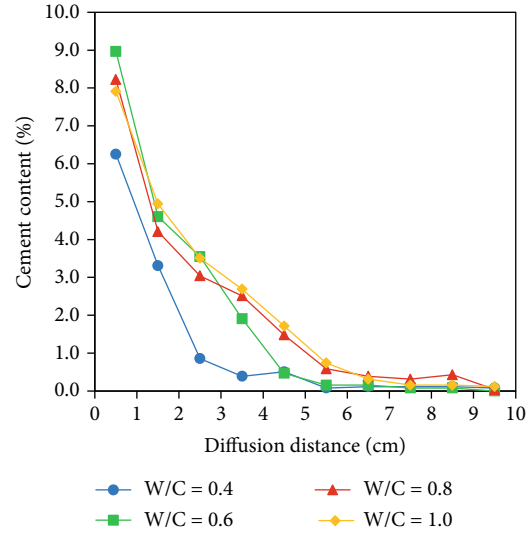

Figure 13: The distribution of penetrated cement content in sand columns (tests 2, 4, 5, and 6).

Once the cement particles eventually clog the soil samples' pores thoroughly, a dense cement cake forms above the soil column (see Figure 18(d)). This cake, also called the filter cake, can be seen as a porous filter constructed by the fine cement particles and the soil particles. It will stop the solid cement particles from penetrating and just allow the water in slurry to pass through. The filter cake is formed at the contact surface between the soil and the slurry because the slurry's velocity and the solid concentration at the contact surface are maximum, which is most conducive to particle clogging.

The formation condition of cement filter cake can be analyzed by the critical opening-particle size ratio for the particle clogging occurrence [15, 23], which means the clogging definitely happens (particle clogging probability is 1) as the opening-particle size ratio is smaller than this value. From the research on the clogging of cement particle [15] in sand, this critical value is 3. In this study, we observed the cement filter cake in all of our grouting tests. The values of b_{K-C}/d_{90} for different soil samples in this work are all smaller than or equal to 3 (see Table 4), which are consistent with the critical value proposed by previous research [15].

4.2. Reduced Permeability of the Soil Column after the Cement Infiltration. From numerous studies dealing with the permeability of sand, the value of permeability coefficient k is determined by the physical properties of the fluid, the soil particles, and the porosity of the packed sands. With the cement particles retained (or called penetrated) in the soil column due to filtration, the porosity and the specific

Table 4: Measured porosity for the different sands and specific surfaces determined from the grain distribution curves.

Sand	Porosity (%)	Specific surface (m^{-1})	b_{K-C} (μm)	b_{K-C}/d_{90}
Coarse	30.3	5538	122	3.0
Medium	35.1	8529	98	2.4
Fine	39.2	15080	66	1.6

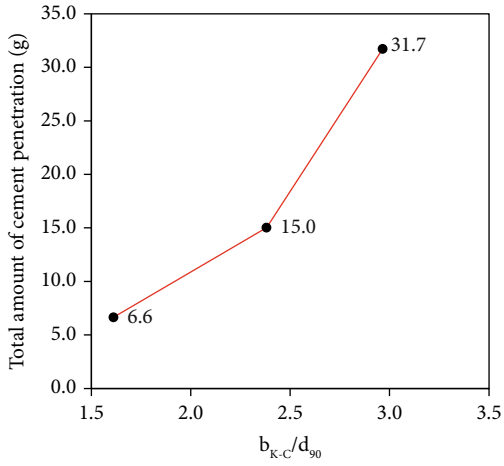

Figure 14: The relationship between b_{K-C}/d_{90} and the total amount of cement penetration.

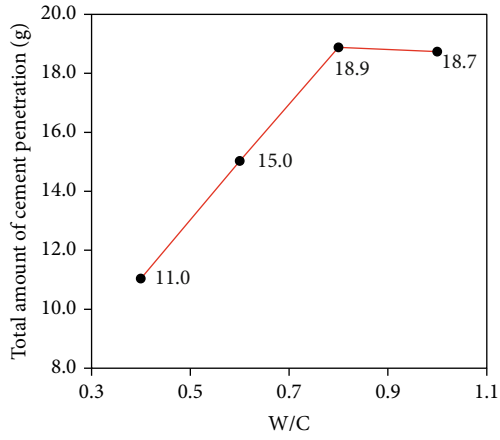

Figure 15: The relationship between W/C and the total amount of cement penetration.

surface area of the soil decrease. Accordingly, the value of the soil column's permeability is reduced. According to widely used Kozeny-Carman function [19], the permeability coefficient k of soil can be calculated by

$$k = \frac{g}{\nu C} \times \frac{1}{S_0^2} \times \frac{n^3}{(1-n)^2}, \quad (4)$$

where S_0 represents the specific surface area, ν is the fluid's kinematic viscosity, and n is the porosity of the soil column. C represents the Kozeny–Carman constant, reported as five

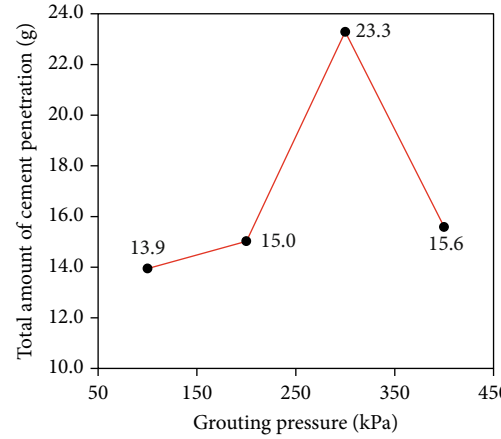

Figure 16: The relationship between grouting pressure and the total amount of cement penetration.

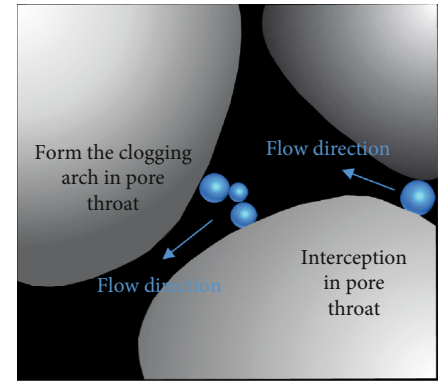

Figure 17: Schematic of two types of particle clogging.

by Zhou et al. [19] for uniform spheres. When the cement particles are retained in the soil column, they become a part of the porous media. The cement particle's specific surface area and the solid volume should be substituted into Equation (4) to calculate the permeability of the soil column after the cement filtration. The dependence of the cement particles on the permeability of the medium-sized soil column utilized in this work is shown in Figure 19.

From this figure, with the increase of the retained cement content in the soil column, the permeability of the soil column k decreases. When cement content is larger than 2%, the permeability of the medium-sized soil column utilized in this work decreases almost exponentially. The value of k with a cement content of 10% is approximately 10^{-3} times that for the clean saturated soil column. The reduced permeability means that the fluid pressure is dramatically lost in the soil column; accordingly, the cement's subsequent penetration rate and distance decrease.

4.3. Dewatering of the Cement Slurry after the Formation of Filter Cake. With continuous grouting, the cement particles clog the soil samples' pores and form a dense cement cake above the soil column (see Figure 18(d)). After the filter cake's formation, the maximum penetration distance of the slurry in soil tends to stabilize. However, the upper surface

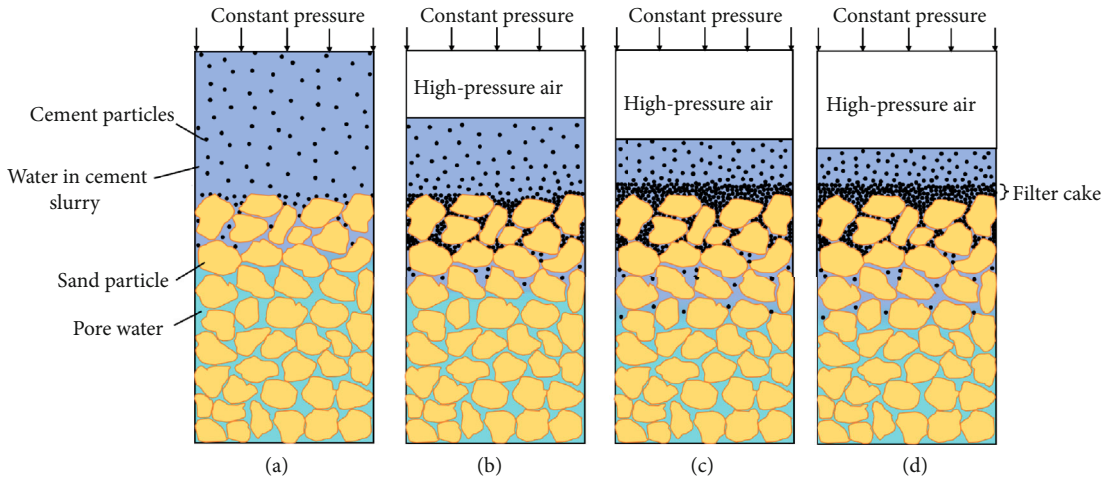

Figure 18: Schematic of the development of the cement penetration, retention into the soil, and the cement filter cake formation above the soil column.

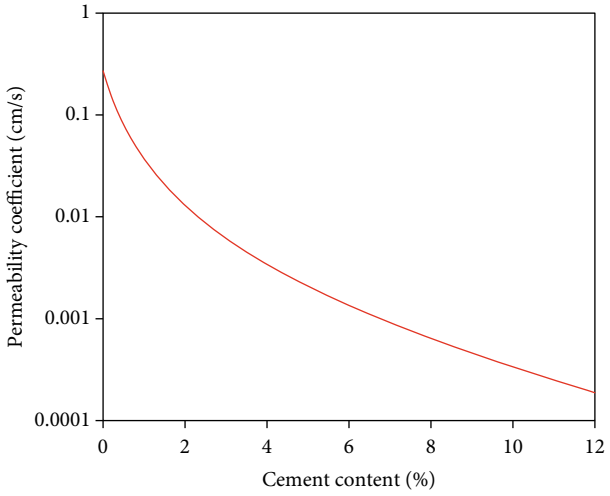

Figure 19: Relationship between cement content and permeability coefficient of medium sand.

of the cement slurry continues to develop gently under the grouting pressure, as shown in Figures 8–10 and sketched in Figures 18(c) and 18(d). That means that the water in cement slurry is drained out (dewatering) because of mass conservation and the incompressibility of the slurry. The formed filter cake stops cement particles' injecting but allows the water in cement-slurry passing through. This phenomenon that slurry is dewatered and thicken above the grouting body after the filter cake formation should be noticed in the grouting design for practical projects.

5. Conclusions

In this study, laboratory tests are conducted to study the filtration of cement-based grouting in saturated sand. By utilizing the visualization grouting device and the ETDA test, the variation of the penetration distance with time and the cement content distribution in the soil column can be measured. The influence of three factors, namely, sand samples' pore size, cement slurry's water-cement ratio, and the value of constant grouting pressure, on the filtration behaviors was discussed in detail. The main conclusions are obtained as follows:

In the case of the same grouting materials, with increasing the ratio size of the pore size to cement particles, the infiltration (or called penetration) depth and the amount increase significantly regardless of the hydraulic grouting conditions.

The cement penetration does not continuously increase with the growth of the grouting pressure. Excessive grouting pressure will accelerate the formation of the filter cake and decrease the subsequent cement particle infiltration.

With the growth of the water-cement ratio, the cement slurry penetration rate and the maximum penetration distance increase continuously. While, in this work, when the water-cement ratio exceeds 0.8, the improvement of the cement penetration by increasing the water-cement ratio is not significant.

The reduced permeability of the soil column because of the cement filtration (retention) was analyzed. When the retained cement content is larger than 2%, the permeability k decreases almost exponentially with the increase of the cement content. The value of k for soil with 10% retained cement content is approximately 10^{-3} times that for the clean saturated soil. In the lower-permeable soil column, fluid pressure loses more, reducing subsequent penetration rates and the distance.

Additionally, pressure filtration of the cement slurry (dewatering and thickening) was observed after the formation of the cement filter cake (see Figure 19). This decreases the effectiveness of cement grouting since subsequent grouting cannot penetrate the soil.

From the viewpoint of particle clogging in the pore throats of the grouting body, the abovementioned grouting parameters determine the probability and occurrence time of particle clogging collectively, leading to different filtration behaviors. More clogging means less penetration, and the filter cake forms more quickly. To alleviate filtration and inject

more cement, particle clogging should be avoided by increasing the size ratio of the pore of the grouting body to cement particles, the water-cement ratio, and choosing an appropriate grouting pressure.

It is noted that the rheological behavior of cement slurry also plays a crucial role in the filtration effect of the cement-based grouts [2, 15]. In this work, the cement slurry does not harden significantly during the short grouting time. Thus, the rheological physics of the cement slurry and its influence on filtration is out of the scope of this work and will be discussed in our future work. The results obtained in this work are helpful to understand the whole filtration process, the mechanism of filtration behaviors, and their deciding factors. Some suggestions are also provided for determining the appropriate grouting parameters for practical grouting projects.

Data Availability

Some or all data, models, or code generated or used during the study are available from the corresponding author by request.

Conflicts of Interest

The authors declare that they have no conflict of interest.

Acknowledgments

This work was supported by the National Natural Science Foundation of China (Grant nos. 52108352, 52078464, and U2006225). The authors are grateful for the above supports.

References

[1] T. Xu and A. Bezuijen, "Experimental study on the mechanisms of bentonite slurry penetration in front of a slurry TBM," *Tunnelling and Underground Space Technology*, vol. 93, article 103052, 2019.

[2] G. Zhu, Q. Zhang, R. Liu, J. Bai, W. Li, and X. Feng, "Experimental and numerical study on the permeation grouting diffusion mechanism considering filtration effects," *Geofluids*, vol. 2021, Article ID 6613990, 11 pages, 2021.

[3] A. Flora, G. Modoni, S. Lirer, and P. Croce, "The diameter of single, double and triple fluid jet grouting columns: prediction method and field trial results," *Géotechnique*, vol. 63, no. 11, pp. 934–945, 2013.

[4] D. Ma, S. Kong, Z. Li, Q. Zhang, Z. Wang, and Z. Zhou, "Effect of wetting-drying cycle on hydraulic and mechanical properties of cemented paste backfill of the recycled solid wastes," *Chemosphere*, vol. 282, article 131163, 2021.

[5] D. Li, X. Li, Y. Hu et al., "Study on dispersion of cement grout in sand considering filtration effect through the EDTA titration test," *Geofluids*, vol. 2020, Article ID 6620979, 9 pages, 2020.

[6] Z. Zhou, H. Zang, S. Wang, X. Du, D. Ma, and J. Zhang, "Filtration behaviour of cement-based grout in porous media," *Transport in Porous Media*, vol. 125, no. 3, pp. 435–463, 2018.

[7] J. S. Dolado and K. van Breugel, "Recent advances in modeling for cementitious materials," *Cement and Concrete Research*, vol. 41, no. 7, pp. 711–726, 2011.

[8] P. Herzig, D. M. Leclerc, and P. L. Goff, "Flow of suspensions through porous media-application to deep filtration," *Industrial and Engineering Chemistry*, vol. 62, no. 5, pp. 8–35, 1970.

[9] T. Krause, *Schildvortrieb mit flüssigkeits-und erdgestützter Ortsbrust*, Mitteilungen des Instituts für Grundbau und Bodenmechanik der Technischen Universität Braunschweig, 1987.

[10] W. Broere, *Tunnel face stability and new CPT applications*, Delft University Press, 2002.

[11] O. S. Q. Yousif, M. Karakouzian, N. O. A. Rahim, and K. A. Rashed, "Physical clogging of uniformly graded porous media under constant flow rates," *Transport in Porous Media*, vol. 120, no. 3, pp. 643–659, 2017.

[12] D. Ma, J. Wang, X. Cai et al., "Effects of height/diameter ratio on failure and damage properties of granite under coupled bending and splitting deformation," *Engineering Fracture Mechanics*, vol. 220, article 106640, 2019.

[13] D. Ma, J. Zhang, H. Duan et al., "Reutilization of gangue wastes in underground backfilling mining: overburden aquifer protection," *Chemosphere*, vol. 264, Part 1, article 128400, 2021.

[14] Z. Zhou, X. Du, S. Wang, X. Cai, and L. Chen, "Micromechanism of the diffusion of cement-based grouts in porous media under two hydraulic operating conditions: constant flow rate and constant pressure," *Acta Geotechnica*, vol. 14, no. 3, pp. 825–841, 2019.

[15] M. Axelsson, G. Gustafson, and Å. Fransson, "Stop mechanism for cementitious grouts at different water-to-cement ratios," *Tunnelling and Underground Space Technology*, vol. 24, no. 4, pp. 390–397, 2009.

[16] F. Bouchelaghem and L. Vulliet, "Mathematical and numerical filtration–advection–dispersion model of miscible grout propagation in saturated porous media," *International Journal for Numerical and Analytical Methods in Geomechanics*, vol. 25, no. 12, pp. 1195–1227, 2001.

[17] Z. Saada, J. Canou, L. Dormieux, J. C. Dupla, and S. Maghous, "Modelling of cement suspension flow in granular porous media," *International Journal for Numerical and Analytical Methods in Geomechanics*, vol. 29, no. 7, pp. 691–711, 2005.

[18] Y. S. Kim and A. J. Whittle, "Particle network model for simulating the filtration of a microfine cement grout in sand," *Journal of Geotechnical and Geoenviromental Engineering*, vol. 135, no. 2, pp. 224–236, 2009.

[19] J. Zhou, K. Fang, and K. Yang, "Bearing capacity of grouted pile considering grout filtration," in *Proceedings of Geo Shanghai 2018 International Conference: Fundamentals of Soil Behaviours*, A. Zhou, J. Tao, X. Gu, and L. Hu, Eds., pp. 645–650, Springer, Singapore, 2018.

[20] P. C. Carman, "Permeability of saturated sands, soils and clays," *The Journal of Agricultural Science*, vol. 29, no. 2, pp. 262–273, 1939.

[21] B. Ahlén, *Effect of cementation and compaction on hydraulic and acoustic properties of porous media*, Chalmers tekniska högskola och Göteborgs universitet, 1993.

[22] S. Mondal, C.-H. Wu, and M. M. Sharma, "Coupled CFD-DEM simulation of hydrodynamic bridging at constrictions," *International Journal of Multiphase Flow*, vol. 84, pp. 245–263, 2016.

[23] J. Dai and J. R. Grace, "Blockage of constrictions by particles in fluid-solid transport," *International Journal of Multiphase Flow*, vol. 36, no. 1, pp. 78–87, 2010.

[24] H. Sun, S. Xu, X. Pan, L. Shi, X. Geng, and Y. Cai, "Investigating the jamming of particles in a three-dimensional fluid-

driven flow via coupled CFD-DEM simulations," *International Journal of Multiphase Flow*, vol. 114, pp. 140–153, 2019.

[25] I. Zuriguel, A. Garcimartin, D. Maza, L. A. Pugnaloni, and J. M. Pastor, "Jamming during the discharge of granular matter from a silo," *Physical Review E*, vol. 71, no. 5, article 051303, 2005.

[26] A. Guariguata, M. A. Pascall, M. W. Gilmer et al., "Jamming of particles in a two-dimensional fluid-driven flow," *Physical Review E*, vol. 86, no. 6, article 061311, 2012.

Hindawi
Geofluids
Volume 2022, Article ID 1302260, 12 pages
https://doi.org/10.1155/2022/1302260

Research Article

Theoretical Research on Grouting in Deep Loose Layers Based on the Cylindrical Diffusion Model of Radial Tube Flow

Xuesong Wang,[1] **Hua Cheng**,[1,2,3] **Zhishu Yao**,[1] **Chuanxin Rong**,[1] **Xianwen Huang**,[1] **and Longhui Guo**[1]

[1]*School of Civil Engineering and Architecture, Anhui University of Science and Technology, Huainan, Anhui 232001, China*
[2]*School of Resources and Environmental Engineering, Anhui University, Hefei, Anhui 230601, China*
[3]*Anhui Province Key Laboratory of Building Structure and Underground Engineering, Anhui Jianzhu University, Hefei, Anhui 230601, China*

Correspondence should be addressed to Hua Cheng; hcheng@aust.edu.cn

Received 19 January 2022; Revised 25 February 2022; Accepted 2 March 2022; Published 25 March 2022

Academic Editor: Xueming Du

Grouting in deep, loose layers are a complex process in which many modes such as infiltration, splitting, and compaction coexist. It is of great significance to establish a realistic, simplified physical model to study the law of slurry diffusion. Herein, a cylindrical diffusion model of radial tube flow is established, and the control differential equations of both the Bingham slurry diffusion velocity in a single tube and the diffusion velocity of the radial tube flow are deduced. Additionally, the calculation formulas for the diffusion radius and slurry pressure distribution function are obtained. The rationality of the theory is verified by combining our results with those of the field grouting test of the Guotun coal mine. The results show that the cylindrical diffusion model of radial tube flow can successfully characterize the slurry diffusion law of grouting in a deep, loose layer. The slurry pressure attenuation shows distinguishable stages: within the first 30% of the diffusion radius, the slurry pressure decreased sharply by approximately 70%, and the slurry pressure decreases slowly in the later stages. Furthermore, the diffusion radius has a nonlinear, negative correlation with the height of the grouting section and the comprehensive injection rate of formation; the change rate is relatively more gradual, and there are no distinguishable stages. The research results provide a theoretical basis for reasonably determining the grouting parameters of deep, loose layers in the future.

1. Introduction

As a common treatment method for antiseepage, plugging, and reinforcement of underground engineering, grouting methods are widely used in mine water plugging and reinforcement, water and mud inrush treatment in tunnel fault fracture zones, foundation pit supports, dam reinforcement, and other fields [1–3]. Grouting in deep and loose layers has the typical "three high characteristics" of high ground stress, high permeability, and high grouting pressure [4, 5]. In addition, the uncertainty of the change in soil layer properties during the deposition process leads to many modes of slurry diffusion, such as splitting, permeability, and compaction, and its diffusion mechanism and design theory have significantly lag between engineering practice and research [6, 7].

Regarding the diffusion of split grouting slurry, the main established mathematical models include the flat-plate diffusion model that does not consider the change in crack width and the plane radiation circle diffusion model that does consider the change in crack width [8–10]. The main research topics are slurry diffusion radius and velocity distribution, pressure distribution, and viscosity temporal and spatial distribution in the process of migration. Regarding infiltration grouting, numerous studies have been conducted with a combination of different flow patterns of slurry and different diffusion models. The slurry flow patterns of Newtonian, Bingham, and power-law fluids have been investigated. The established diffusion models mainly include the spherical, cylindrical, and cylindrical-hemispherical models [11–14]. Regarding compaction grouting, the fluid–solid coupling

effect between the slurry and soil is mainly studied in combination with the theories of ball hole expansion or column hole expansion and soil nonlinear compaction. The research focus is mainly on considering different yield criteria, dilatancy, strain softening, different moduli of tension, and compression of soil [15–17].

The above researches ignored the tortuous effect in the process of slurry diffusion and assumed that the diffusion channels of slurry were straight. There was a large deviation between the theoretical calculation results and the engineering practice. Through comparison, some scholars [18–20] have found that the slurry diffusion law considering the tortuous effect was more consistent with the grouting test results, and the calculation error was smaller. It is of great significance to consider the tortuous effect in the design of grouting parameters in porous media. In addition, the abovementioned research only discusses a particular diffusion mode of the slurry, but the process of grouting in deep, loose layers involves multiple diffusion modes [21, 22]. The grouting theory of the single diffusion mode cannot be applied when designing the grouting parameters in deep, loose layers. The grouting construction parameter design is not significantly influenced by the slurry diffusion mode but focuses on the design of parameters such as grouting pressure and diffusion radius [23, 24]. Therefore, it is necessary to establish a grouting diffusion theory suitable for deep, loose layers, which simultaneously weakens the slurry diffusion mode and can be better suited to guide the design of grouting parameters.

Grotenhuis et al. [25, 26] characterized the slurry diffusion channel in sand with a straight circular tube and assumed the diffusion of the slurry in the sand to be represented by the flow of the slurry in the circular tube. The model can characterize both the split grouting and infiltration grouting mechanisms and can be used to calculate parameters such as the grouting pressure and diffusion radius. Based on this and considering the tortuous effect of the slurry diffusion path, this study considers the slurry diffusion channel in sand to be a tortuous circular tube and establishes the cylindrical diffusion model of the radial tube flow of the slurry in a deep, loose sand layer. First, the control differential equation of the Bingham slurry diffusion velocity in a single tube is derived, and the permeability coefficient considering tortuosity is used to replace the average radius of the seepage tubes in the injected layer within the differential equation. Subsequently, the diffusion velocity control equation of the radiation tube flow is derived, and the calculation formulas for the diffusion radius and slurry pressure distribution function are obtained. Finally, combined with the field grouting test results of the Guotun coal mine, the rationality of the theory is verified, and the attenuation law of the grouting pressure and the influential factors on the diffusion radius are discussed for the diffusion area. The research results provide a reference for future guidance of the design of grouting parameters in deep and loose layers.

2. Cylindrical Diffusion Model of Radial Tube Flow

2.1. Basic Assumptions and Model Establishment. To simplify the calculation and establish the diffusion model of the slurry in a deep, loose sand layer, the following assumptions are made within this study:

(1) The diffusion mode of the slurry in the layer is weakened, and the diffusion of slurry in splitting cracks and pores is regarded as the flow of slurry in tortuous tubes

(2) The slurry is an incompressible Bingham fluid, and the slurry flow pattern does not change during grouting

(3) The slurry velocity on the inner wall of the tube is 0, which satisfies the no-slip boundary condition

(4) The energy loss of the slurry flowing through the bend of the tube was ignored

Based on the abovementioned assumptions, a cylindrical diffusion model of the radial tube flow of the slurry in a deep, loose sandy soil layer is constructed, where the height of the grouting section is h, and the diffusion radius is R. N horizontal circuitous circular tubes with radius r_0 radiate from the vicinity of the grouting tube, where r_0 is the comprehensive average radius of the tubes, and the diffusion of the slurry in the sand layer is regarded as the flow of the slurry in circuitous circular tubes. The specific values of N and r_0 of the tubes are difficult to determine, but it is possible to simplify the theoretical derivation process by eliminating these two parameters. Therefore, a cylindrical surface coaxial within the grouting tube is selected, where the height of the cylindrical surface is equal to the height h of the grouting section ,and the radius is set to R_0, which satisfies the following requirement:

$$N\pi r_0^2 = 2\pi R_0 h. \tag{1}$$

It is worth noting that R_0 is neither the grouting tube radius nor the drilling radius. This cylindrical surface is an imaginary cylindrical surface selected for the convenience of the subsequent theoretical derivation, which is referred to as the virtual divergent surface in this study. According to Equation (1), the sum of the cross-sectional areas of all tubes is equal to the side surface area of the divergence surface, which is equivalent to the radial divergence of the slurry from the virtual divergence surface within the tortuous circular tube. A schematic of the diffusion model is shown in Figure 1.

2.2. Diffusion Velocity Control Differential Equation of Bingham Slurry in a Single Tube. The Bingham fluid rheological equation is as follows [27]:

$$\tau = \tau_0 + \eta_g \dot{\gamma}, \tag{2}$$

where τ is the shear stress between grout layers, τ_0 is the shear yield strength of the slurry, η_g is the viscosity coefficient of the slurry at 25°C, and $\dot{\gamma} = -\mathrm{d}v/\mathrm{d}\rho$ is the shear rate of the slurry.

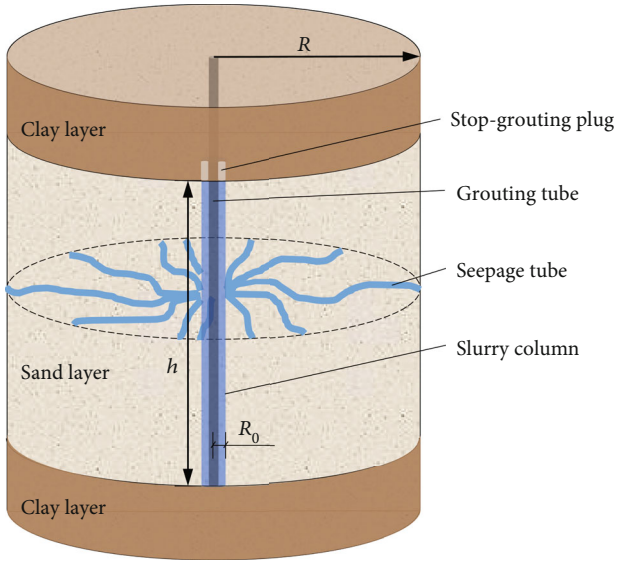

Figure 1: Cylindrical diffusion model of radial tube flow.

The actual length of the tortuous circular tube is $\chi(R - R_0)$, the radius is r_0, the slurry pressure upon entry is the initial grouting pressure, and the slurry pressure at the end is the hydrostatic pressure p_w at this point. The x-axis of the natural coordinate system along the axis of the tortuous circular tube is established, and the intersection of the x-axis and the grouting tube axis is taken as the coordinate origin. The slurry flow direction is along the positive x-axis. $[0, R_0]$ is the straight-line section, and $[R_0, \chi(R - R_0) + R_0]$ is the tortuous section, as shown in Figure 2(a). The attenuation value of the slurry pressure along the x-axis was set as $p(x)$. Note that the value of $p(x)$ represents the attenuation value of the slurry pressure, which is therefore distinguished from the slurry pressure. The boundary conditions are

$$\begin{cases} x = R_0, p = 0, \\ x = \chi(R - R_0) + R_0, p = p_0 - p_w. \end{cases} \tag{3}$$

A section of the cylindrical fluid microelement with radius ρ and length dx and its axial force is shown in Figure 2(b), which is obtained from the equilibrium conditions of the axial force:

$$\{[p_0 - p(x + dx)] - [p_0 - p(x)]\} \cdot \pi\rho^2 + \tau \cdot 2\pi\rho \cdot dx = 0, \tag{4}$$

which can be simplified to

$$p(x + dx) - p(x) = \frac{2\tau}{\rho} dx. \tag{5}$$

Let $dp = p(x + dx) - p(x)$, and then Equation (5) can be simplified to

$$dp = \frac{2\tau}{\rho} dx. \tag{6}$$

Therefore, along the slurry flow direction, the pressure attenuation gradient can be expressed as follows:

$$\lambda = \frac{dp}{dx} = \frac{2\tau}{\rho}. \tag{7}$$

The pressure attenuation gradient, λ, is the attenuation speed of the pressure along the flow direction. It can be seen from Equation (7) that λ is positively correlated with the slurry shear stress, τ, and negatively correlated with radial distance, ρ. τ is positively correlated with the slurry viscosity. The greater the viscosity, the more difficult it is to overcome the shear stress, the greater τ is, and the faster the pressure attenuation is. When the radial distance ρ is equal to the tube radius r_0, the average starting pressure gradient of the slurry flowing in the tube is

$$\lambda_0 = \frac{2\tau_0}{r_0}, \tag{8}$$

where λ_0 is the average starting pressure gradient of the slurry, τ_0 is the shear yield strength of the slurry, and r_0 is the comprehensive average radius of the tubes, which is positively correlated with the effective porosity of sand, and is the parameter after homogenizing the pore channel size of sand. According to [28], the calculation formula for r_0 is

$$r_0 = \frac{\sum_{i=1}^{n} N_i r_i^4}{\sum_{i=1}^{n} N_i r_i^3} \approx \left(\frac{\sum_{i=1}^{n} N_i r_i^4}{\sum_{i=1}^{n} N_i}\right)^{\frac{1}{4}}, \tag{9}$$

where N_i is the number of tubes with a cross-section radius of r_i $(i = 1, 2, \cdots, n)$.

From Equation (7), it is then possible to obtain the following:

$$\tau = \frac{\rho}{2} \cdot \frac{dp}{dx}. \tag{10}$$

Substituting Equation (10) into Equation (2) results in

$$-\frac{dv}{d\rho} = \frac{1}{\eta_g}\left(\frac{\rho}{2} \cdot \frac{dp}{dx} - \tau_0\right). \tag{11}$$

When $\tau \le \tau_0$, the slurry moves as a piston, $dv/d\rho = 0$, with a radius of r_p and a speed of v_p. Using Equation (11), we obtain

$$r_p = \frac{2\tau_0}{dp/dx}. \tag{12}$$

When $\tau > \tau_0$, the slurry moves in a laminar flow. From Equation (11), we can separate the variables and integrate, resulting in

$$v = -\frac{1}{\eta_g}\left(\frac{\rho^2}{4} \cdot \frac{dp}{dx} - \tau_0\rho\right) + C_1, \tag{13}$$

where C_1 is the integration constant.

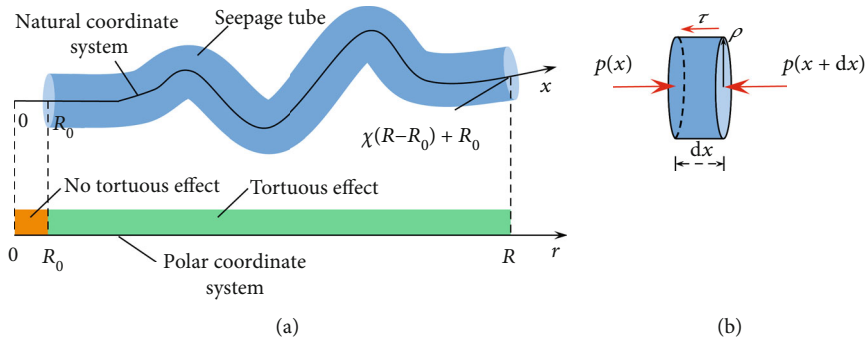

Figure 2: Coordinate system and fluid microelement stress diagram.

Substituting the no-slip boundary condition, i.e., $\rho = r_0$, the integration constant is determined to be

$$C_1 = \frac{1}{\eta_g}\left(\frac{r_0^2}{4}\cdot\frac{dp}{dx} - \tau_0 r_0\right). \tag{14}$$

Therefore, the velocity distribution of the laminar flow in $[r_p, r_0]$ is

$$v = \frac{1}{\eta_g}\left[\frac{r_0^2-\rho^2}{4}\cdot\frac{dp}{dx} - \tau_0(r_0-\rho)\right], \tag{15}$$

and the fluid velocity of the piston-like flow in $[0, r_p]$ is

$$v_p = \frac{1}{\eta_g}\left[\frac{r_0^2-r_p^2}{4}\cdot\frac{dp}{dx} - \tau_0(r_0-r_p)\right]. \tag{16}$$

The velocity distribution in the circular tube is a truncated paraboloid shape, and the flow rate per unit time, q_1, in a single tube is

$$q_1 = \pi r_p^2 v_p + \int_{r_p}^{r_0} 2\pi\rho v d\rho. \tag{17}$$

Substituting Equations (15) and (16) into Equation (17), we obtain

$$q_1 = \frac{\pi r_0^4}{8\eta_g}\cdot\frac{dp}{dx}\cdot\left[1 - \frac{4}{3}\left(\frac{r_p}{r_0}\right) + \frac{1}{3}\left(\frac{r_p}{r_0}\right)^4\right]. \tag{18}$$

The average velocity, $\bar{v}$, within the tube section is

$$\bar{v} = \frac{r_0^2}{8\eta_g}\cdot\frac{dp}{dx}\cdot\left[1 - \frac{4}{3}\left(\frac{r_p}{r_0}\right) + \frac{1}{3}\left(\frac{r_p}{r_0}\right)^4\right]. \tag{19}$$

Substituting Equation (12) into Equation (19) results in

$$\bar{v} = \frac{r_0^2}{8\eta_g}\cdot\frac{dp}{dx}\cdot\left[1 - \frac{4}{3}\left(\frac{2\tau_0/r_0}{dp/dx}\right) + \frac{1}{3}\left(\frac{2\tau_0/r_0}{dp/dx}\right)^4\right]. \tag{20}$$

From Equation (20), it can be seen that when $2\tau_0/r_0/dp/dx = 1$, $\bar{v} = 0$. Specifically, when the pressure gradient $\lambda = 2\tau_0/r_0 = \lambda_0$, the average flow in the circular tube is 0.

To satisfy $dp/dx = \lambda_0$ and $\bar{v} = 0$, Equation (20) is rewritten as

$$\bar{v} = \frac{r_0^2}{8\eta_g}\cdot\frac{dp}{dx}\cdot\left\{1 - \frac{\lambda_0}{dp/dx} - \frac{1}{3}\cdot\frac{\lambda_0}{dp/dx}\cdot\left[1 - \left(\frac{\lambda_0}{dp/dx}\right)^3\right]\right\}. \tag{21}$$

In the grouting process, $dp/dx \gg \lambda_0$ [28], the third term in the curly bracket of Equation (21) is ignored in order to obtain an approximate slurry diffusion velocity control differential equation, as follows:

$$\bar{v} = \frac{r_0^2}{8\eta_g}\cdot\left(\frac{dp}{dx} - \lambda_0\right). \tag{22}$$

Owing to the uneven spatial distribution of the pore structure in the injected layer, the average radius, r_0, of the seepage tube in the injected layer in Equation (22) is difficult to measure directly. However, the permeability coefficient can be easily obtained through laboratory tests. Therefore, the expression of the permeability coefficient was used to replace r_0 within this study. The relationship between the permeability coefficient and r_0 is derived as follows:

The relationship between the permeability coefficient K and permeability k is [29]

$$K = k\frac{\gamma}{\eta}, \tag{23}$$

where γ is the gravity of the fluid, and η is the viscosity coefficient of the fluid.

The permeability of porous media is independent of the fluid characteristics and only depends on the porosity, capillary diameter, and tortuosity of the porous media. The existing theory only uses porosity and capillary diameter to characterize the permeability of porous media, without considering the nonnegligible parameter of tortuosity [28]. It is worth noting that because permeability is independent of the fluid characteristics, to simplify the calculation, the fluid

selected in the process of deriving permeability is the laminar Newtonian fluid, which does not conflict with the Bingham fluid studied within this research.

According to the generalized Hagen Poiseuille equation [30], the flow through all tubes per unit time is

$$q = \frac{nA\pi r_0^4}{8\eta\chi} \cdot \frac{\mathrm{d}p}{\mathrm{d}l}, \tag{24}$$

where q is the flow through the pore section, n is the number of circular tubes per unit area, A is the cross-sectional area, and $\mathrm{d}p/\mathrm{d}l$ is the pressure gradient.

In the laminar flow state, the flow of fluid in porous media satisfies Darcy's law, and the flow through the pore section per unit time is

$$q = \frac{kA}{\eta} \cdot \frac{\mathrm{d}p}{\mathrm{d}l}. \tag{25}$$

Through theoretical derivation, Li et al. [31] highlighted how the tube flow and seepage flow are unified, and the formulas of the two mathematical models are equivalent; they are simply expressed by different parameters. In combination with Equations (24) and (25), the permeability considering tortuosity is

$$k = \frac{n\pi r_0^4}{8\chi}. \tag{26}$$

The porosity of the tube model is

$$\varphi = n\pi r_0^2 \chi. \tag{27}$$

When combining Equations (26) and (27), we find

$$k = \frac{\varphi r_0^2}{8\chi^2}. \tag{28}$$

Therefore, the permeability coefficient considering tortuosity is

$$K = \frac{\varphi r_0^2 \gamma}{8\eta\chi^2}. \tag{29}$$

Setting the viscosity ratio of slurry to water to β, we obtain

$$\beta = \frac{\eta_g}{\eta_w}, \tag{30}$$

where η_w is the viscosity coefficient of water at 25°C.

Combining Equations (29) and (30) results in

$$\frac{r_0^2}{8\eta} = \frac{\chi^2 K_w}{\beta\varphi\gamma_w}, \tag{31}$$

where K_w is the permeability coefficient of water in a porous medium.

Therefore, Equation (22) can be transformed into

$$\bar{v} = \frac{\chi^2 K_w}{\beta\varphi\gamma_w} \cdot \left(\frac{\mathrm{d}p}{\mathrm{d}x} - \lambda_0\right). \tag{32}$$

Equation (32) is the approximate slurry diffusion velocity control differential equation of the Bingham slurry in a single tube.

2.3. Diffusion Velocity Control Equation of Radial Tube Flow. The flow and diffusion path of the slurry in the deep, loose layer was tortuous, as shown in Figure 3. Tortuosity is used to characterize the tortuous effect of fluid particle motion diffusion [32, 33], which is commonly defined as

$$\chi = \frac{l_t}{l}, \tag{33}$$

where χ is the tortuosity of the tube which commonly takes the values obtained by related scholars of 1.4 ~ 1.6 [28]. The average value used within this research is 1.5, l_t is the actual length of the diffusion trace, and l is the effective length of the diffusion path.

The effective porosity of the injected layer is the ratio of the pore volume filled by the slurry to the volume of the injected soil layer, and the relationship with the porosity of the soil layer is

$$\varphi' = \alpha\varphi, \tag{34}$$

where φ' is the effective porosity of the injected layer, φ is the actual porosity of the injected layer, and α is the pore injection coefficient of approximately 0.15~0.2 for silty clay and 0.3 ~ 0.5 for soft soil and fine sand [34].

In the hollow cylindrical layer of $[R_0, (x - R_0)/\chi + R_0]$, the effective porosity is

$$\varphi' = \frac{N\pi r_0^2 (x - R_0)}{\pi h\left\{\left[(x - R_0)/\chi + R_0\right]^2 - R_0^2\right\}}. \tag{35}$$

Combining Equations (1) and (35) results in

$$\varphi' = \frac{2\chi^2 R_0}{x + (2\chi - 1)R_0}. \tag{36}$$

It can be seen from Equation (36) that the effective porosity decreases with an increase in the diffusion distance, which is consistent with practice. An increase in the slurry diffusion distance means that the slurry pressure gradient gradually decreases. When it is less than the starting pressure gradient of the slurry flow in small tubes, the slurry will not enter these small tubes. When the distance from the grouting tube increases, the number of pores that the slurry can enter gradually decreases; that is, the effective porosity gradually decreases.

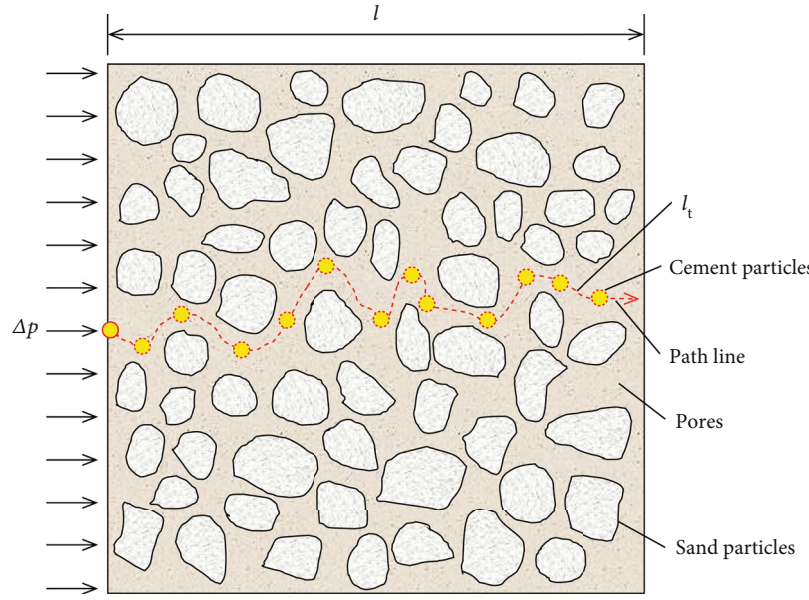

Figure 3: Schematic of slurry diffusion tortuous effect.

The slurry column radius can be obtained by combining Equations (34) and (36), such that

$$R_0 = \frac{\alpha\varphi}{2\chi^2 - (2\chi - 1)\alpha\varphi}x. \tag{37}$$

It can be seen from Equation (37) that during grouting, the slurry column radius changes with the change in effective porosity and diffusion distance, which is not a fixed value.

Let

$$\xi = \frac{\alpha\varphi}{2\chi^2 - (2\chi - 1)\alpha\varphi}, \tag{38}$$

where ξ is a parameter selected to simplify the formula, which is related to α, φ, and χ, and is calculated by Equation (38).

Then,

$$R_0 = \xi x. \tag{39}$$

Because the slurry is incompressible, the slurry injection flow is equal to the outflow flow of the cylindrical surface outside the slurry column,

$$q = \frac{\bar{v}}{\chi} \cdot 2\pi R_0 h. \tag{40}$$

Combining Equations (39) and (40) results in

$$\bar{v} = \frac{\chi q}{2\pi\xi h x}. \tag{41}$$

2.4. Slurry Diffusion Radius and Pressure Distribution. Through combining Equations (32) and (41), we obtain

$$\frac{\mathrm{d}p}{\mathrm{d}x} = \frac{q\beta\varphi\gamma_w}{2\pi\xi h\chi K_w}\frac{1}{x} + \lambda_0. \tag{42}$$

Subsequently, integrating Equation (42) results in

$$p(x) = \frac{q\beta\varphi\gamma_w}{2\pi\xi h\chi K_w}\ln x + \lambda_0 x + C. \tag{43}$$

When the following boundary conditions are implemented, we have

$$x = R_0, p = 0. \tag{44}$$

The integration constant is determined to be

$$C = -\frac{q\beta\varphi\gamma_w}{2\pi\xi h\chi K_w}\ln R_0 - \lambda_0 R_0 \tag{45}$$

By substituting Equation (45) into Equation (43), we obtain

$$p(x) = \frac{q\beta\varphi\gamma_w}{2\pi\xi h\chi K_w}\ln\frac{x}{R_0} + \lambda_0(x - R_0). \tag{46}$$

Equation (46) describes the relationship between the pressure attenuation value and the path distance of the diffusion curve. Three transformations are required to transform this into the relationship between the pressure attenuation value and diffusion distance. First, the function image is shifted to the right by the a factor ofR_0. Then, the ordinate of the function is unchanged, and the abscissa becomes $1/\chi$ the original. Finally, the function image is shifted to the left by a factor of R_0. The transformed function is $p(\chi(x - R_0)$

$+R_0$), and to clarify the difference, the abscissa of the new function is represented by the letter r, representing the slurry diffusion distance, and the ordinate is represented by $\tilde{p}$, representing the slurry pressure attenuation value at the diffusion distance R. Then, the relationship between the pressure attenuation value and the diffusion distance is

$$\tilde{p}(r) = \frac{q\beta\varphi\gamma_w}{2\pi\xi h\chi K_w} \ln \frac{\chi(r-R_0)+R_0}{R_0} + \lambda_0\chi(r-R_0). \quad (47)$$

The pressure attenuation value at the diffusion radius R is

$$\tilde{p}(R) = \frac{q\beta\varphi\gamma_w}{2\pi\xi h\chi K_w} \ln \frac{\chi(R-R_0)+R_0}{R_0} + \lambda_0\chi(R-R_0). \quad (48)$$

Therefore, the initial grouting pressure is

$$p_0 = p_w + \frac{q\beta\varphi\gamma_w}{2\pi\xi h\chi K_w} \ln \frac{\chi(R-R_0)+R_0}{R_0} + \lambda_0\chi(R-R_0). \quad (49)$$

The slurry pressure distribution function, $P(r)$, in the diffusion area is

$$P(r) = p_0 - \tilde{p}(r) = p_w + \frac{q\beta\varphi\gamma_w}{2\pi\xi h\chi K_w} \ln \frac{\chi(R-R_0)+R_0}{\chi(r-R_0)+R_0} + \lambda_0\chi(R-r). \quad (50)$$

However, the grouting diffusion radius, R, is usually unknown, and its calculation formula needs to be deduced. According to Equation (41), when the diffusion radius is R, the slurry column radius is

$$R_0 = \xi R. \quad (51)$$

The volume of the slurry filled in the layer is equal to the total amount of slurry injected, such that

$$\alpha\varphi\pi\left(R^2 - R_0^2\right)h + \pi R_0^2 h = Q. \quad (52)$$

Namely,

$$\left[\xi^2 + \alpha\varphi\left(1-\xi^2\right)\right]\pi R^2 h = Q. \quad (53)$$

Let

$$\eta = \xi^2 + \alpha\varphi\left(1-\xi^2\right), \quad (54)$$

where η is the comprehensive injection rate of the layer.

The grouting diffusion radius can be calculated according to the grouting volume, grouting section height, and comprehensive injection rate of the layer as follows:

$$R = \sqrt{\frac{Q}{\pi h\eta}}. \quad (55)$$

Therefore, the initial grouting pressure is

$$p_0 = p_w + \frac{q\beta\varphi\gamma_w}{2\pi\xi h\chi K_w} \ln \frac{\chi\left(\sqrt{Q/\pi h\eta} - R_0\right) + R_0}{R_0} + \lambda_0\chi\left(\sqrt{\frac{Q}{\pi h\eta}} - R_0\right), \quad (56)$$

and the slurry pressure distribution function, $P(r)$, in the diffusion area is

$$P(r) = p_w + \frac{q\beta\varphi\gamma_w}{2\pi\xi h\chi K_w} \ln \frac{\chi\left(\sqrt{Q/\pi h\eta} - R_0\right) + R_0}{\chi(r-R_0)+R_0} + \lambda_0\chi\left(\sqrt{\frac{Q}{\pi h\eta}} - r\right). \quad (57)$$

3. Results and Discussion

3.1. Field Test Verification and Analysis. To verify the applicability of the cylindrical diffusion model of radial tube flow established in this study, we compared the theoretical calculations with the field test results of ground drilling grouting in the Guotun coal mine. The main, auxiliary, and air shafts of the Guotun coal mine in Shandong Province pass through the loose layer with a thickness of 561.20~587.40 m. After the mine was put into operation, owing to the drainage of the mine, the above three shafts deviated to the asymmetric mining working face of the mine. The maximum deflection displacements of the main shaft and auxiliary shaft to the west were 284 mm and 299 mm, respectively, and the maximum deflection displacements to the north were 30 mm and 103 mm, respectively, which seriously threaten the production safety of the mine. After many demonstrations, it was decided to adopt the scheme of ground drilling grouting around the shaft to control the shaft deflection displacements. The engineering site diagram and schematic diagram of the ground drilling grouting of the vertical shaft are shown in Figure 4. To scientifically formulate the grouting implementation scheme, reasonably select the grouting parameters, and to ensure the safety of the existing shaft, 11 water injection tests and 6 grouting tests were completed in different layers in 7 test holes around the main, auxiliary, and air shafts of the Guotun coal mine. 5 grouting tests were conducted on the water-bearing sand layers over different layers of the loose layer within the 3rd wind inspection hole.

Single cement slurry was used for grouting. The main grouting material is 42.5 ordinary portland cement, which is prepared by adding water to the cement. The water

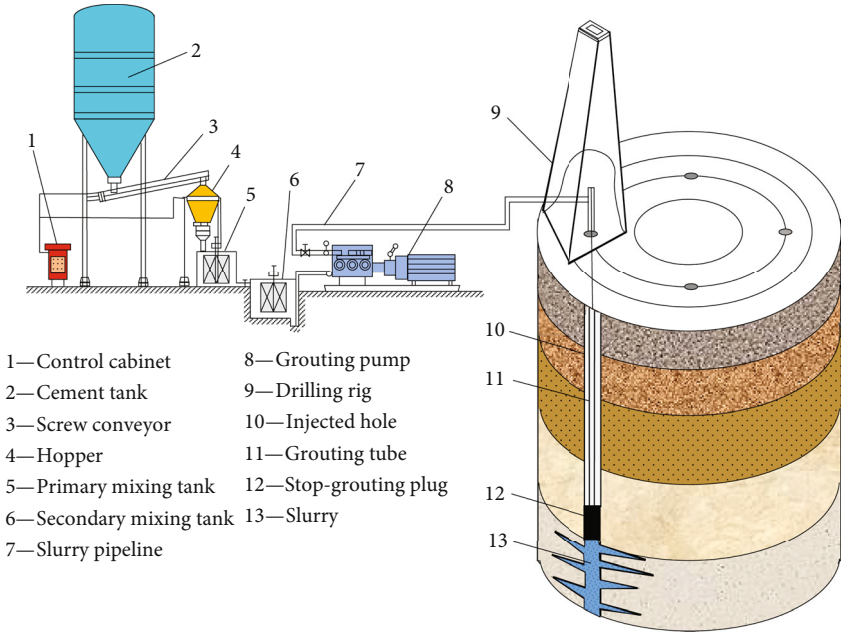

Figure 4: Vertical shaft ground drilling grouting.

Table 1: Physical parameters of the core soil samples taken from the 3rd wind inspection hole.

Soil sample no.	Soil sample type	h (m)	φ	K
01	Fine sand	180.60~180.75	0.3106	1.138
02	Silty sand	281.20~281.35	0.3333	1.126
03	Silty sand	352.15~352.30	0.3154	1.079
04	Fine sand	444.15~444.30	0.3674	1.080
05	Fine sand	552.00~552.35	0.2538	1.824
06	Silty sand	560.20~560.35	0.3637	0.981

Note: h is the coring depth (m), φ is the porosity, and K is the permeability coefficient, 10^{-5} m/s.

cement ratio of slurry used on site is 1.25 : 1 and 1 : 1, and the slurry with water cement ratio of 1 : 1 is mainly used. The physical parameters of the core soil sample taken from the 3rd wind inspection hole are listed in Table 1, and the grouting test results of each grouting section are listed in Table 2.

Substituting the relevant parameters from Tables 1 and 2 into Equation (56), the theoretically calculated values of the initial grouting pressure of the ZJ3, ZJ4, and ZJ5 grouting sections were 9.05 MPa, 7.31 MPa, and 5.46 MPa, respectively, and the associated errors of the initial grouting pressure values in Table 2 were -9.41%, 9.27%, and 13.75%, respectively. Substituting the relevant parameters from Tables 1 and 2 into Equation (55), the theoretically calculated values of the diffusion radius of the ZJ3 to ZJ5 grouting sections were 6.57 m, 6.35 m, and 6.84 m, respectively, and the errors of the design value were -17.88%, -20.63%, and -14.50%, respectively, which are all within the engineering acceptable range [35–37], thus verifying the rationality of the theoretical model proposed in this study.

3.2. Slurry Pressure Attenuation Law. Substituting the relevant parameters from Tables 1 and 2 into Equation (57), the slurry pressure distribution curves in the diffusion zone of the ZJ3 to ZJ5 grouting sections were obtained, as shown in Figure 5. The attenuation of the slurry pressure has distinguishable stages, which decrease sharply near the grouting tube and gradually away from the grouting tube. We calculated the slurry pressure value, pressure attenuation value, and attenuation percentage at different diffusion distances, where the calculation results are listed in Table 3. At a diffusion distance of 1 m, the slurry pressure attenuation of the ZJ3 to ZJ5 grouting sections were 60.32%, 60.52%, and 51.67% of the total pressure attenuation within the diffusion range, respectively. At a diffusion distance of 2 m, the slurry pressure attenuation of the ZJ3 to ZJ5 grouting sections were 74.51%, 74.89%, and 68.61% of the total pressure attenuation within the diffusion range, respectively. Beyond a diffusion distance of 2 m, the attenuation rate of the slurry pressure slows down, which is approximately a low-speed linear attenuation. Within the first 30% of the diffusion radius, the slurry pressure decreases sharply by approximately 70%; within the last 70% of the diffusion radius, the slurry pressure decreases gradually to the remaining 30%. This relationship is consistent with the engineering practices and trends of the measured data within the relevant literature [38–40]. The reason for this is that there is a high velocity of the slurry in the area close to the grouting tube, and a lower velocity of the slurry in the area far away from the grouting tube. According to Equation (32), the slurry pressure gradient is linearly and positively correlated with the slurry velocity;

Table 2: Grouting test results of the 3rd wind inspection hole.

Grouting section no.	H (m)	t (h)	p_0 (MPa)	Q (m^3)	R (m)	Diffusion radius calculation error (%)
ZJ5	175.05~196.11	31.30	4.24~4.80	290	6.83	-14.63
ZJ4	247.34~282.00	26.40	4.89~6.69	220	6.34	-20.75
ZJ3	332.27~364.27	23.50	7.18~9.99	206	6.57	-17.88
ZJ2	430.33~462.43	22.40	8.73~13.40	140	—	—
ZJ1	540.46~574.90	20.50	11.82~13.92	166	—	—

Note: H is the depth of the grouting section, t is the grouting time, p_0 is the injection point pressure, Q is the grouting amount, and R is the theoretically calculated value of the diffusion radius. Owing to the first grouting in the ZJ1 grouting section, the grouting was stopped when only 166 m^3 of slurry was injected, and the grouting in the ZJ2 grouting section was stopped when only 140 m^3 of slurry was injected, owing to the slurry leakage from the stop-grouting plug.

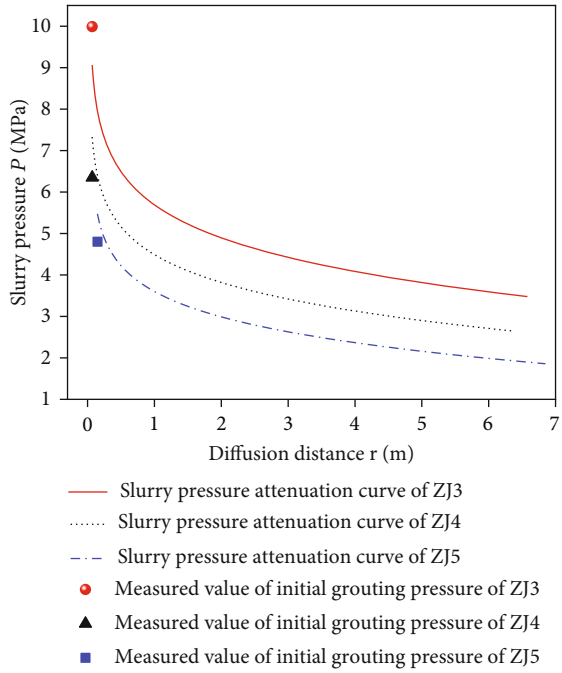

Figure 5: Pressure attenuation law of slurry.

Table 3: Slurry pressure attenuation.

Parameters	Grouting section	0	1 m	2 m	R
$P(r)$ (MPa)	ZJ3	9.05	5.69	4.90	3.48
	ZJ4	7.31	4.49	3.82	2.65
	ZJ5	5.46	3.60	2.99	1.86
$\tilde{p}(r)$ (MPa)	ZJ3	0	3.36	4.15	5.57
	ZJ4	0	2.82	3.49	4.66
	ZJ5	0	1.86	2.47	3.60
$\tilde{p}(r)/p_0 - p_w$ (%)	ZJ3	0	60.32	74.51	100
	ZJ4	0	60.52	74.89	100
	ZJ5	0	51.67	68.61	100

so, the pressure gradient decreases gradually along the diffusion direction; specifically, and the pressure decreases more slowly.

3.3. Analysis of Influencing Factors on the Diffusion Radius. When considering the field grouting parameters of the Guotun coal mine combined with Equation (55), the effects of grouting volume, grouting section height, and comprehensive layer injection rate on the grouting diffusion radius are discussed. The comprehensive layer injection rates were 0.05, 0.06, 0.07, 0.08, and 0.09, the grouting volume was 200 m^3, 250 m^3, 300 m^3, 350 m^3, and 400 m^3, and the heights of the grouting sections were 20 m, 25 m, 30 m, 35 m, and 40 m.

When the grouting section height is taken to be 30 m, the influence of the grouting volume and the comprehensive layer injection rate on the slurry diffusion radius was studied, as shown in Figure 6(a). When the comprehensive layer injection rate is taken to be 0.07, the influence of the grouting volume and grouting section height on the slurry diffusion radius is studied, as shown in Figure 6(b). When the grouting volume was 300 m^3, the influence of the grouting section height and comprehensive layer injection rate on the slurry diffusion radius was studied, as shown in Figure 6(c).

As can be seen from Figures 6(a) and 6(b), when the same grouting section height and comprehensive layer injection rate are considered, the diffusion radius increases with an increasing grouting volume, but the growth range gradually decreases. The possibility of improving the slurry diffusion radius solely by increasing the grouting volume gradually decreases. According to Figures 6(a)–6(c), the diffusion radius has a nonlinear negative correlation with the grouting section height and the comprehensive layer injection rate, the rate of change is relatively slow, and there are no distinguishable stages. Under the condition of the same grouting volume and grouting section height, it was found that increasing the comprehensive layer injection rate reduces the diffusion radius, while the grouting volume in the unit volume soil layer increases, which can effectively improve the mechanical properties of the injected layer. In engineering, multiple grouting parameters are usually coordinated and controlled to achieve the designed diffusion radius and reinforcement strength. For example, before formal grouting on site, water injection tests are often carried out to increase the hydraulic permeability of the layer, which can improve the comprehensive layer injection rate. Accordingly, the design grouting

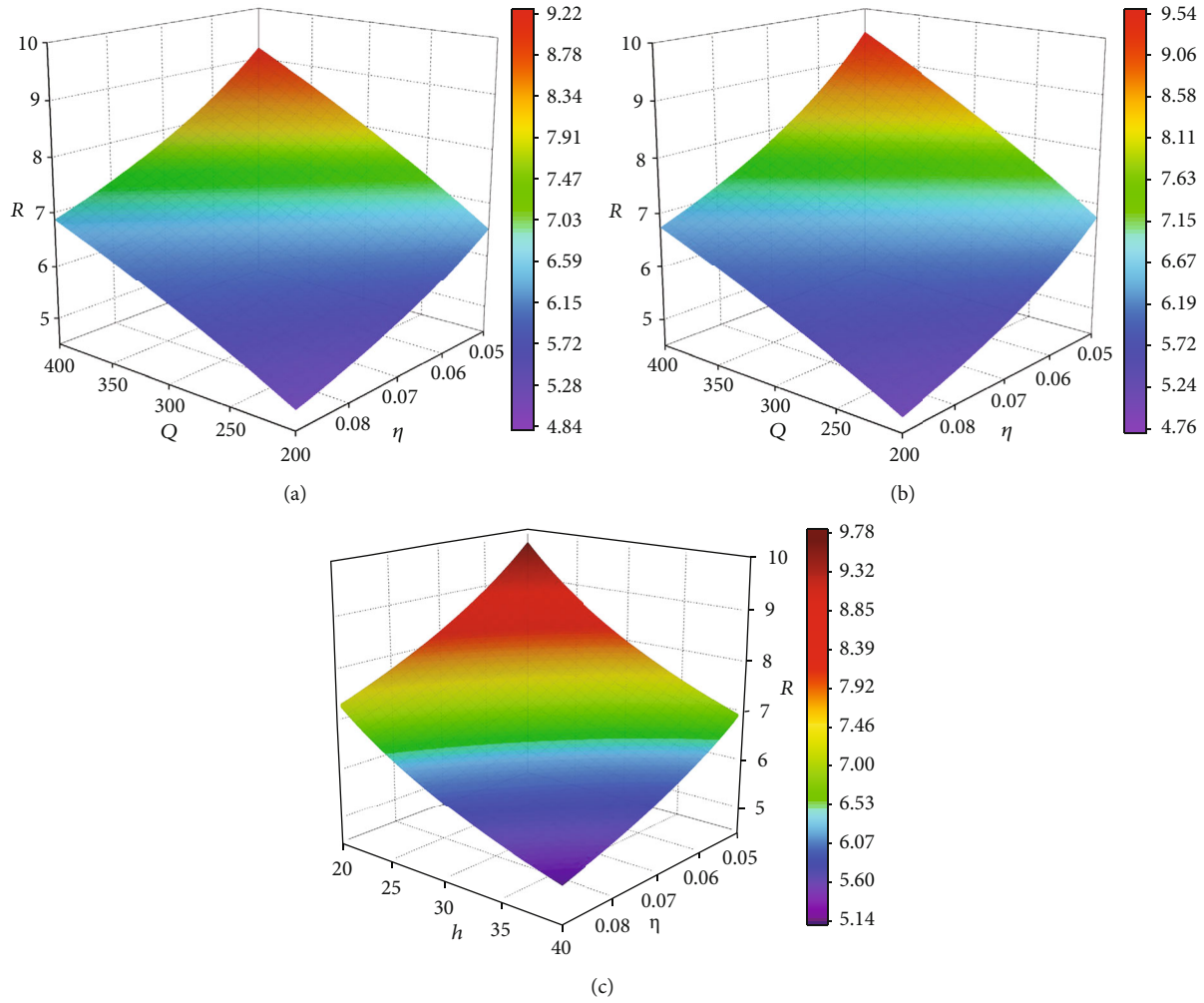

Figure 6: Analysis of the influencing factors of the grouting diffusion radius. (a) $R - Q - \eta$ 3D function image. (b) $R - Q - h$ 3D function image. (c) $R - h - \eta$ 3D function image.

volume should also be increased to achieve the desired grouting diffusion radius.

4. Conclusions

(1) The cylindrical diffusion of grouting in the deep, loose layer is regarded as the flow diffusion of slurry in a certain number of tortuous circular tubes radiated by the slurry column. The cylindrical diffusion model of the radial tube flow in a deep, loose layer is established, and the variation laws of key parameters such as slurry pressure and diffusion radius in the process of grouting are realized

(2) The permeability coefficient considering tortuosity is derived, and the average radius of the seepage tubes in the injected layer is equivalently replaced by the permeability coefficient. The diffusion velocity approximate control differential equation of the Bingham slurry in a single tube, the diffusion velocity control equation of the radiation tube flow, and the slurry pressure distribution function in the diffusion area are obtained

(3) By combining the model results with the field grouting test results in the Guotun coal mine, the rationality of the cylindrical diffusion model of radial tube flow was verified, and the attenuation law of the grouting pressure in the diffusion area is obtained. It was found that the attenuation of the slurry pressure exhibits distinguishable stages. Within the first 30% of the diffusion radius, the slurry pressure decreases sharply by approximately 70%; within the last 70% of the diffusion radius, the slurry pressure decreases gradually to the remaining 30%

(4) The calculation formula of the grouting diffusion radius is deduced, and the effects of the grouting volume, grouting section height, and comprehensive layer injection rate on the grouting diffusion radius are discussed. It is found that the diffusion radius

has a nonlinear positive correlation with the grouting volume, but the corresponding growth range gradually decreases. The diffusion radius has a nonlinear negative correlation with the grouting section height and the comprehensive layer injection rate; the rate of change is relatively low, and no distinguishable stages are observed

Data Availability

The data used to support the findings of this study are available from the corresponding author upon request.

Conflicts of Interest

The authors declare that there are no conflicts of interest regarding the publication of this paper.

Acknowledgments

The authors gratefully acknowledge the financial support of the National Natural Science Foundation of China (No. 51874005, No. 51674006, No. 51878005).

References

[1] P. Li, Q. S. Zhang, S. C. Li, and X. Zhang, "Time-dependent empirical model for fracture propagation in soil grouting," *Tunnelling and Underground Space Technology*, vol. 94, p. 103130, 2019.

[2] A. T. C. Goh, "Deterministic and reliability assessment of basal heave stability for braced excavations with jet grout base slab," *Engineering Geology*, vol. 218, pp. 63–69, 2017.

[3] A. Sohrabi-Bidar, A. Rastegar-Nia, and A. Zolfaghari, "Estimation of the grout take using empirical relationships (case study: Bakhtiari dam site)," *Bulletin of Engineering Geology and the Environment*, vol. 75, no. 2, pp. 425–438, 2016.

[4] B. Ren, W. Mu, B. Jiang et al., "Grouting mechanism in water-bearing fractured rock based on two-phase flow," *Geofluids*, vol. 2021, Article ID 5585288, 18 pages, 2021.

[5] P. Li, Q. Zhang, X. Zhang, S. Li, X. Li, and J. Zuo, "Grouting diffusion characteristics in faults considering the interaction of multiple grouting," *International Journal of Geomechanics*, vol. 17, no. 5, p. 04016117, 2017.

[6] G. Zhu, Q. Zhang, R. Liu, J. Bai, W. Li, and X. Feng, "Experimental and numerical study on the permeation grouting diffusion mechanism considering filtration effects," *Geofluids*, vol. 2021, Article ID 6613990, 11 pages, 2021.

[7] X. Du, H. Fang, S. Wang, B. Xue, and F. Wang, "Experimental and practical investigation of the sealing efficiency of cement grouting in tortuous fractures with flowing water," *Tunnelling and Underground Space Technology*, vol. 108, p. 103693, 2021.

[8] X. Liu, H. Cheng, J. Lin, C. Rong, M. Li, and H. Xu, "Study of the mechanism of fracture grouting in deeply buried rock strata based on Bingham fluid slurry," *Advances in Civil Engineering*, vol. 2019, Article ID 6943239, 10 pages, 2019.

[9] H. Cheng, X. Liu, J. Lin, L. Zhang, M. Li, and C. Rong, "Study on fracturing and diffusion mechanism of nonslab fracturing grouting," *Geofluids*, vol. 2020, Article ID 8838135, 9 pages, 2020.

[10] W. Mu, L. Li, T. Yang, G. Yu, and Y. Han, "Numerical investigation on a grouting mechanism with slurry-rock coupling and shear displacement in a single rough fracture," *Bulletin of Engineering Geology and the Environment*, vol. 78, no. 8, pp. 6159–6177, 2019.

[11] Z. Zhao, T. Wang, and X. Jin, "Study on permeation grouting rules for loess and method for predicting migration radius," *KSCE Journal of Civil Engineering*, vol. 25, no. 8, pp. 2876–2883, 2021.

[12] G. N. Karahan and O. Sivrikaya, "Designing singular jet grouting column for sandy soils," *Environmental Earth Sciences*, vol. 77, no. 12, pp. 1–11, 2018.

[13] Y. Fu, X. Wang, S. Zhang, and Y. Yang, "Modelling of permeation grouting considering grout self-gravity effect: theoretical and experimental study," *Advances in Materials Science and Engineering*, vol. 2019, Article ID 7968240, 16 pages, 2019.

[14] K. Fang, T. Zhao, Y. Tan, and Y. Qiu, "Prediction of grouting penetration height along the shaft of base grouted pile," *Journal of Marine Science and Engineering*, vol. 7, no. 7, p. 212, 2019.

[15] J. Yun, J. Park, Y. Kwon, B. Kim, and I. Lee, "Cement-based fracture grouting phenomenon of weathered granite soil," *KSCE Journal of Civil Engineering*, vol. 21, no. 1, pp. 232–242, 2017.

[16] N. Shrivastava and K. Zen, "Finite element modeling of compaction grouting on its densification and confining aspects," *Geotechnical and Geological Engineering*, vol. 36, no. 4, pp. 2365–2378, 2018.

[17] Z. Wang, J. Zou, and H. Yang, "A new approach for the fracture grouting pressure in soil mass," *Advances in Mechanical Engineering*, vol. 10, 2018.

[18] Z. Zhou, X. Du, Z. Chen, Y. Zhao, and L. Chen, "Grout dispersion considering effect of pore tortuosity," *The Chinese Journal of Nonferrous Metals*, vol. 26, no. 8, pp. 1721–1727, 2016.

[19] Q. Zhang, H. Wang, R. Liu et al., "Infiltration grouting mechanism of porous media considering diffusion paths of grout," *Chinese Journal of Geotechnical Engineering*, vol. 40, no. 5, pp. 918–924, 2018.

[20] X. Chen and C. Yuan, "Law of columnar penetration of Bingham type slurry in porous media," *Journal of Mining and Safety Engineering*, vol. 38, no. 4, pp. 800–809, 2021.

[21] J. Liu, Q. Zhang, L. Zhang, F. Peng, Z. Li, and X. Weng, "Model test on segmental grouting diffusion process in muddy fault of tunnel engineering," *Geofluids*, vol. 2020, 12 pages, 2020.

[22] B. Ren, L. Wang, H. Fan, K. Ding, K. Wang, and C. Jiang, "Unsteady approximate model of grouting in fractured channels based on Bingham fluid," *Geofluids*, vol. 2021, Article ID 6671982, 13 pages, 2021.

[23] J. Liu, K. Yuen, W. Chen, X. Zhou, and W. Wang, "Grouting for water and mud inrush control in weathered granite tunnel: a case study," *Engineering Geology*, vol. 279, p. 105896, 2020.

[24] X. Huang, Z. Yao, H. Cai, X. Li, and H. Chen, "Performance evaluation of coaxial borehole heat exchangers considering ground non-uniformity based on analytical solutions," *International Journal of Thermal Sciences*, vol. 170, p. 107162, 2021.

[25] R. T. Grotenhuis, *Fracture Grouting in Theory: Modelling of Fracture Grouting in Sand*, Delft University of Technology, Delft, 2004.

[26] A. Bezuijen, R. T. Grotenhuis, A. F. V. Tol, J. W. Bosch, and J. K. Haasnoot, "Analytical model for fracture grouting in

sand," *Journal of Geotechnical and Geoenvironmental Engineering*, vol. 137, no. 6, pp. 611–620, 2011.

[27] S. Wang, B. Yu, Q. Zheng, Y. Duan, and Q. Fang, "A fractal model for the starting pressure gradient for Bingham fluids in porous media embedded with randomly distributed fractal-like tree networks," *Advances in Water Resources*, vol. 34, no. 12, pp. 1574–1580, 2011.

[28] X. Y. Kong, *Advanced Seepage Mechanics*, China University of Science and Technology Press, Hefei, 2020.

[29] E. A. Saied and M. E. Khalifa, "Some analytical solutions for groundwater flow and transport equation," *Transport in Porous Media*, vol. 47, no. 3, pp. 295–308, 2002.

[30] P. K. Kundu, I. M. Cohen, and D . Dowling, *Fluid Mechanics*, American Academic Press, Waltham, 2016.

[31] C. Li and X. Zhang, "Unification of flow equations in tubes and in porous media," *Xinjiang Petroleum Geology*, vol. 28, no. 2, pp. 252-253, 2007.

[32] L. Chen, Q. Kang, R. Pawar, Y. He, and W. Tao, "Pore-scale prediction of transport properties in reconstructed nanostructures of organic matter in shales," *Fuel*, vol. 158, pp. 650–658, 2015.

[33] D. Fan and A. Ettehadtavakkol, "Analytical model of gas transport in heterogeneous hydraulically-fractured organic-rich shale media," *Fuel*, vol. 207, pp. 625–640, 2017.

[34] M. Chang and R. Huang, "Observations of hydraulic fracturing in soils through field testing and numerical simulations," *Canadian Geotechnical Journal*, vol. 53, no. 2, pp. 343–359, 2016.

[35] J. I. Adachi and E. Detournay, "Plane strain propagation of a hydraulic fracture in a permeable rock," *Engineering Fracture Mechanics*, vol. 75, no. 16, pp. 4666–4694, 2008.

[36] Q. Zhang, L. Zhang, R. Liu, S. Li, and Q. Zhang, "Grouting mechanism of quick setting slurry in rock fissure with consideration of viscosity variation with space," *Tunnelling and Underground Space Technology*, vol. 70, pp. 262–273, 2017.

[37] Z. Zhang, H. Xie, R. Zhang et al., "Deformation damage and energy evolution characteristics of coal at different depths," *Rock Mechanics and Rock Engineering*, vol. 52, no. 5, pp. 1491–1503, 2019.

[38] B. Xue, X. Du, J. Wang, and X. Yu, "A scaled boundary finite-element method with B-differentiable equations for 3D frictional contact problems," *Fractal and Fractional*, vol. 6, no. 3, p. 133, 2022.

[39] Z. Wang, S. Shen, C. Ho, and Y. Kim, "Investigation of field-installation effects of horizontal twin-jet grouting in Shanghai soft soil deposits," *Canadian Geotechnical Journal*, vol. 50, no. 3, pp. 288–297, 2013.

[40] L. P. Chegbeleh, T. M. Akabzaa, J. A. Akudago, and S. M. Yidana, "Investigation of critical hydraulic gradient and its application to the design and construction of bentonite-grout curtain," *Environmental Earth Sciences*, vol. 78, no. 12, 2019.

Hindawi
Geofluids
Volume 2022, Article ID 7751265, 10 pages
https://doi.org/10.1155/2022/7751265

Research Article

A Study of Dynamic Loading and Unloading Damage of Fiber-Reinforced Concrete under Confining Pressure

Chao Lin,[1] **Li Rao**,[1] **Cheng-Lin Zhang**,[1] **Zhi-Wen Yang**,[1] **Fang Chen**,[1] **Qing You**,[1] **and Xian-Jun Tan**[2]

[1]*Physical Science and Technology College, Yichun University, Yichun 336000, Jiangxi, China*
[2]*Institute of Rock and Soil Mechanics, Chinese Academy of Sciences, Wuhan, Hubei 430000, China*

Correspondence should be addressed to Li Rao; raoli-ycu@hotmail.com

Received 10 November 2021; Revised 6 January 2022; Accepted 28 January 2022; Published 2 March 2022

Academic Editor: Xueming Du

Considering the influence of confining pressure in the actual service environment of concrete in underground projects, the damage characteristics of fiber-reinforced concrete under the action of confining pressure are evaluated according to the variation of measured permeability values by means of a triaxial ultralow permeability damage test system. The tests were carried out according to the stress loading and unloading paths of 1⟶5⟶10⟶15⟶20⟶10⟶5⟶1 MPa for an axial pressure when the confining pressure value was 1 MPa and kept constant. Firstly, the damage permeability of the fiber-reinforced concrete specimens was verified to be significantly lower than that of the ordinary concrete under the same confining pressure. Secondly, by conducting single loading and unloading tests at different loading rates (0.5, 1.0, 1.5, and 3.0 MPa/s), it was confirmed that the loading rate had a significant effect on the damage cracking of the specimens, with the faster the loading rate, the more pronounced the damage characteristics. Finally, a triaxial cyclic dynamic load test with a confining pressure value of 1 MPa and an axial loading speed of 1.5 MPa/s was carried out, revealing that the damage characteristics of the test blocks changed from elastic deformation to obvious plastic deformation damage as the number of loading times increased.

1. Introduction

As a new type of building material, fiber-reinforced concrete has good crack resistance and corresponding durability, enjoying a wide application prospect in the development of urban underground space [1]. During the actual service period, the fiber-reinforced concrete structure of urban underground engineering is in a complex stress environment, and the damage and cracking characteristics of the fiber-reinforced concrete structure under multiaxial stress conditions are different from those under uniaxial action mode. In actual working conditions, the fiber-reinforced concrete structure of urban underground engineering will be affected by certain confining pressure. Confining pressure has a certain synergistic effect on controlling plastic deformation of the fiber-reinforced concrete structure and improving elastic limit [2, 3]. The fiber-reinforced concrete specimen is a typical strain rate-sensitive material. Under the condition of dynamic loading, the damage stress state of the fiber-reinforced concrete test blocks is no longer similar to the conventional quasi-static state. For example, under the conditions of high-speed loading and cyclic dynamic loading, the loading speed has a great influence on the degree of damage and cracking. Therefore, it is necessary to discuss the dynamic mechanical damage performance of fiber-reinforced concrete materials [4–7].

In the study of dynamic damage mechanism of quasi-brittle materials under confining pressure, Liu [8] studied the impact dynamic load mechanical properties of amphibolite under different confining pressure values (0 MPa~2 MPa) and different strain rates. The results show that under the same confining pressure, with the increase of strain rate, the dynamic compressive strength of amphibolite shows a linear increase trend, which conforms to the strain rate correlation of strength, and the dynamic enhancement factor is approximately linear with the logarithm of strain rate. Within the same strain rate range, as the confining pressure increases, the strength enhancement effect becomes

more obvious, showing a stronger confining pressure restraint effect. Lu and Wang [9] studied the loading damage test of biotite granite under the conditions of 0 MPa~3 MPa confining pressure and medium and high strain rate. The test results show that when the confining pressure is constant, the dynamic compressive strength of granite increases logarithmically with the increase of strain rate, and the peak strain also increases with the increase of strain rate; the elastic modulus is poorly sensitive to confining pressure and strain rate, and the greater the strain rate, the more severe the rock fragmentation phenomenon under the premise of a constant strain rate, the dynamic compressive strength of granite rapidly increases with the increase of confining pressure, and the failure mode of the material changes from axial splitting under low confining pressure to compression-shear failure under high confining pressure; under high confining pressure, the stress-strain curve of granite has obvious brittle-ductile transition characteristics. Li [10] simulated the damage, deformation, strength evolution, and other failure characteristics of the circular roadway under the conventional triaxial constraint for three kinds of thick-walled cylindrical sandstone samples. Zhang [11] used the thick-walled cylindrical test block; after unloading the inner cavity load, continued to unload the outer cavity load of the undamaged thick-walled cylindrical limestone test block; and conducted a preliminary research on the unloading failure mode. Wu [10, 12] carried out loading and unloading tests of limestone test blocks under different confining pressures, focusing on the failure mode of the samples under the condition of pressure relief in the hole, and revealed the damage failure mechanism.

Jia [13], based on the triaxial test of salt rock under multiple sets of confining pressures, used hyperbolic equations to fit the tensile and shear Mohr–Coulomb criteria to correct the sharp angle on the yield surface. The effects of the damage and confining pressure were added to the improved Mohr–Coulomb criterion, which can describe the mechanical characteristics of strain hardening, softening, and brittle-plastic transition of salt rock under different confining pressures. Zhou [14] obtained the quantitative relationship between elastic modulus and confining pressure and internal variables based on the cyclic loading test of Jinping marble. Based on the Mohr–Coulomb criterion, the law of internal friction angle and cohesion with internal variables is obtained. The internal friction angle in the yield function is replaced by the dilatancy angle to establish a plastic potential function. According to the noncorrelated flow rule, an elastoplastic coupled constitutive model of marble considering the confining pressure effect is given. The model can reflect the expansion characteristics of the rock with the change of confining pressure, but it uses many undetermined parameters, and because the research object is Jinping marble, the model is based on test results, and whether it is applicable to other rocks needs further verification. Wu and Li [15] produced a number of cylindrical concrete specimens and wrapped FRP cloth around the concrete specimens to limit the radial deformation during concrete loading. The deformation of concrete under multiaxial action was studied, and the reciprocating loading effect was obtained. Under the stress-strain curve, the confining pressure of the FRP sheet on concrete was studied.

In order to study the influence of confining pressure constraint and loading speed on the damage and cracking law of fiber-reinforced concrete, we carried out dynamic loading and unloading damage penetration tests of fiber-reinforced concrete under confining pressure [16–21]. Under the condition of constant confining pressure of 1 MPa and loading speed (0.5, 1.0, 1.5, and 2.0 MPa/s), a triaxial loading mechanical damage test of test blocks was carried out to study the influence of loading speed change on the damage degree of test blocks. Furthermore, triaxial multiple cyclic loading tests with confining pressure of 1 MPa and axial loading speed of 1.5 MPa/s were carried out to reveal the evolution law of damage penetration of test blocks with the increase of loading and unloading times.

2. Principle of Ultralow Permeability Damage Test under Confining Pressure

The appearance of internal cracks of fiber-reinforced concrete structures after loading damage will reduce impermeability. The permeability change rule obtained from triaxial loading stress measurement can more truly reflect the actual situation of internal loading damage and cracking of fiber-reinforced concrete [22–25]. Due to the quality of raw materials, construction operations, curing conditions, and other factors, it is difficult to avoid microcracks after pouring and molding. Except for surface cracks, microcracks in the concrete matrix are difficult to find and identify. Therefore, with the help of ultralow permeability damage testing system, the research on dynamic loading damage mechanism of fiber-reinforced concrete test blocks under confining pressure is conducted. The absolute permeability of that fiber-reinforced concrete specimen is obtained from the experiment, and the permeability measurement of the specimen is carried out based on Darcy's law, and the gas used is high purity nitrogen. The dynamic loading damage mechanism of test blocks under confining pressure is revealed through the laboratory nitrogen steady-state test evaluation.

For the calculation equation of nitrogen permeability in a stable state, it is to necessary take into account the influence of gas slip and inertial resistance, which is beneficial for the calculation equation to coincide with the actual situation of a gas stable state. In terms of the means of gas permeability measurement, nitrogen is used as the permeable medium of test block loading damage, and the following factors need to be considered: nitrogen is characterized by high compression. In a normal test environment, the relative density of a gas is relatively low. The influence of gravity factors can be ignored in the measured calculation of damage permeability. Nitrogen, under the pressure, enjoys fast flow speed at the crack position of the test block, and thus the slip speed of nitrogen needs to be considered.

Generally, the principle of nitrogen permeability calculation formula is based on the characteristics of homogeneity, isotropy, and temperature commonness of the internal medium of the test block. In actual working

conditions, the material characteristics of the test block are difficult to meet the ideal requirements, and the test block is usually calculated as a cylinder. According to the corresponding relationship between the calculation direction of damage permeability and axial space, the actual calculation is mainly divided into two types: axial damage permeability is parallel to the axial direction of the test block based on the measured direction; Radial damage permeability can be defined as transverse damage permeability based on the measured direction, which is consistent with the cross-section of the test block.

The mathematical model for calculating the damage and permeability of steady-state test blocks loaded with nitrogen can be described as follows:

$$k_g = \frac{2\mu p_r q_r}{G_f (p_1 - p_2)(p_1 + p_2)}, \quad (1)$$

where k_g is the measured value of permeability of the test block, $e-16\,\mathrm{m}^2$; p_r is the pressure under the measured environment, pa; q_r is the measured nitrogen flow velocity per unit volume; p_1 is the pressure upstream of the test block inlet, pa; p_2 is the downstream pressure of the test block outlet, pa; and G_f is a geometric revision factor.

$$G_f = \frac{\pi r^2}{L}, \quad (2)$$

where r is the radius of the test block, m and L is the length of the test block, m.

Brief description of nitrogen slip effect: In the actual measurement and calculation of low permeability materials, the slip effect of nitrogen is obvious, and Klinkenberg relation is usually used to correct the calculation of damage permeability as follows:

$$\mathrm{k}_g = k_s\left(1 + \frac{b}{p_m}\right), \quad (3)$$

where k_s is the inherent permeability of the medium inside the test block, p_m is the average pressure of the test block, and b is the uniform unit constant.

In the test, the upstream gas pressure is controlled by the pressure-reducing valve, and the downstream end is directly connected with the atmosphere. At the same time, the loading stress state of the test block is changed; the state information and flow rate information of the test block are collected and recorded; and the damage permeability of the fiber-reinforced concrete test block is calculated.

3. Test Preparation

3.1. Experimental Equipment. The experiment adopts a constant temperature ultralow permeability damage test system, and the accuracy can reach $1e-23\,\mathrm{m}^2$. The whole set of equipment is accurate in control and collection with a high degree of automation and thus can realize accurate measurement of permeability of low permeability medium. The partition arrangement of the test system is shown in Figure 1. The whole system consists of a pressure control system, pipeline and clamper system, data acquisition, recording system, and so on. The pressure control system is composed of axial pressure, confining pressure control system, and air pressure control system. The axial and confining pressure are controlled by two ISCO pressure pumps, while the gas pressure is controlled by a gas pressure reducing valve connected with the gas cylinder. The pipeline system is also composed of two parts: one is a confining and axial pressure control pipeline (transmit confining pressure and axial pressure) and the other is a gas migration pipeline (transport high purity gas used for infiltration). The clamper system consists of a rubber sleeve, a containing cavity, a cushion block, and the like, wherein the cylindrical sample is placed in the rubber sleeve, the cushion block is placed into the clamping sample from the upper and lower ends, and then the rubber jacket is placed in the containing cavity; The data acquisition and recording system consists of an electronic balance that automatically records reading books and a control system of a computer terminal. This system records various data in the test.

The steady-state method was adopted for the test block loading gas permeability test, and the permeability gas was high purity nitrogen. The gas permeability test not only studied the influence of fiber addition on the permeability of fiber-reinforced concrete but also studied the influence law of axial stress on the permeability of fiber-reinforced concrete test block. Considering the actual working conditions, infrastructure projects with shallow burial depth and low confining pressure are adopted for the development of urban underground space. The actual confining pressure of 1~2 MPa is reasonable for the site selection environment. During the test, the test block was put into the clamping system first, and the pipeline connection was normal, so as to maintain the tightness of the clamping chamber and prevent the leakage of pressure liquid. The pressure load was slowly applied to the test block in the form of step loading; the confining pressure pump kept the set pressure unchanged; and the axial pressure is set to step loading and unloading mode. According to the influence law of triaxial loading on the damage permeability of the test block, the loading stress path shall be 1⟶5⟶10⟶15⟶20⟶10⟶5⟶1 MPa. The gas pressure at the upstream of the test block was 0.5 MPa, and we recorded the volume of permeated gas at the downstream by drainage method and converted the mass of discharged boiled water into the gas volume by electronic balance. The computer terminal automatically collected the data of the electronic balance and processed it into flow data for storage.

3.2. Preparation of Test Block. We cured the fiber-reinforced concrete standard cube test block that has been poured and cured to 28 days old. Then, the test block was made into a cylindrical test block with a diameter of 50 mm and a height of 40 mm (error control within ±1 mm) through drilling core and surface polishing. The test block parameters are shown in Table 1. Parallel control tests are required for fiber-reinforced concrete test blocks with the same content. The physical picture of the test blocks used in the damage penetration test is shown in Figure 2(a), and the schematic diagram of the loading direction of the test block is shown in Figure 2(b).

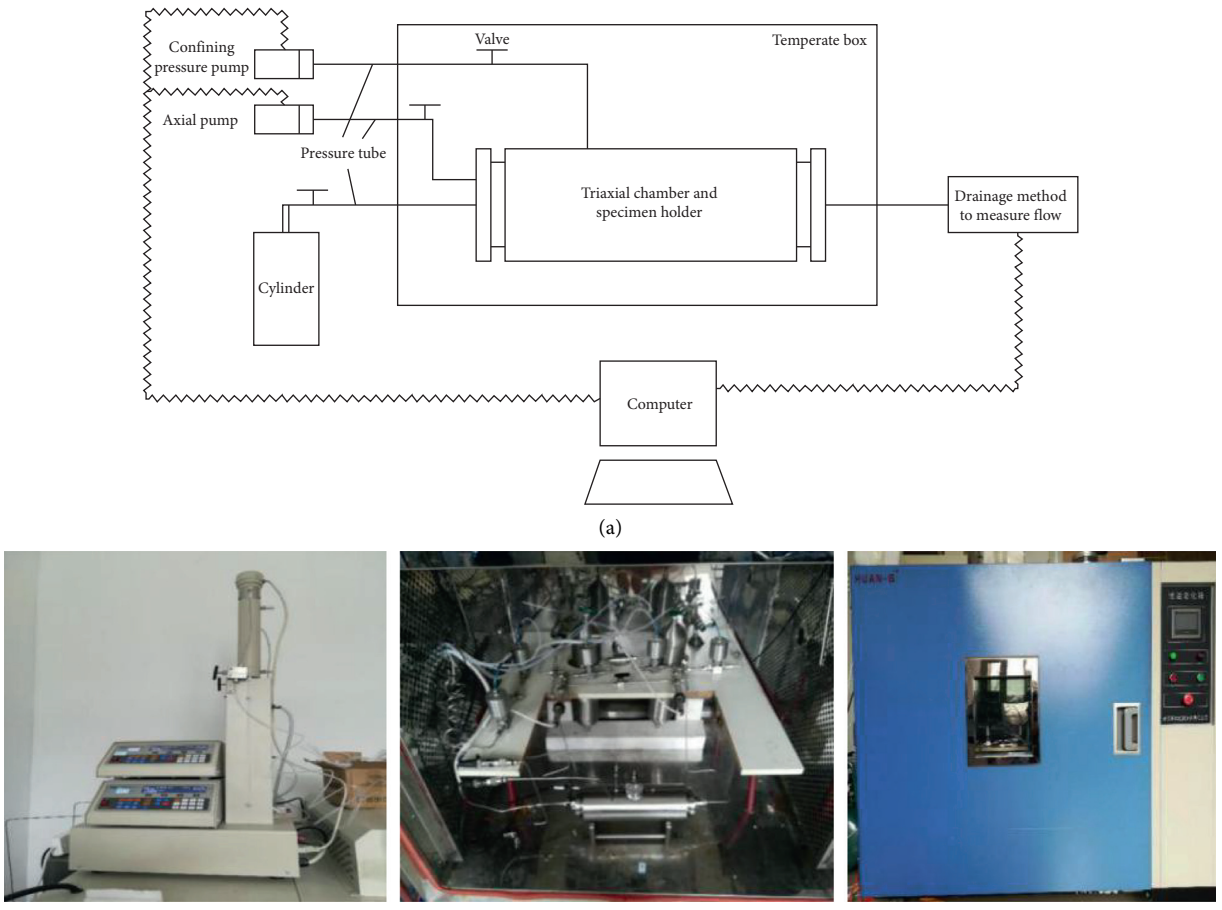

Figure 1: Ultralow permeability damage test system: (a) schematic diagram and (b) physical picture.

Table 1: Test block parameters of damage penetration loading test under confining pressure.

Number	Strength level	Test blocks number (n)	Fiber content (kg/m^3)	Test block size	
				Diameter (mm)	Height (mm)
C50S1.2-1	C50	16	1.2	50	40
C50S1.2-2	C50	16	1.2	50	40
C50S0-1	C50	16	0	50	30
C50S0-2	C50	16	0	50	30

In order to improve the measurement accuracy of dynamic loading damage permeability of fiber-reinforced concrete test blocks under confining pressure, it is necessary to place the prepared concrete test blocks in an oven at 60°C for 12 h, remove free moisture in the test blocks, let them cool down naturally, and store them in plastic sealed bags for subsequent tests.

4. Study of Loading and Unloading Damage Penetration of Test Blocks under Confining Pressure

4.1. Study of Damage and Penetration of Test Blocks under Static Loading and Unloading. According to the GB50081-2002 Test Method for Mechanical Properties of Concrete, when the strength grade of concrete is between C30 and C60, the static loading speed should be controlled at 0.5~0.8 MPa/s. This section focuses on the evaluation of damage characteristics of test blocks under static confining pressure, and the loading speed is controlled at 0.5 MPa/s. We carried out the load damage permeability test of the test block when the confining pressure value is 1 MPa with C50S1.2 fiber-reinforced concrete test block and C50S0 ordinary concrete test block (the measured number of test blocks in each group is 2), and the loading speed was 0.5 MPa/s. The measured data are shown in Table 2. The measured data curve of the damage permeability test of fiber-reinforced concrete test block under the condition of single loading and unloading is shown in Figure 3.

As can be seen from Figure 3, both the fiber-reinforced concrete test block and the ordinary concrete test block show that the permeability increases with the increase of axial

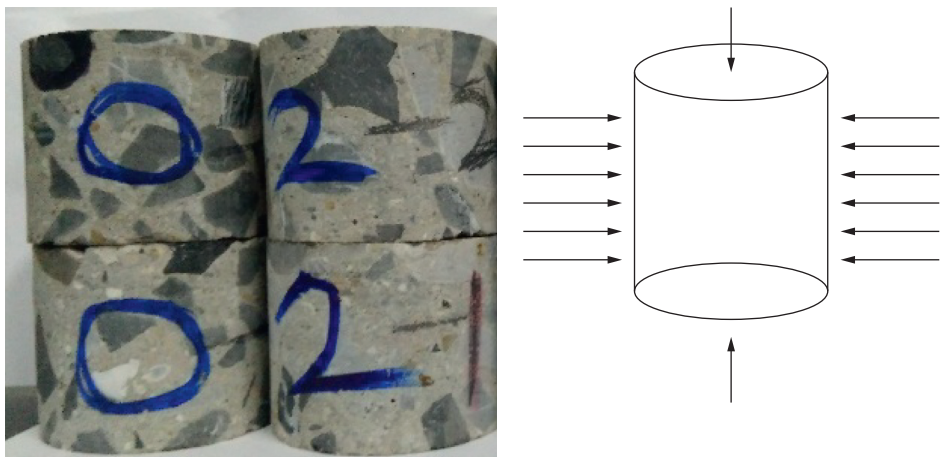

(a) (b)

Figure 2: (a) Physical picture of the test blocks in the damage permeation loading test and (b) schematic diagram of confining pressure and axial loading of the test block.

Table 2: Measured permeability of single loading and unloading test (the confining pressure value is 1 MPa).

Axial Load (MPa)	C50S1.2-1	C50S1.2-2	C50S0-1	C50S0-2
		Measured value of permeability ($e-16\ m^2$)		
1	2.65	2.37	2.66	2.54
5	3.12	2.60	3.05	2.86
10	3.41	5.54	6.76	7.39
15	5.68	6.97	11.20	12.45
20	7.95	7.77	13.35	14.67
10	4.92	4.64	8.96	6.82
5	3.86	3.38	4.32	4.40
1	3.62	3.52	4.08	4.15

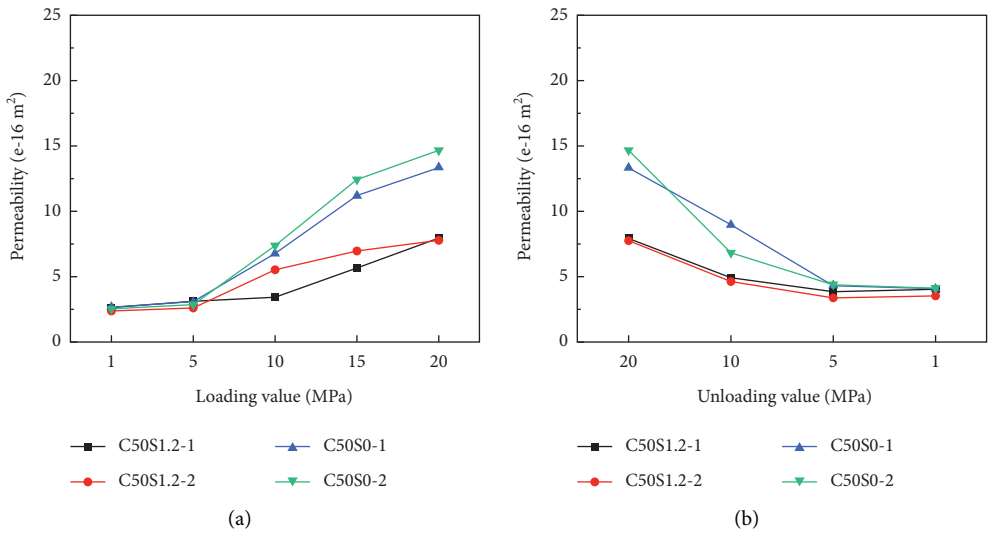

Figure 3: Change of loading and unloading damage permeability law of confining pressure 1 MPa test block: (a) load phase and (b) unload phase.

loading pressure. When the axial loading is 1~5 MPa, the permeability of the test block increases slowly, and when the axial loading is 5~15 MPa, the permeability increases rapidly. When the loading peak value of the fiber-reinforced concrete test block reaches 20 MPa, the permeability peak value is $7.95e-16\ m^2$, and the permeability peak value of the

ordinary concrete test block is $14.67e-16\,m^2$, which indicates that the cracking damage degree of the ordinary concrete test block under loading is greater than that of the fiber-reinforced concrete test block. The unloading speed is still kept at 0.5 MPa/s. From the data curve, it can be seen that when the permeability of the test block is unloaded from the peak value to the initial loading value, the permeability basically decreases to that of the initial state, and the loading damage of the test block is mainly manifested as elastic deformation. However, the test block still causes slight cracking damage after single loading and unloading, which leads to the inability to completely restore the permeability to the initial level. The permeability of the fiber-reinforced concrete test block after unloading is $3.62e-16\,m^2$, which is slightly lower than the permeability of the ordinary concrete after unloading $4.08e-16\,m^2$, indicating that the damage and cracking degree of the fiber-reinforced concrete is lower than that of the ordinary concrete under the same loading and unloading conditions.

4.2. Damage and Permeability Evaluation of Test Block under Single Loading and Unloading under Different Loading Velocity. Considering the constant confining pressure value of 1 MPa and the change of loading speed (0.5, 1.0, 1.5, and 3.0 MPa/s), we carried out single loading and unloading damage permeability test of fiber-reinforced concrete test blocks with a strength grade of C50. The measured values of loading permeability of test blocks are shown in Table 3. The loading and unloading damage penetration of the test block is shown in Figure 4.

According to the damage permeability curve of fiber-reinforced concrete test blocks under different loading speeds, the following conclusions are obtained:

(1) The loading speed has a great influence on the damage permeability of the test block. When the loading speed is 0.5 MPa/s, the confining pressure is 1 MPa, and the axial loading is 20 MPa, the peak damage permeability of the test block is $5.45e-16\,m^2$, and when the loading speed is increased to 1.0 MPa/s, the peak damage permeability of the test block is $7.77e-16\,m^2$. The degree of damage and cracking is further increased. When the loading speed is increased to 1.5 MPa/s, the peak damage permeability of the test block is $28.35e-16\,m^2$. When the loading speed is increased to 3 MPa/s, the peak damage permeability of the test block is sharply increased to $122.37e-16\,m^2$, and the test block has an obvious cracking failure.

(2) Through the comparison and analysis of the measured values of the damage permeability of the test block, it can be seen that when the loading rate is 0.5~1.0 MPa/s, the permeability of the test block basically recovers to the initial value after a single loading and unloading test, which indicates that the damage deformation of the test block is mainly manifested as elastic damage at this stage. When the loading speed is increased to 1.5 MPa/s, the permeability of the test block after unloading is $8.17e-16\,m^2$, which is obviously higher than the initial value of $2.66e-16\,m^2$, indicating that the test block has plastic damage. When the loading rate is increased to 3 MPa/s, the permeability of the test block after unloading is $39.37e-16\,m^2$, which is much higher than the initial value of $2.74e-16\,m^2$, indicating that the test block has obvious plastic damage.

4.3. Evaluation of Damage and Permeability of Test Blocks under Rapid Cyclic Loading and Unloading. Under conventional test conditions, the loading speed of fiber-reinforced concrete test block is generally controlled at 0.5~0.8 MPa/s. This section mainly studies the damage characteristics of fiber-reinforced concrete test block under dynamic load and cyclic loading and unloading. It can be seen from the research results of the previous section that the loading speed has a great influence on the damage of the test block. Therefore, this section focuses on the damage penetration test of C50S0 ordinary concrete and C50S1.2 fiber-reinforced concrete under fast cyclic loading and unloading. The confining pressure is kept constant at 1 MPa, and the loading speed is increased to 1.5 MPa/s. Four cyclic loading and unloading tests were carried out in turn through the same stress loading and unloading path. When the fourth cyclic axial pressure is unloaded to 1 MPa, the data are recorded and analyzed at the end of the test. The loading and unloading path of the test stress is shown in Figure 5. Under cyclic dynamic load conditions, the measured values of loading permeability of fiber-reinforced concrete test blocks are shown in Tables 4 and 5, and the loading and unloading damage permeability of test blocks are shown in Figures 6 and 7.

The research shows that the permeability of the test block increases with the increase of axial compression loading in the loading stage, mainly showing that with the increase of axial compression, the crack expansion of the test block leads to the increase of the measured permeability value. At the beginning of the loading stage, the slope of the curve of permeability changing with axial pressure is relatively moderate, and with the increase of axial pressure, the slope of the curve of permeability changing with axial pressure gradually becomes steeper. In the unloading stage, the permeability decreases with the decrease of axial pressure, which is mainly manifested as the fracture tends to close due to axial pressure unloading. In the initial stage of unloading, the slope of the curve of permeability with axial pressure is larger and continues to decrease with axial pressure, while the slope of the curve of permeability with axial pressure gradually slows down. The research shows that the loading stage (10~15 MPa) is the critical stage of damage infiltration of test blocks, which can be defined as the transition stage of elastoplastic damage infiltration.

At the peak loading stages of four cycles, the permeability of fiber-reinforced concrete test block is 28, 31, 35, and $39e-16\,m^2$, respectively, and when the axial load is unloaded to 1 MPa, the permeability of fiber-reinforced

Table 3: Measured permeability of C50S1.2 test block in dynamic loading and unloading test (the confining pressure value is 1 MPa).

Axial Load (MPa)	Loading speed, 0.5 MPa/s	Loading speed, 1.0 MPa/s	Loading speed, 1.5 MPa/s	Loading speed, 3.0 MPa/s
	Measured value of permeability ($e-16\,m^2$)			
1	2.55	2.68	2.66	2.74
5	3.46	3.60	7.15	13.55
10	3.55	4.54	11.34	29.39
15	3.68	5.87	21.48	76.34
20	5.45	7.77	28.35	122.37
10	4.34	5.24	17.68	56.54
5	3.77	4.28	10.24	43.56
1	3.34	3.77	8.17	39.75

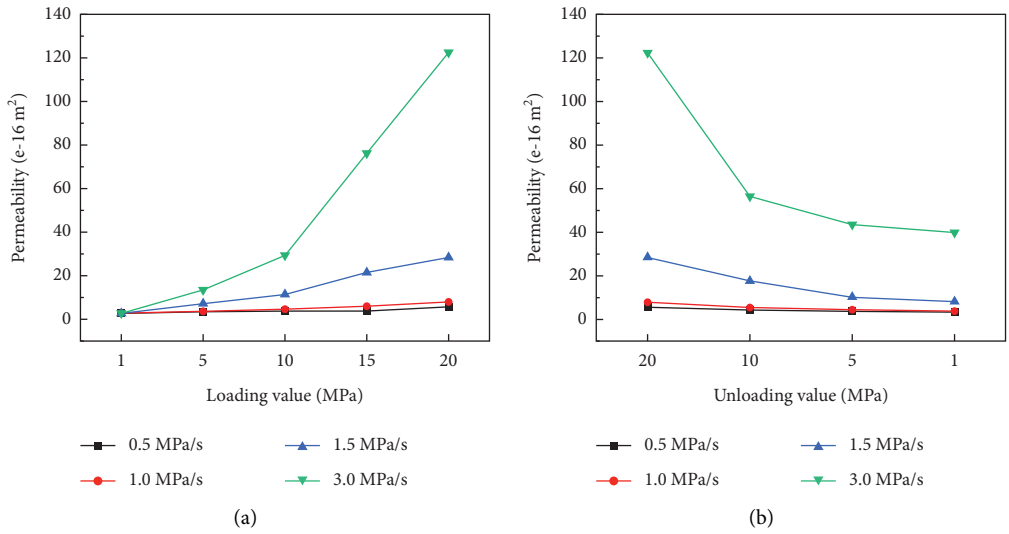

Figure 4: Change of damage penetration law of C50S1.2 test block in dynamic loading and unloading test: (a) load phase and (b) unload phase.

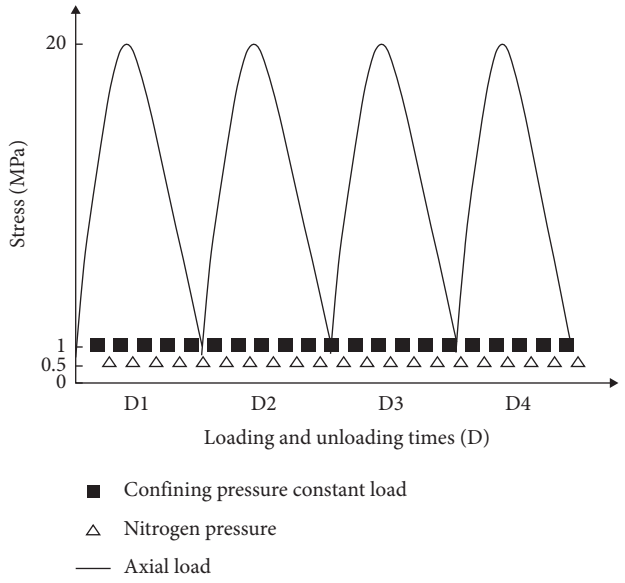

Figure 5: Cyclic loading and unloading path of test block.

Table 4: Measured permeability of C50S1.2-1 test block in cyclic loading and unloading test.

Axial load (MPa)	Cycle 1	Cycle 2	Cycle 3	Cycle 4
	Measured value of permeability ($e-16\ m^2$)			
1	2.66	8.17	10	13
5	7.15	9	13	15
10	11.34	13	16	18
15	21.48	24	26	28
20	28.35	31	35	39
15	22	25	28	31
10	17.68	19	22	25
5	10.24	13	15	17
1	8.17	10	13	16

Table 5: Measured permeability of C50S1.2-2 test block in cyclic loading and unloading test.

Axial load (MPa)	Cycle 1	Cycle 2	Cycle 3	Cycle 4
	Measured value of permeability ($e-16\ m^2$)			
1	2.39	7.14	11	12
5	6.15	10	12	15
10	12.37	14	17	19
15	20.45	23	26	27
20	27.37	30	34	38
15	21	23	29	30
10	16.66	17	21	24
5	9.25	14	15	18
1	7.14	11	12	17

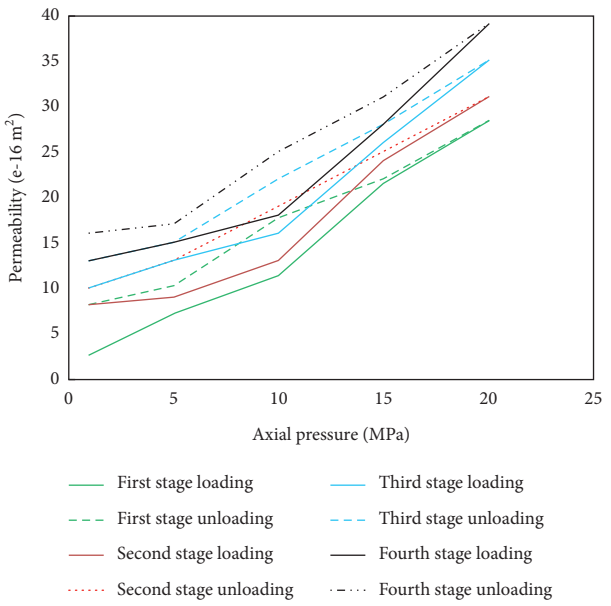

Figure 6: Change of damage penetration law of C50S1.2-1 test block in cyclic loading and unloading test.

concrete test block corresponding to the four cycles is 8, 10, 13, and $16e-16\ m^2$, respectively. It can be seen that the damage permeability of the test block increases with the increase of loading and unloading times. Under the action of cyclic loading and unloading, the damage degree of the test block increases, and the permeability of each stage is higher

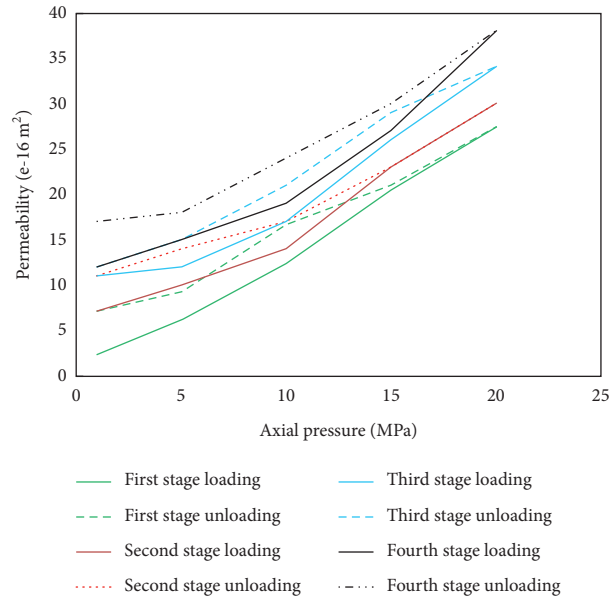

Figure 7: Change of damage penetration law of C50S1.2-2 test block in cyclic loading and unloading test.

than that of the previous stage. The test block has obvious plastic deformation damage, which is mainly manifested in the fact that the crack permeability after unloading is significantly higher than the initial permeability after loading.

5. Conclusions

Considering the presence of confining pressure in engineering practice, a study on the dynamic loading damage mechanism of fiber-reinforced concrete specimens under confining pressure was carried out with the aid of an ultralow permeability damage test system, and the following conclusions were mainly obtained:

(1) The damage characteristics of fiber-reinforced concrete and ordinary concrete specimens in a single loading and unloading under the same confining pressure were studied, which shows that under the same confining pressure and loading and unloading conditions, the damage permeability of the fiber-reinforced concrete specimens is significantly lower than that of the ordinary concrete. The penetration rate in the unloading phase of the test basically overlaps with that in the loading phase, which is mainly characterized by elastic damage.

(2) Considering that the loading speed is an important factor affecting the damage cracking of fiber-reinforced concrete, damage penetration tests were carried out on the triaxial single loading and unloading of fiber-reinforced concrete specimens under the conditions of varying loading speeds (0.5, 1.0, 1.5, and 3.0 MPa/s) with a constant confining pressure of 1 MPa. The study shows that the loading speed has a great influence on the degree of damage and cracking of the specimen. When the loading speed is increased from 0.5 MPa/s to 1.5 MPa/s, the

maximum permeability at the peak of loading increases from $5.45e-16\,m^2$ to $28.35e-16\,m^2$, and the rapid increase of permeability indicates that the degree of damage and cracking of the specimen becomes larger. When the loading speed reached 3 MPa/s, the permeability of the unloading phase could not coincide with that of the loading phase, and the permeability of the specimen at the end of unloading was $39.37e-16\,m^2$ that was significantly higher than the initial measured value of $2.74e-16\,m^2$.

(3) A triaxial cyclic loading and unloading test was carried out at a circumferential pressure of 1 MPa and a loading rate of 1.5 MPa/s. A total of four cycles of loading and unloading tests were carried out using the same loading path. The study shows that the damage penetration of the test blocks increases with the number of loading and unloading cycles.

Data Availability

The data used to support the findings of this study are available from the corresponding author upon request.

Conflicts of Interest

The authors declare that there are no conflicts of interest.

Authors' Contributions

C.L. conceptualized the study; L.R., Q.Y., and F.C. performed the experiment; Z.-W.Y. and X.-J.T. performed the analysis; C.L., L.R., and Q.Y. wrote the manuscript; and C.L. contributed to the funding acquisition. All authors have read and agreed to the final version of the manuscript.

Acknowledgments

The authors kindly thank the laboratory and experimental equipment provided by the Institute of Rock and Soil Mechanics, Chinese Academy of Sciences. This research was funded by the National Natural Science Foundation of China (Grant No. 51379200) and also by the Project of Science and Technology from the Department of Education in Jiangxi, China (GJJ190835).

References

[1] Y. Guan, D. Niu, B. Wu, and J. Wang, "Research on meso stochastic damage constitutive model of fiber concrete under compression," *Journal of Xi'an University of Architecture and Technology (Natural Science Edition)*, vol. 47, no. 5, pp. 678–683, 2015.

[2] G. Walton, A. Hedayat, E. Kim, and D. Labrie, "Post-yield strength and dilatancy evolution across the brittle-ductile transition in Indiana limestone," *Rock Mechanics and Rock Engineering*, vol. 50, no. 4, pp. 1–20, 2017.

[3] G. Aráoz and B. Luccioni, "Modeling concrete like materials under sever dynamic pressures," *International Journal of Impact Engineering*, vol. 76, pp. 139–154, 2015.

[4] Z. Li and Z. Liu, "Review of concrete dynamic constitutive models," *Journal of Tianjin University: Natural Science and Engineering Technology Edition*, vol. 48, no. 10, pp. 853–863, 2015.

[5] A. Gholampour, T. Ozbakkaloglu, and R. Hassanli, "Behavior of rubberized concrete under active confinement," *Construction and Building Materials*, vol. 138, pp. 372–382, 2017.

[6] F. Gong, Si Xuefeng, X. Li, and M. Tao, "Research on dynamic Mohr-Coulomb criterion and Hoek-Brown criterion based on strain rate effect," *Chinese Journal of Nonferrous Metals*, vol. 26, no. 8, pp. 1763–1773, 2016.

[7] D. Unteregger, B. Fuchs, and G. Hofstetter, "A damage plasticity model for different types of intact rock," *International Journal of Rock Mechanics and Mining Sciences*, vol. 80, pp. 402–411, 2015.

[8] J. Li, J. Xu, X. Lu, Z. Wang, and L. Zhang, "Study on dynamic behavior and damage constitutive model of rock under impact loading with confining pressure," *Engineering Mechanics*, vol. 29, no. 1, pp. 55–63, 2012.

[9] Z. Lu and Z. Wang, "Triaxial test study on dynamic characteristics of granite considering medium and high strain rates," *Chinese Journal of Geotechnical Engineering*, vol. 38, no. 6, pp. 1087–1094, 2016.

[10] X. Li, Q. Wu, L. Dong, and L. Chen, "Research on the mechanical properties of thick-walled cylindrical sandstone with filling," *Chinese Journal of Geotechnical Engineering*, vol. 37, no. 12, pp. 2149–2156, 2015.

[11] H. Zhang, H. Liu, Y. He, and L. J. Han, "Unloading test and rock strength failure of rock thick-walled cylinder under three-dimensional compression," *Journal of University of Science and Technology Beijing*, vol. 33, no. 7, pp. 800–805, 2011.

[12] C. Su, B. Li, and Q. Wu, "Experimental study on deformation and strength characteristics of limestone pore samples under compression," *Chinese Journal of Rock Mechanics and Engineering*, vol. 35, pp. 2739–2748, 2016.

[13] S. Jia, J. Luo, J. Yang, and M. Gao, "Research on elastoplastic damage constitutive model of salt rock considering the effect of confining pressure," *Rock and Soil Mechanics*, vol. 36, no. 4, pp. 1549–1556, 2015.

[14] H. Zhou, F. Yang, C. Zhang, and R. Xu, "Research on elastoplastic coupling mechanical model of marble considering confining pressure effect," *Chinese Journal of Rock Mechanics and Engineering*, vol. 31, no. 12, pp. 2389–2399, 2012.

[15] Y. F. Wu and P. Li, "Stress-strain behavior of actively and passively confined concrete under cyclic axial load," *Composite Structures*, vol. 149, pp. 369–384, 2016.

[16] J. C. Zhang, W. Y. Xu, H. L. Wang, R. B. Wang, Q. X. Meng, and S. W. Du, "A coupled elastoplastic damage model for brittle rocks and its application in modelling underground excavation," *International Journal of Rock Mechanics and Mining Sciences*, vol. 84, pp. 130–141, 2016.

[17] D. Grgic, "Constitutive modelling of the elastic-plastic, visco-plastic and damage behaviour of hard porous rocks within the unified theory of inelastic flow," *Acta Geotechnica*, vol. 11, no. 48, pp. 95–126, 2016.

[18] X. Yuan, H. Liu, and Z. Wang, "Study on meso-damage and plasticity of rock under compression load," *Chinese Journal of Computational Mechanics*, vol. 30, no. 1, pp. 149–155, 2013.

[19] X. Yuan, H. Liu, and Z. Wang, "Research on elastoplastic damage constitutive model of rock based on Drucker-Prager criterion," *Rock and Soil Mechanics*, vol. 33, no. 4, pp. 1103–1108, 2012.

[20] N. Erarslan and D. J. Williams, "Experimental, numerical and analytical studies on tensile strength of rocks," *International*

Journal of Rock Mechanics and Mining Sciences, vol. 49, no. 1, pp. 21–30, 2012.

[21] J. Liu, P. Cao, and D. Han, "The influence of confining stress on optimum spacing of TBM cutters for cutting granite," *International Journal of Rock Mechanics and Mining Sciences*, vol. 88, pp. 165–174, 2016.

[22] X. Liu, J. Liu, and H. Feng, "Experimental study on unloading mechanical properties of sandstone under different initial unloading levels and water pressure," *Chinese Journal of Geotechnical Engineering*, vol. 40, no. 6, pp. 1143–1151, 2018.

[23] H. Deng, Z. Wang, J. Li, and Q. Jiang, "Research on the influence of unloading rate and pore water pressure on the unloading characteristics of sandstone," *Chinese Journal of Geotechnical Engineering*, vol. 39, no. 11, pp. 1976–1983, 2017.

[24] Q. Wu, X. Li, and F. Zhao, "Research on failure characteristics of limestone tunnel specimens under pressure relief conditions," *Chinese Journal of Rock Mechanics and Engineering*, vol. 36, no. 6, pp. 1424–1433, 2017.

[25] W. Chen, S. Lu, X. Guo, and C. Qiao, "Unloading confining pressure for brittle rock and mechanism of rock burst," *Chinese Journal of Geotechnical Engineering*, vol. 32, no. 6, pp. 963–969, 2010.

Hindawi
Geofluids
Volume 2022, Article ID 3504488, 15 pages
https://doi.org/10.1155/2022/3504488

Research Article

Numerical Simulation of the Diffusion of Fissure Slurry at High Temperature

Jiandong Niu,[1] Yong Sun,[1] Jianxin Liu,[2] Huimei Li,[1] Xiaojun Tan,[1] Ning Han,[1] Bin Wang,[1] and Liangliang Qiu[3]

[1]*School of Civil Engineering, Central South University, Changsha 410000, China*
[2]*Swan College, Central South University of Forestry and Technology, Changsha 410000, China*
[3]*Changsha Hengde Geotechnical Engineering Technology Co., Ltd., Changsha 410000, China*

Correspondence should be addressed to Jianxin Liu; 6996@hdyt.cn

Received 21 December 2021; Revised 27 January 2022; Accepted 10 February 2022; Published 2 March 2022

Academic Editor: Xueming Du

Deep-buried tunnel at high-ground temperature is prone to the sudden surge of water when crossing the water-rich formation, resulting in casualties and economic losses. Slurry injection is a common and effective method of governance for addressing this issue. However, there has been little research into pulping at high-ground temperature, with most of the existing research focusing on room temperature conditions. We studied two kinds of slurry commonly used in grouting, cement slurry and cement-sodium silicate slurry. Indoor testing was used in this paper to clarify the effect of temperature on slurry viscosity, and numerical simulation was used to study slurry diffusion in flat cracks at different temperatures. The results showed that in a hydrostatic environment, the spread rate of slurry was independent of temperature and type of slurry. For the same kind of slurry, the higher the temperature, the greater the maximum slurry pressure. The higher the temperature in a flow environment, the faster the slurry diffusion. As the temperature rised, the grouting pressure required for crack sealing decreased at first then rises. In a flow environment, the sealing effect of cement-sodium silicate slurry was superior to that of cement slurry.

1. Introduction

With the continuous construction of deep-buried tunnels all over the world, there are more and more high-temperature tunnels. Groundwater is a harmful component for tunnels [1–5], because it will not only reduce the strength of the surrounding rock but also sudden surges of water may happen when the treatment is not at the time [6–9], resulting in casualties and property damage, and the construction progress may be delayed [10–13]. During operation, groundwater infiltration accelerates the rusting of steel bars in the lining and shortens the service life of the equipment [14–17], increasing the difficulty of maintenance. Grouting is now a widely used groundwater treatment method due to its ease of construction, low cost, and good governance effect [18–23]. Cement and cement-sodium silicate slurry is widely used in the pulping project due to a wide range of raw materials and is nontoxic harmless [24–30].

In recent decades, scholars have done a lot of research on slurry. Li et al. [31] proposed an SDS method to consider the space-time evolution characteristics of slurry viscosity, which describes the slurry diffusion and settlement behavior in the dynamic water of cracks, and realizes the visualization of the slurry diffusion process. Considering the effect of shear rate on the Bingham model, Shamu et al. [32] proposed a new design framework to consider the length of slurry propagation. Yan et al. [33] have developed a hybrid formula for a unified pipe network method combined with a zero-thickness interface unit, which can simulate the crack grouting process and capture the expansion behavior of cracks in the grouting process. Liu et al. [34–35] proposed a numerical flow method for simulating the permeation process of crack rock body grout, and it was discovered that increasing the injection pressure can increase the crack aperture and improve slurry injection efficiency, but it destroys the structure of the rock mass and weakens the injection

effect. Li et al. [36] carried out a closed seepage test on single-cracked chlorite schist and found that although the growth of rock strength after slurry injection was not ideal, the grout was very effective in reducing permeability. Rafi et al. [37] proposed a new method of slurry analysis to estimate the spread distance of the grout and the size of the crack expansion at a certain time by considering the slurry volume, slurry pressure, ground stress, and the sum of fluid rheum characteristics. Zhang et al. [38] proposed two step-by-step calculation methods to describe the grouting process by dividing the circular slurry area into infinitesimal annular elements, corresponding to the injection pressure boundary conditions and the slurry flow boundary conditions, by dividing the circular slurry area into infinitely small ring units. Xiao et al. [39] analyzed the relationship between crack distribution and slurry characteristics based on discontinuous deformation theory and found that the amount of grout consumed by the crack network was subject to the normal distribution. Du et al. [40] conducted a cement slurry diffusion test in zigzag cracks and discovered that the sealing efficiency of the high fractal dimension is greater than that of the low tortuous fractal dimension of the crack near the injection source, whereas the mode away from the grout source is the opposite [40].

However, the research of domestic and foreign scholars mainly focuses on the diffusion law of slurry at room temperature, and there is less research on the process of the transport of slurry in high-temperature environment. Therefore, it is necessary to explore and study the diffusion characteristics of slurry at high temperatures.

Based on the typical water-rich high-ground temperature tunnel site conditions, the high-temperature environment is simulated indoors, and the viscosity of cement and cement-sodium silicate (C-S) is measured at different temperatures. The relationship between the diffusion law and temperature of the two types of slurry in the environments of dynamic water and hydrostatic water is revealed through numerical simulation.

2. The Viscosity of the Slurry at Different Temperatures

In this paper, the viscosities of cement and C-S slurry at 25°C, 40°C, 60°C, and 80°C were measured in the laboratory to simulate the change of slurry viscosity in high-temperature environment and provide the material basis for numerical simulation.

The viscosity of the slurry was tested by the Chinese SNB-2 microcomputer digital display viscometer. All the required experimental materials were weighed and heated to 25°C, 40°C, 60°C, and 80°C, then mixed in the beaker according to the proportion, and stirred evenly. Finally, the beaker was tested for viscosity using the SNB-2 computer digital viscometer. Three groups of repeated experiments were carried out for each slurry under various temperature conditions, and the average value of the three groups of results was taken as the slurry's viscosity value.

Cement slurry uses P.O.42.5 ordinary sodium silicate cement, and water is ordinary tap water. Water-cement ratio is 0.6, and each sample is mixed with 300 g cement and 180 ml water. Viscosity is measured every 10 min, lasting 120 min. Each C-S slurry is composed of 350 ml liquid A and 70 ml liquid B. Among them, cement slurry, which is P.O.42.5 ordinary silicate cement, is a liquid, and the water-cement ratio is 0.6. Liquid B is a solution of 25 Baume degree sodium silicate diluted with 40 Baume degree sodium silicate. Every 2.5 s, the viscosity is measured. The measurement is terminated when the viscosity exceeds 75 Pa·s. Figures 1 and 2 show the measurements. The viscosity equations of two different slurries at different temperatures obtained by fitting are shown in Table 1 [41].

The viscosity of cement and C-S slurry increases with the increase of temperature and with the increase of hydration time. Because of the long hydration reaction time of cement slurry, the viscosity of slurry increases slowly. For C-S slurry, the viscosity of the slurry increases suddenly after a while, and an increase in temperature reduces the time required for viscosity rise.

3. Finite Element Model

3.1. Model Boundary Condition. The diffusion of slurry is simulated by COMSOL Multiphysics. The motion of slurry in the fissure is regarded as a stratosphere, and water and slurry are regarded as two insoluble fluids. The viscosity characteristics of the slurry are measured by experimental data.

The actual rock mass fractures are simplified as the models of single fissure between two parallel plates with constant aperture, and the spatial scale changes of rock mass fractures are ignored to establish the fracture model shown in Figure 3 [42–44]. The crack length is 3 m, the width is 1 m, the opening is 1 mm, the slurry hole diameter is 6 cm, and the center of the slurry hole is 0.5 m from the upper and lower boundaries and 1 m from the left boundary. The free triangle mesh is employed, and it is moderately encrypted near the slurry hole. Two lines are set up in the model to detect changes in pressure within the model, and the line arrangement is shown in Figure 4. The upper and lower boundary of the model is impermeable, and the slurry hole adopts the fixed flow rate boundary, which equates the slurry process to the slurry velocity by the slurry hole wall method. Take the water pressure at the model's outlet as the standard; that is, the pressure at the outlet is zero. The left and right sides are free-flow boundaries in a hydrostatic environment. The right side is still the free-flow boundary in the dynamic flow environment, while the left side is the flow boundary using the fixed head boundary. The working conditions are shown in Table 2.

3.2. Governing Equation of Motion. Regardless of the compression of slurry and water, the Navier–Stokes equation in full form is used to react with the fundamental relationship between fluid flow and force of the continuous equation:

$$\begin{aligned} \rho(u \cdot \nabla) &= \nabla[-pI + K] + F, \\ \rho\nabla(u) &= 0, \\ K &= \mu\left(\nabla u + (\nabla u)^{\mathrm{T}}\right). \end{aligned} \tag{1}$$

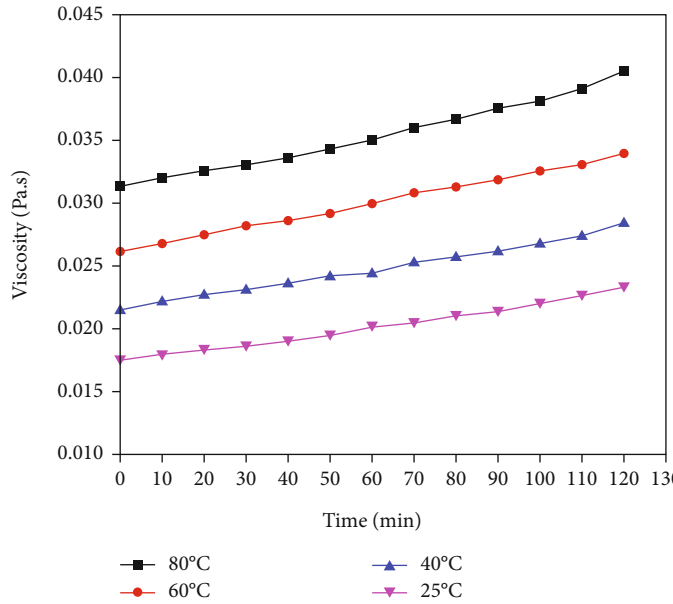

Figure 1: Time-varying viscosity curve of the cement slurry at different temperatures.

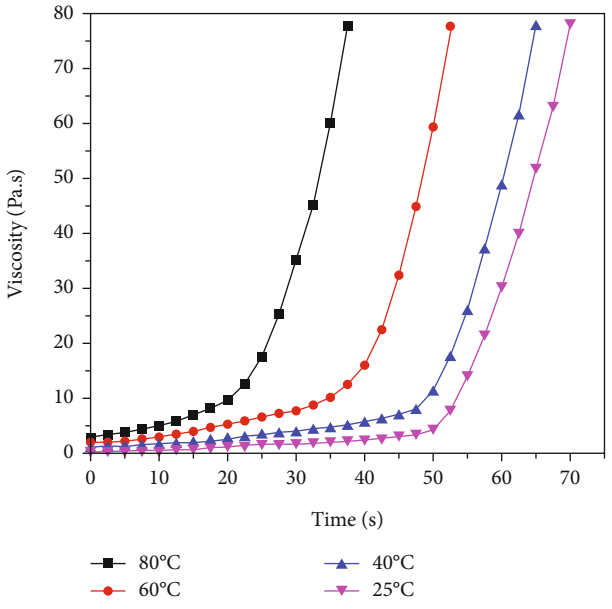

Figure 2: Time-varying viscosity curve of the cement-sodium silicate slurry at different temperatures.

In the formula, ρ is the fluid density; u is the velocity field, p is the fluid pressure, F is the volume force on the fluid, and μ is the power viscosity.

The horizontal set method is adopted to track the movement of slurry water interface, and the governing equation is

$$\frac{\partial \phi}{\partial t} + u\nabla\phi = \gamma\nabla\left(\epsilon_{ls}\nabla\phi - \phi(1-\phi)\frac{\nabla\phi}{|\nabla\phi|}\right). \quad (2)$$

In the formula, ϕ is the level set variable, t is the time, γ is the reinitialization parameters, and ϵ_{1s} is the control interface thickness parameters.

Table 1: Temperature and wildlife count in the three areas covered by the study.

Type of slurry	Temperature [°C]	The time-varying characteristic equations of viscosity
Cement slurry	20	$\mu = 0.01736 + 4.78571 \times 10^{-5}\, t$
	40	$\mu = 0.02144 + 5.39011 \times 10^{-5}\, t$
	60	$\mu = 0.02614 + 6.45055 \times 10^{-5}\, t$
	80	$\mu = 0.03096 + 7.35165 \times 10^{-5}\, t$
C-S slurry	20	$\mu = 2.71354 \times 10^{-11}\, t^{6.76022}$
	40	$\mu = 2.18059 \times 10^{-8}\, t^{5.38292}$
	60	$\mu = 8.93584 \times 10^{-5}\, t^{3.50253}$
	80	$\mu = 3.21232 \times 10^{-4}\, t^{3.4143}$

μ: viscosity; t: time. For cement, the unit of t is [min]. For C-S, the unit of t is [s].

4. Law Analysis of the Hydrostatic Environment

4.1. Diffusion Pattern of the Hydrostatic Environment. Through simulation, it is found that the diffusion shapes of the two grout at different temperatures are almost the same in the hydrostatic environment, and all of them show the morphology as shown in Figure 5, where the red part represents the slurry and the blue part represents the water.

The diffusion speed of the slurry along the four directions is equal, and the diffusion area is circular. The slurry's diffusion is then blocked by the boundary, the spread to the boundary is slowed, and the slurry's diffusion shape changes.

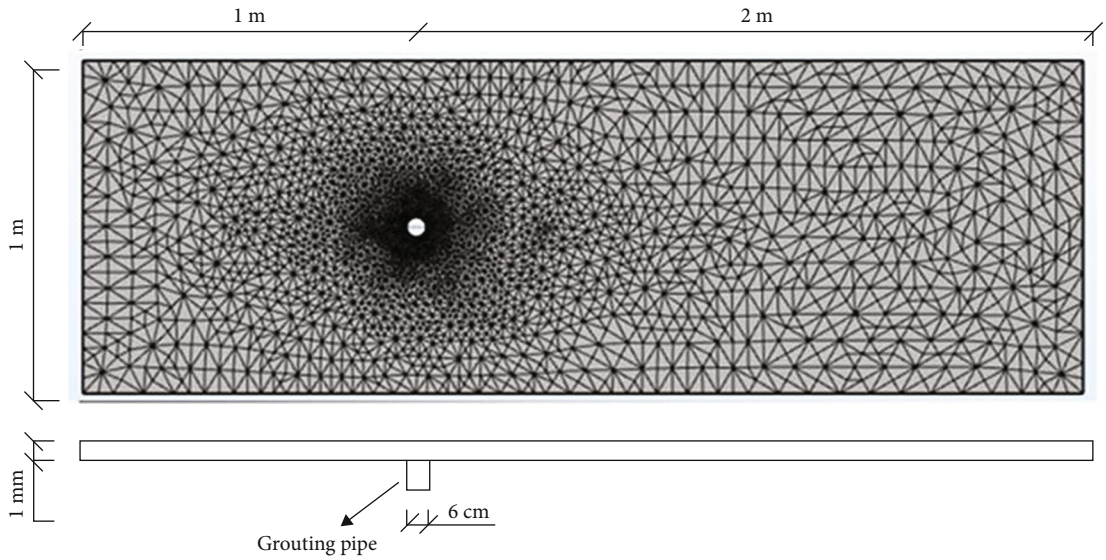

Figure 3: Geometric model and mesh division.

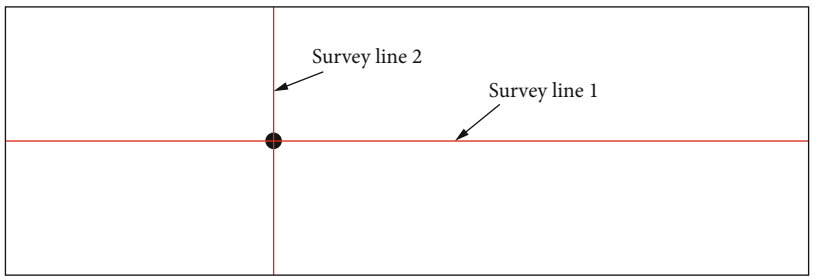

Figure 4: Arrangement of survey line.

Table 2: Working conditions.

Type of grouting slurry	Grouting rate [m/s]	Inlet pressure [kPa]	Temperature[°C]
Ordinary cement	0.20	0	25, 40, 60, 80
C-S	0.20	0	25, 40, 60, 80
Ordinary cement	0.50	10	25, 40, 60, 80
C-S	0.15	28	25, 40, 60, 80

Furthermore, the figure clearly shows that the slurry's diffusion rate is high at first, but as the pulping progresses, the diffusion radius increases, and the diffusion rate gradually decreases, and at 25 s, the slurry diffuses to the crack boundary and the slurry sealing is completed. It can be considered that the diffusion of grout in a hydrostatic environment is independent of temperature and type of grouting slurry.

4.2. Pressure Field Variation

4.2.1. Pressure Contour. Similar to the diffusion trajectory, the shape of pressure isolines at different grout types and temperatures is the same, and all of them show the morphology as shown in Figure 6, which is circular near the slurry hole and is more densely distributed, while the pressure contours away from the position of the slurry hole are sparse, indicating that the pressure decreases rapidly in the fluid. The pressure contours begin to appear further away from the slurry holes as the pulping progress, indicating that the pressure's influence range is expanding, and this part of the pressure contours is not a closed curve due to the obstruction of the boundary.

4.2.2. Grouting Time Distribution. However, the numerical value of the pressure contour is different at different temperatures and slurry types. The slurry pressure rises as the ground temperature rises. Figure 7 shows the relationship between injection pressure and time by monitoring the position pressure of the injection hole. It can be seen that for cement slurry, the slurry pressure increases linearly over time, and for every 20°C increase in temperature, the slurry pressure increases by an average of 10 Pa. For C-S slurry, when the temperature is below 60°C, the injection pressure also increases linearly over time, but when the temperature reaches 80°C, the growth rate of the injection pressure increases with the injection time, and the pressure increases with time. For the same type of slurry, the higher the

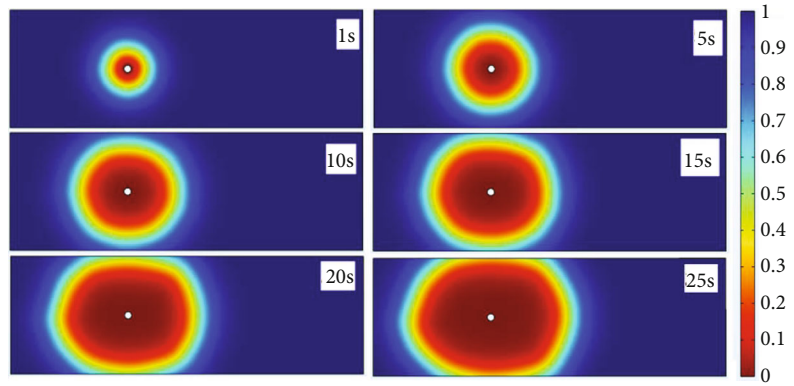

Figure 5: Static water diffusion morphology.

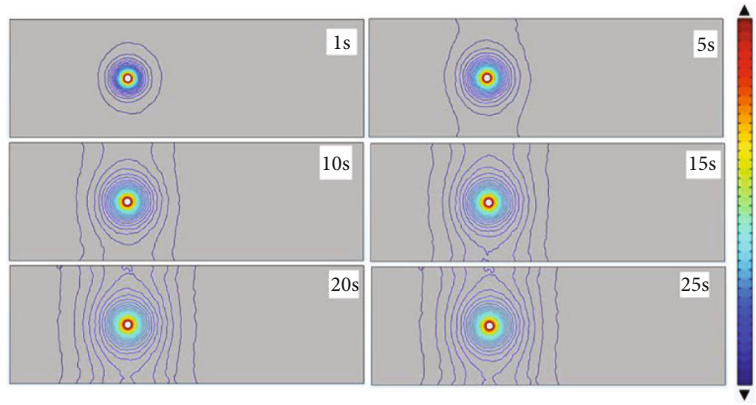

Figure 6: Pressure contour.

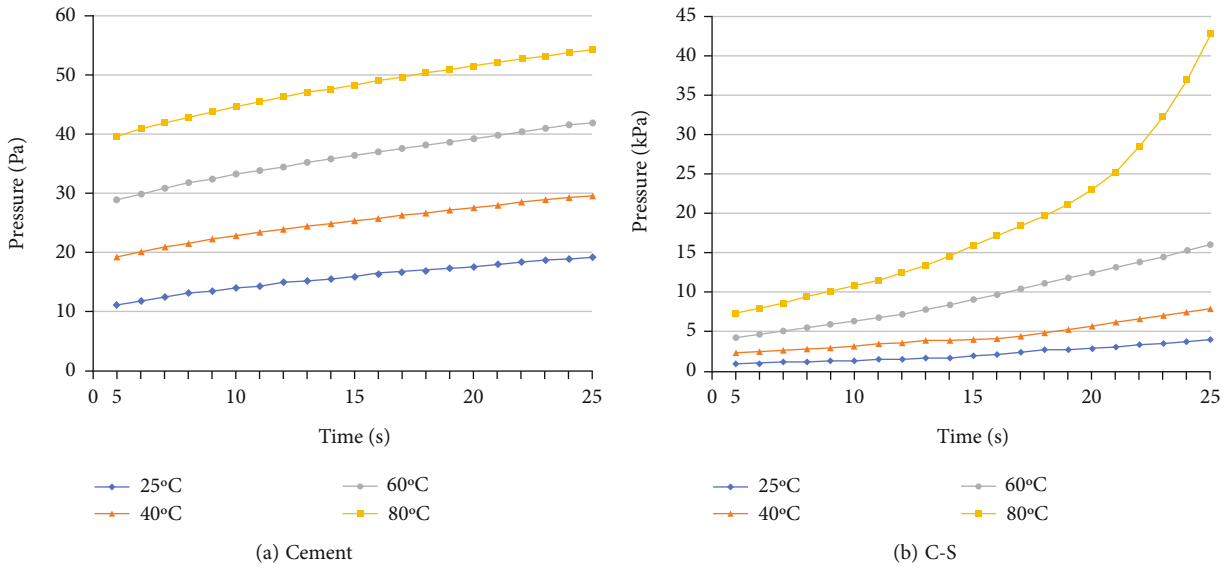

(a) Cement (b) C-S

Figure 7: Pressure time variation.

temperature, the higher the viscosity at the same time and the faster the viscosity growth rate, and C-S slurry injection pressure is much higher than cement slurry injection pressure, C-S slurry pressure growth rate is much higher than cement growth rate, and C-S slurry pressure is hundreds of times cement pressure.

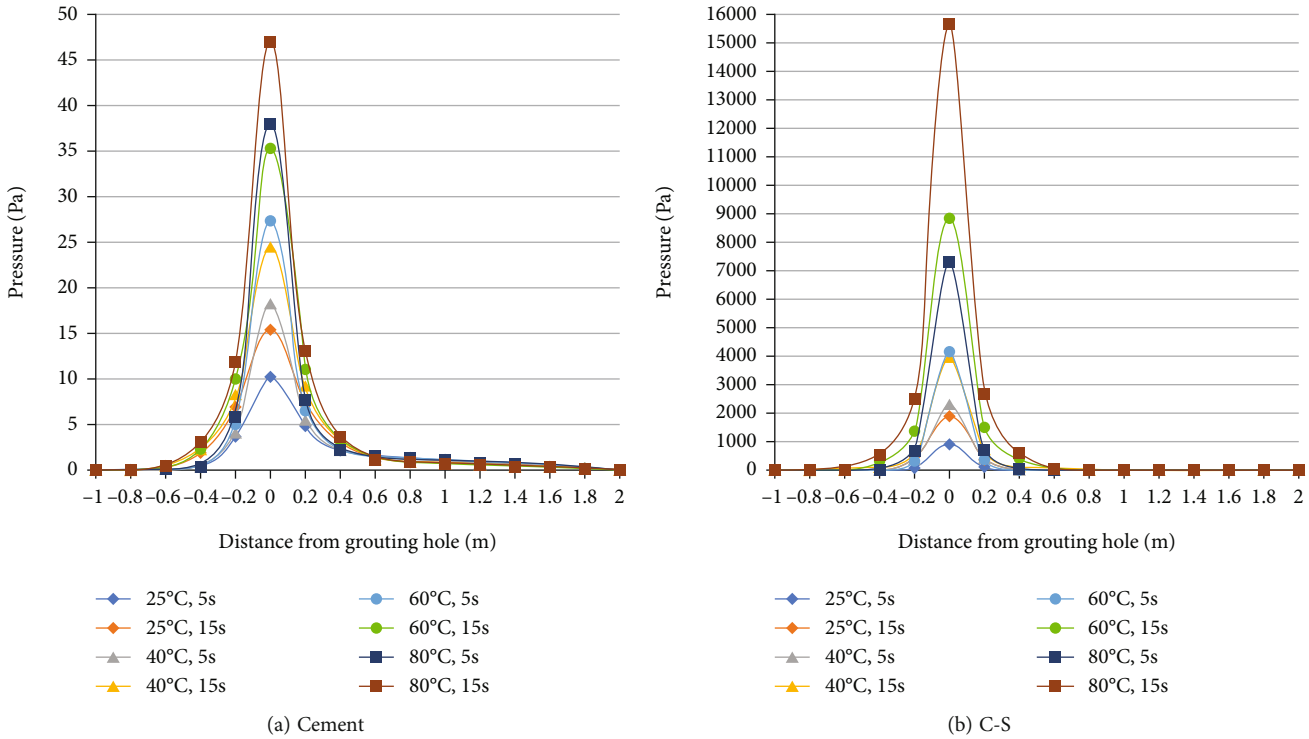

Figure 8: Pressure distribution on survey line 1.

4.2.3. Pressure Spatial Distribution. With the injection hole as the center, the pressure distribution on line 1 and line 2 can be monitored with the change of slurry type and temperature; as shown in Figures 8 and 9, the distribution of specific pressure size can be obtained. The analysis of these graphs reveals that the injection pressure increases all along the line as the injection process progresses, and that the higher the temperature at the same time, the greater the pressure on the measuring line, and the greatest increase in pressure at the injection hole. In addition, on line 1, the pressure in the fluid gradually approaches 0 Pa, i.e., the outflow boundary pressure, and the later the time, the higher the temperature, the greater the pressure, and the longer it takes to drop to 0 Pa. Because of the boundary blocking, the pressure on line 2 will not be reduced to 0 Pa, and the minimum pressure will increase as injection time and temperature increase. Furthermore, the pressure in the fluid is the symmetrical distribution of the injection hole, and the pressure of C-S slurry at the same position is much greater than the pressure of cement slurry.

Although the size of the pressure in the fluid changes with temperature, time, type of slurry, etc., the law of attenuation has not changed: the attenuation of the injection pressure slows as it moves away from the slurry hole, and the attenuation of the pressure of 0.2 m in the injection hole is completed 80% and 90% in 0.4 m, the higher the temperature, the faster the pressure attenuation speed near the slurry hole, which is also in line with the distribution of the pressure contour, and the pressure attenuation speed on line 2 is lower than the measuring line 1.

5. Diffusion Law of the Flow Environment

5.1. Diffusion Morphology Analysis. Under the condition of flow environment, the diffusion trajectory of grout becomes different due to the scour of water flow.

5.1.1. Cement Slurry. It is a cement slurry because of its small viscosity; so, the ability to resist the flow of water washing is weak. In the process of filling, most of the cement slurry is taken away by the water flow. Furthermore, the diffusion of cement slurry varies greatly in different directions: cement slurry primarily spreads along the water, and diffusion in the reverse water direction is almost nonexistent. The distribution of cement slurry in a wavy shape can be seen near the model's exit. Furthermore, while the viscosity of cement slurry increases slightly with temperature, it is still insufficient to resist the washing of water flow. The change in cement grout diffusion morphology with increasing temperature is not obvious in the simulated period, and all of them show the morphology shown in Figure 10.

5.1.2. C-S Slurry. C-S slurry as a quick condensate, viscosity can be raised in a short period to a value sufficient to resist the flow of water wash and seal the fissure, and the temperature effect is also very obvious. Unlike static water injection slurry, the initial slurry sealing speed is slower in dynamic water due to the strong flushing of water flow, and with the injection of slurry, C-S slurry viscosity increases, the ability to resist water flow is stronger, blocking speed is faster, and the higher the temperature. The time required

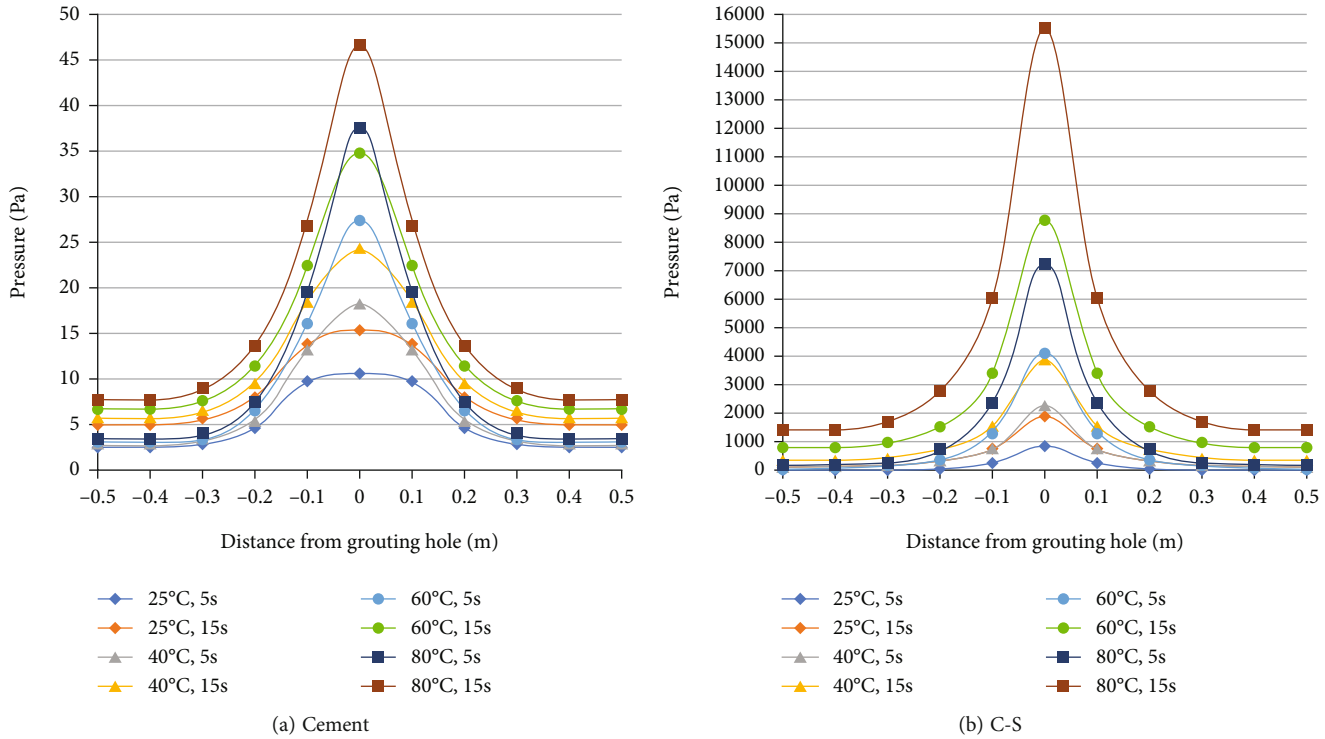

Figure 9: Pressure distribution on survey line 2.

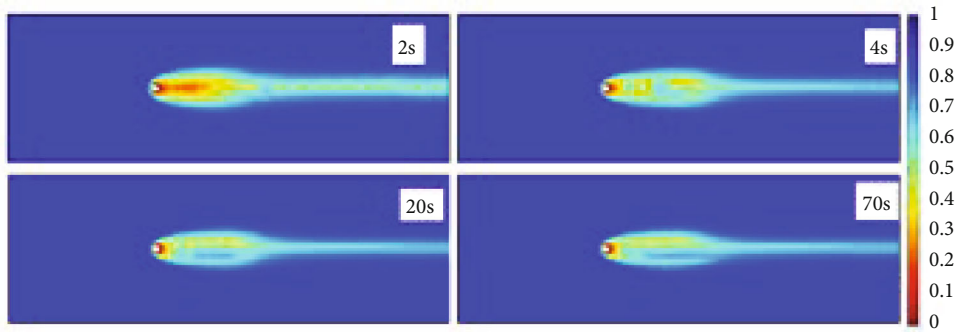

Figure 10: Diffusion morphology of cement.

for blocking is shorter, and the time required for blocking is 75 s, 70s, 55 s, and 50s, respectively, at 25°C, 40°C, 60°C, and 80°C. The specific diffusion trajectory of the C-S slurry is shown in Figure 11. It can be seen that the diffusion of C-S slurry is divided into three stages.

In the first stage, due to the low viscosity of C-S slurry, most of the C-S slurry is taken away by water flow, only after the injection hole retains the lower part of C-S slurry reverse water, and the spread of both sides is very small.

In the second stage, with the injection of slurry, C-S slurry viscosity continues to increase, it begins to be able to resist the wash of water flock, C-S slurry gradually spread to both sides and the opposite side of the water, and the reverse water side diffusion rate is slower than on both sides due to the more intense flushing.

In the third stage, due to the spread of C-S slurry to both sides, the fissure is gradually blocked, the water flow speed is slowing down, the flushing effect of the water flow is decreasing, the diffusion speed of the opposite waterside is gradually accelerated, and in the direction of vertical water flow, because the water flow channel becomes narrow, the water flow rate decreases slowly, which leads to the water flow on both sides of the injection hole is still strong, so that the flow rate of C-S slurry in this direction is less than the diffusion speed of C-S slurry in the direction of the reverse water.

As the temperature of water increases, the first two stages of the slurry take up less and less time, and when it reaches 80°C, the first stage is no longer observed. In addition, the temperature increases. The time required for crack sealing is also decreasing, with temperature increases from

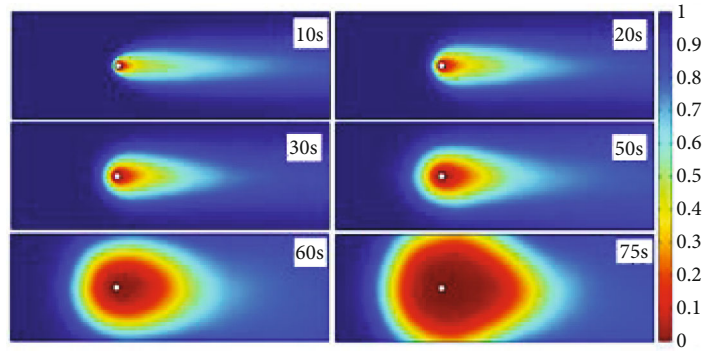

(a) 25°C

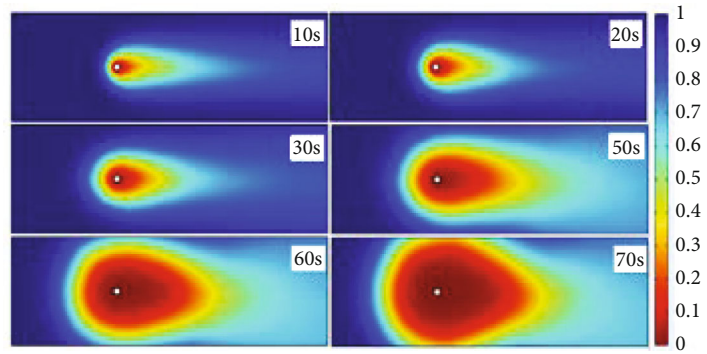

(b) 40°C

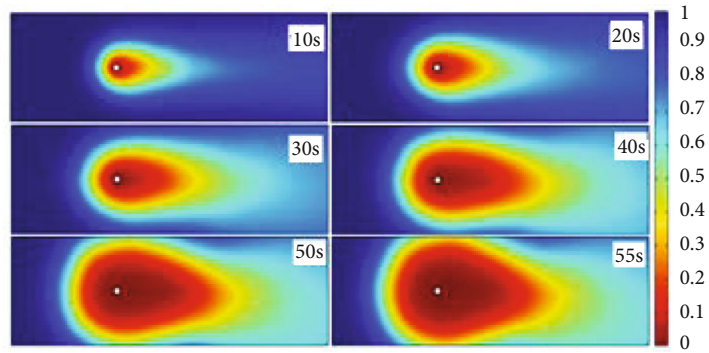

(c) 60°C

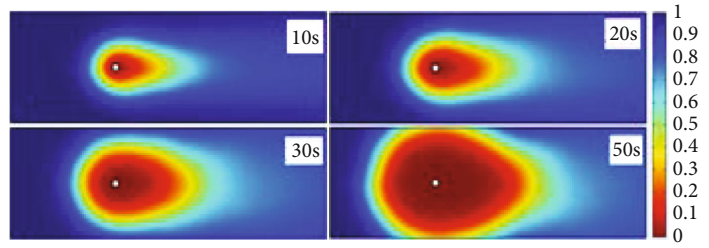

(d) 80°C

Figure 11: Diffusion patterns of C-S grout at different temperatures.

25°C to 40°C, from 40°C to 60°C reducing crack sealing time by 5 s, and time to seal from 40°C to 60°C decreasing by 15 s. The analysis suggests that when the temperature is lower, the viscosity change is relatively small, and the slurry efficiency changes little, whereas when the temperature is higher, the flow rate of the slurry is the dominant factor in the time required for sealing, limiting the further reduction of the blocking time.

In this model, it can be seen that in this model, C-S slurry dynamic water pressure is higher, and the slurry flow rate is lower, but it can complete the sealing of the fissure in a short period, and at the same time, the cement slurry is still

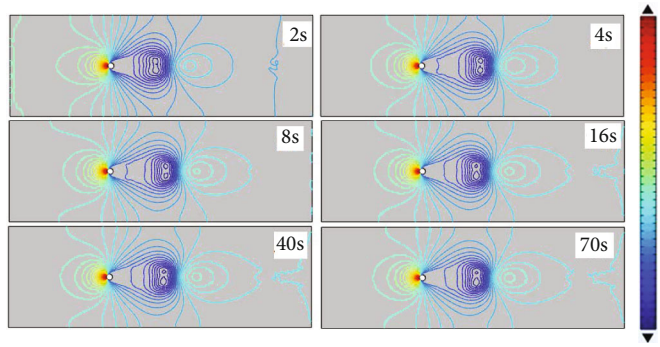

Figure 12: Cement slurry pressure contour.

not resistant to flushing and cannot complete the crack sealing work. Therefore, in the dynamic water environment, C-S slurry blocking effect is better than cement slurry.

5.2. Pressure Field Variation

5.2.1. Variation in Cement Slurry Pressure Field

(1) Pressure Contour. The viscosity of cement changes at different temperatures is small enough in the dynamic water environment to cause the pressure contour to change significantly, the pressure contour distribution at different temperatures is the same, the numerical size difference does not exceed 5%, and the specific distribution is shown in Figure 12. The pressure distribution around the slurry hole is extremely complex at this point.

It can be seen that the distribution of pressure contours can be divided into three parts: the left side of the slurry hole, the spread of the two sides of the slurry increasing, that is, the head of the "comet," and the spread of the two sides of the slurry suddenly reduced, that is, the tail of the "comet." The pressure value is high on the left side of the injection hole, the pressure contour forms a closed shape through the slurry hole, and the distribution at the injection hole is dense. Because of the winding, the pressure at the head of a comet is minimal or even negative, and the pressure contours are very dense at the comet's head and tail junction. The pressure contours in the tail area are closed ring-shaped and sparsely distributed.

(2) Pressure Time Distribution. The distribution of pressure contours can be seen, and the injection hole reverse water measurement pressure is the largest; so, the reaction pressure at this position changes over time, as shown in Figure 13. In the initial stage of slurry injection, the pressure rises rapidly, basically stable after 8 s, the pressure size at different temperatures is the same, and the difference is not more than 5%; so, the rapid increase of cement slurry pressure is not related to the viscosity change of cement slurry, presumably due to the change of slurry diffusion pattern makes the water's winding movement change, so that the pressure is rising rapidly.

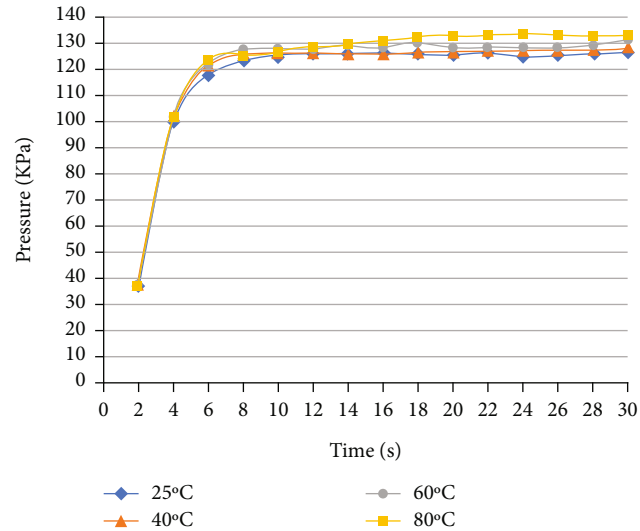

Figure 13: Grouting pressure varies with time of cement slurry.

(3) Pressure Spatial Distribution. Monitor the distribution of pressure on line 1 and line 2, as shown in Figure 14. On line 1, on the reverse waterside, the slurry pressure decays rapidly after moving away from the injection hole, the attenuation of 0.2 m pressure in the injection hole is 80%, and 90% is done within 0.4 m. On the water side, a clear negative pressure zone is produced due to the flow of water, the pressure along the direction of the water first drops and then rises, to 0.8 m rise to the maximum value, and then began to slowly drop to 0, and the longer the injection time, the larger the negative pressure area and the greater the minimum and maximum pressure. On line 2, the pressure increases from a negative value that increases to a maximum value at 0.1 m and remains the same, and the value decreases with the injection.

5.2.2. Variation in C-S Slurry Pressure Field. Unlike cement slurry, the change of viscosity of C-S slurry at different temperatures is very significant, which makes the change of pressure at different temperatures obvious.

(1) Pressure Contour. The change of pressure contour in the pulping process is shown in Figure 15 and can be roughly

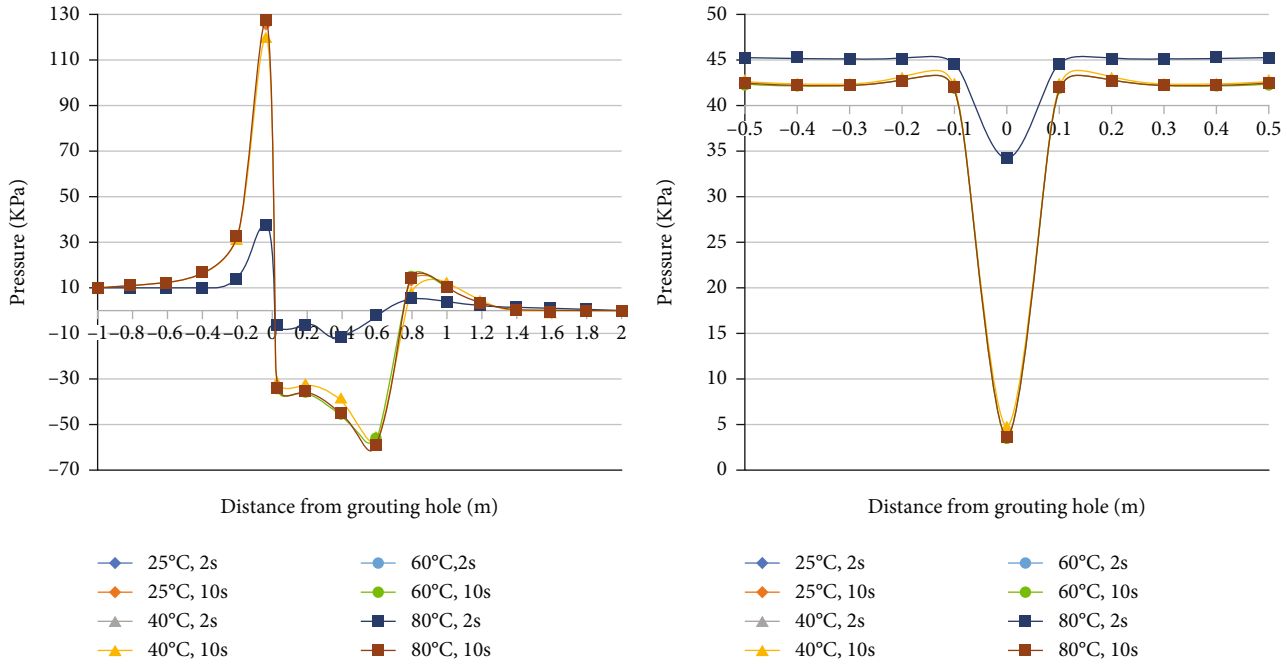

Figure 14: Variation of cement slurry pressure space.

divided into four stages. In the first stage, the pressure contours near the injection hole are all passed through the injection hole, the pressure contours on the inverse water side of the injection hole are elliptical, the pressure contours on both sides are the dividing line of the slurry hole, the pressure contours on the counter water side of the slurry hole are curved in the direction of reverse water, and the pressure contours on the water side of the slurry hole are curved in the direction of the water. The pressure contour is perpendicular to the initial flow rate of the moving water on the down water side away from the injection hole. In the second stage, the pressure contours on the inverse water side of the injection hole gradually extend outwards and change from closed to nonclosed, and the pressure contours become sparse. In the third stage, the nonclosed pressure contours on the inverted water side of the injection holes gradually disappear, and the closed pressure contours that wrap the slurry holes begin to appear near the injection holes, and the closer the injection holes, the denser the pressure contours. In the fourth stage, the vertical pressure contour appears on the inverse water side of the injection hole, and the pressure contour in the model is similar to the shape of the pressure contour in the slurry hole. Furthermore, as the temperature rises, the time required for the first two stages decreases gradually. At 40°C, the first stage of the pressure contour is difficult to observe, and when the temperature reaches 80°C, the first and second stages are difficult to observe.

To monitor the pressure on the water side of the slurry hole, Figure 16 is obtained. The analysis found that at the beginning of the injection, the slurry because of the small viscosity of C-S slurry, low diffusion, and the winding effect of the water flow is strong, and the pressure is greater. With the pulping, the C-S slurry spreads further, the winding action is reduced, and the pressure gradually decreases; then, because the viscosity of the slurry is high, it becomes the main factor affecting the pressure size, and the pressure begins to rise as the viscosity increases. When the local temperature is above 40°C, the viscosity of the slurry is large, the effect of the increase of viscosity on the pressure has been dominant, and the pressure increases with the injection time.

For all temperatures, the growth rate of pressure increases over time, and at a certain point in time, the same time as the corresponding temperature of the rapid growth of viscosity, that is, the higher the temperature, the sooner the rapid growth and the faster the growth rate. Furthermore, the maximum pressure required for slurry cannot be determined simply by comparing temperatures; at high temperatures, the viscosity of the slurry is higher, but it is faster to seal the fissure; so, the maximum injection pressure required is lower. The maximum pressure at 60°C is the smallest of all temperatures simulated in this paper.

(2) Pressure Spatial Distribution. Monitor the distribution of pressure on line 1 and line 2, as shown in Figure 17. The spatial distribution law of C-S slurry in moving water is similar to that in static water, whether it is line 1 or line 2, the pressure is decreasing after staying away from the injection hole, and the closer the injection hole, the faster the drop speed, in the range of 0.2 m that can decay by 80%. Furthermore, the longer the slurry time, the higher the pressure at the same position, and the faster the pressure drops. On line 1, the

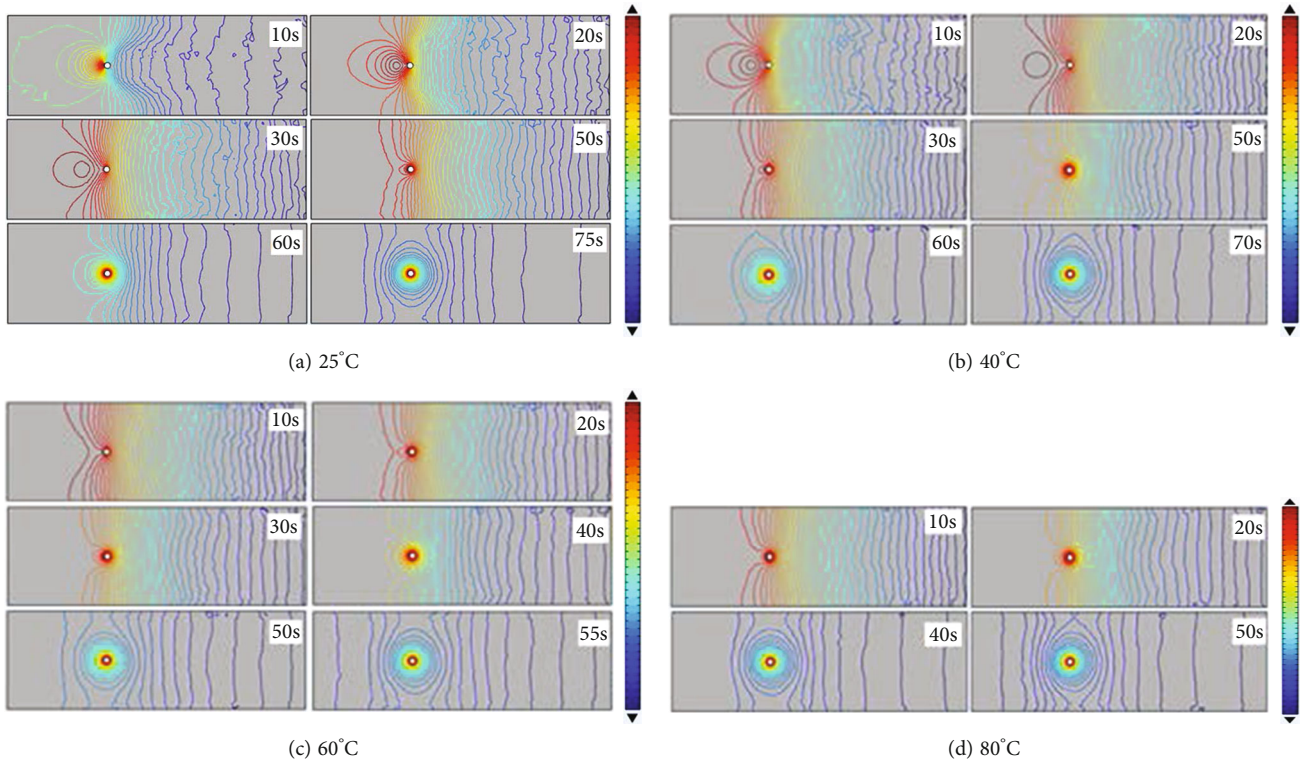

Figure 15: C-S slurry pressure contour.

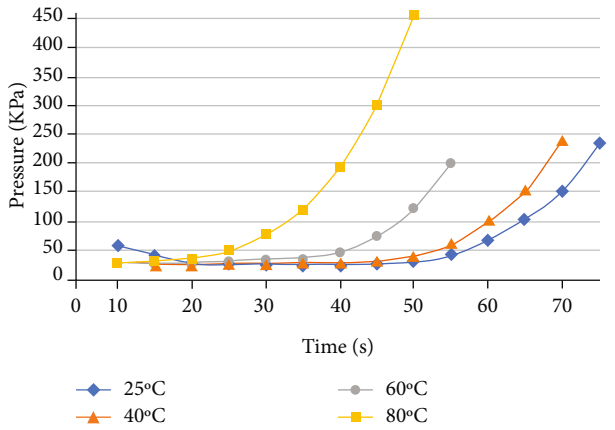

Figure 16: Grouting pressure varies with time of C-S slurry.

pressure on the right side of the injection slurry hole is lower than the pressure on the left side of the injection hole at the same distance due to the influence of the backwater side, and the pressure attenuation speed on the right side is faster; on line 2, the same distance, the longer the slurry time, and the higher the temperature, the greater the pressure, and the faster the pressure drop.

6. Discussion

Previous researchers have carried out extensive grouting laboratory tests as well as theoretical and numerical experiments. To verify the accuracy of numerical simulation in this study, the room temperature part of simulation results was qualitatively compared with the study results of Li et al. [45].

Li et al. used C-S grout for the grouting test, the cement used in the test was P.O.32.5, and the volume ratio of W: S was 1 : 1. The grouting model is 4 m long and 2 m wide, the grouting hole diameter is 5 mm, and the grouting speed of Li et al. is 0.4 m/s. [46] For a hydrostatic environment, the volume ratio of C: S is 1 : 1. [47] For the flow environment, the flow velocity is 0.6 m/s. [48] The comparison of the results is shown in Figures 18 and 19.

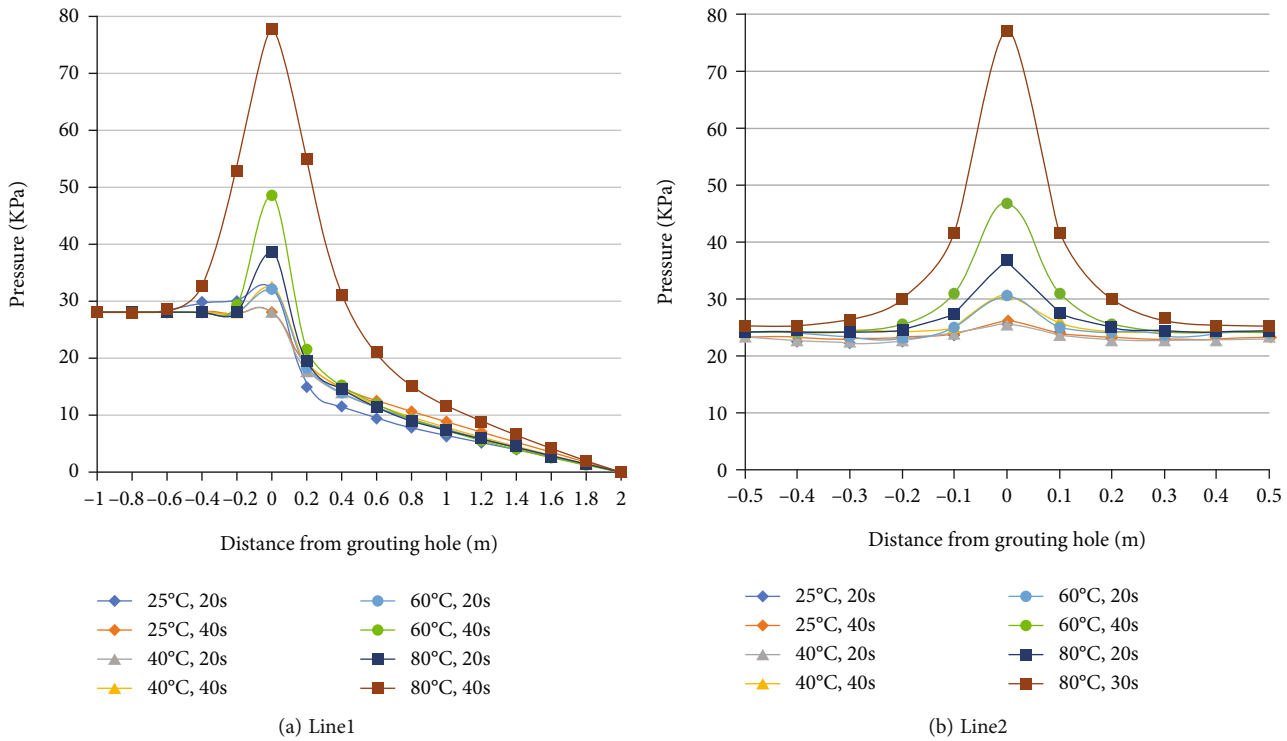

(a) Line1 (b) Line2

Figure 17: Variation in the pressure space of C-S slurry.

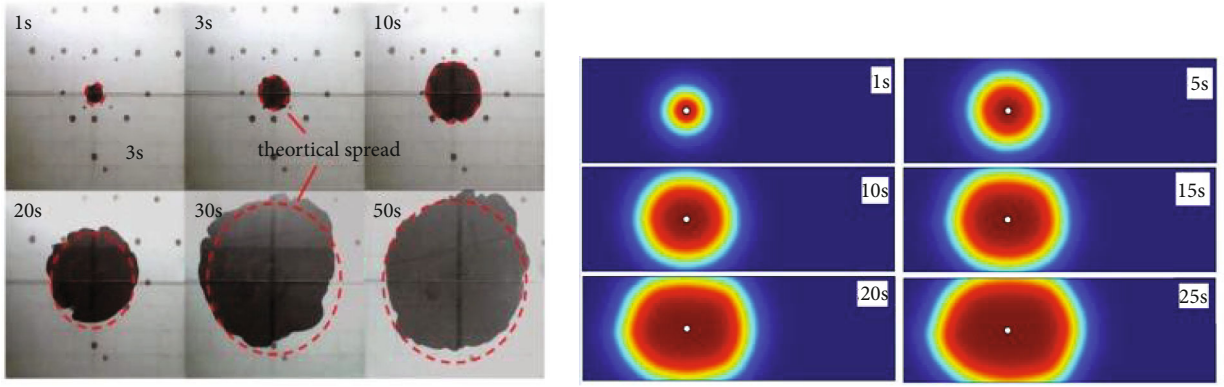

(a) Experimental results of Li et al. (b) Simulation results of C-S slurry

Figure 18: Comparison of results in hydrostatic environment.

(a) Experimental results of Li et al.

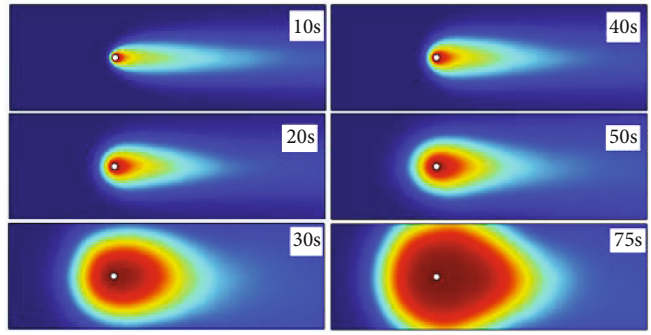

(b) Simulation results of C-S slurry

Figure 19: Comparison of results in a flow environment.

In the hydrostatic environment, the diffusion behavior of slurry is circular, and the simulation results are consistent with the experimental results. In the flow environment, the grout initially has an elliptical distribution, and then the diffusion form of the grout gradually changes from a closed elliptic shape to a U-shaped shape, with the diffusion range in the upstream direction being smaller than the diffusion range in the downstream direction. The simulation results agree well with the experimental results.

Based on the above analysis, the diffusion behavior of grout and grouting pressure change at room temperature is similar to the experimental law of other scholars. The results show that the established values are stable and feasible in fractured media and can be used to analyze fracture grouting at different temperatures.

7. Conclusion

Slurry injection is a commonly used engineering treatment, but the diffusion characteristic C-S of slurry will change in the high-temperature environment. A numerical simulation study on the diffusion law of high-temperature betting slurry was conducted based on the viscosity characteristic C-S of cement and water glass measured by indoor tests at different temperatures. From this study, we can draw the following conclusions.

(1) Under a hydrostatic environment, the diffusion rate of slurry is independent of the temperature and the type of slurry, the time required for the slurry to seal the fissure is the same, but the temperature change, and the slurry type will lead to a change in the injection pressure: the same slurry, the higher the temperature, and the higher the pressure required for slurry injection

(2) In the flow environment, C-S slurry blocking effect is better than the cement slurry blocking effect; at the same time, C-S slurry has been able to seal the cracks, and cement slurry viscosity is still not enough to resist the washing of water flow

(3) For cement slurry, the effect of temperature change on the diffusion pattern of slurry and the injection pressure is not obvious. The higher the temperature of the C-S slurry, the shorter the time required to seal, but the pressure rises faster, and the final sealing gap requires injection pressure to be reduced and then increased

Data Availability

The data used to support the findings of this study are available from the corresponding author upon request.

Conflicts of Interest

The authors declare that there is no conflict of interest regarding the publication of this paper.

Authors' Contributions

Jiandong Niu and Yong Sun contributed equally to this work.

.

Acknowledgments

The authors would like to thank the Natural Science Foundation of Hunan Province and the College Student

Innovation and Entrepreneurship Training Program. This research is supported by the Natural Science Foundation of Hunan Province [2021JJ30832] and the College Student Innovation and Entrepreneurship Training Program [S20211053306618].

References

[1] H. Strømsvik, "The significance of hydraulic jacking for grout consumption during high pressure pre-grouting in Norwegian tunnelling," *Tunnelling and Underground Space Technology*, vol. 90, pp. 357–368, 2019.

[2] J. Niu, B. Wang, H. Wang et al., "An intelligent prediction method of the karst curtain grouting volume based on support vector machine," *Geofluids*, vol. 2020, Article ID 8892106, 14 pages, 2020.

[3] P. Q. Mo, H. H. Chen, and H. S. Yu, "Undrained cavity expansion in anisotropic soils with isotropic and frictional destructuration," *Acta Geotechnica*, pp. 1–22, 2021.

[4] P. Q. Mo, A. M. Marshall, and Y. Fang, "Cavity expansion-contraction-based method for tunnel-soil-pile interaction in a unified clay and sand model: drained analysis," *International Journal of Geomechanics*, vol. 21, no. 5, article 04021055, 2021.

[5] Y. G. Chen, Z. Sun, W. M. Ye, and Y. J. Cui, "Adsorptive removal of Eu(III) from simulated groundwater by GMZ bentonite on the repository conditions," *Journal of Radioanalytical and Nuclear Chemistry*, vol. 311, no. 3, pp. 1839–1847, 2017.

[6] H. Li, Y. Zhang, J. Wu, X. Zhang, L. Zhang, and Z. Li, "Grouting sealing mechanism of water gushing in karst pipelines and engineering application," *Construction and Building Materials*, vol. 254, article 119250, 2020.

[7] C. Zhang, J. Y. Fu, J. F. Yang, X. Ou, X. Ye, and Y. Zhang, "Formulation and performance of grouting materials for underwater shield tunnel construction in karst ground," *Construction and Building Materials*, vol. 187, pp. 327–338, 2018.

[8] Y. B. Lai, S. Li, J. Q. Guo, Z. G. Zhu, and X. Huang, "Analysis of seepage and displacement field evolutionary characteristics in water inrush disaster process of karst tunnel," *Geofluids*, vol. 2021, Article ID 5560762, 2020 pages, 2021.

[9] Y. G. Chen, X. M. Liu, H. N. Lei, W. M. Ye, and Y. J. Cui, "Adsorption property of Pb(II) by the laterite-bentonite mixture used as waste landfill liner," *Advances in Civil Engineering*, Article ID 2879156, 2011 pages, 2019.

[10] J. Niu, Y. Sun, B. Wang et al., "Grouting treatment of water and mud inrush in fully weathered granite tunnel: a case study," *Geofluids*, vol. 2020, Article ID 8838769, 18 pages, 2020.

[11] Y. Mei, X. Y. Zhang, X. Z. Nong, and L. Y. Fu, "Experimental study of the comprehensive technology of grouting and suspension under an operating railway in the cobble stratum," *Transportation Geotechnics*, vol. 30, article 100612, 2021.

[12] P. Q. Mo and H. S. Yu, "Undrained cavity-contraction analysis for prediction of soil behavior around tunnels," *International Journal of Geomechanics*, vol. 17, no. 5, article 04016121, 2017.

[13] Y. G. Chen, X. X. Dong, X. D. Zhang, W. M. Ye, and Y. J. Cui, "Oedometric compression and thermal volume behavior of compacted Gaomiaozi bentonite saturated with salt solution," *Geomechanics for Energy and the Environment*, vol. 25, article 100186, 2021.

[14] X. L. Gan, J. L. Yu, X. N. Gong, Y. Hou, N. Liu, and M. Zhu, "Response of operating metro tunnels to compensation grouting of an underlying large-diameter shield tunnel: A case study in Hangzhou," *Underground Space*, 2021.

[15] S. M. Wang, C. He, L. Nie, and G. C. Zhang, "Study on the long-term performance of cement-sodium silicate grout and its impact on segment lining structure in synchronous backfill grouting of shield tunnels," *Tunnelling and Underground Space Technology*, vol. 92, article 103015, 2019.

[16] P. Q. Mo, X. W. Gao, W. B. Yang, and H. S. Yu, "A cavity expansion-based solution for interpretation of CPTu data in soils under partially drained conditions," *International Journal for Numerical and Analytical Methods in Geomechanics*, vol. 44, no. 7, pp. 1053–1076, 2020.

[17] Y. G. Chen, Y. Q. Cai, K. Pan, W. M. Ye, and Q. Wang, "Influence of dry density and water salinity on the swelling pressure and hydraulic conductivity of compacted GMZ01 bentonite-sand mixtures," *Acta Geotechnica*, pp. 1–18, 2021.

[18] X. Y. Ye, H. Moayedi, M. Khari, and L. K. Foong, "Metaheuristic-hybridized multilayer perceptron in slope stability analysis," *Smart Structures and Systems*, vol. 26, no. 3, pp. 263–275, 2020.

[19] W. Q. Mu, D. Y. Wang, L. C. Li et al., "Cement flow in interaction rock fractures and its corresponding new construction process in slope engineering," *Construction and Building Materials*, vol. 303, article 124533, 2021.

[20] J. D. Niu, Z. W. Li, W. H. Gu, and K. Chen, "Experimental study of split grouting reinforcement mechanism in filling medium and effect evaluation," *Sensors*, vol. 20, no. 11, article 3088, 2020.

[21] J. S. Yang, C. Zhang, J. Y. Fu, S. Wang, X. Ou, and Y. Xie, "Pre-grouting reinforcement of underwater karst area for shield tunneling passing through Xiangjiang River in Changsha, China," *Tunnelling and Underground Space Technology*, vol. 100, article 103380, 2020.

[22] P. Q. Mo and H. S. Yu, "Drained cavity expansion analysis with a unified state parameter model for clay and sand," *Canadian Geotechnical Journal*, vol. 55, no. 7, pp. 1029–1040, 2018.

[23] X. Y. Ye, S. Y. Wang, Q. Li, S. Zhang, and D. C. Sheng, "Negative effect of installation on performance of a compaction-grouted soil nail in poorly graded Stockton beach sand," *Journal of Geotechnical and Geoenvironmental Engineering*, vol. 146, no. 8, article 04020061, 2020.

[24] X. Y. Ye, S. Y. Wang, S. Zhang, X. Xiao, and F. Xu, "The compaction effect on the performance of a compaction-grouted soil nail in sand," *Acta Geotechnica*, vol. 15, no. 10, pp. 2983–2995, 2020.

[25] X. Y. Ye, Q. Wang, S. Y. Wang, S. Sloan, and D. C. Sheng, "Performance of a compaction-grouted soil nail in laboratory tests," *Acta Geotechnica*, vol. 14, no. 4, pp. 1049–1063, 2019.

[26] X. Y. Ye, S. Y. Wang, Q. Wang, S. W. Sloan, and D. C. Sheng, "The influence of the degree of saturation on compaction-grouted soil nails in sand," *Acta Geotechnica*, vol. 14, no. 4, pp. 1101–1111, 2019.

[27] X. Y. Ye, S. Y. Wang, X. Xiao, S. Sloan, and D. C. Sheng, "Numerical study for compaction-grouted soil nails with multiple grout bulbs," *International Journal of Geomechanics*, vol. 19, no. 2, article 04018193, 2019.

[28] X. Y. Ye, Z. J. Lyu, and L. K. Foong, "Hybridized dragonfly, whale and ant lion algorithms in enlarged pile's behavior," *Smart Structures and Systems*, vol. 25, no. 6, pp. 765–778, 2020.

[29] Y. G. Chen, L. L. Guan, S. Y. Zhu, and W. J. Chen, "Foamed concrete containing fly ash: Properties and application to

backfilling," *Construction and Building Materials*, vol. 273, article 121685, 2021.

[30] S. C. Li, D. D. Pan, Z. H. Xu, P. Lin, and Y. C. Zhang, "Numerical simulation of dynamic water grouting using quick-setting slurry in rock fracture: the Sequential Diffusion and Solidification (SDS) method," *Computers and Geotechnics*, vol. 122, article 103497, 2020.

[31] T. J. Shamu, L. Zou, and U. Håkansson, "A nomogram for cement-based rock grouting," *Tunnelling and Underground Space Technology*, vol. 116, article 104110, 2021.

[32] X. Yan, Z. Z. Sun, and Q. Q. Dong, "The unified pipe-interface element method for simulating the coupled hydro- mechanical grouting process in fractured rock with fracture propagation," *Engineering Fracture Mechanics*, vol. 256, article 107993, 2021.

[33] X. W. Liu, C. Hu, Q. S. Liu, and J. He, "Grout penetration process simulation and grouting parameters analysis in fractured rock mass using numerical manifold method," *Engineering Analysis with Boundary Elements*, vol. 123, pp. 93–106, 2021.

[34] X. W. Liu, H. X. Chen, Q. S. Liu, B. Liu, and J. He, "Modelling slurry flowing and analyzing grouting efficiency under hydro-mechanical coupling using numerical manifold method," *Engineering Analysis with Boundary Elements*, vol. 134, pp. 66–78, 2022.

[35] Z. Li, H. X. Liu, Z. L. Dun, L. W. Ren, and J. J. Fang, "Grouting effect on rock fracture using shear and seepage assessment," *Construction and Building Materials*, vol. 242, article 118131, 2020.

[36] J. Rafi and H. Stille, "A method for determining grouting pressure and stop criteria to control grout spread distance and fracture dilation," *Tunnelling and Underground Space Technology*, vol. 112, article 103885, 2021.

[37] Q. S. Zhang, L. Z. Zhang, R. T. Liu, S. C. Li, and Q. Q. Zhang, "Grouting mechanism of quick setting slurry in rock fissure with consideration of viscosity variation with space," *Tunnelling and Underground Space Technology*, vol. 70, pp. 262–273, 2017.

[38] F. Xiao, J. L. Shang, and Z. Y. Zhao, "DDA based grouting prediction and linkage between fracture aperture distribution and grouting characteristics," *Computers and Geotechnics*, vol. 112, pp. 350–369, 2019.

[39] X. M. Du, H. Y. Fang, S. Y. Wang, B. H. Xue, and F. M. Wang, "Experimental and practical investigation of the sealing efficiency of cement grouting in tortuous fractures with flowing water," *Tunnelling and Underground Space Technology*, vol. 108, article 103693, 2021.

[40] J. D. Niu, B. Wang, C. Feng, and K. Chen, "Experimental research on viscosity characteristics of grouting slurry in a high ground temperature environment," *Materials*, vol. 13, no. 14, article 3221, 2020.

[41] Z. Xu, C. Liu, X. Zhou, G. Gao, and X. Feng, "Full-scale physical modelling of fissure grouting in deep underground rocks," *Tunnelling and Underground Space Technology*, vol. 89, pp. 249–261, 2019.

[42] X. Y. Xu, Z. J. Wu, H. Sun, L. Weng, Z. Chu, and Q. Liu, "An extended numerical manifold method for simulation of grouting reinforcement in deep rock tunnels," *Tunnelling and Underground Space Technology*, vol. 115, article 104020, 2021.

[43] Q. S. Liu and L. Sun, "Simulation of coupled hydro-mechanical interactions during grouting process in fractured media based on the combined finite-discrete element method," *Tunnelling and Underground Space Technology*, vol. 84, pp. 472–486, 2019.

[44] F. Sha, S. C. Li, R. T. Liu, Q. S. Zhang, and Z. F. Li, "Performance of typical cement suspension-sodium silicate double slurry grout," *Construction and Building Materials*, vol. 200, pp. 408–419, 2019.

[45] S. C. Li, R. T. Liu, Q. S. Zhang, and X. Zhang, "Protection against water or mud inrush in tunnels by grouting: a review," *Journal of Rock Mechanics and Geotechnical Engineering*, vol. 8, no. 5, pp. 753–766, 2016.

[46] Y. X. Guo, Q. S. Zhang, F. Xiao, R. T. Liu, Z. J Wang, and Y. K. Liu, "Grouting rock fractures under condition of flowing water," *Carbonates and Evaporites*, vol. 35, no. 3, Article ID 96, 2020.

[47] Q. S. Zhang, L. Z. Zhang, R. T. Liu et al., "Laboratory experimental study of cement-silicate slurry diffusion law of crack grouting with dynamic water," *Rock Soil Mech*, vol. 36, no. 8, pp. 59–68, 2015.

[48] L. Z. Zhang, Q. S. Zhang, R. T. Liu et al., "Penetration grouting mechanism of quick setting slurry considering spatiotemporal variation of viscosity," *Rock Soil Mech*, vol. 38, no. 2, pp. 443–452, 2017.

Hindawi
Geofluids
Volume 2022, Article ID 5350650, 15 pages
https://doi.org/10.1155/2022/5350650

Research Article

Model Test and Numerical Simulation Analysis on Freezing Effect of Different Freezers in Freeze-Sealing Pipe-Roof Method

Haibing Cai,[1] **Yujie Liu**,[1] **Rongbao Hong**,[1] **Mengkai Li**,[1] **Zongjin Wang**,[2] **and Hanglong Ding**[1]

[1]*School of Civil Engineering and Architecture, Anhui University of Science and Technology, Huainan, Anhui 232001, China*
[2]*China Coal Special Drilling Engineering Co., Ltd., Hefei 230001, China*

Correspondence should be addressed to Haibing Cai; haibingcai@163.com

Received 29 October 2021; Accepted 21 December 2021; Published 27 January 2022

Academic Editor: Xinyu Ye

The Gongbei Tunnel Project is a key phased project of the Zhuhai Connection Line of the Hong Kong–Zhuhai–Macao Bridge, and the freeze-sealing pipe-roof (SFPR) method was first applied successfully. During this period, in order to obtain the best arrangement of freezers, three configurations, that is, solid pipe with circular freezer (SCF), empty pipe with double circular freezer (EDCF), and empty pipe with special-shaped freezer (ESF), were designed to analyze their freezing effects. The model test results show that the freezing temperature fields excited by different arrangements of freezers are obviously different, and the freezing effect of ESF is the best. The numerical simulation results indicate that the temperature cloud diagram of SCF at 42 h is butterfly-shaped after opening the limit pipes, and the temperature cloud diagrams of ESF and EDCF are the same as the model test results. However, the processing method of ESF is relatively complex, which adopts arc angle steel welding requiring a lot of reverse welding and high welding quality. Eventually, EDCF is recommended to ensure the quality of frozen walls due to its lower cost and better freezing effect. This research plays a basic role in the implementation of the freeze-sealing pipe-roof method.

1. Introduction

With the further progress of urbanization, the development and utilization of urban underground space are facing an increasingly harsh construction environment [1], especially, it is more severe during the construction of urban tunnels in shallow and water-rich strata. Under this background of urban construction, the artificial ground freezing (AGF) method has been widely used due to its environmental friendliness [2]. So far, projects using AGF technique, such as the cross-passage construction of Zhuji Intercity Rail Transit, China [3], the turn-back tunnel construction of Guangzhou Metro Line 3 Tianhe Station, China [4], the tunnel construction of Nanjing Metro Line 2 Xinjiekou Station, China [5], and so on, have all achieved good social benefits. Besides, the frozen wall formed by the AGF method mainly plays a role in water sealing [6], and its bearing capacity is relatively weak compared with the steel pipe jacking structure. Some successful applications of steel pipe jacking structure in the tunnel excavation are as follows: rectangular pipe jacking construction between two parallel tunnels in Nanjing, China [7], four parallel pipe jacking construction under Guan River, China [8], two steel pipe jacking construction under Yangtze River, China [9], and so on. These presupporting methods provided good construction conditions for tunnel excavation but exposed the weakness of water sealing, especially in long distance curved pipe-jacked projects. Hu et al. [10] have been committed to combining the two construction methods to obtain better engineering application value, and four research methods, that is, theoretical analysis [11], numerical simulation [12], model test [13], and field monitoring [6], have been implemented to verify the feasibility of this new construction method. This novel method is named freeze-sealing pipe-roof (SFPR) method, an auxiliary method combining the pipe-roof method and artificial freezing

method, where the steel pipe-roof mainly plays a role in load bearing and the frozen soil curtain mainly plays a role in water sealing. Benefitting from the support of the above research, SFPR has successfully solved many construction problems of the Gongbei tunnel, including shallow buried depth, large section [14], abundant water, large curvature, etc.

However, there are still many possibilities available for the research of freezers arranged in steel pipes, such as the shape of the freezer, number of the freezer, location of the freezer, and so on. Four mainstream methods can be used to study these problems; they are theoretical analysis, numerical simulation, model test, and field monitoring. Qi et al. [15] studied the temperature field expansion of basin-shaped freezing method through physical model test and numerical simulation; it shows the gradual development of freezing from backwater surface to front water surface under seepage condition. Liu et al. [16] studied the freezing effect considering the pipe inclination in the unit cell model by prescribing various values of freeze pipe spacing based on a coupled thermohydraulic finite element method. Vitel et al. [17] studied the heat transfer between the freeze pipe and the surrounding ground and established a developed model to conduct parametric studies on operating conditions, refrigerant type, system geometry, or ground properties through numerical simulation. It is not difficult to see that model test and numerical simulations are more popular.

In view of this, this paper studies the distribution law of the freezing temperature field excited by different arrangements of freezers, based on the SFPR method construction of the Gongbei tunnel. Specifically, the model test and numerical simulation of three configurations are designed by using the wet-heat similarity criterion. They are solid pipe with circular freezer (SCF) freezing configuration, empty pipe with double circular freezer (EDCF) freezing configuration, and empty pipe with special-shaped freezer (ESF) freezing configuration, respectively. All the basic research is the expansion and enrichment of the SFPR technique, which also provides a favorable reference for the follow-up projects similar to the Gongbei tunnel.

2. Project Overview

As a critical part of the Zhuhai connection highway of the Hong Kong–Zhuhai–Macao Bridge project, the Gongbei tunnel is located in the Xiangzhou District of Zhuhai City and has a length of 2.74 km. That length is divided into an open excavation section of the sea area (1225 m length), an underground excavation section of the port (255 m length), and an open excavation section of the land area (1229 m length). Amongst these divisions, the underground excavation section of the port is the largest undercut tunnel in the world, with a buried depth of 4–5 m and an excavation section area of 337 m^2. The plane layout of the underground excavation section of the Gongbei tunnel is shown in Figure 1. Furthermore, this section passes through the Gongbei port with poor geological and sensitive environmental conditions, such as high groundwater level, soft stratum, dense building groups, and mass population flow. It is required not to affect the normal passage of the Gongbei port and normal use of surrounding buildings and underground pipelines during the construction of the Gongbei tunnel.

As a new construction technique that combines the pipe jacking method with the artificial ground freezing method, the freeze-sealing pipe-roof method has been proposed and applied to the construction of the Gongbei tunnel. As shown in Figure 2, 36 steel pipes with a diameter of 1620 mm are arranged around the Gongbei tunnel, in which the odd-numbered pipes are filled with microexpansive concrete, while the even-numbered pipes are not filled with any materials. Besides, in each odd-numbered pipe, two Φ125 mm circular freezing pipes are embedded for soil freezing, and one Φ159 mm limit pipe is embedded to control the scope of the frozen curtain. Correspondingly, two special-shaped freezing pipes are welded on the inner wall of each even-numbered pipe to intensify the soil freezing.

In this paper, a new freezing configuration that empty pipe with a double circular freezer (EDCF) is proposed based on the exiting two freezing configurations (SCF and ESF), and it has the advantages of lower cost and convenient processing. Therefore, it is meaningful to determine the optimal arrangement of freezers from many aspects among these three freezing configurations.

3. Design of Model Test

3.1. Similarity Criterion

3.1.1. Temperature Field Similarity. The heat conduction equation of the frozen zone and the unfrozen zone is as follows:

$$\frac{\partial \theta_n}{\partial \tau} = a_n\left(\frac{\partial^2 \theta_n}{\partial r^2} + \frac{1}{r}\frac{\partial \theta_n}{\partial r}\right), \tag{1}$$

where θ_n is temperature; when $n = 1$, it is the temperature in the unfrozen zone; when $n = 2$, it is the temperature in the unfrozen zone; τ is time; a_n is the thermal conductivity coefficient.

The temperature boundary conditions are as follows:

$$\begin{cases} \theta(r, 0) = \theta_0, \\ \theta(\infty, \tau) = \theta_0, \\ \theta(\rho, \tau) = \theta_D, \\ \theta(r_0, \tau) = \theta_y, \end{cases} \tag{2}$$

where θ_0 is the initial temperature of soil; θ_D is the freezing temperature; θ_y is the brine temperature.

Besides, at the frozen front ($r = \rho$), the heat balance equation is as follows:

$$\lambda_2 \frac{\partial \theta_2}{\partial r}\Big|_{r=\rho} - \lambda_1 \frac{\partial \theta_1}{\partial r}\Big|_{r=\rho} = B\frac{\mathrm{d}\rho}{\mathrm{d}\tau}, \tag{3}$$

where B is the latent heat; λ_1 is the thermal conductivity in the unfrozen zone, while λ_2 is the thermal conductivity in the frozen zone.

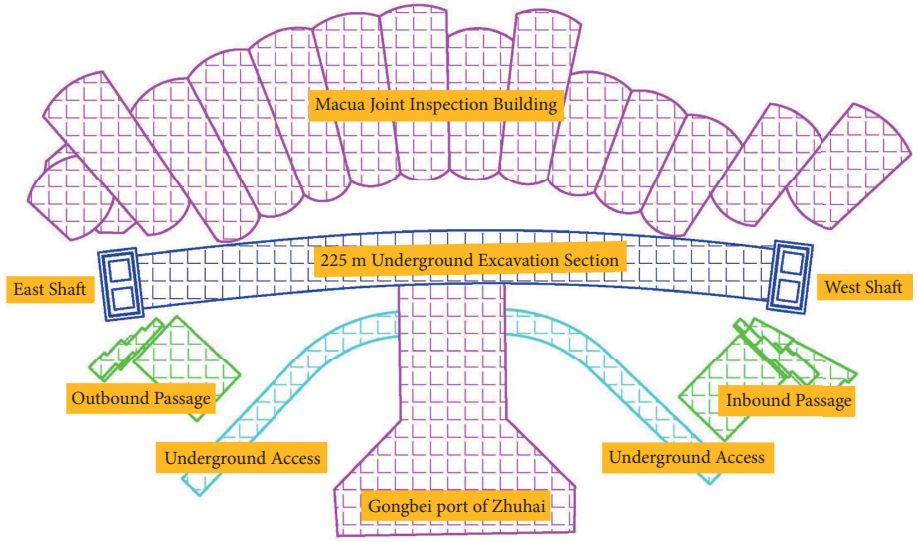

Figure 1: Layout chart of the Gongbei undercut tunnel.

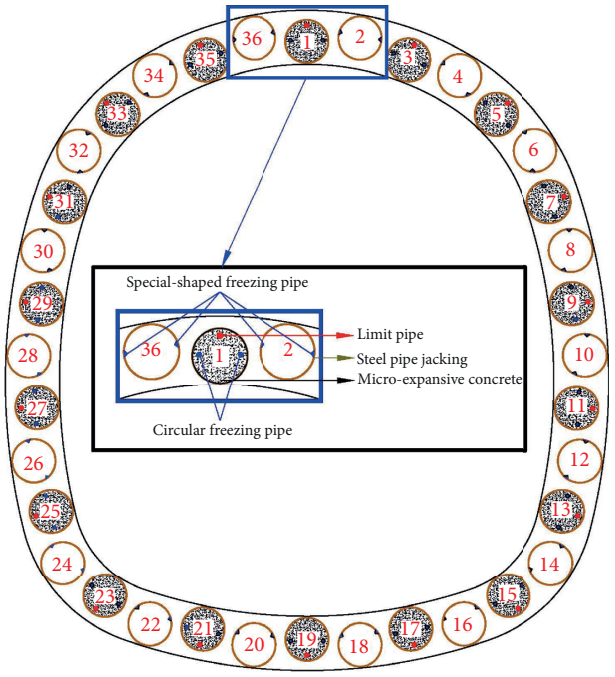

Figure 2: Layout of the pipe curtain.

According to the differential equation of the freezing temperature field, the similarity criterion equation of the freezing temperature field can be obtained as follows [18, 19]:

$$F\left(F_0, K_0, L_0, \theta\right) = 0, \tag{4}$$

where F_0 is the Fourier criterion, $F_0 = a\tau/r^2$, a is the temperature diffusivity of sand (m^2/s), τ is time (h), r is the frozen wall position; K_0 is Kosovic's criterion, $K_0 = Q/tc$, Q is the latent heat released when the unit mass of sand is frozen (J/g), t is the temperature (°C), and c is the specific heat (J/(g°C)); L_0 is the geometric criterion; θ is the temperature criterion, including sand initial temperature θ_0, brine temperature θ_y and freezing temperature θ_D.

3.1.2. Moisture Field Similarity. The governing equation of water migration is as follows:

$$\frac{\partial h}{\partial \tau} = b\left(\frac{\partial^2 h}{\partial r^2} + \frac{1}{r}\frac{\partial h}{\partial r}\right), \tag{5}$$

where h is the humidity; b is the moisture conductivity coefficient.

The moisture boundary conditions are as follows:

$$\begin{cases} h(r,0) = h_0, \\ h(\infty,\tau) = h_0, \\ h(\rho,\tau) = 0, \end{cases} \tag{6}$$

where h_0 is the initial humidity.

According to the differential equation of the moisture field, the similarity criterion equation of the moisture field can be obtained as follows:

$$F(F_h, H_h, L_h) = 0, \tag{7}$$

where F_h is the Fourier criterion, $F_h = b\tau/r^2$, b is the moisture conductivity coefficient of sand, τ is time(h), r is the frozen wall position; H_h is the humidity criterion, $H = h/h_0$; L_h is the geometric criterion.

3.1.3. Scaling Laws. If the model material is the same as the prototype material, the thermal conductivity scaling law $C_a = 1$ and the specific heat scaling law $C_c = 1$. The latent heat scaling law $C_Q = 1$ can be obtained by guaranteeing that the model soil moisture content is the same as the prototype. It can be deduced from equation (4) that

$$\begin{aligned} C_\tau &= C_l^2, \\ C_t &= 1, \end{aligned} \tag{8}$$

where C_τ is the time scaling law, C_t is the temperature scaling law, and C_l is the geometric scaling law, which is $C_l = 10$ for this model test. The test discussed in this paper focused on the distribution of the temperature field, providing a comparison of the optimum results of the FSPR process. Because the tests were conducted at a partial scale, the saturated sand used in the test was reformulated according to the nature of the undisturbed soil at the Gongbei Tunnel Project site to ensure the scaling law of materials.

The velocity of saltwater in the freezing tube can be described by the following:

$$v' = C_l v, \tag{9}$$

where v' is the velocity of saltwater in the freezer of the model, and v is the velocity of saltwater in the freezer of the prototype.

The dimensions of the jacking pipe and freezers are shown in Table 1 according to the geometric similarity ratio. Besides, in the model test, low-temperature brine consistent with the engineering site is selected as the refrigerant. The freezers are sealed and connected with rubber pipes with an inner diameter of 8 mm, and the flow through the single pipe is controlled as 0.5 m^3/h (0.5 m^3/h in engineering site), while the velocity of the refrigerant is controlled as 165.8 m/min (16.58 m/min in engineering site), according to equation (9).

3.2. Design of Model Box. The test is carried out in the freezing station of the project department of Liuzhuang Mine, China. The size of the test box is 3.3 m × 1.2 m × 1.5 m, and the thickness of the steel plate is 6 mm. The height of the pipe curtain from the bottom of the model box is 520 mm. All the inner surface of the steel plate is laid with foam insulation board with a thickness of 100 mm. The design drawing of the model box is shown in Figure 3.

Figure 4 shows the photographs of three freezing configurations in the model box. Figure 4(a) shows the solid pipe with a circular freezer (SCF), and the steel jacking pipe is filled with a C30 crushed stone concrete. Two circular freezers are symmetrically distributed in the horizontal direction of pipe jacking, while two limiting pipes are symmetrically distributed in the vertical direction of pipe jacking. Figure 4(b) shows an empty pipe with a double circular freezer (EDCF). Four circular freezers are symmetrically arranged in the horizontal position of the pipe jacking and wrapped with cement mortar. Figure 4(c) shows an empty pipe with a special-shaped freezer (ESF). Two special-shaped freezers made of angle steels are symmetrically arranged at the horizontal position of the pipe jacking. After the pipes and test elements are arranged, the saturated sand is backfilled. Meanwhile, the thermodynamic tests are carried out to obtain the water content, dry density, freezing point, thermal conductivity and et al. of the saturated sand, and test results are shown in Table 2.

3.3. Design of Freezing System. Figure 5 shows the low-temperature circulating brine refrigeration system used in the model test. The temperature of brine circulating in the freezers is controlled as −21°C, while the temperature of brine circulating in the limiting pipes is controlled as 7°C. Each freezing pipe was equipped with an independent switch.

3.4. Design of Monitoring System. Figure 6 shows the temperature monitoring points distributed at the three directions (0°, 45°, and 90°) surrounding the SCF, EDCF, and ESF.

The monitoring system adopts the TDS-630 multipoint test system, and the temperature sensor of the thermocouple is selected as the test material. The CW-500 digital temperature measurement system is also used as the second temperature measurement system to ensure measurement accuracy and reliability. The temperature monitoring points of the two temperature sensor systems are arranged in the box in an 'axisymmetric' manner, as shown in Figure 7.

The monitoring time is 0.5 h (the fastest is 15 min) in the early freezing period, and it is adjusted to 1 h in the late freezing period. Besides, the system is set to automatically collect data, and the monitoring time interval is appropriately extended after data stabilization.

3.5. Model Test Process

(1) Before the test, the physical indexes such as moisture content, dry density, freezing temperature, and thermal conductivity of the saturated sand were measured by cutting ring sampling. The test time, ambient temperature, and initial temperature of the sand in the box were recorded before freezing.

Table 1: Dimensions of jacking pipe and freezers.

Name	Original dimension (mm)	Model dimension (mm)
Pipe jacking (inner diameter)	1590	159
Circular freezer (inner diameter)	80	8
Special-shaped freezer (angle steel)	125 × 125	12.5 × 12.5
Limit pipe (inner diameter)	80	8

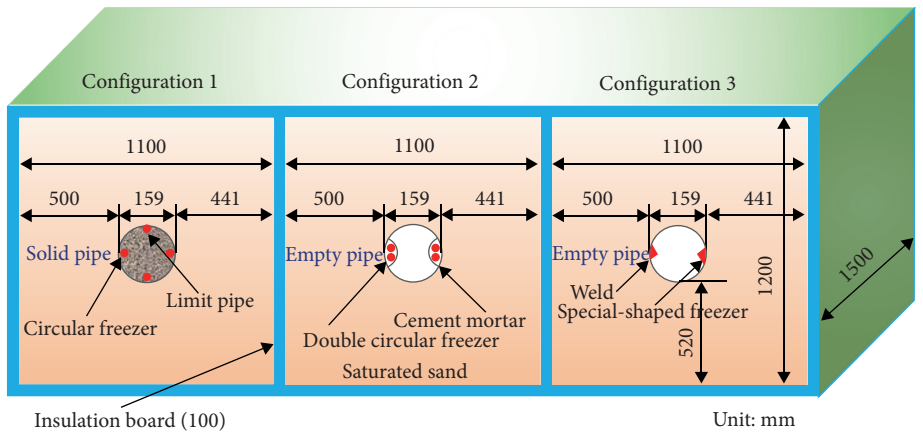

Figure 3: Schematic diagram of model box.

(a) (b) (c)

Figure 4: Pipe jacking layout drawing: (a) SCF; (b) EDCF; (c) ESF.

Table 2: Properties of the test soil.

Test soil	Saturated moisture (%)	Density ($g \cdot cm^{-3}$) ρ	Density ($g \cdot cm^{-3}$) ρ_d	Thermal capacity ($kJ \cdot kg^{-1}°C^{-1}$)	Thermal conductivity ($W \cdot m^{-1}K^{-1}$)	Freezing temperature (°C)
Saturated sand	40.29	1.435	1.317	1.372 1.683	1.475 1.087	−10 20

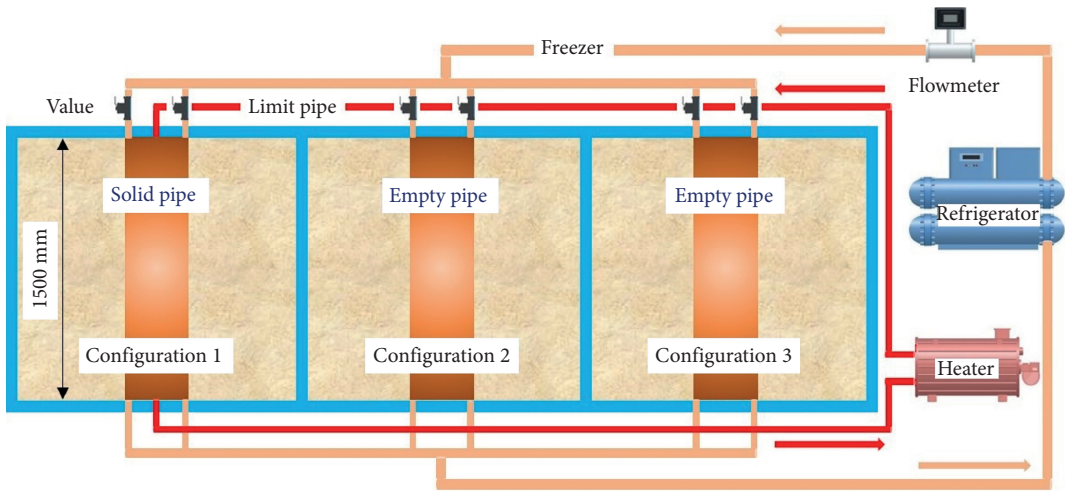

Figure 5: Freezing system of the model test.

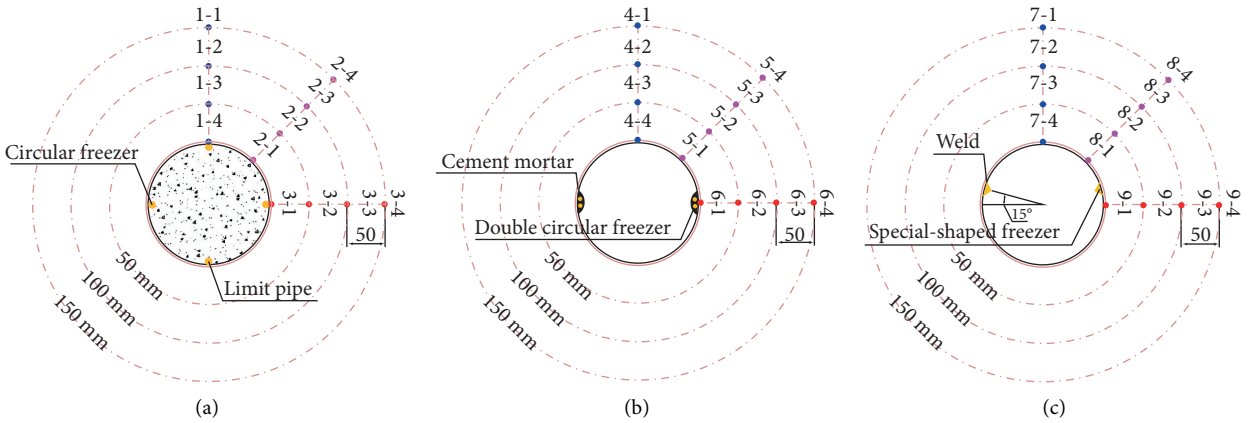

Figure 6: Arrangement of temperature monitoring points: (a) SCF; (b) EDCF; (c) ESF.

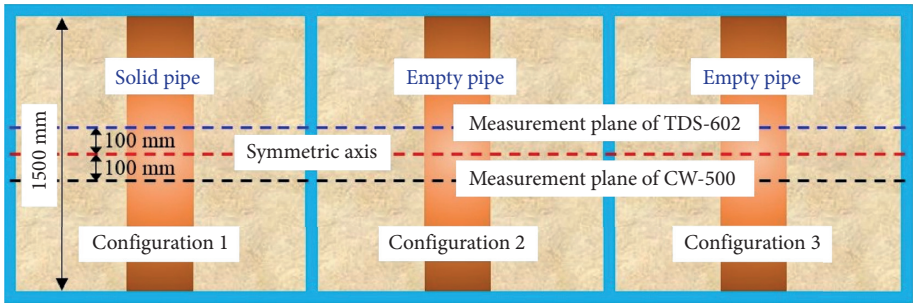

Figure 7: Arrangement of measurement plane.

(2) The refrigerator is opened to ensure that the brine temperature in the brine tank is fully reduced to the design temperature.

(3) The low-temperature brine system began to circulate, and all the test areas were simultaneously actively frozen. The test system comprehensively

worked, and the temperature data were regularly monitored until the end of the first test process (the temperature of the measuring point at 100 mm above the pipe jacking was reduced to −1°C). At this time, the thickness of the frozen wall reached the designed thickness (360 mm in total).

(4) The active freezing time was set to 42 h. The limiting-pipe test was carried out to study the effect of the limiting-pipe. When the active freezing was 21 h, the limiting brine constant temperature heater was opened, and the limiting brine circulation was carried out.

(5) After freezing to the specified test time, the refrigeration unit stopped supplying cold, and the normal temperature brine was circulated in the circular freezing pipe. All the test areas entered the forced thawing period until the saturated sand returned to normal temperature. The thawing time was controlled according to the temperature data of the measuring points.

4. Analysis of Model Test Results

4.1. Freezing Effect of SCF. Figure 8 shows the 'temperature-time' curves of the monitoring points at 90°, 45°, and 0°, respectively. The legend with '∗' represents the freezing mechanism that opens the limiting pipes after freezing for 21 h, while the legend without '∗' represents the freezing mechanism that does not open the limiting pipes through the freezing period.

Figure 8 demonstrates that the temperature change trend of each temperature measurement point around the pipe jacking in the horizontal direction and in the 45° angle direction with the horizontal direction is consistent. The temperature decreases with time, and the temperature drop is larger in the early stage of freezing and smaller in the later stage. The closer to the freezers, the greater the temperature drop is, while the farther away from the freezers it is, the smaller the temperature drop is, and the smoother the curve is

When the limit pipe is opened at 21 h, the temperature rises, especially at the temperature measuring points 1–4 ∗, 2–1 ∗ , and 3–1 ∗, it shows a jump rise, while it gradually tends to be stable after the limit pipe is opened for a period of time. Besides, the temperature of the temperature measurement point far from the limit pipe also increases, but its increasing range is smaller than that close to the limit pipe. The test result also shows that the temperature influences the range of the limit pipe within a 100 mm radius, and the limit pipe only slows down the rate of temperature decrease, but it does not increase the temperature.

Therefore, opening the limit pipe can effectively control the temperature and ensure the temperature around the pipe jacking changes evenly.

4.2. Freezing Effect of SCF, EDCF, And ESF. Figure 9 shows the 'temperature-time' curves of the monitoring points at 90°, 45°, and 0° in SCF, EDCF, and ESF, respectively.

Furthermore, Figure 9 demonstrates that the temperature change law is basically the same at the same monitoring direction among three freezers arrangements. They all show a 'layered' downward trend with the increasing radius. From the temperature drop trend, the early temperature drop rate of all measuring points is large, and then the later temperature drop rate gradually tends to 0. Besides, the temperature of the ESF decreases faster in the same freezing time, and the freezing effect is better. The closer to ESF it is, the faster the early temperature drop rate is, and the greater the final cooling range is.

The following equations are provided to study the specific changes of temperature:

$$V_c = \frac{t_b - t_a}{T}, \tag{10}$$

where V_c is the average temperature drop rate within the selected time interval (°C/h); t_a and t_b are the initial and final temperature of the selected time interval; T is the interval of freezing time. Here, it is 21 h.

Figure 10 illustrates that the temperature drop rate of SCF is 0.69°C/h at 100 mm, 0.96°C/h at 50 mm, and 1.29°C/h at the place close to pipe jacking. The temperature drop rate of EDCF is 0.53°C/h at 100 mm, 0.77°C/h at 50 mm, and 1.08°C/h at the place close to pipe jacking. The temperature drop rate of ESF is 0.71°C/h at 100 mm, 0.97°C/h at 50 mm, and 1.34°C/h at the place close to pipe jacking. During the period from 21 h to 42 h, the temperature drop rates of the three freezers arrangements are low. The average temperature drop rate of ESF is the largest, the formation time of frozen wall is the shortest, and the freezing effect is the best. However, ESF adopts arc angle steel welding, which is difficult to operate, and considerable seam welding and overhead welding must be performed. The welding requirements are high, the freezing liquid may easily leak, and the maintenance cost is high in the later stage. Therefore, EDCF can be used instead of ESF to ensure the freezing effect of the frozen wall.

4.3. Freezing Effect of the Loop Monitoring Points. The temperature distribution in 42 h is obtained by combining the temperature monitoring points of SCF, EDCF, and ESF in the circumferential direction of 0, 50, 100, and 150 mm, and the 'temperature-time' curve is drawn as shown in Figure 11.

Figure 11 demonstrates that the temperature drop gradient at the temperature measuring point, 0 mm away from the pipe jacking, is the largest. Meanwhile, the temperature drop gradient at the temperature measuring point, 150 mm away from the pipe jacking, is the smallest. It also illustrates that the temperature drop rate at the 45° oblique in the horizontal direction is greater than that at the horizontal direction, while the temperature drop rate at the horizontal direction is greater than that at the vertical direction.

4.4. Temperature Cloud Diagram. The temperature cloud diagram is drawn by Surfer software to show the evolution of the temperature field, as shown in Figure 12.

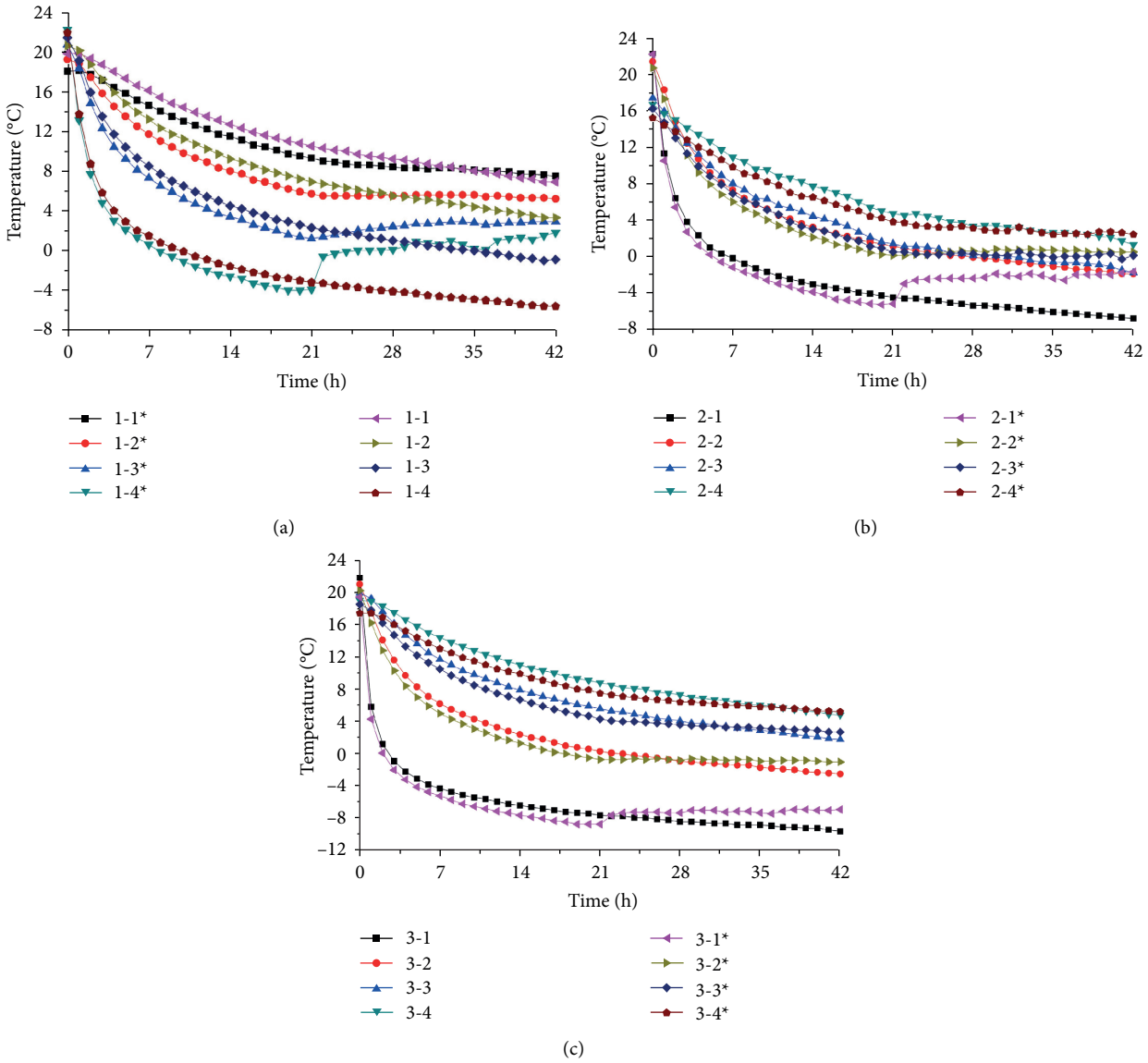

Figure 8: Temperature-time curves of SCF: (a) 90° monitoring points; (b) 45° monitoring points; (c) 0° monitoring points.

Figure 12(a) shows that the temperature cloud diagram of SCF at 42 h is butterfly-shaped, and the frozen wall above the limit pipe is thinner than that of EDCF and ESF. The development of the frozen soil curtain is effectively controlled when the limit pipe is opened, and the central temperature of the pipe jacking is also increased. Besides, the thickness of frozen soil in three freezing configurations is similar. That is, the frozen soil above the pipe jacking is thinner than that below the pipe jacking after freezing for 21 h, and the central temperature of ESF is the lowest.

5. Numerical Simulation and Discussion

5.1. Model Establishment. In order to more comprehensively understand the distribution of the freezing temperature field under the three configurations, the corresponding two-dimensional numerical models are established, as shown in Figure 13.

The heat transfer analysis module in ANSYS is adopted as the numerical simulation method using ANSYS software due to its high fidelity [20–22]. The grid system of the computational domain is created using a quadrilateral element, and its density is higher near the steel pipes and the freezers. The numerical model used in this paper has a minimum element size of 0.3 mm, which has a good mesh element quality and faster convergence results [23].

5.2. Boundary Condition. This model has three boundaries: the first boundary is the soil boundary, which is counted as insulation, and the initial soil temperature is set to 20°C. The second boundary and the third boundary are the freezer's wall and limiting-pipe wall, respectively, which are considered as the Dirichlet boundary condition with temperatures of −21°C and 7°C, respectively.

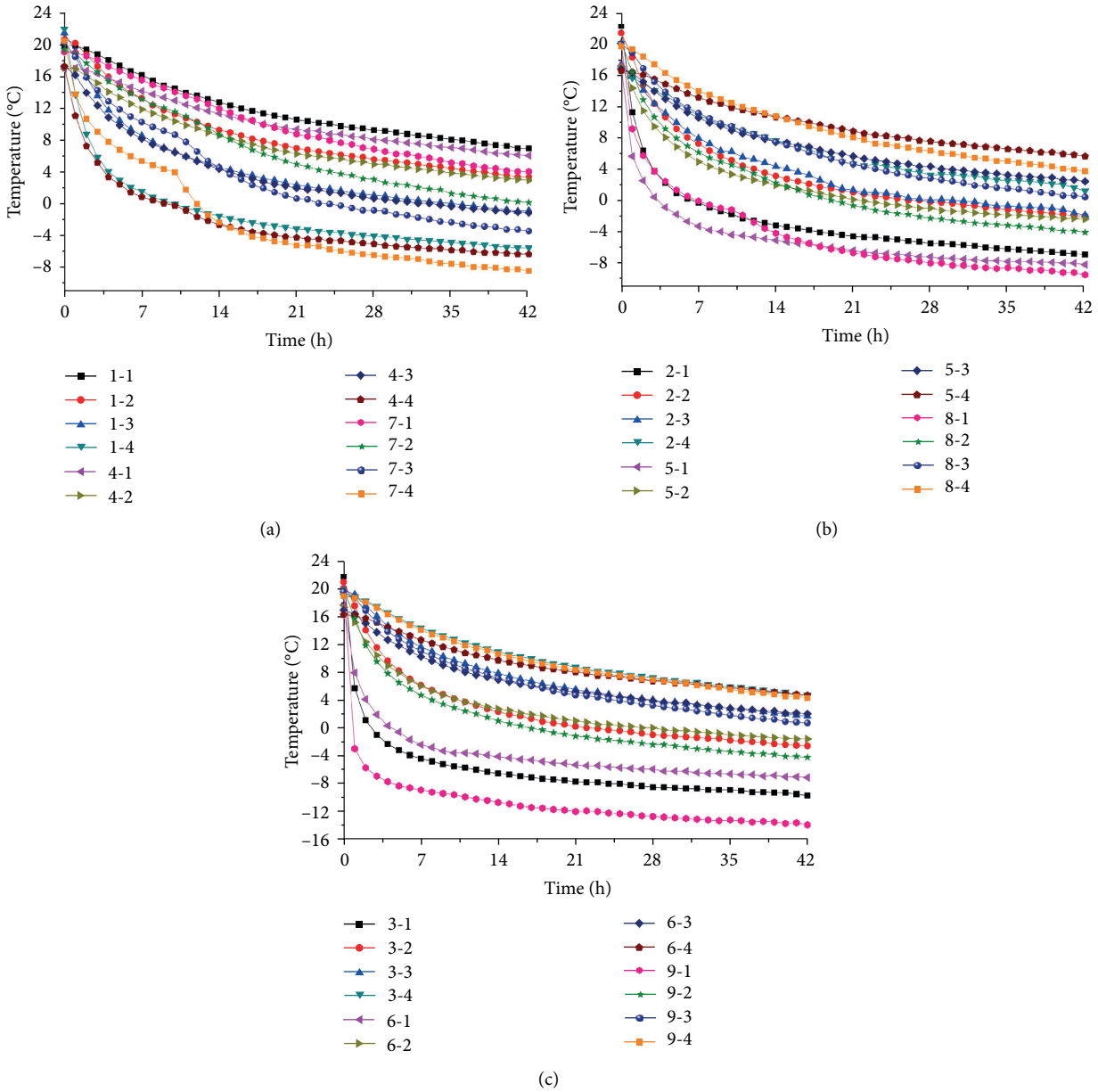

Figure 9: Temperature-time curves of SCF, EDCF, and ESF: (a) 90° monitoring points; (b) 45° monitoring points; (c) 0° monitoring points.

5.3. Freezing Temperature Field Simulation Results Discussion. Figure 14 shows the freezing temperature field of three configurations at 21 h and 42 h, respectively. It can be seen from Figure 13 that the temperature field around the steel pipe is evenly distributed. That is, the thickness of the frozen wall at the direction that upper, lower, left, and right of the steel pipe is basically the same, after freezing for 21 h. In engineering application, it is hoped that the development speed of frozen wall in the connecting direction of left and right freezers will be strengthened, which is conducive to the formation of closed frozen soil curtain between pipe jacking. Meanwhile, it is hoped that the development speed of the frozen wall perpendicular to the connecting line will be weakened, which is conducive to controlling the frost heave and thaw settlement of the formation. From Figure 14(b), the thickness of the frozen wall perpendicular to the connecting line of the freezers is effectively controlled after opening the limiting pipes, which forms a butterfly-shaped temperature field, the same of measured result. Besides, the freezing effect of EDCF and ESF is almost the same, which shows EDCF can replace ESF from the perspective of the convenience of production and processing.

In order to further evaluate the reliability of the model test, the temperature measurement results at the same position in the numerical simulation and the model test are compared as shown in Figure 15.

Figure 15(a) and 15(b) show that the results of numerical simulation and model test are in good agreement. Due to the regulation of the limit pipe, the temperature at the top of SCF is finally maintained at about 4°C, which can effectively

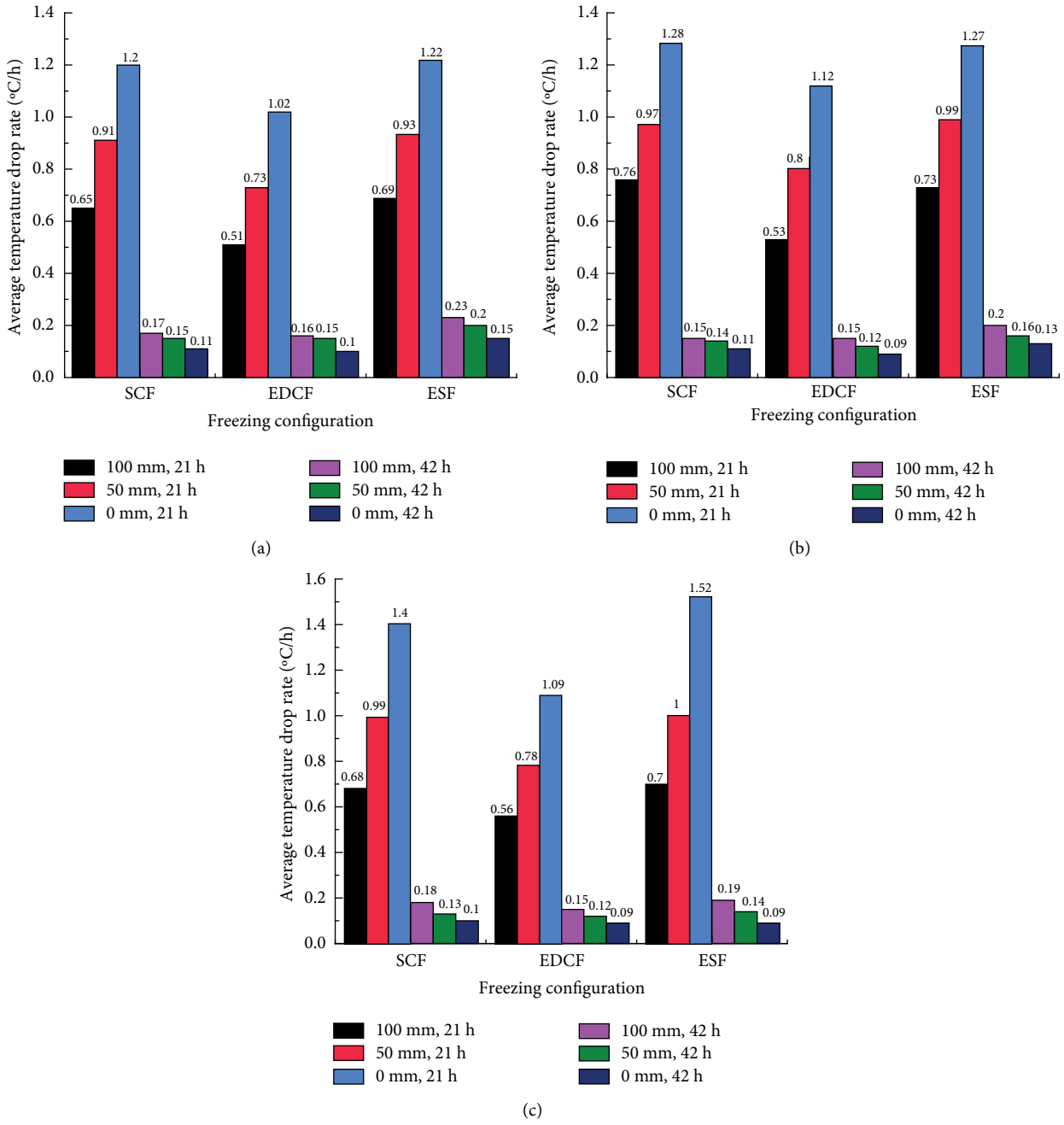

Figure 10: Average temperature drop rate of SCF, EDCF, and ESF: (a) 90° monitoring points; (b) 45° monitoring points; (c) 0° monitoring points.

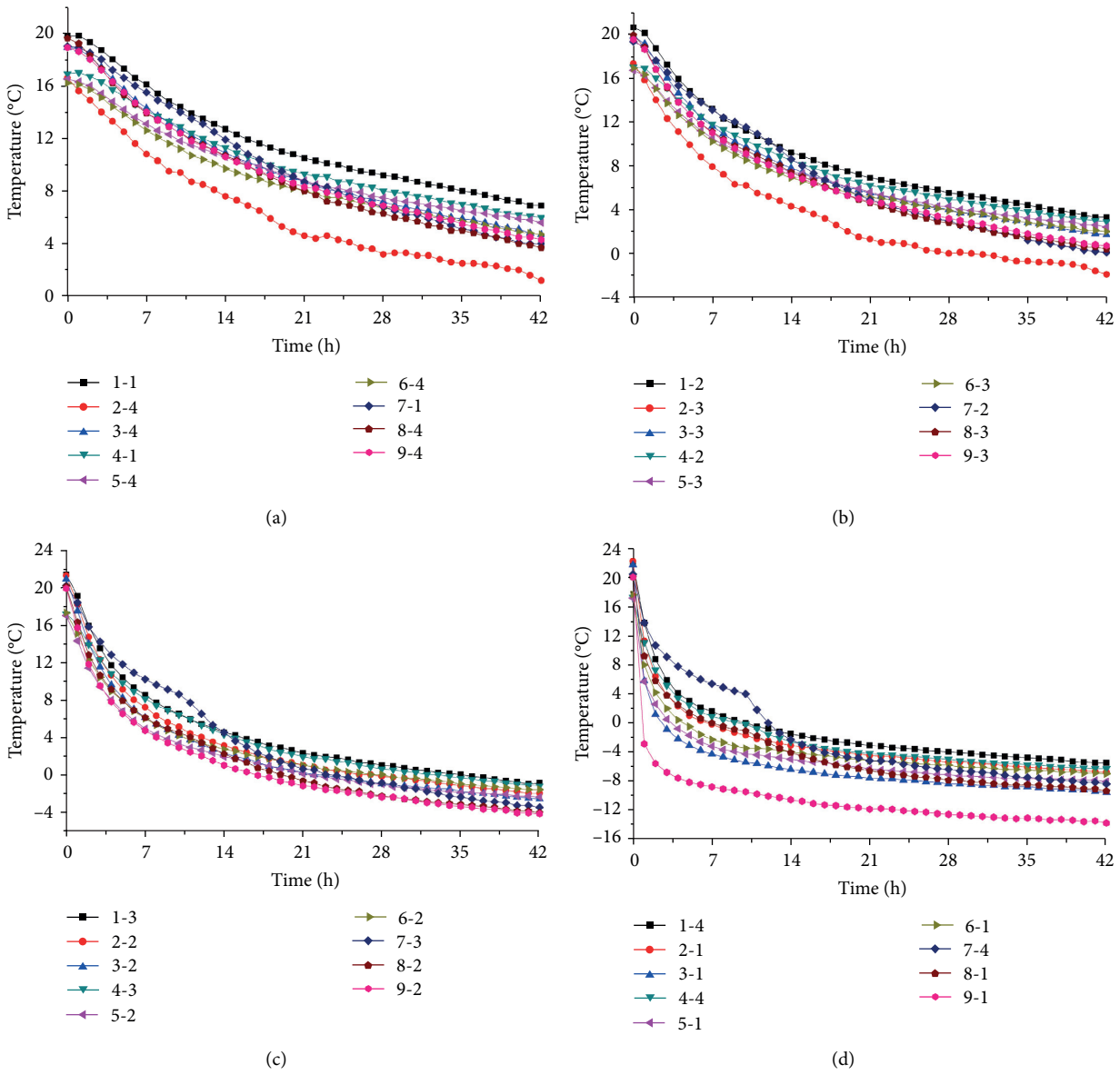

Figure 11: Temperature-time curves of the loop monitoring points: (a) 150 mm; (b) 100 mm; (c) 50 mm; (d) 0 mm.

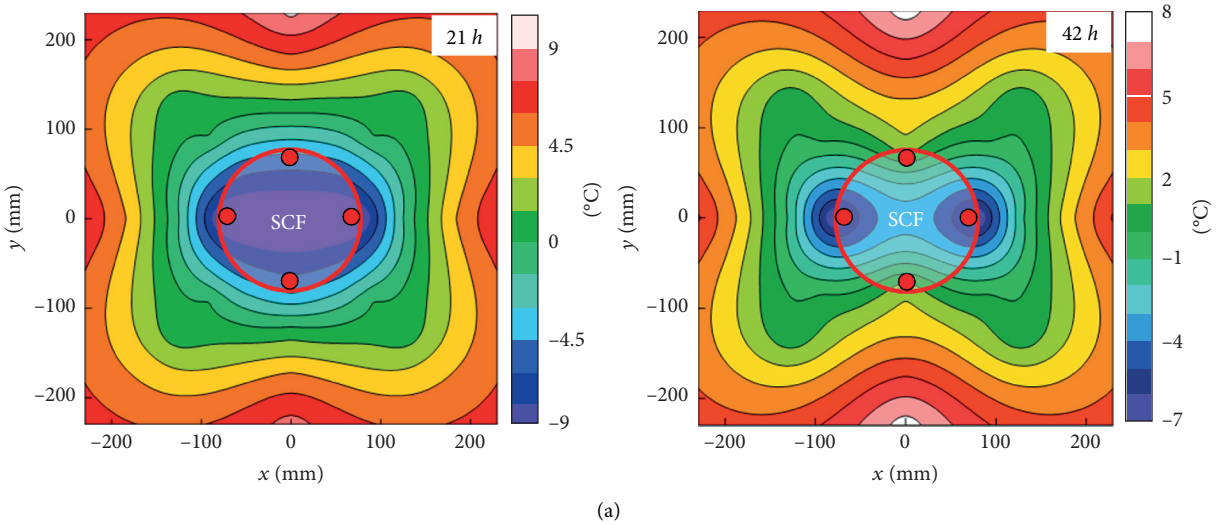

Figure 12: Continued.

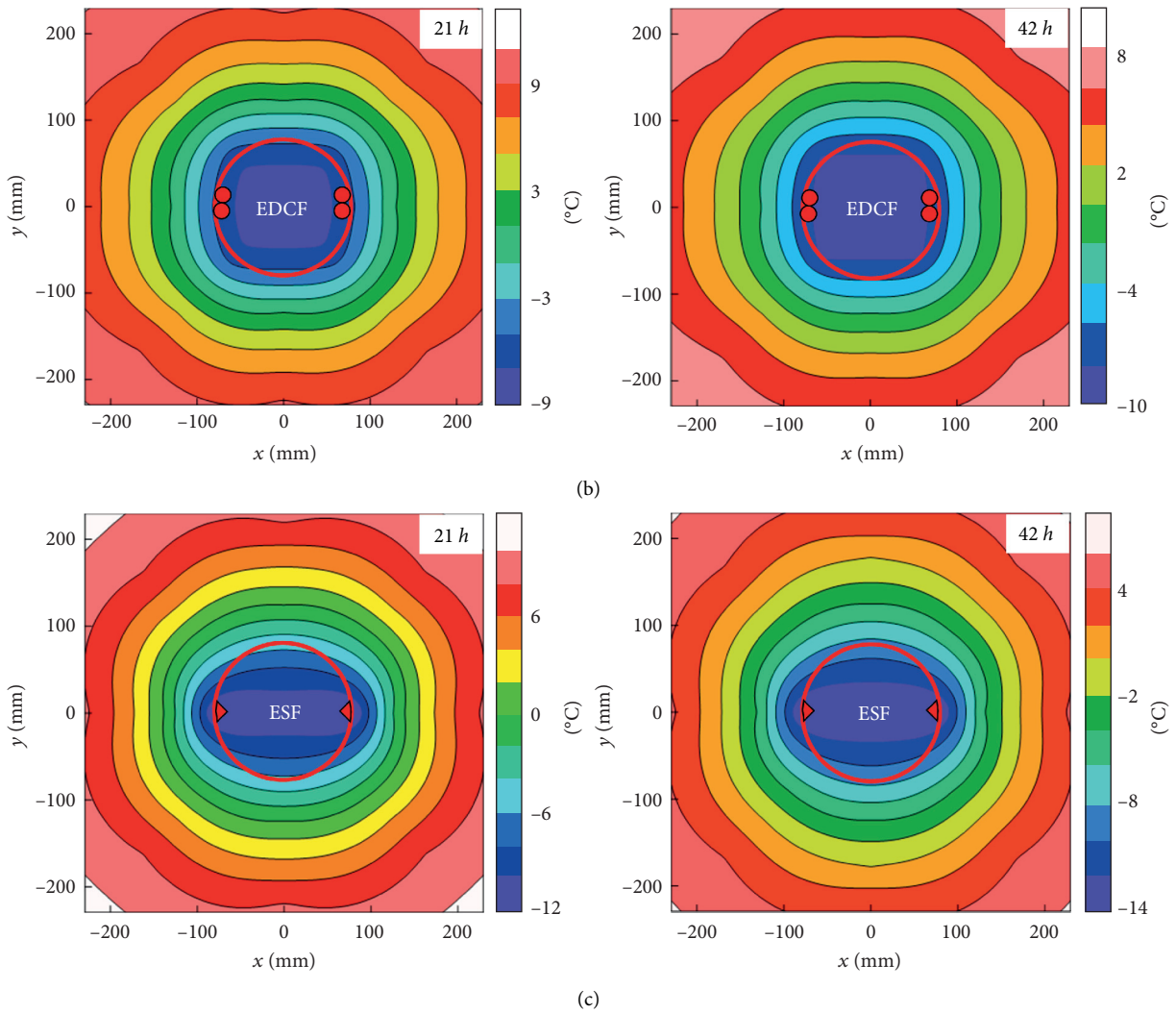

Figure 12: Temperature contour of the freeze-sealing pipe-roof: (a) SCF; (b) EDCF; (c) ESF.

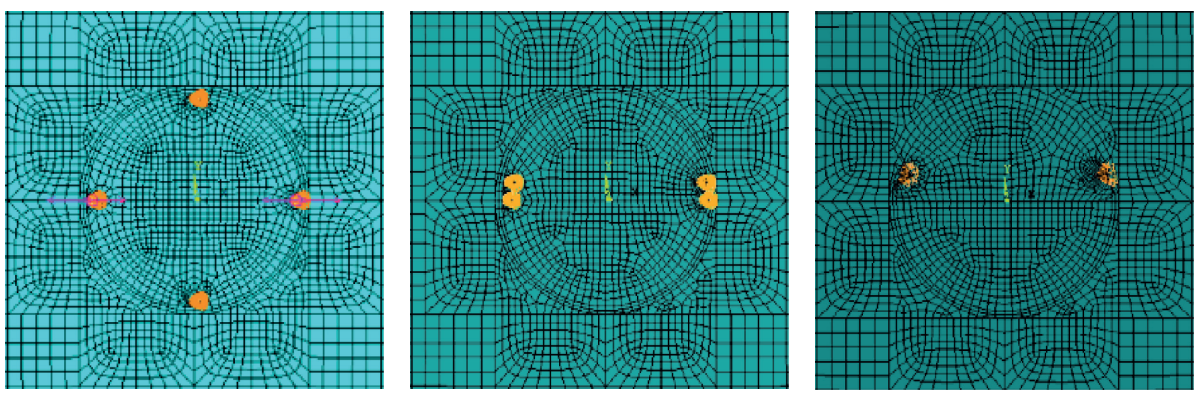

Figure 13: Meshing diagram: (a) SCF; (b) EDCF; (c) ESF.

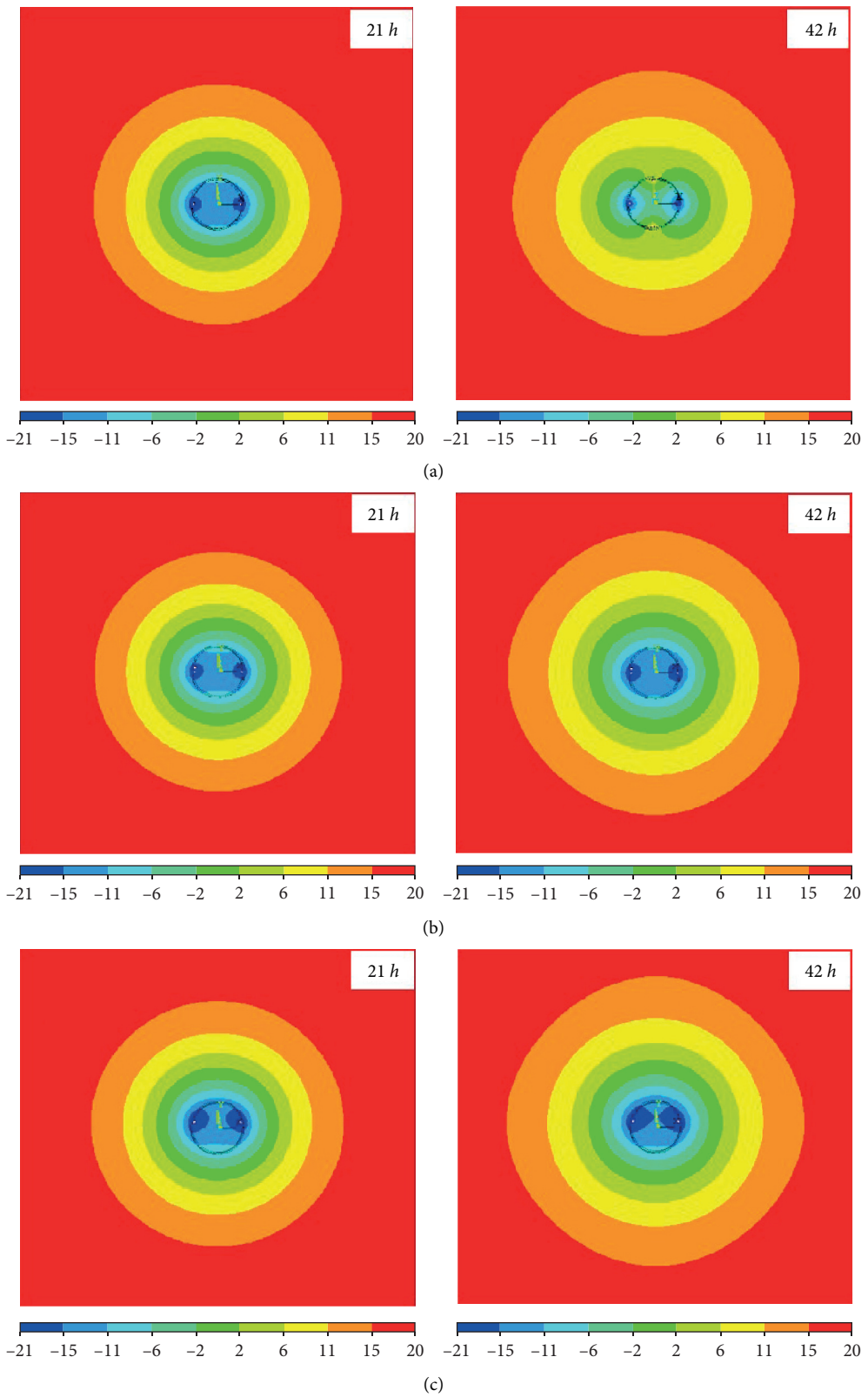

Figure 14: Freezing temperature field: (a) SCF; (b) EDCF; (c) ESF.

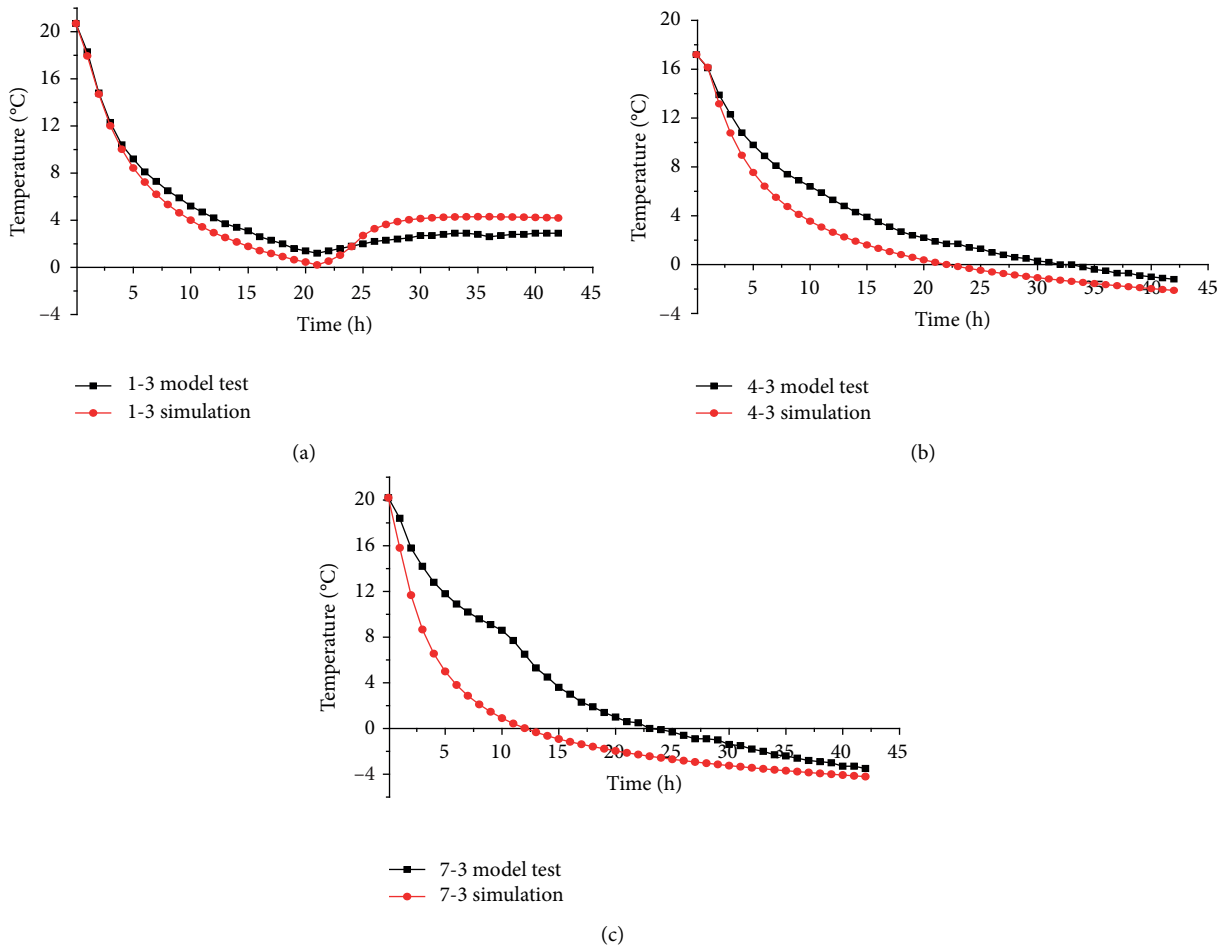

Figure 15: Temperature variation comparison diagram: (a) SCF; (b) EDCF; (c) ESF.

control the frost heave of the formation. Figure 15(c) shows a certain deviation between the model test and numerical simulation before 21 h. The temperature in the model test is higher than that in numerical simulation. During the model test, there was brine leakage at the mouth of the special-shaped freezer, but it was repaired quickly after finding this problem. Besides, the temperature drop process of EDCF is easier than that of ESF. The freezing effect of ESF is confirmed as the best amongst the three different arrangements (SCF, EDCF, and ESF) through model tests and numerical simulations.

6. Conclusions

In this study, the model test and numerical simulation methods are used to conduct an in-depth analysis of the freezing temperature field under different layouts of the freeze-sealing pipe-roof single pipe to obtain the optimal structural type and layout of the freezing device. The main contents and achievements of this study are as follows:

(1) A large-scale model test system of single-pipe freezing was established on the basis of the similarity criterion, and a comparative study was conducted on the temperature field of single-pipe freezing considering three arrangement modes freezers (SCF, EDCF, and ESF). The results showed that the temperature drop rates of SCF, EDCF, and ESF were 0.69°C/h, 0.53°C/h, and 0.71°C/h at 100 mm; 0.96°C/h, 0.77°C/h, and 0.97°C/h at 50 mm; 1.29°C/h, 1.08°C/h, and 1.34°C/h at 0 mm; after freezing for 21 h. Besides, the temperature drop rates of the three arrangements of freezers are all low after freezing for 42 h.

(2) The numerical simulation results showed that the temperature cloud diagram of SCF at 42 h is butterfly-shaped after opening the limit pipes, while the temperature cloud diagrams of ESF and EDCF are oval, and its results are highly consistent with the model test results.

(3) The model test results and numerical simulation results all showed that the freezing effect of ESF is the best amongst the three arrangements of freezers (SCF, EDCF, and ESF). However, the special-shaped freezer adopts arc angle steel welding, which is difficult to operate, and considerable welds and overhead welding must be performed. The welding requirements are high, and the freezing liquid may easily leak. Moreover, the maintenance cost is high in the later stage.

Therefore, EDCF instead of ESF can be considered to ensure the freezing effect of the frozen soil wall.

Data Availability

The datasets generated and analyzed during the current study are available from the corresponding author upon reasonable request.

Conflicts of Interest

The authors declare that there are no conflicts of interest regarding the publication of this paper.

Acknowledgments

This research was supported by the National Natural Science Foundation of China (Grant no. 51778004); Research Activities Funding for Reserve Candidate of Academic and Technical Leaders of Anhui Province, China (Grant no. 2018H170); Academic Funding for Top-notch Talents in University Disciplines (Majors) of Anhui Province, China (Grant no. gxbjZD10); and Graduate Innovation Funding of Anhui University of Science and Technology (no. 2020CX2024).

References

[1] Z. Hong, X. Hu, and T. Fang, "Analytical solution to steady-state temperature field of Freeze-Sealing Pipe Roof applied to Gongbei tunnel considering operation of limiting tubes," *Tunnelling and Underground Space Technology*, vol. 105, Article ID 103571, 2020.

[2] A. Afshani and H. Akagi, "Artificial ground freezing application in shield tunneling," *Japanese Geotechnical Society Special Publication*, vol. 3, no. 2, pp. 71–75, 2015.

[3] L. Zheng, Y. Gao, Y. Zhou, T. Liu, and S. Tian, "A practical method for predicting ground surface deformation induced by the artificial ground freezing method," *Computers and Geotechnics*, vol. 130, Article ID 103925, 2021.

[4] Q. Yan, W. Wu, C. Zhang, S. Ma, and Y. Li, "Monitoring and evaluation of artificial ground freezing in Metro tunnel construction-A case study," *KSCE Journal of Civil Engineering*, vol. 23, no. 5, pp. 2359–2370, 2019.

[5] J. Hu, Y. Liu, Y. Li, and K. Yao, "Artificial ground freezing in tunnelling through aquifer soil layers: a case study in nanjing Metro line 2," *KSCE Journal of Civil Engineering*, vol. 22, no. 10, pp. 4136–4142, 2018.

[6] X. Hu, S. Deng, and H. Ren, "In situ test study on freezing scheme of freeze-sealing pipe roof applied to the Gongbei tunnel in the Hong Kong-Zhuhai-Macau Bridge," *Applied Sciences*, vol. 7, no. 1, p. 27, 2016.

[7] Y. Sun, F. Wu, W. J. Sun, H. M. Li, and G. J. Shao, "Two underground pedestrian passages using pipe jacking: case study," *Journal of Geotechnical and Geoenvironmental Engineering*, vol. 145, no. 2, Article ID 05018004, 2019.

[8] S. L. Shen, Q. L. Cui, C. E. Ho, and Y. S. Xu, "Ground response to multiple parallel microtunneling operations in cemented silty clay and sand," *Journal of Geotechnical and Geoenvironmental Engineering*, vol. 145, no. 5, Article ID 04016001, 2016.

[9] L. Zhen, J.-J. Chen, P. Qiao, and J.-H. Wang, "Analysis and remedial treatment of a steel pipe-jacking accident in complex underground environment," *Engineering Structures*, vol. 59, no. 2, pp. 210–219, 2014.

[10] X. D. Hu, X. Y. Li, Y. H. Wu, L. Han, and C. B. Zhang, "Effect of water-proof in Gongbei Tunnel by freeze-sealing pipe roof method with field temperature data," *Chinese Journal of Geotechnical Engineering*, vol. 41, no. 12, pp. 2207–2214, 2019.

[11] X. Hu, Z. Hong, and T. Fang, "Analytical solution to steady-state temperature field with typical freezing tube layout employed in freeze-sealing pipe roof method," *Tunnelling and Underground Space Technology*, vol. 79, pp. 336–345, 2018.

[12] Y. Duan, C. Rong, H. Cheng, H. Cai, Z. Wang, and Z. Yao, "Experimental and numerical investigation on improved design for profiled freezing-tube of FSPR," *Processes*, vol. 8, no. 8, p. 992, 2020.

[13] X. Hu, T. Fang, J. Chen, H. Ren, and W. Guo, "A large-scale physical model test on frozen status in freeze-sealing pipe roof method for tunnel construction," *Tunnelling and Underground Space Technology*, vol. 72, pp. 55–63, 2018.

[14] Z. Zhou, J. Zhao, Z. Tan, and X. Zhou, "Mechanical responses in the construction process of super-large cross-section tunnel: a case study of Gongbei tunnel," *Tunnelling and Underground Space Technology*, vol. 115, Article ID 104044, 2021.

[15] Y. Qi, J. Zhang, H. Yang, and Y. Song, "Application of artificial ground freezing technology in modern urban underground engineering," *Advances in Materials Science and Engineering*, vol. 2020, Article ID 1619721, 12 pages, 2020.

[16] Y. Liu, K.-Q. Li, D.-Q. Li, X.-S. Tang, and S.-X. Gu, "Coupled thermal-hydraulic modeling of artificial ground freezing with uncertainties in pipe inclination and thermal conductivity," *Acta Geotechnica*, vol. 2, 2021.

[17] M. Vitel, A. Rouabhi, M. Tijani, and F. Guérin, "Modeling heat transfer between a freeze pipe and the surrounding ground during artificial ground freezing activities," *Computers and Geotechnics*, vol. 63, pp. 99–111, 2015.

[18] G. X. Cui, *Similarity Theory and Model Test*, China University of Mining and Technology Press, Xuzhou, China, 1990.

[19] Z. S. Yao, H. Cheng, and H. B. Xia, "Model test study on frost-heaving force in retaining structure of row-piles and frozen soil wall of super deep foundation pit," *Chinese Journal of Rock Mechanics and Engineering*, vol. 26, no. 2, pp. 415–420, 2007.

[20] H. B. Cai, H. Cheng, Z. S. Yao, and H. Wang, "Numerical analysis of ground displacement due to orthotropic frost heave of frozen soil in freezing period of tunnel," *Chinese Journal of Rock Mechanics and Engineering*, vol. 34, pp. 1667–1676, 2015.

[21] Y. M. Lai, S. Y. Liu, Z. W. Wu, and W. B. Yu, "Approximate analytical solution for temperature fields in cold regions circular tunnels," *Cold Regions Science and Technology*, vol. 34, pp. 43–49, 2002.

[22] X.-D. Hu, T. Fang, and Y.-G. Han, "Mathematical solution of steady-state temperature field of circular frozen wall by single-circle-piped freezing," *Cold Regions Science and Technology*, vol. 148, pp. 96–103, 2018.

[23] R. Hong, H. Cai, and M. Li, "Integrated prediction model of ground Surface deformation during tunnel construction using local horizontal freezing technology," *Arabian Journal for Science and Engineering*, vol. 10, 2021.